

# Contents

1. <i>Introduction</i>	13
1.1. Supramolecular Chemistry	14
1.2. Molecular Recognition	15
1.3. Supramolecular Devices	16
2. <i>Fundamental Principles</i>	21
2.1. Supramolecular Photochemistry	21
2.2. Basic Concepts	23
2.3. Photoinduced Energy Transfer	27
2.3.1. The Coulombic Mechanism	29
2.3.2. The Exchange Mechanism	30
2.3.3. Excimers and exciplexes	31
2.4. Photoinduced Electron Transfer	32
2.4.1. The Electronic Factor	33
2.4.2. The Nuclear Factor	35
3. <i>Methods</i>	37
3.1. Photophysical Techniques	37
3.1.1. Electronic Absorption Spectra	37
3.1.2. Luminescence Spectra	38
3.1.3. Luminescence Quantum Yield	39
3.1.4. Time-resolved Luminescence Measurements	40
3.1.5. Nanosecond Transient Absorption Spectra	41
3.1.6. Femtosecond Transient Absorption Spectra	42
3.1.7. Two-Photon Induced Luminescence Spectra	45
3.1.8. Stopped-flow spectrophotometry	47
3.2. Photochemical Measurements	48
3.3. Electrochemical Techniques	49
3.3.1. Cyclic Voltammetry	50
3.3.2. Differential Pulse Voltammetry	51
3.3.3. Chronoamperometry	51
3.3.4. Spectroelectrochemistry	52

4. <i>Materials</i>	53
4.1. Supramolecules and Large Molecules	53
4.2. Dendrimers	54
4.3. Metal Complexes	59
4.4. Macrocycles	62
4.5. Conjugated Polymers	66
5. <i>Dendrimers</i>	73
5.1. Light Harvesting Dendrimers	73
5.1.1. Recognition-mediated Intercomponent Energy-transfer	73
5.1.2. Temperature-dependent Intradendrimer Energy-transfer	89
5.2. Dendrimers Containing 4,4'-Bipyridinium Units	110
5.2.1. Aromatic Electron-Acceptors based on N-Heterocycles	110
5.2.2. Charge-Pooling Dendrimers	137
5.2.3. Dendrimers as Hosts	149
5.2.4. Dendrimers as Guests	154
6. <i>Metal Complexes</i>	197
6.1. Phosphino-Aminothiazoline Pt(II) Complexes	197
6.2. Crown Ether containing Ru(II) Complexes	218
7. <i>Macrocycles</i>	234
7.1. Shape-Persistent Macrocycles	234
7.2. Furan-containing [n.2] Cyclophanes	266
8. <i>Conjugated Polymers</i>	282
8.1. Polyfluorene	282
8.2. Fluorene-based Conjugated Copolymers	291
9. <i>List of Publications</i>	306





## **1. Introduction**

Pristine state is dense and hot.

Then our universe grows.

And keeps expanding.

Matter annihilates originating light.

Progressive cooling allows remaining elementary particles to slow down and aggregate.

Later atoms come. Their combinations form molecules which in turn associate in more and more complex structures till life emerges and beyond.

We cannot get out our universe.

Anyway there's a bunch of things we can do into it.

Chemists deal with matter.

And its transformations.

They create molecules rearranging atoms —but handling molecules— into an infinite variety of combinations, at least until they have imagination.

Some of them hold molecules together trying to gain control on increasing complexity.

Life is the highest expression of complex matter.

Complexity does not result by mere addition of molecular components, but implies their mutual interactions.

Novel features appear at each level of complexity, peculiar of the whole system rather than the sum of components.

Such features characterize each level of complexity and cannot exist, even conceptually, at the levels below.

On the basis of the chemical components at lower levels and of their interactions and integrating them in order to connect a level to the others, increasing complexity can be described and explained.

Supermolecules represent a step towards complexity compared to molecules as the latter do to atoms.

Some visionaries aim to control and direct matter organization together with emerging structures and functions, so dreaming to bridge the gap between the inanimate and life. Yet, there may be expressions of the processes characterizing life other than we know. So other forms of life can exist and one might try to set up fundamentals for the creation of artificial forms of life.

### **1.1. Supramolecular Chemistry**

In a historical perspective, as evidenced by Jean-Marie Lehn,<sup>1</sup> supramolecular chemistry originated from Paul Ehrlich's idea that molecules have to bind to react,<sup>2</sup> thus introducing the concept of receptor. Binding processes have to be selective as outlined by Emil Fischer's lock-and-key image of steric fit,<sup>3</sup> implying geometrical complementarity and by Alfred Werner's work on coordination chemistry,<sup>4</sup> pointing out that binding requires interactional complementarity.

Despite these concepts have been recognized and studied since long time, only in the late 70s supramolecular chemistry emerged as a discipline. Its development required concomitant acceptance of novel ideas arising from unprecedented conceptualization of experimental observations, availability of powerful chemico-physical techniques for analyzing structures and

---

[1] J.-M. Lehn, *Supramolecular Chemistry: Concepts and Perspectives*, VCH, Weinheim, 1995.

[2] P. Ehrlich, *Studies on Immunity*, Wiley, New York, 1906.

[3] E. Fischer, *Ber. Deutsch. Chem. Ges.*, 1894, 27, 2985.

[4] A. Werner, *Zeitschr. Anorg. Chem.*, 1893, 3, 267.

properties of the new systems, and the fascinating and high interdisciplinary character of the emerging field that attracted increasing number of scientists. Its consecration led to the award of the Nobel Prize in Chemistry to C.J. Pedersen,<sup>5</sup> D.J. Cram,<sup>6</sup> and J.-M. Lehn<sup>7</sup> in 1987.

The most authoritative and widely accepted definition of supramolecular chemistry is that given by J.-M. Lehn, namely “*chemistry beyond the molecule*”. Supramolecules are organized entities of higher complexity resulting from the association of two or more chemical species held together by intermolecular forces.<sup>1,4</sup> Molecular chemistry rules over the covalent bond due to the great achievements of organic synthesis after the second world war; supramolecular chemistry aims to establish its power over intermolecular bond.

Intermolecular interactions define stability, lability, selectivity, and mutual action and conformational rearrangements of the supermolecules. Intermolecular interactions are the basis of recognition reaction, transport, regulation, transduction, etc. processes that allow life. Scientists can find inspiration in Nature to design artificial systems. Realization of systems displaying highly selective processes and capable of efficiently performing functions requires control over intermolecular forces and their proper handling.

## 1.2. Molecular Recognition

Molecular recognition<sup>1</sup> is defined by the information and the energy involved in selection and binding of substrate(s) by a given receptor molecule. Molecular recognition phenomena imply formation of supramolecular species characterized by peculiar structural, thermodynamic and kinetic features determined by molecular information stored in receptor and substrate(s) leading to selective binding.

---

[5] C.J. Pedersen, *Angew. Chem. Int. Ed. Engl.*, 1988, 27, 1021.

[6] D.J. Cram, *Angew. Chem. Int. Ed. Engl.*, 1988, 27, 1009.

[7] J.-M. Lehn, *Angew. Chem. Int. Ed. Engl.*, 1988, 27, 89.

Molecular information resides in the geometrical features such as size shape conformation chirality, and in the electronic properties of the molecules taking part in recognition phenomena. Strong and selective recognition implies match of either steric and interactional complementarity between the binding domains. Lability of the supramolecular adducts represents the rate determining step in reading out the information carried by molecular components.

Furthermore, stability and selectivity of the supermolecule depend on the medium and result from a subtle balance between solvation (of both receptor and substrate) and complexation (i.e. 'solvation' of the substrate by the receptor). Consequently, binding properties might markedly be affected by the medium when charged species are involved.

Once again, biological systems provide the highest and most complex examples of molecular recognition leading to selective binding, recognition, reaction, transport, regulation, transduction, etc. processes.

### **1.3. Supramolecular Devices**

One of the most important challenges in science and technology is pursuing further miniaturization. Instead of carving matter into smaller and smaller pieces, an alternative and promising strategy towards technology at the nanometer scale is offered by the small-upward (bottom-up) approach, which starts from atom<sup>8</sup> or molecules and builds up to nanostructures. Chemists, by the nature of their discipline, are already at the bottom, since they are able to manipulate atoms and molecules. Therefore they are in the ideal position to develop bottom-up strategies for the construction of nanoscale devices and machines.

---

[8] The idea that atoms could be used to construct nanoscale machines was first raised by R. P. Feynman, "*There is plenty of room at the bottom*". The key sentence of Feynman's talk is the following: "*The principle of physics do not speak against the possibility of maneuvering things atom by atom*". (a) R.P. Feynman, *Eng. Sci.*, 1960, 23, 22. (b) R.P. Feynman, *Saturday Rev.*, 1960, 43, 45.

Molecules began to be conceived as much more convenient building blocks than atoms to build more complex systems. The main reasons at the basis of this idea are as follows: (i) molecules are stable species, whereas atoms are difficult to handle; (ii) Nature starts from molecules, not from atoms, to construct the great number and variety of nanodevices and nanomachines that sustain life; (iii) most of the laboratory chemical processes are dealing with molecules, not with atoms; (iv) molecules are objects that already exhibit distinct shapes and carry device-related properties (e.g., properties that can be manipulated by photochemical and electrochemical inputs); (v) molecules can self-assemble or can be connected to make larger structures.<sup>9</sup>

The concept of molecules as nanoscale objects exhibiting their own shape, size, and properties has been confirmed by new, very powerful techniques, such as single-molecule fluorescence spectroscopy and the various types of probe microscopies, capable of “seeing”<sup>10</sup> or “manipulating”<sup>11</sup> single molecules. It has been possible, for example, to make ordered arrays of molecules and even to investigate bimolecular chemical reactions at the single molecule level.<sup>12</sup>

The macroscopic concepts of a device can be straightforwardly extended to the molecular level.<sup>13</sup> A *molecular-level device* can be defined as an assembly of a discrete number of molecular components -a supramolecular structure- designed to achieve a specific function. Each molecular component performs a single act, while the entire supramolecular assembly performs a more complex function, which results from the cooperation of the various

- 
- [9] V. Balzani, A. Credi, M. Venturi, *Molecular Devices and Machines: Concepts and Perspectives for the Nanoworld*, Wiley-VCH, Weinheim, 2008
- [10] (a) *Single Molecule Spectroscopy*, (Eds.: R. Rigler, M. Orrit, I. Talence, T. Basché), Springer-Verlag, Berlin, 2001. (b) W.E. Moerner, *J. Phys. Chem. B*, 2002, 106, 910. (c) *Single Molecule Detection in Solution* (Eds.: Ch. Zander, J. Enderlein, R.A. Keller), Wiley-VCH, Weinheim, 2002.
- [11] S.-W. Hla, G. Meyer, K.-H. Rieder, *ChemPhysChem*, 2001, 2, 361.
- [12] See, e.g.: T. Christ, F. Kulzer, P. Bordat, T. Basché, *Angew. Chem. Int. Ed.*, 2001, 40, 4192.
- [13] (a) V. Balzani, A. Credi, M. Venturi, in *Supramolecular Science: Where It is and Where It is Going* (Eds.: R. Ungaro, E. Dalcanale), Kluwer, Dordrecht, 1999, p. 1. (b) V. Balzani, A. Credi, M. Venturi, in *Stimulating Concepts in Chemistry* (Eds.: M. Shibasaki, J.F. Stoddart, F. Vögtle), Wiley-VCH, Weinheim, 2000, p. 255.

components. Molecular-level devices operate via electronic and/or nuclear rearrangements and, like macroscopic devices, they need energy to operate and signals to communicate with the operator.

The first steps along the bottom-up strategy consist in the designing molecular-level structures capable of responding to external stimuli. Information processing at the supramolecular level is recognition-dependent: molecular recognition phenomena may be transduced into processes and signals, by the use of suitable molecular components undergoing structural organization through intercomponent interactions and conformational rearrangements into the resulting supermolecule and responding to external stimulations.<sup>1</sup>

Supramolecular devices have to functionally integrate operations of each molecular component after being structurally organized. Such a structural organization may be more easily achieved covalently linking molecular components. Recognition and self-assembly introduce relevant difficulties in programming supramolecular devices that can be overcome taking advantage by powerful strategies and techniques of synthetic chemistry. Moreover, reversibility and resistance to fatigue should be enhanced preventing disassembling of the supramolecular devices.

Integration of the operations of the individual components giving rise to the novel functional properties, in fact, confers supramolecular character to the resulting structure regardless of the nature of the bonds that link the units.

In the case of chemical systems that are investigated from the viewpoint of the effects caused by external stimulations, the definition of supramolecular species can be based on the degree of intercomponent electronic interactions.<sup>1,14,15</sup> In more general terms, when the interaction energy between units is small compared to the other relevant energy parameters, a

---

[14] (a) V. Balzani and F. Scandola, *Supramolecular Photochemistry*, Ellis Horwood, New York, 1991. (b) V. Balzani, F. Scandola in *Comprehensive Supramolecular Chemistry* (Eds.: J.L. Atwood, J.E.D. Davies, D.D. Macnicol, F. Vögtle), Pergamon Press, Oxford, 1996, Vol. 10, p. 687.

[15] V. Balzani, *Tetrahedron*, 1992, 48, 10443.

system can be considered a supramolecular species. Therefore, species made of covalently-linked (but weakly interacting) components can be taken as belonging to the supramolecular domain.



## **2. Fundamental Principles**

### **2.1. Supramolecular Photochemistry**

Nuclei and electrons are charged particles and their motions in atoms and molecules generate oscillating electric and magnetic fields. Light consists of oscillating electric and magnetic fields. If the frequency of the light oscillation and the frequency of the electron or molecule "transition motion" match, an atom or molecule can absorb energy from light. Thus light absorption is widely used to probe the nature of matter (that's the aim of spectroscopy).

Photochemistry describes chemico-physical processes occurring in molecules undergoing electronic transitions upon absorption of near UV and visible light.

Supramolecular photochemistry deals with entities constituted by photoactive components that may be expected to undergo mutual perturbation, so giving rise to novel photophysical and photochemical properties peculiar of the supramolecular systems. It should be noted that the properties of each component of a supramolecular species, i.e., of an assembly of weakly interacting molecular components, can be determined from the study of the isolated components or of suitable model molecules.

Properties arising in supramolecular species are not the simple superposition of those of the component units. As already stated, increasing complexity gives rise to novel features. Processes involving two or more components, such as intercomponent energy, electron or proton transfer, substrate binding, photochemical reactions, catalysis, etc. take place in a supermolecule rather than between the isolated units.

Besides photons, molecules can process electrons. Consequently, novel electrochemical properties may emerge in a supermolecular system defining the field of supramolecular electrochemistry.

Molecules can process chemical species, carrying high information content due to their multiple molecular (size, shape and charge) and supramolecular (geometry, strength and selectivity of the binding processes) features.

Yet, molecules can generate electrons and ions upon photoexcitation, photons and ions upon electrical stimulation so tightly connecting the domains of supramolecular chemistry to photochemistry and electrochemistry.

Using simple experimental and theoretical models, supramolecular photochemistry provides useful tools in investigating complex photobiological processes such as photosynthesis and vision. Mimicking natural phenomena consequently follows: since early examples of triads for vectorial charge separation<sup>16</sup> and light harvesting antennae,<sup>17</sup> some scientists attempt to move toward realization of artificial photosynthesis. Besides processes, Nature suggests building blocks for the construction of photoactive devices such as porphyrins, carotenoids, quinones, phthalocyanins, etc.

Also current macroscopic devices can stimulate minds: they make use of electrical and light signals to transfer, store and retrieve information. Although it is not necessarily the case that the components of chemical computer<sup>18</sup> have to operate in ways analogous to those of conventional silicon-based computers, it seems likely that information processing at the molecular level will be essentially based on electrical and light stimuli.

Photons can supply the energy that make the supramolecular devices work, without accumulation of waste products. Furthermore, the use of light presents multiple advantages such as: (i) easy and rapid switching on and off; (ii) lasers provide the opportunity of

---

[16] P. Seta, E. Bienvenue, A.L. Moore, P. Mathis, R.V. Bensasson, P. Liddell, P.J. Pessiky, A. Joy, T.A. Moore, D. Gust, *Nature*, 1985, 316, 653.

[17] B. Alpha, V. Balzani, J.-M. Lehn, S. Perathoner, N. Sabbatini, *Angew. Chem. Int. Ed. Engl.*, 1987, 26, 1266.

[18] (a) D. Rouvray, *Chem. Br.*, 1998, 34(2), 26. (b) D. Rouvray, *Chem. Br.*, 2000, 36(12) 46. (c) P. Ball, *Nature*, 2000, 406, 118. (d) R. Dagani, *Chem. Eng. News*, 2000, October 16, 27. (e) *Sci. Am.*, 2001, 285(3), Special issue on Nanotechnology.

confining the excitation energy in narrow space and short time domains; (iii) photons can be useful to “read” the state of the system and thus controlling and monitoring the operations of the machine.

It should be remarked that the previously mentioned applications are still far in the future: the most of the studies have been performed in solution while useful supramolecular devices and machines require high order degree of components and their interfacing with the macroscopic world of the potential users. Anyway there is great interest on these topics: concepts stimulate research, scientific results refine and suggest concepts requiring new terminology, growing simultaneously and feeding on each other.

## 2.2. Basic Concepts

The first event in most photophysical and photochemical processes is the absorption of photon by a molecule:

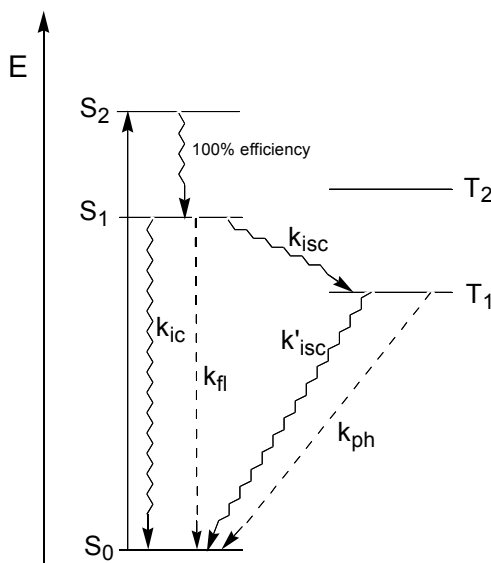


Figure 2.1. Jablonski diagram for an organic molecule. S<sub>n</sub> Singlet state, T<sub>n</sub> Triplet state, k<sub>isc</sub> intersystem crossing rate constant, k<sub>ic</sub> internal conversion rate constant, k<sub>f</sub> fluorescence rate constant, k<sub>ph</sub> phosphorescence rate constant.

As reported in the Jablonski diagram (Figure 2.1.), in most cases the ground state of organic molecules is a singlet state ( $S_0$ ), while the excited states are either singlets ( $S_1$ ,  $S_2$ , etc) and triplets ( $T_1$ ,  $T_2$ , etc). In principle, transitions between states having the same spin value are allowed, whereas those between states of different spin are forbidden. Therefore, the electronic absorption bands observed in the UV-Visible spectrum usually correspond to  $S_0 \rightarrow S_n$  transitions.

Excited states are unstable species that undergo deactivation by intrinsic (first order kinetics) processes releasing light and heat or photoproducts different from the original molecules. When a molecule is excited to upper singlet excited states, it usually undergoes a fast and unitary efficient radiationless deactivation (internal conversion, ic) to the lowest singlet excited state,  $S_1$ . Such an excited state undergoes deactivation via three competing processes: nonradiative decay to the ground state (internal conversion, rate constant  $k_{ic}$ ); radiative decay to the ground state (fluorescence,  $k_f$ ); conversion to the lowest triplet state  $T_1$  (intersystem crossing,  $k_{isc}$ ). In its turn,  $T_1$  can undergo deactivation via nonradiative (intersystem crossing,  $k'_{isc}$ ) or radiative (phosphorescence,  $k_{ph}$ ) decay to the ground state  $S_0$ .

The kinetic constants of the deactivation processes usually cannot be measured directly. What can be easily measured is the lifetime ( $\tau$ ) of an excited state, i.e. the time needed to reduce the excited state concentration by a factor corresponding to Neper constant, which is given by the reciprocal of the summation of the first order deactivation rate constants:

$$\tau (S_1) = 1 / (k_{ic} + k_f + k_{isc}) \quad (2)$$

$$\tau (T_1) = 1 / (k'_{isc} + k_{ph}) \quad (3)$$

The orders of magnitude of  $\tau (S_1)$  and  $\tau (T_1)$  are approximately  $10^{-9}$ - $10^{-7}$  s and  $10^{-3}$ - $10^0$  s, respectively. When the molecule contains heavy atoms, the formally forbidden intersystem crossing and phosphorescence processes become faster.

Any process has its own quantum yield, i.e., the ratio between the number of photons or molecules produced and the number of absorbed photons. These quantities, obviously ranging between 0 and 1, are given by the following expressions:

$$\Phi_{fl} = k_{fl} / (k_{ic} + k_{fl} + k_{isc}) \quad (4)$$

$$\Phi_{ph} = k_{ph} k_{isc} / [(k'_{isc} + k_{ph}) (k_{ic} + k_{fl} + k_{isc})] \quad (5)$$

Electronically excited states obtained when molecules absorb light of suitable energy (eq. 1.) are species with quite different properties compared with those of the ground state molecule.<sup>19</sup> In fluid solution, excited states can easily undergo deactivation interacting with other chemical species (second order kinetics). From a functional point of view, photoinduced energy- and electron-transfer processes, represented in eqs. 6. and 7.-8., are the most interesting among all bimolecular deactivation pathways:




---

[19] (a) V. Balzani, F. Scandola, *Supramolecular Photochemistry*, Chichester, UK:Horwood, 1991. (b) N. J. Turro, *Modern Molecular Photochemistry*, Benjamin, 1978. (c) A. Gilbert, J. Baggott, *Essentials of Molecular Photochemistry*, Backwell, Oxford, 1991. (d) J. R. Lakowicz, *Principles of Fluorescence Spectroscopy*, Plenum, New York, 1999.

## *Supramolecular Photoactive Systems*

In both cases luminescence of the A species is quenched; the B species luminescence can be sensitized by energy-transfer, while charge-separation occurs by electron-transfer.

Suitable choice of the A and B species and their structural organization lead to the assembly of a supramolecular species, i.e., A-B. As previously discussed, A-B properties cannot be exactly predicted by those of the isolated A and B but, only integrating features of the isolated molecular components the peculiarities of the resulting supermolecule can be described and explained.

After the absorption of a photon by the A unit (eq. 9.), the B unit takes part in deactivation processes of the excited state localized on the A component via energy- (eq. 10.) and electron- (oxidative, eq. 11. and reductive, eq. 12.) transfer:



In the absence of chemical complications, regeneration of the starting ground state system occurs: photoinduced energy-transfer is followed by radiative and/or non-radiative deactivation of the excited acceptor B (eq. 13.), while photoinduced electron-transfer processes are followed by spontaneous back electron-transfer reactions (eqs. 14. and 15.):





It should be useful to remark that, besides photo- and electro-active units performing programmed operations and structural components spatially organizing active units, ancillary components may be used to perturb or even modify properties arising by the interactions involving the other components. This is particularly evident analyzing the role of the bridging units in mediating energy- and electron-transfer processes between donor and acceptor moieties in supramolecular systems.<sup>20</sup>

### 2.3. Photoinduced Energy Transfer

The thermodynamic ability of an excited state to undergo energy-transfer processes is related to the zero-zero spectroscopic energy,  $E_{0-0}$ , of the involved units:

$$\begin{aligned} \Delta G &= G(A) + G(B^*) - G(A^*) - G(B) = \\ &= -\Delta G(^*A,A) + \Delta G(^*B,B) \cong E_{0-0}(^*B,B) - E_{0-0}(^*A,A) \leq 0 \end{aligned}$$

$$\text{so, } E_{0-0}(^*A,A) \geq E_{0-0}(^*B,B) \quad (16)$$

The energy-transfer process must obey energy conservation and requires electronic interaction between donor and acceptor units. Energy transfer in a supramolecular system can be viewed as a radiationless transition between two “localized” electronically excited states

[20] (a) N.G. Lokan, M.N. Paddon-Row, M. Koeberg, J.W. Verhoeven, *J. Am. Chem. Soc.*, 2000, 122, 5075. (b) A.M. Napper, I. Read, D.H. Waldeck, N.J. Head, A.M. Oliver, M.N. Paddon-Row, *J. Am. Chem. Soc.*, 2000, 122, 5220. (c) D.M. Guldi, C. Luo, M. Prato, A. Troisi, F. Zerbetto, M. Scheloske, E. Dietel, W. Bauer, A. Hirsch, *J. Am. Chem. Soc.*, 2001, 123, 9166.

(“localized” on A and B, eq. 10.). Therefore, the rate constant can be obtained by an appropriate Fermi “golden rule” expression:

$$k_{\text{en}} = (4\pi/h) (H^n)^2 FC^n \quad (17)$$

where  $H^n$  is the electronic coupling between the two excited states interconverted by the energy-transfer process and  $FC^n$  is an appropriate Franck-Condon factor.

The electronic factor  $H^n$  is a two-electron matrix element involving the HOMOs and LUMOs of the energy-donor and energy-acceptor components.

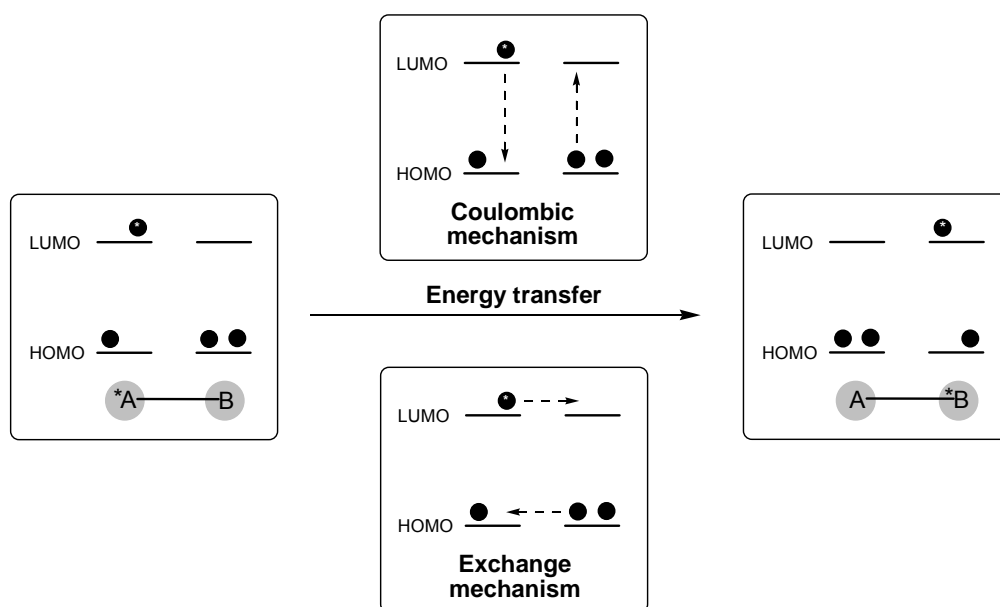


Figure 2.2. Pictorial representation of the coulombic and exchange energy-transfer mechanisms.

Following standard arguments,<sup>19,21</sup> this factor can be split into two additive terms, a *coulombic* term and an *exchange* term. The two terms have different dependences on various

[21] K.D. Demadis, C.M. Hartshorn, T.J. Meyer, *Chem. Rev.*, 2001, 101, 2655.

parameters of the system (spin of ground and excited states, donor-acceptor distance, etc.) and each of them can become predominant depending on the specific system and experimental conditions. The orbital aspects of the two mechanisms are schematically represented in Figure 2.2.

### 2.3.1. The Coulombic Mechanism

The coulombic (also called resonance, Förster-type,<sup>22</sup> or through-space) mechanism is a long-range mechanism that does not require physical contact between donor and acceptor. It can be shown that the most important term within the coulombic interaction is the dipole-dipole term,<sup>22</sup> that obeys the same selection rules as the corresponding electric dipole transitions of the two partners. Therefore, coulombic energy transfer is expected to be efficient in systems in which the radiative transitions connecting the ground and the excited state of each partner have high oscillator strength.

The rate constant for the dipole-dipole coulombic energy transfer can be expressed as a function of the spectroscopic and photophysical properties of the two molecular components:

$$k_{\text{en}}^{\text{F}} = 8.8 \times 10^{-25} \frac{K^2 \Phi}{n^4 \tau r_{\text{AB}}^6} J_{\text{F}} \quad (18)$$

$$J_{\text{F}} = \frac{\int F(\bar{\nu}) \varepsilon(\bar{\nu}) / \bar{\nu}^4 \, d\bar{\nu}}{\int F(\bar{\nu}) \, d\bar{\nu}} \quad (19)$$

where  $K$  is an orientation factor which accounts for the directional nature of the dipole-dipole interaction ( $K^2 = 2/3$  for random orientation),  $\Phi$  and  $\tau$  are the luminescence quantum yield

---

[22] T. Förster, *Discuss. Faraday Soc.*, 1959, 27, 7.

and lifetime of the donor, respectively,  $n$  is the solvent refractive index,  $r_{AB}$  is the distance (in Å) between donor and acceptor, and  $J_f$  is the Förster overlap integral between the luminescence spectrum of the donor,  $F(\bar{\nu})$ , and the absorption spectrum of the acceptor,  $\varepsilon(\bar{\nu})$ , on an energy scale ( $\text{cm}^{-1}$ ). With a good spectral overlap integral and appropriate photophysical parameters, the  $1/r_{AB}^6$  distance dependence allows energy transfer to occur efficiently over distances largely exceeding the molecular diameters. The typical example of an efficient coulombic mechanism is that of singlet-singlet energy transfer between large aromatic molecules, a process used by nature in the antenna systems of the photosynthetic apparatus.<sup>23</sup>

### 2.3.2. The Exchange Mechanism

The exchange (also called Dexter-type<sup>24</sup>) mechanism requires orbital overlap between donor and acceptor, either directly or mediated by the bridge (through-bond) and therefore displays an exponential decay with distance. The exchange interaction may be regarded (Figure 2.2.) as a double electron-transfer process, one electron moving from the LUMO of the excited donor to the LUMO of the acceptor, and the other from the acceptor HOMO to the donor HOMO.

$$k_{\text{en}}^{\text{D}} \sim B_{\text{en}} \exp(-\beta^{\text{en}} r) \quad (20)$$

$$\beta^{\text{en}} \sim \beta^{\text{el}} + \beta^{\text{ht}} \quad (21)$$

This important insight clearly evidences that the attenuation factor  $\beta^{\text{en}}$  for exchange energy transfer should be approximately equal to the sum of the attenuation factors for two separated electron-transfer processes, i.e.,  $\beta^{\text{el}}$  for electron transfer between the LUMOs of the

---

[23] T. Pullerits, V. Sundström, *Acc. Chem. Res.*, 1996, 29, 381.

[24] D.L. Dexter, *J. Chem. Phys.*, 1953, 21, 836.

donor and acceptor, and  $\beta^{\text{ht}}$  for the electron transfer between the HOMOs (superscript ht stays for hole transfer from the donor to the acceptor). This prediction has been confirmed by experiments.<sup>25</sup>

The spin selection rules for this type of mechanism arise from the need to obey spin conservation in the reacting pair as a whole. This allows the exchange mechanism to be operative in many cases in which the excited states involved are spin-forbidden in the usual spectroscopic sense. Thus, the typical example of an efficient exchange mechanism is that of triplet-triplet energy transfer.

Although the exchange mechanism was originally formulated in terms of direct overlap between donor and acceptor orbitals, it is clear that it can be extended to cover the case in which coupling is mediated by the intervening medium (i.e., the connecting bridge), as discussed below for electron-transfer processes (superexchange mechanism).

### **2.3.3. Excimers and exciplexes**

When a molecular component is at the excited state may undergo relatively strong electronic interactions with other components at the ground state. New chemical species arise, called excimers (from excited dimers) or exciplexes (from excited complexes), depending on whether the two interacting units have the same or different chemical nature (see 5.1.1. and 5.1.2.).

The excimer and exciplex formation is a reversible process and that both may decay radiatively. Emission of an excimer or exciplex is always displaced to lower energy compared to the monomer and usually corresponds to a broad and rather weak band resulting in the quenching of monomer luminescence. Excimers are usually obtained when an excited state of an aromatic molecule interacts with the ground state of a molecule of the same type. Exciplexes are obtained when an electron donor (acceptor) excited state interacts with an

---

[25] G.L. Closs, D.M. Johnson, J.R. Miller, P. Piotrowiak, *J. Am. Chem. Soc.*, 1989, 111, 3751.

electron acceptor (donor) ground state molecule. For example, between excited states of aromatic molecules (electron acceptors) and amines (electron donors).

Supramolecular species may undergo non negligible electronic interactions between adjacent chromophoric units already in the ground state. In such a case, the absorption spectrum of the species may substantially differ from the sum of the absorption spectra of the component units. When the units have the same chemical nature, the interaction leads to formation of dimers (see Section 5.2.2.). When the two units are different, the interaction is usually charge-transfer in nature with formation of charge-transfer complexes (see Section 5.2.4.). Excitation of such dimers leads to an excited state that is substantially the same as the corresponding excimers, and excitation of the charge-transfer ground state complexes leads to an excited state that is substantially the same as that of the corresponding exciplexes.

## 2.4. Photoinduced Electron Transfer

For photoinduced electron-transfer processes,<sup>26</sup> the relevant excited-state thermodynamic parameters are the reduction potentials of the  $A^+/*A$  (eq. 11.) and  $*A/A^-$  (eq. 12.) couples. It should be recalled that, because of its higher energy content, an excited state is both a stronger reductant and a stronger oxidant than the corresponding ground state.<sup>19</sup> To a first approximation, the redox potentials of excited state couples may be calculated from the potentials of the ground state couples and the zero-zero electronic excitation energy, as shown by eqs. 22. and 23.:<sup>27</sup>

$$E(A^+/*A) \approx E(A^+/A) - E_{0-0} \quad (22)$$

---

[26] Common electron-transfer theories are based on the assumption that just one electron is transferred. For multi-electron transfer processes, see: S.S. Skourtis, D.N. Beratan, in *Electron Transfer in Chemistry* (Ed.: V. Balzani), Wiley-VCH, Weinheim, 2001, Vol. 1, p. 109.

[27] V. Balzani, F. Bolletta, M.T. Gandolfi, M. Maestri, *Top. Curr. Chem.*, 1978, 75, 1.

$$E^*(A/A^-) \approx E(A/A^-) + E_{0-0} \quad (23)$$

From a kinetic viewpoint, electron-transfer processes involving excited states, as well as those involving ground state molecules, can be dealt with in the frame of the Marcus theory<sup>28</sup> and of the successive, more sophisticated theoretical models.<sup>29,30,31</sup> From a quantum mechanical viewpoint, both the photoinduced (eqs. 11. and 12.) and back electron-transfer (eqs. 14. and 15.) processes can be viewed as radiationless transitions between different, weakly interacting electronic states of the A–B supermolecule. The rate constant of such processes is given by an appropriate Fermi “golden rule” expression:

$$k_{el} = (4\pi/\hbar) (H^e)^2 FC^e \quad (24)$$

where  $H^e$  and  $FC^e$  are the electronic coupling and the Franck-Condon density of states, respectively.

### 2.4.1. The Electronic Factor

In the absence of any intervening medium (through-space mechanism), the electronic factor decreases exponentially with increasing distance:

---

[28] (a) R.A. Marcus, *Annu. Rev. Phys. Chem.*, 1964, 15, 155. (b) R.A. Marcus, N. Sutin, *Biochim. Biophys. Acta*, 1985, 811, 265.

[29] P.F. Barbara, T.J. Meyer, M.A. Ratner, *J. Phys. Chem.*, 1996, 100, 13148.

[30] (a) M.D. Newton, in *Electron Transfer in Chemistry* (Ed.: V. Balzani), Wiley-VCH, Weinheim, 2001, Vol. 1, p. 3. (b) K.D. Demadis, C.M. Hartshorn, T.J. Meyer, *Chem. Rev.*, 2001, 101, 2655. (c) F. Scandola, C. Chiorboli, M.T. Indelli, M.A. Rampi, in *Electron Transfer in Chemistry* (Ed.: V. Balzani), Wiley-VCH, Weinheim, 2001, Vol. 3, p. 337.

[31] M.N. Paddon-Row, in *Electron Transfer in Chemistry* (Ed.: V. Balzani), Wiley-VCH, Weinheim, 2001, Vol. 3, p. 179.

$$H^{\text{el}} = H^{\text{el}}(0) \exp \left[ -\frac{\beta^{\text{el}}}{2} (r_{\text{AB}} - r_0) \right] \quad (25)$$

where  $r_{\text{AB}}$  is the donor-acceptor distance,  $H^{\text{el}}(0)$  is the interaction at the “contact” distance  $r_0$ , and  $\beta^{\text{el}}$  is an appropriate attenuation parameter. The 1/2 factor arises because originally  $\beta^{\text{el}}$  was defined as the exponential attenuation parameter for rate constant rather than for electronic coupling, (eq. 26.):

$$k_{\text{el}} \propto \exp(-\beta^{\text{el}} r_{\text{AB}}) \quad (26)$$

For donor-acceptor components separated by vacuum,  $\beta^{\text{el}}$  is estimated to be in the range 2–5 Å<sup>-1</sup>. When donor and acceptor are separated by “matter” (i.e., solvent or bridging components), the electronic coupling can be mediated by mixing of the initial and final states of the system with virtual, high energy electron-transfer states involving the intervening medium (superexchange mechanism).<sup>30,32</sup> The second order perturbation expression describing the superexchange coupling is:

$$H^{\text{el}} = \frac{H_{ie} H_{fe}}{\Delta E_e} + \frac{H_{ih} H_{fh}}{\Delta E_h} \quad (27)$$

where  $H_{ie}$ ,  $H_{fe}$ ,  $H_{ih}$ , and  $H_{fh}$  are the appropriate donor-bridge and bridge-acceptor coupling elements, and  $\Delta E_e$  and  $\Delta E_h$  are the energy differences between the virtual states and the initial or final state (these energy differences are taken at the transition state nuclear geometry, where the initial and final state have the same energy). From eq. 27. it follows that

---

[32] H.M. McConnell, *J. Chem. Phys.*, 1961, 35, 508.

easily reducible bridges are good electron-transfer mediators, and easily oxidizable bridges are good hole transfer mediators. In the case of modular bridges, the superexchange model can be extended to involve virtual electron-transfer states localized on each single modular unit.

### 2.4.2. The Nuclear Factor

The  $FC^{\text{el}}$  term of eq. 24. is a thermally averaged Franck-Condon factor connecting the initial and final states. It contains a sum of overlap integrals between the nuclear wavefunctions of initial and final states of the same energy. Both inner and outer (solvent) vibrational modes are included. It was shown<sup>28b</sup> that in the high temperature limit ( $\hbar\nu < k_B T$ ), an approximation sufficiently accurate for many room temperature processes, the nuclear factor takes the simple form:

$$FC^{\text{el}} = \left( \frac{1}{4\pi \lambda k_B T} \right)^{1/2} \exp \left[ - \frac{(\Delta G^0 + \lambda)^2}{4 \lambda k_B T} \right] \quad (28)$$

where  $\lambda$  is the sum of the inner ( $\lambda_i$ ) and outer ( $\lambda_o$ ) reorganizational energies. The exponential term of eq. 28. is the same as that predicted by the classical Marcus model based on parabolic energy curves for initial and final states.<sup>28</sup> Both classical and quantum mechanical models contain an important prediction, namely that three distinct kinetic regimes exist, depending on the driving force of the electron-transfer process: (i) a normal regime for small driving forces ( $-\lambda < \Delta G^0 < 0$ ) in which the process is thermally activated and its rate increases with increasing driving force; (ii) an activationless regime ( $-\lambda = \Delta G^0$ ) in which a change in the driving force does not cause large changes in the reaction rate; (iii) an “inverted” regime for strongly exoergonic processes ( $-\lambda > \Delta G^0$ ) in which the rate of the process decreases with increasing driving force. The three kinetic regimes are schematically shown in terms of classical Marcus' parabolæ in Figure 2.3., where the difference in the

predictions of the classical and quantum mechanical models in the inverted region (parabolic vs linear decrease of  $\ln k_{ei}$  with increasing driving force) is also sketched.<sup>33</sup>

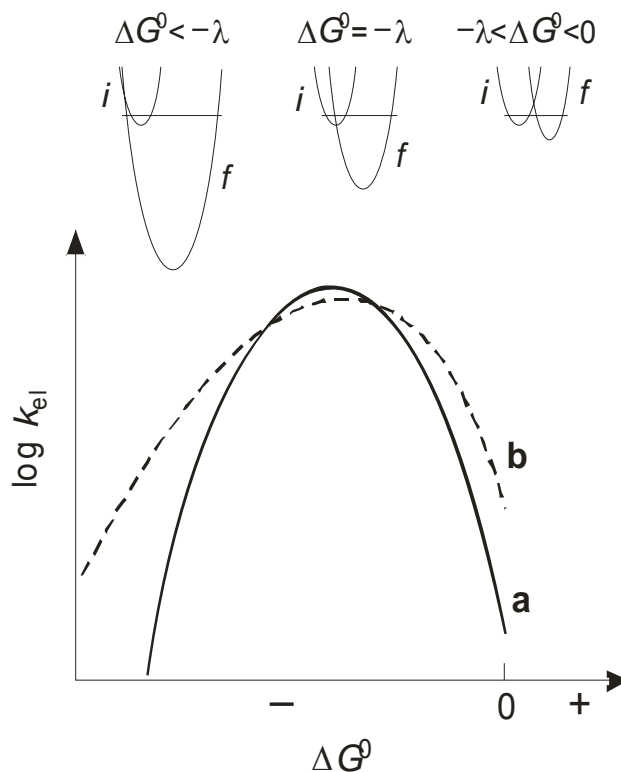


Figure 2.3. Free energy dependence of electron-transfer rate ( $i$ , initial state;  $f$ , final state) according to the classical (a) and quantum mechanical (b) treatments. The three kinetic regimes (normal, activationless, and “inverted”, from thright to left) are also shown schematically in terms of Marcus' parabolæ.

[33] For an experimental observation of the whole bell-shaped  $\ln k_{ei}$  vs  $\Delta G^0$  curve, see: N. Mataga, H. Chosrowjan, Y. Shibata, N. Yoshida, A. Osika, T. Kikuzawa, T. Okada, *J. Am. Chem. Soc.*, 2001, 123, 12422.

## 3. Methods

### 3.1. Photophysical Techniques

#### 3.1.1. Electronic Absorption Spectra

All the absorption spectra in the 190–1100 nm range are recorded at room temperature on solutions contained in quartz cuvettes (optical pathlength 1 cm and 5 cm, Hellma®) by using a Perkin Elmer  $\lambda$  40 spectrophotometer. The precision on the wavelength values is  $\pm 2$  nm. Molar absorption coefficient values are determined using the Lambert–Beer law; the experimental error can be estimated to be around  $\pm 5\%$ .

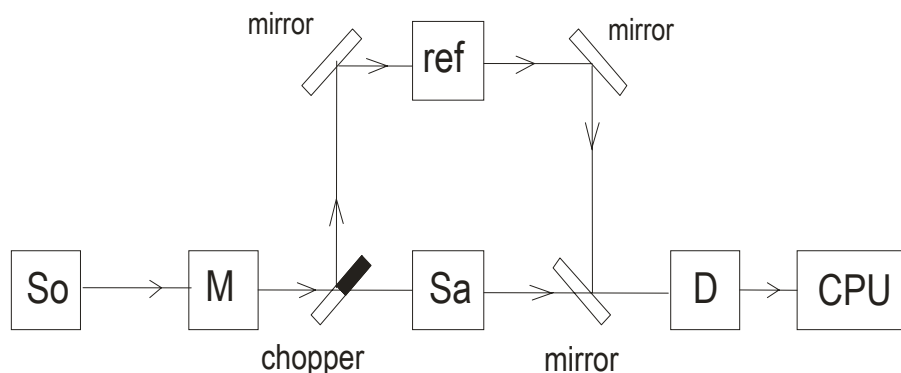


Figure 3.1. Experimental set up of a spectrophotometer: So is the light source (W lamp operative within 1100 and 320 nm, D<sub>2</sub> lamp from 320 to 190 nm); M is a diffraction grating (monochromator); Sa is the sample and ref the reference; D is the detector for transmitted light (usually a photomultiplier tube) and a CPU unit that elaborates signals; chopper and mirrors position is illustrated.

### 3.1.2. Luminescence Spectra

Fluorescence and phosphorescence emission and excitation spectra in the 250-900 nm range are recorded with Perkin Elmer LS 50 spectrofluorimeters equipped with Hamamatsu R928 or R955 photomultiplier. In case of weak luminescence signals the more sensitive Fluorolog 3 from ISA (Jobin Yvon-Spex) is used.

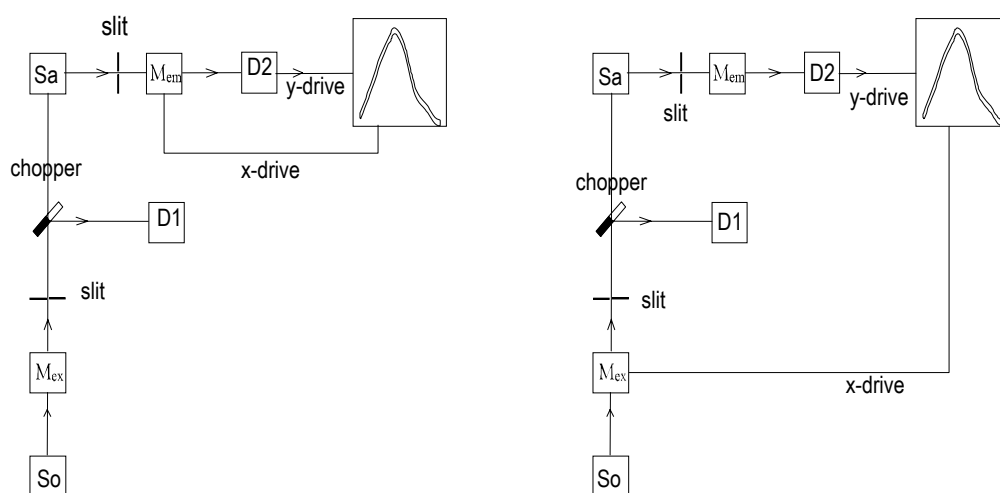


Figure 3.2. Experimental set up of a spectrofluorimeter: So is the light source (Xe lamp producing 2 $\mu$ s long flashes at 50Hz); two monochromators select excitation and emission wavelength; Sa is the sample; two photomultiplier tubes D are placed after the M units to detect the luminescence signal (D2) and to correct lamp emission profile; emission intensity is elaborated by CPU unit vs. emission or excitation wavelength in emission and excitation spectra respectively; chopper and slits position is illustrated.

Room temperature spectra are recorded in the same spectrofluorimetric suprasil quartz cuvettes described for the electronic absorption spectra. In order to have comparable luminescence intensity measurements some correction had to be applied to the experimental data. These corrections have to be introduced to take into account instrumental geometrical effects and the distribution of the exciting light among the chemical species effectively present

in the solution.<sup>34</sup> Spectra in frozen matrix at 77 K have been taken using quartz (or glass) tubes with an internal diameter of about 2 mm and a 20 cm length immersed in liquid nitrogen. A transparent dewar (glass or quartz) with a cylindrical terminal part having a 1 cm external diameter is employed. Such a device easily fit into the sample holder of the spectrofluorimeters above described. Measurements of emission spectra and lifetimes as a function of temperature were performed by inserting a quartz cell in a cryostat equipped with a temperature controller (model TCI) by Oxford Instruments.

Luminescence spectra recorded in the 650-900 nm region are corrected for the non-linear response of the photomultiplier towards photons of different wavelength referring to a previously experimentally determined calibration curve. The precision on the wavelength values was  $\pm 2$  nm.

Luminescence spectra in the near infrared (NIR) region are recorded by a home-made apparatus based on an Edinburgh CD900 spectrofluorimeter, which uses a Xenon lamp as the excitation source and a liquid nitrogen cooled hyperpure germanium crystal as a detector.

### 3.1.3. Luminescence Quantum Yield

Luminescence quantum yields are determined on solution samples at room temperature referring to the relative method optimized by Demas and Crosby.<sup>35</sup> The quantum yield is expressed as:

$$\Phi_S = \Phi_R (A_S/A_R) (n_S/n_R)^2 \quad (29)$$

where  $\Phi$ , A and n indicate the luminescence quantum yield, the area subtended by the emission band (in the intensity versus frequency spectrum) and the refractive index of the

---

[34] a) A. Credi, L. Prodi, *EPA Newsletter* 1996, 58, 50. b) A. Credi, L. Prodi, *Spectrochimica Acta A* 1998, 54, 159.

[35] J. N. Demas, G. A. Crosby, *J. Phys. Chem.* 1971, 75, 991.

solvent used for the preparation of the solution, respectively; the subscripts S and R stand for sample and reference, respectively.  $A_S$  and  $A_R$  must be relative to the same instrumental conditions. Absorption at the excitation wavelength have to be the same in both reference and sample. Different standards<sup>36</sup> are selected depending on the spectral region of interests eliminating correction for detection response. The experimental error is  $\pm 15\%$ .

### 3.1.4. Time-resolved Luminescence Measurements

Excited state lifetimes in the range 0.5ns – 30 $\mu$ s are measured with an Edinburgh Instrument time correlated single-photon counting technique.<sup>19d</sup>

The excitation impulse is obtained by a gas discharge lamp (model nF900, filled with nitrogen or deuterium, depending on excitation requirements) delivering pulses with duration of 0.5ns (FWHM) and frequency comprised between 1 and 100 kHz or by a pulsed diode lasers (288 and 406 nm by Picoquant are available). A photomultiplier tube (Hamamatsu R928P) amplified and cooled at  $-20^\circ\text{C}$  is used as stop detector. Software implement allow deconvolution of the excitation profile by the radiative decay profile.

Lifetimes in the range between 100 ns and 100 ms are measured by single flash technique (equipment described in section 3.1.5.) where an individual laser shot, by means of its high peak power i.e.  $[\text{N}/\text{h}\nu \text{ s}^{-1} \text{ cm}^{-2}]$ , generate a high number of molecules at the excited state and their emission decay is followed by a photodiode. Reliability of the lifetime values is obtained averaging 32 acquisitions.

Phosphorescence lifetimes in the range between 10  $\mu$ s and 2 s are measured with the same Perkin Elmer LS 50 spectrofluorimeter employed for the luminescence spectra acquisition. In this case the excitation pulse is generated by a Xe lamp (0.5 - 50 Hz) and the emission

---

[36] a) *Handbook of Photochemistry*, 3rd Edition (Eds. M. Montalti, A. Credi, L. Prodi, M.T. Gandolfi), CRC Taylor & Francis, Boca Raton, 2006; b) I. B. Berlman, *Handbook of Fluorescence Spectra of Aromatic Molecules Academic*, London, 1965. and references therein.

decay profile generated by sampling method through acquisition of the emission intensity at increasing delay times from the excitation pulse.

All the mentioned techniques are in the time-domain. so the excitation energy is provided by a short pulse of monochromatic light. The experimental error on the lifetime measurements is  $\pm 10\%$ .

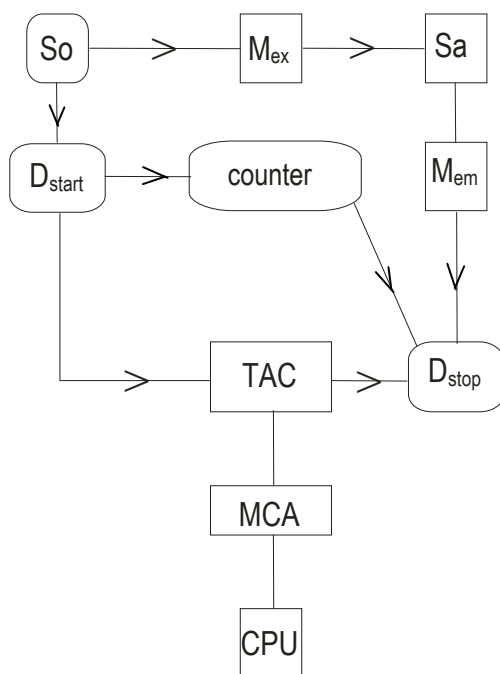


Figure 3.3. Experimental set up of a single photon counter: So is the light source (see text); two monochromators select excitation and emission wavelength; Sa is the sample; photomultiplier tube  $D_{start}$  is placed before the  $M_{ex}$  to trigger TAC and  $D_{stop}$  placed after the  $M_{em}$  to stop TAC; TAC is the acronym of time-to-amplitude converter and measures a tension value function of the elapsed time between two photons of the same flash reach  $D_{start}$  and  $D_{stop}$ ; multichannel analyzer MCA places each tension value in a channel related to the single radiative event; CPU finally reconstructs the emission decay profile of the excited state mediating a great number of radiative events.

### 3.1.5. Nanosecond Transient Absorption Spectra

Nanosecond transient absorption experiments are performed in deaerated solutions obtained by consecutive freeze-pump-thaw cycles. A Continuum Surelite SLI-10 Nd:YAG laser is used to

excite the sample with 10-ns pulses (through second, third and fourth harmonic generation pulses at 532, 355, 266 nm respectively are available). The monitoring beam is supplied by a Xe arc lamp, and the signal detected by a red sensitive photodiode after passing through a high radiance monochromator, then recorded by a Tektronix TDS640A digitizer oscilloscope and transferred to a PC computer. Differential absorption spectra are recorded point-by-point at fixed wavelength, where also kinetic measurements were made. 32 individual laser shots have been averaged to improve the reliability of each acquisition.

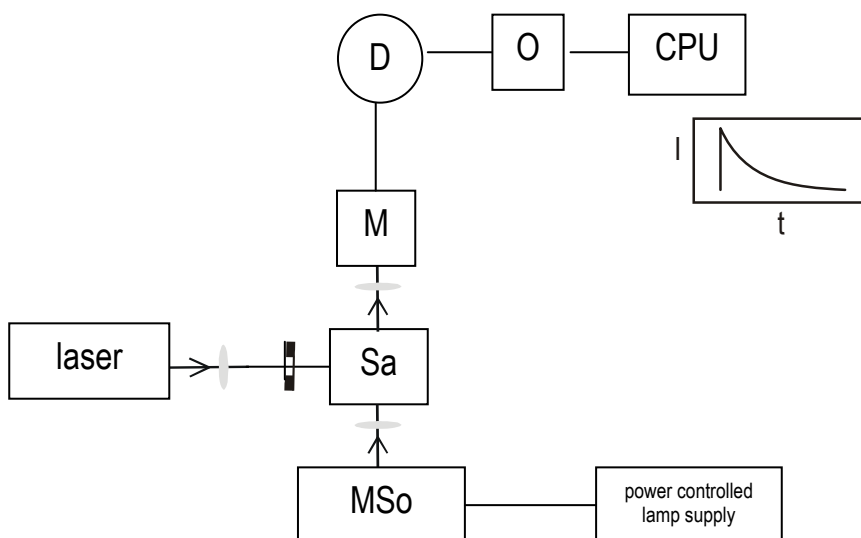


Figure 3.4. Experimental set up for transient absorption experiments: laser provides excitation light, MSo is the monitoring beam (see text); a monochromator selecting emission wavelength is placed after the sample Sa; a photodiode D collects signal then converted by a digital oscilloscope O.

### 3.1.6. Femtosecond Transient Absorption Spectra

Femtosecond time-resolved experiments have been performed in the Chemistry Department at Ferrara University under supervision of Dr. Chiorboli using the spectrometer schematically described in Figure 3.5. It uses the Spectra-Physics Hurricane system as the laser source.

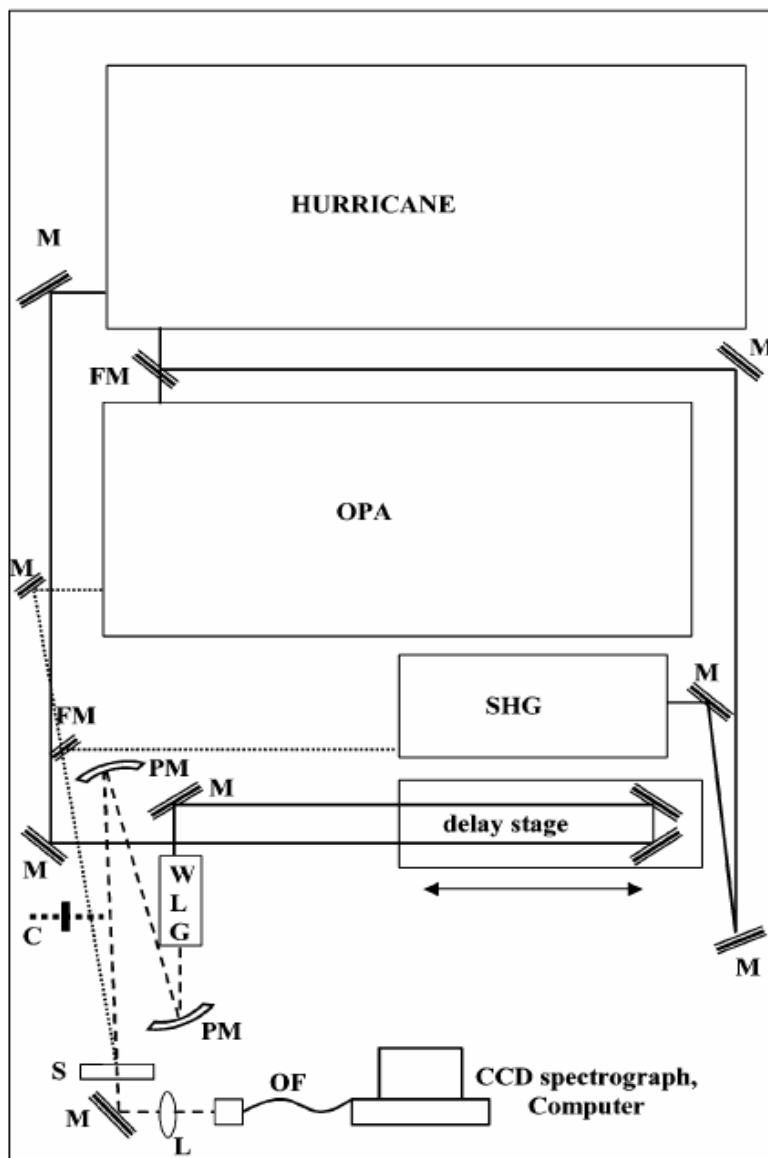


Figure 3.5. Schematic layout of the ultrafast spectroscopy setup. Continuous line, fundamental (800 nm); dashed line, white light continuum probe; dotted line, pump beam; M, mirror; PM, parabolic mirror; L, lens; OF, optical fiber; S, sample; C, chopper; FM, flipping mirror; OPA, optical parametric amplifier; WLG, white light generator; SHG, second harmonic generator.

This system comprises a seed laser (Mai Tai, cw diode pumped laser and a mode-locked Ti:sapphire pulsed laser), a pump laser (Evolution, diode-pumped Q-switched Nd:YLF laser), a

stretcher, a Ti:sapphire regenerative amplifier, and a compressor. The output of the system consists of pulses of 800 nm, 1 mJ, 100 fs (FWHM) at a repetition rate of 1 kHz.

The design of the pump-probe spectroscopic setup is inspired by the BORODIN spectrometer of Ultrafast Spectrometers, Bowling Green, OH. The Hurricane output is first split (50%) in two beams. One of these (pump) is converted to useful excitation wavelengths by coupling it into a second-harmonic generator (for 400 nm excitation) or into an optical parametric amplifier (Spectra-Physics OPA 800, for tunable wavelengths in the region 320-700 nm). The other beam (probe) is first passed through a computer-controlled delay line (Physik Instrumente M-415.DG, 150 mm linear positioning stage), and then focused on a 1 mm thick sapphire plate (Crystal System, Inc., HEMLUX grade) to generate a white light continuum (effective useful range, 450-750 nm). The pump beam is passed through a computer-controlled optical chopper (Scitec Instruments, 320C) rotating at a frequency of 30 Hz, and focused, with a spot size of about 2 mm, on the sample cell. The sample cell is a 1 mm optical path quartz cylindrical cell (Hellma, 120 QS) placed in a variable-speed rotating holder. The white light continuum probe beam is collimated and focused into the sample cell, superimposed to the pump beam, at an angle of ca. 5°. To minimize the temporal chirp in the spectrum, parabolic mirrors are used to collimate and focus the white light probe beam. After passing through the sample cell, the white continuum is coupled into a 100  $\mu\text{m}$  optical fiber connected to a CCD spectrograph (Ocean Optics, PC 2000). Typically, time-resolved absorption spectra were acquired averaging over 4000 excitation pulses at any delay time. The delay line, the CCD spectrograph, and the chopper are computer-controlled by a LabVIEW (National Instruments) software routine developed by Ultrafast Spectrometers, Bowling Green, OH. These routines allow automatic spectral acquisition at any selected delay-line settings. Kinetic traces at chosen wavelengths can be extracted from the accumulated transient absorption data with 100 fs pump and probe pulses. The effective time resolution of the ultrafast spectrometer, that is, the rise time of an "instantaneous" signal, is ca. 300 fs. The temporal chirp over the 450-750 nm range of the

white light probe pulse is ca. 200 fs. The maximum temporal window of the experiment, limited by the optical delay stage, is 0-1000 ps.

### 3.1.7. Two-Photon Induced Luminescence Spectra

Two-photon absorption (TPA) spectra have been measured using two-photon induced fluorescence (TPIF) spectroscopy.<sup>37,38</sup>

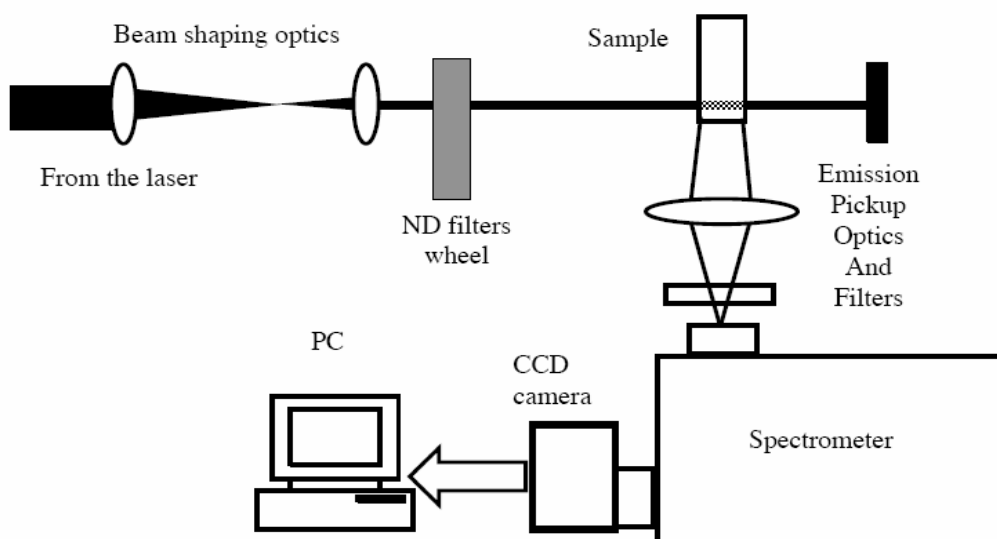


Figure 3.6. Experimental setup for the TPA cross section measurements. TPIF spectra of the standard and sample are recorded at the same excitation wavelength in low excitation power regime to remove the contributions from other nonlinear effects such as excited state absorption or three-photon absorption, etc. Effective TPA is also verified by measuring the quadratic dependence of the TPIF intensity on the laser pump fluence, indicating that the signal originated from a pure nonlinear optical process.

[37] C. Xu and W. W. Webb, *J. of Am. Opt. Soc.*, 1996, 13, 481.

[38] Rumi, M.; Ehrlich, J. E.; Heikal, A. A.; Perry, J. W.; Barlow, S.; Hu, Z.; McCord-Maughon, D.; Parker, T. C.; Röckel, H.; Thayumanavan, S.; Marder, S. R.; Beljonne, D.; Brédas, J.-L. *J. Am. Chem. Soc.* 2000, 122, 9500.

The samples are excited via TPA process by directing a tightly collimated ( $\sim 120 \mu\text{m}$ ), high intensity laser beam on the sample (Figure 3.6.). These measurements have been accomplished at the UCSB Optical Characterization Facility directed by Dr. Mikhailovsky.

The emission from the sample is collected at a  $90^\circ$  angle by a high numerical aperture lens and directed to a spectrometer's entrance slit. To avoid internal filter effects, the excited volume is located near the cell wall on the collection optics side. This configuration minimizes the fluorescence path inside the sample cell and thus reduces self-absorption. The radiation dispersed by the spectrometer is detected by a thermoelectrically cooled charge coupled device (CCD) camera (Roper Scientific Spec10:100B/TE). Excitation pulses with typical duration of 90 fs and energy of  $\sim 6 \text{ nJ}$  within the spectral range 700 - 1000 nm are produced by the mode-locked Ti:Sapphire laser (Spectraphysics Tsunami) with a repetition rate of 82 MHz. For the spectral range 620 - 700 nm, femtosecond optical parametric amplifier (OPA) is used. Signal output of the OPA (Spectraphysics OPA-800C) is upconverted into the visible range of spectrum using the second harmonic generation (SHG) process in  $\beta$ -barium borate crystal, which yielded 120 fs pulses with energy of  $\sim 30 \mu\text{J}$  and a repetition rate of 1 kHz. A neutral density filter wheel is used to attenuate the energy of the laser pulses down to the desirable level. Two-photon induced luminescence spectra of a standard and the samples are recorded at the same excitation wavelength. The two-photon absorption cross section of the sample,  $\beta_x$  can be expressed as:

$$\beta_x = \beta_{ref} \frac{\phi_{ref}}{\phi_x} \frac{c_{ref}}{c_x} \frac{I_{0,ref}^2}{I_{0,x}^2} \frac{I_{em,x}}{I_{em,ref}} K \quad (30)$$

here, the index *ref* denotes values related to the reference measurements. The integrated photoluminescence intensities collected by detector is denoted as  $I_{em}$  and  $\phi$  is the fluorescence

quantum yield. The number density of the molecules in solution is denoted as  $c$ , where  $\beta_{ref}$  means the TPA cross section of the reference molecule. Assuming that all experimental parameters are identical during the series of measurements, except the power of the pump radiation ( $I_0$ ) and sample specific parameters,  $\phi$  and  $K$  is a correction factor that takes into account the difference in refractive indices of the solvents of the samples and the reference material. It depends on the excitation beam geometry. In case of nearly-collimated beams,  $K = n_{ref}^2 / n^2$ . In all measurements, the concentration of the chromophores is adjusted around  $10^{-5}$  M, to avoid emission self-quenching. Absorption and emission spectra of samples are monitored. Samples do not exhibit any sign of degradation within the timescale of the measurements. The reference standard utilized is fluorescein dye ( $10 \mu\text{M}$  in aqueous solution at pH 11 with  $\phi = 0.93$ ), which has a  $\beta$  value of  $38 \pm 9.7 \text{ GM}$  at 782 nm under these conditions.<sup>37</sup> *p*-Bis(*o*-methylstyryl)benzene in cyclohexane ( $10^{-4}$  M) is used as a reference for measurements in the spectral range below 700 nm.<sup>39</sup> TPIF studies are performed in a low excitation power regime, which is verified by measuring the quadratic dependence of the TPIF signal on the laser pump intensity.

### 3.1.8. Stopped-flow spectrophotometry

Reaction kinetic profiles are collected on air-equilibrated solutions at 293 K with an Applied Photophysics SX 18 MV stopped-flow spectrophotometer interfaced to a computer for data collection and analysis. The optical path length of the cell is 1 cm, and the driving ram for the mixing system has been operated at the recommended  $\text{N}_2$  pressure of 8.5 bar. Under these conditions, the time required to fill the 1-cm observation cell is experimentally determined to be  $< 1.3 \text{ ms}$  (based on a test reaction). The concentration of the reactants after mixing is in the range from  $5 \times 10^{-6}$  to  $10^{-4}$  M. The kinetic absorbance and emission curves

---

[39] S. M. Kennedy and F. E. Lytle, *Anal. Chem.*, 1986, 58, 2643.

are analyzed with a kinetic treatment of a simple second-order rate equation and result fully satisfactory.

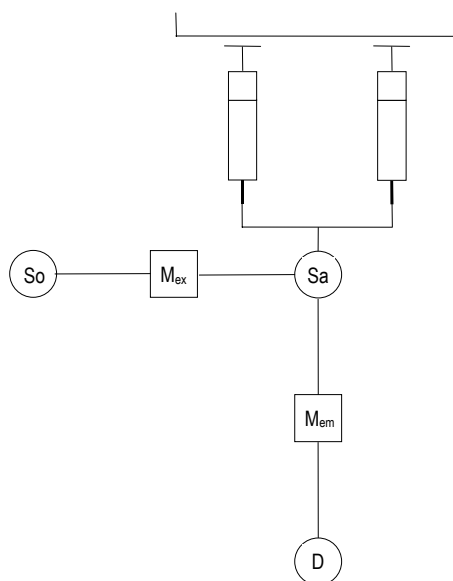


Figure 3.7. Experimental set up of a stopped-flow spectrophotometer: So is the light source; M are diffraction gratings (monochromators); Sa is the sample holder filled by two syringes mixing interacting components; D is the detector.

### 3.2. Photochemical Measurements

Continuous irradiation experiments are performed by means of a Q400 Hanau medium pressure mercury lamp (150 W). Wavelengths of 287, 313, 365 and 436 nm are isolated by means of interference filters (Oriel) so selecting a narrow spectral range. The irradiated solution (known volume and concentration of the sample) is contained in a spectrophotometric cell. The intensity of the incident light (ranging between  $10^{-7}$  –  $10^{-8}$  einstein/min depending by the selected wavelength), measured by the ferrioxalate actinometer,<sup>40</sup> is continuously monitored.

Photosensitized reduction experiments are also performed. Solutions, with 9-methylanthracene as a photosensitizer and triethanolamine as a sacrificial reductant are used.

[40] (a) E. Fischer, *EPA Newsletter*, 1984, 33. (b) C. G. Hatchard and C. A. Parker, *Proc. R. Soc. London, Ser. A*, 1956, 235, 518.

The solutions are degassed by repeated freeze-pump-thaw cycles and irradiated at chosen wavelength with light from a medium pressure Hg lamp equipped with an interference filter.

Photoreaction quantum yield are determined by monitoring the changes in absorbance associated with the disappearance of the reactants or the formation of the products, at a wavelength where the absorbance could be related to the concentration of these species.

### 3.3. Electrochemical Techniques

Electrochemical experiments are carried out in argon-purged (solvents by Romil Hi-Dry™) solutions at room temperature with an EcoChemie Autolab 30 multipurpose instrument interfaced to a personal computer. The working electrode is a glassy carbon electrode (0.08 cm<sup>2</sup>, Amel); its surface is routinely polished with 0.3 mm alumina-water slurry on a felt surface, immediately prior to use. The counter electrode is a Pt spiral and a silver wire is employed as a quasi-reference electrode (QR).

A three electrode system is necessary because the potential applied in the electrochemical cell drops because of the ohmic loss due to the consistence resistance of the solution ( $R_s$  in eq. 31.). Furthermore, current density values are not low enough to neglect the second term in the right part of eq. 31.:<sup>41</sup>

$$E_{\text{appl.}} = E_w + iR_s \quad (31)$$

The potentials reported are referred to SCE by measuring the AgQR potential with respect to ferrocene (known oxidation potential vs SCE in various solvents).<sup>42</sup>

---

[41] A. J. Bard, L. R. Faulkner, *Electrochemical Methods*, 1980, J. Wiley & Sons, Inc.

[42] D. Dubois, G. Monitot, W. Kutner, M. T. Jones, K. M. Kadish, *J. Phys. Chem.* 1992, 96, 7137.

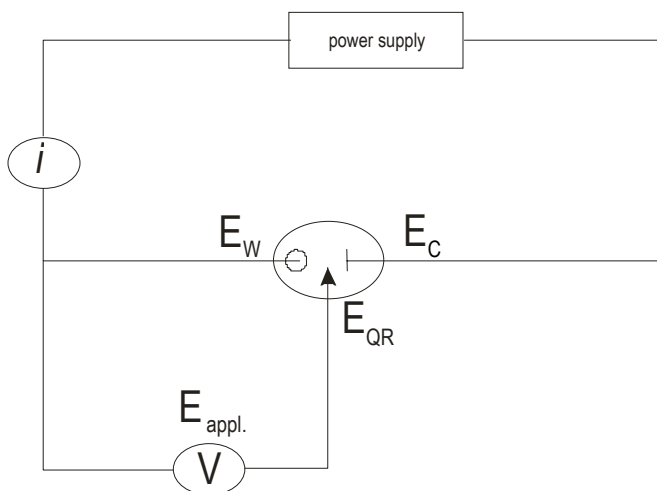


Figure 3.8. Experimental set up of a three electrodes device:  $E_W$  is the working electrode,  $E_C$  is the counter electrode,  $E_{QR}$  is the quasi-reference electrode.

The concentration of the compounds examined is of the order of  $10^{-4} - 10^{-3}$  M; 0.1 M tetrabutylammonium hexafluorophosphate ( $TBAPF_6$ ) is added as supporting electrolyte.

### 3.3.1. Cyclic Voltammetry

Cyclic voltammograms are obtained with sweep rates in the range  $0.02 - 1.0 \text{ V s}^{-1}$ ; the IR compensation implemented within the Autolab 30 is used, and every effort is made throughout the experiments in order to minimize the resistance of the solution. In any instance, the full reversibility of the voltammetric wave of ferrocene is taken as an indicator of the absence of uncompensated resistance effects. The reversibility of the observed processes is established by using the criteria of (i) separation of 60 mV between cathodic and anodic peaks; (ii) the close to unity ratio of the intensities of the cathodic and anodic currents, and (iii) the constancy of the peak potential on changing sweep rate in the cyclic voltammograms. For reversible processes, the halfwave potential values are calculated from the average of the potential values for anodic and cathodic peaks.

The number of electrons exchanged in a redox process has been evaluated by comparison of the current intensity of the corresponding voltammetric wave with that obtained for species

undergoing redox processes which involve a known number of electrons. The following expression is used:<sup>43</sup>

$$n_S/n_R = (I_S C_R / I_R C_S) (M_S / M_R)^{0.275} \quad (32)$$

where  $n$ ,  $I$ ,  $C$  and  $M$  indicate the number of electrons exchanged in the process, the current intensity of the corresponding voltammetric wave, the concentration and the molecular mass, respectively; the subscripts S and R refer to sample and reference, respectively. The term containing the molecular masses apply the correction for differences in the diffusion coefficient of the electroactive species.

The experimental error on the potential values is estimated to be lower than  $\pm 10$  mV.

### 3.3.2. Differential Pulse Voltammetry

Differential pulse voltammetry<sup>41</sup> is performed with a scan rate of 20 or 4 mV s<sup>-1</sup>, a pulse height of 75 or 10 mV, and a duration of 40 ms. The halfwave potential values obtained from cyclic voltammograms have to match the peak values found in differential pulse voltammograms. The number of electrons exchanged in each process can be estimated by comparing the areas of the differential pulse voltammogram peaks of the sample and a suitable reference compound taking into account corrections for differences in diffusion coefficients of the species; the so found number has to match the number of exchanged electrons estimated by eq. 31. in cyclic voltammetry experiments.

### 3.3.3. Chronoamperometry

The diffusion coefficients and the numbers of exchanged electrons are obtained independently by chronoamperometry as described in the literature.<sup>44</sup> A Pt disk with a

---

[43] J. B. Flanagan, S. Margel, A. J. Bard, F. C. Anson, *J. Am. Chem. Soc.* 1978, 100, 4248.

diameter of 50 mm is used as a working electrode and the experiments are carried out for 5 s, with 0.05 s sample time, at potential values corresponding to the cathodic peak of the first reversible reduction wave. The current intensities in steady-state conditions are determined from cyclic voltammetry experiments by using the same working electrode of the chronoamperometric experiments and sweep rate of  $10 \text{ mV s}^{-1}$ .

### **3.3.4. Spectroelectrochemistry**

Spectroelectrochemical experiments are performed in an optically transparent thin layer electrode (OTTLE) cell constituted by two quartz windows, a three electrode set melt-sealed in a polyethylene spacer. The three electrodes are: two Pt minigrids (32 wires/cm) as working and counter electrodes and a silver wire as quasi-reference electrode, positioned very close to the working electrode to minimize ohmic resistance. The cell has a sandwich type arrangement. The light is passed through the central part of the working electrode minigrid (ca. 80% transmittance) and the light path is of the order of 100-200  $\mu\text{m}$ . Diffusion of electrogenerated species between the electrodes is negligible on the experimental time scale (10-50 s). The solution used for spectroelectrochemical experiments has been prepared as previously described for cyclic voltammetry. In order to establish the right potential window corresponding to the redox process of interest, a thin layer cyclic voltammogram is recorded at 5 mV/s before the spectroelectrochemistry. After refilling the OTTLE cell with new solution, the electrolysis potential is varied with 20-50 mV steps and UV-VIS-NIR absorption spectra are recorded with an Agilent Technologies 8543 diode array spectrophotometer.

---

[44] G. Denuault, M.V. Mirkin, A.J. Bard, *J. Electroanal. Chem.* 1991, 308, 27-38.

## 4. Materials

### 4.1. Supramolecules and Large Molecules

It was previously mentioned how the definition of supramolecular species can be better based on the degree of intercomponent electronic interaction, rather than the nature of the binding interactions between the molecular components. This concept is illustrated in Figure 4.1.<sup>14b,45</sup>

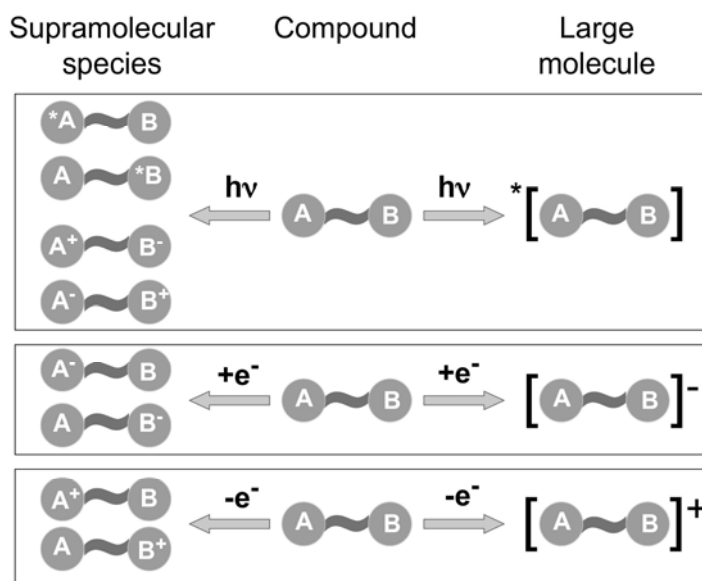


Figure 4.1. Schematic representation of the difference between a supramolecular system and a large molecule based on the effects caused by a photonic or an electronic input.

In the case of a photochemical stimulation, a system  $A \sim B$ , consisting of two units ( $\sim$  indicates any type of bond that keeps the units together), can be defined a supramolecular

[45] J. W. Steed, J. L. Atwood, *Supramolecular Chemistry*, Wiley, Chichester, 2000.

species if light absorption leads to excited states that are substantially confined on either A or B, or causes an electron transfer from A to B (or viceversa). By contrast, when the excited states are substantially delocalized on the entire system, the species can be better considered as a large molecule.

Similarly (Figure 4.1.), oxidation and reduction of a supramolecular species can substantially be described as oxidation and reduction of specific units, whereas oxidation and reduction of a large molecule leads to species where the hole or the electron are delocalized on the entire system. As already stated, when the interaction energy between molecular components is small compared to the other relevant energy parameters, a system can be considered a supramolecular species, regardless of the nature of the bonds that link the units.

It should be noted that the properties of each component of multicomponent species, i.e. of an assembly of weakly interacting molecular components, can be known from the study of the isolated units or of suitable model molecules, as reported in the characterization of supermolecular systems described in chapters 5., 6., and 7. However, this approach is not useful in investigating large molecules as shown in chapter 8.

## 4.2. Dendrimers

Dendrimers are repetitively branched, yet constitutionally well-defined macromolecules, exhibiting high monodispersity.<sup>46</sup> These nanoscopic compounds can contain selected chemical units in predetermined sites of their structure (core, branches, periphery) whose mutual interactions can lead to unusual, sometimes unpredictable, chemo-physical properties resulting in a wide range of potential applications.<sup>47</sup>

---

[46] a) F. Vögtle, G. Richardt, N. Werner, *Dendritische Moleküle*, Teubner, Stuttgart, 2007; b) J.M. Frechet, D.A. Tomalia, *Dendrimers and other Dendritic Polymers*, Wiley, New York, 2001; c) G.R. Newkome, F. Vögtle, *Dendrimers and Dendron*, Wiley-VCH, Weinheim, 2002.

[47] For some recent reviews, see: a) P.A. Chase, R.J.M.K. Gebbink, G. van Koten, *J. Organomet. Chem.* 2004, 689, 4016-4054; b) W. Ong, M. Gomez-Kaifer, A.E. Kaifer, *Chem. Commun.* 2004, 1677-1683; c) M. Ballauff, C.N. Likos, *Angew. Chem. Int. Ed.* 2004, 43, 2998-3020; d) A.M.

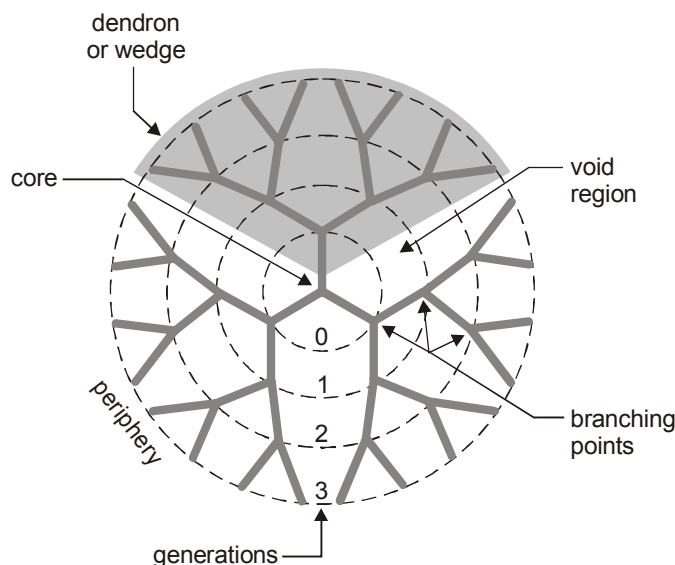


Figure 4.2. Schematic representation of a dendrimer; chemical species can be placed at the branching points, at the core and periphery and also hosted in the internal cavities.

Dendrimers containing photoactive and/or electroactive moieties are currently attracting much attention since they can be designed to perform useful functions. In the dendritic structure, in fact, the electronic interaction between nearby units is usually small in the ground state, so that each unit can be independently excited and the dendrimer absorption spectrum is close to the summation of the spectra of the component units. When a single chromophoric group is in an excited state, however, the interaction with the nearby units is often strong enough to change its luminescence behaviour because of formation of excimers or exciplexes<sup>48</sup> and the occurrence of energy<sup>49</sup> or electron<sup>50</sup> transfer processes. In suitably

---

Caminade, J.P. Majoral, *Acc. Chem. Res.* 2004, 37, 341-348; e) *Prog. Polym. Sci.* 2005, 30(3-4), special issues on Dendrimers and Dendritic Polymers (Eds.: D.A. Tomalia, J.M. Frechet); f) R.W.J. Scott, O.M. Wilson, R.M. Crooks, *J. Phys. Chem. B* 2005, 109, 692-704; g) D. Mery, D. Astruc, *Coord. Chem. Rev.* 2006, 250, 1965-1979; h) *New J. Chem.* 2007, 31(7), special issue on Dendrimers (Ed.: J.P. Majoral).

- [48] (a) G. Bergamini, P. Ceroni, V. Balzani, L. Cornelissen, J. van Heyst, S.-K. Lee and F. Vögtle, *J. Mater. Chem.*, 2005, 15, 2959. (b) F. Pina, P. Passaniti, M. Maestri, V. Balzani, F. Vögtle, M. Gorka, S.-K. Lee, J. Van Heyst and H. Fakhrnabavi, *ChemPhysChem*, 2004, 5, 473. (c) C. Saudan, V. Balzani, P. Ceroni, M. Gorka, M. Maestri, V. Vicinelli and F. Vögtle, *Tetrahedron*, 2003, 59, 3845. (c) T. H. Ghaddar, J. K. Whitesell and M. A. Fox, *J. Phys. Chem. B*, 2001, 105,

designed dendrimers energy transfer processes can be spatially and energetically controlled, thereby opening the way towards the construction of antenna systems for light-harvesting,<sup>51</sup> and solar energy conversion.<sup>51d,52</sup>

Due to the stepwise synthesis, either divergent or convergent,<sup>46</sup> number and position of chromophores and/or luminophores can be implemented in the dendritic structure with high precision. The confinement of multiple photoactive units in a small volume provides signal amplification for sensing purposes,<sup>53</sup> which can be very important for some biological and

- 
8729. (d) M. Maus, S. Mitra, M. Lor, J. Hofkens, T. Weil, A. Herrmann, K. Müllen and F. C. De Schryver, *J. Phys. Chem. A*, 2001, 105, 3961. (e) L. Brauge, A.-M. Caminade, J.-P. Majoral, S. Slomkowski and M. Wolszczak, *Macromolecules*, 2001, 34, 5599. (f) S. F. Swallen, Z. Zhu, J. S. Moore and R. Kopelman, *J. Phys. Chem. B*, 2000, 104, 3988. (g) L. A. Baker and R. M. Crooks, *Macromolecules*, 2000, 33, 9034.
- [49] (a) F. Loiseau, S. Campagna, A. Hameurlaine and W. Dehaen, *J. Am. Chem. Soc.*, 2005, 127, 11352. (b) M. Cotlet, T. Vosch, S. Habuchi, T. Weil, K. Müllen, J. Hofkens and F. De Schryver, *J. Am. Chem. Soc.*, 2005, 127, 9760. (c) J.-P. Cross, M. Lauz, P. D. Badger and S. Petoud, *J. Am. Chem. Soc.*, 2004, 126, 16278; (d) G. Bergamini, C. Saudan, P. Ceroni, M. Maestri, V. Balzani, M. Gorka, S.-K. Lee, J. van Heyst and F. Vögtle, *J. Am. Chem. Soc.*, 2004, 126, 16466.
- [50] (a) W.-S. Li, K. S. Kim, D.-L. Jiang, H. Tanaka, T. Kawai, J. H. Kwon, D. Kim and T. Aida, *J. Am. Chem. Soc.*, 2006, 128, 10527. (b) A. Petrella, J. Cremer, L. De Cola, P. Baeuerle and R. M. Williams, *J. Phys. Chem. A*, 2005, 109, 11687. (c) K. R. J. Thomas, A. L. Thompson, A. V. Sivakumar, C. J. Bardeen and S. Thayumanavan, *J. Am. Chem. Soc.*, 2005, 127, 373. (d) R. Gronheid, A. Stefan, M. Cotlet, J. Hofkens, J. Qu, K. Müllen, M. Van der Auweraer, J. W. Verhoeven and F. C. De Schryver, *Angew. Chem. Int. Ed.*, 2003, 42, 4209. (e) T. H. Ghaddar, J. F. Wishart, D. W. Thompson, J. K. Whitesell and M. A. Fox, *J. Am. Chem. Soc.*, 2002, 124, 8285.
- [51] For some recent reviews, see: a) P. Ceroni, G. Bergamini, F. Marchioni, V. Balzani, *Prog. Polym. Sci.* 2005, 30, 453-473; b) F.C. De Schryver, T. Vosch, M. Cotlet, M. Van der Auweraer, K. Müllen, J. Hofkens, *Acc. Chem. Res.* 2005, 38, 514-522; c) V. Balzani, A. Credi, M. Venturi, *Molecular Devices and Machines: Concepts and Perspectives for the Nanoworld*, Wiley-VCH, Weinheim, 2008, Ch. 6; d) V. Balzani, A. Credi, M. Venturi, *ChemSusChem*, 2008, 1, 26.
- [52] (a) S. Jordens, G. De Belder, M. Lor, G. Schweitzer, M. Van der Auweraer, T. Weil, E. Reuther, K. Müllen and F. C. De Schryver, *Photochem. Photobiol. Sci.*, 2003, 2, 177. (c) U. Hahn, M. Gorka, F. Vögtle, V. Vicinelli, P. Ceroni, M. Maestri and V. Balzani, *Angew. Chem. Int. Ed.*, 2002, 41, 3595. (d) V. Vicinelli, P. Ceroni, M. Maestri, V. Balzani, M. Gorka and F. Vögtle, *J. Am. Chem. Soc.*, 2002, 124, 6461. (e) M.-S. Choi, T. Aida, T. Yamazaki and I. Yamazaki, *Chem. Eur. J.*, 2002, 8, 2668. (f) J. M. Serin, D. W. Brousmiche and J. M. J. Fréchet, *Chem. Commun.*, 2002, 2605.
- [53] (a) M.-H. Xu, J. Lin, Q.-S. Hu and L. Pu, *J. Am. Chem. Soc.*, 2002, 124, 14239. (b) V. J. Pugh, Q. S. Hu, X. Zuo, F. D. Lewis and L. Pu, *J. Org. Chem.*, 2001, 66, 6136. (c) V. Balzani, P. Ceroni, S. Gestermann, C. Kauffmann, M. Gorka and F. Vögtle, *Chem. Commun.*, 2000, 853.

biomedical applications.<sup>54</sup> Furthermore, the presence of multiple chromophores/ luminophores in the same molecule enables the detection of single dendrimer *via* single molecule spectroscopy (SMS).<sup>55</sup> Yet, an increased sensitivity with respect to specific classes of molecules can be established, enabling the detection of very low concentrations of substrates, which is of great interest in molecular recognition phenomena.<sup>56</sup>

Molecular and supramolecular devices can be built up taking advantage by dendritic framework in realizing systems capable of changing the wavelength of light,<sup>57</sup> LEDs,<sup>58</sup> and lasing materials.<sup>59</sup>

- 
- [54] a) Guillaudeau, Steven J.; Fox, Megan E.; Haidar, Yarah M.; Dy, Edward E.; Szoka, Francis C.; Frechet, Jean M. J. *Bioconjugate Chemistry*, 2008, 19(2), 461-469. b) Langereis, Sander; Dirksen, Anouk; Hackeng, Tilman M.; Van Genderen, Marcel H. P.; Meijer, E. W., *New Journal of Chemistry* 2007, 31(7), 1152-1160. c) Krause, Werner; Hackmann-Schlichter, Nicola; Maier, Franz Karl; Muller, Rainer, *Topics in Current Chemistry*, 2000, 210(Dendrimers II).
- [55] a) Oesterling, Ingo; Muellen, Klaus, *Journal of the American Chemical Society*, 2007, 129(15), 4595-4605. b) Sliwa, M.; Flors, C.; Oesterling, I.; Hotta, J.; Mullen, K.; De Schryver, F. C.; Hofkens, J., *Journal of Physics: Condensed Matter*, 2007, 19(44), 445004/1-445004/14. c) De Schryver, F. C.; Vosch, T.; Cotlet, M.; Van der Auweraer, M.; Muellen, K.; Hofkens, J., *Accounts of Chemical Research*, 2005, 38(7), 514-522. d) Masuo, Sadahiro; Vosch, Tom; Cotlet, Mircea; Tinnefeld, Philip; Habuchi, Satoshi; Bell, Toby D. M.; Oesterling, Ingo; Beljonne, David; Champagne, Benoit; Muellen, Klaus; Sauer, Markus; Hofkens, Johan; De Schryver, Frans C., *Journal of Physical Chemistry B*, 2004, 108(43), 16686-16696.
- [56] For some reviews and recent papers, see: a) M.W.P.L. Baars, E.W. Meijer, *Top. Cur. Chem.* 2000, 210, 131-182; b) D. Astruc, F. Chardac, *Chem. Rev.* 2001, 101, 2991-3024; c) C.A. Schalley, B. Baytekin, H.T. Baytekin, M. Engeser, T. Felder, A. Rang, *J. Phys. Org. Chem.* 2006, 19, 479-490, d) T.Darbre, J.-L. Reymond, *Acc. Chem Res.* 2006, 39, 925-934; e) R. van Heerbeek, P.C.J. Kamer, P.N.M.W. van Leeuwen, J.N.H. Reek, *Org. Biomol. Chem.* 2006, 4, 211-223; f) U. Hahn, A. Kaufmann, M. Nieger, O. Julinek, M. Urbanova, F. Vögtle, *Eur. J. Org. Chem.* 2006, 1237-1244; g) M.Gingras, J.-M. Raimundo, Y.M. Chabre, *Angew. Chem. Int. Ed.* 2007, 46, 1010-1017; h) M. Chai, A.K. Holley, M. Kruskamp, *Chem. Commun.* 2007, 168-170; i) F. Puntoriero, P. Ceroni, V. Balzani, G. Bergamini, F. Vögtle, *J. Am. Chem. Soc.* 2007, 129, 10714-10719.
- [57] P. Furuta, J. Brooks, M. E. Thompson and J. M. J. Fréchet, *J. Am. Chem. Soc.*, 2003, 125, 13165.
- [58] a) Bolink, Henk J.; Santamaria, Sonsoles Garcia; Sudhakar, Sundarraj; Zhen, Changgua; Sellinger, Alan, *Chemical Communications*, 2008, 5, 618-620. b) Burn, Paul L.; Lo, Shih-Chun; Samuel, Ifor D. W., *Advanced Materials*, 2007, 19(13), 1675-1688. c) Lo, Shih-Chun; Burn, Paul L., *Chemical Reviews*, 2007, 107(4), 1097-1116.
- [59] a) Lawrence, Justin R.; Namdas, Ebinazar B.; Richards, Gary J.; Burn, Paul L.; Samuel, Ifor D. W., *Advanced Materials*, 2007, 19(19), 3000-3003. b) Ribierre, J. C.; Tsiminis, G.; Richardson,

Dendrimers contain internal dynamic cavities with their own microenvironment different from the bulk of the solution, and show well-defined dimensions close to that of important biological molecules like proteins and bioassemblies. As a result, applications for controlling drug delivery and gene release are foreseen.<sup>60</sup>

Some dendritic structures and their properties are discussed in chapter 5: (i) in section 5.1.1. a dendrimer, synthesized in the Kekulé-Institut für Organische Chemie und Biochemie at Bonn University in the laboratories directed by Prof. Vögtle,<sup>61</sup> acts as a molecular antenna unit efficiently funneling the excitation energy to a ruthenium complex ( $[\text{Ru}(\text{bpy})_2(\text{CN})_2]$  is kindly supplied by Prof. Juris, University of Bologna) which in its turn sensitizes a lanthanide metal ion luminescence through a subtle balance of metal-ligand interactions; (ii) section 5.1.2. describes a family of dendrimers, provided by Prof. Vögtle research group,<sup>62</sup> showing temperature dependent intramolecular energy transfer processes; (iii) in section 5.2.2. is demonstrated how two dendrimers containing multiple electro-active units, synthesized in the Department of Chemistry and Biochemistry of the University of California at Los Angeles by Prof. Stoddart research group,<sup>63</sup> undergo charge-pooling; (iv) the latter dendrimers can be involved in molecular recognition phenomena as multivalent hosts (section 5.2.3.); (v) section 5.2.4. shows, instead, how dendrimers can be involved in molecular recognition phenomena as

---

S.; Turnbull, G. A.; Samuel, I. D. W.; Barcena, H. S.; Burn, P. L., *Applied Physics Letters*, 2007, 91(8), 081108/1-081108/3.

[60] Some recent examples: a) Myc, Andrzej; Patri, Anil K.; Baker, James R., Jr., *Biomacromolecules*, 2007, 8(10), 2986-2989. b) Pan, Bifeng; Cui, Daxiang; Sheng, Yuan; Ozkan, Cengiz; Gao, Feng; He, Rong; Li, Qing; Xu, Ping; Huang, Tuo., *Cancer Research*, 2007, 67(17), 8156-8163. c) Bai, Shuhua; Thomas, Chandan; Rawat, Amit; Ahsan, Fakhru., *Critical Reviews in Therapeutic Drug Carrier Systems*, 2006, 23(6), 437-495.

[61] Saudan, C.; Balzani, V.; Ceroni, P.; Gorka, M.; Maestri, M.; Vicinelli, V.; Vögtle, F. *Tetrahedron* 2003, 59, 3845.

[62] C. Giansante, P. Ceroni, V. Balzani, M. Maestri, S.-K. Lee, F. Vögtle *New J Chem.*, 2007, 31, 1250.

[63] C. M. Ronconi, J. F. Stoddart, V. Balzani, M. Baroncini, P. Ceroni, C. Giansante, M. Venturi, to be submitted

guests (dendritic substrates<sup>64,65</sup> provided by Prof. Vögtle research group while the endo-receptor molecule<sup>66</sup> comes from laboratories directed by Prof. Klärner in the Institut für Organische Chemie at Essen University).

### 4.3. Metal Complexes

In the introduction was stated the importance played by coordination chemistry in settling fundamental principles of supramolecular chemistry. Metal complexes, in fact, clearly show interactional complementarity of the binding processes due to the strength of ion-dipole interactions. Much of the work on supramolecular systems has developed from macrocyclic ligands for metal cations where lone pairs of heteroatoms are attracted by positively charged metal ions. Coordinative bonds are, instead, mostly electrostatic in the case of nonpolarisable metal cations and hard bases (a well-known example is  $\text{Ru}(\text{bpy})_3^{2+}$ ) conferring high degree of covalent character to the bonds. Anyway, describing transition metal complex molecular orbitals as a linear combination of the orbitals of metal and ligands, the supramolecular character of a metal complex emerges. Intrinsic properties of both the metal and ligands either features peculiar of the whole compound are discernible. Metal-centred electronic transitions are those of lower energy and usually symmetry forbidden, while ligand-centred transitions are much higher in energy and also redox processes are commonly localized on the metal and ligands slightly affecting each other. The most common process arising from intercomponent interactions is metal-to-ligand (and viceversa) charge transfer which is allowed conserving angular momentum and usually originates a strong absorption in the visible region of the electromagnetic spectrum. Dissipation of the excitation energy may occur through a long-lived

---

[64] Ceroni, P.; Vicinelli, V.; Maestri, M.; Balzani, V.; Müller, W. M.; Müller, U.; Hahn, U.; Osswald, F.; Vögtle, F. *New J. Chem.* 2001, 25, 989.

[65] V. Balzani, H. Bandmann, P. Ceroni, C. Giansante, U. Hahn, Frank-Gerrit Klärner, W. M. Müller, U. Müller, C. Verhaelen, V. Vicinelli, F. Vögtle, *J. Am. Chem. Soc.*, 2006, 128, 637.

[66] F.-G. Klärner, U. Burkert, M. Kamieth, R. Boese, *J. Phys. Org. Chem.*, 2000, 13, 604.

radiative pathway termed phosphorescence, due to heavy transition metal ions that allow transitions between electronic states with different spin multiplicity through high spin-orbit coupling. Fine tuning of spectroscopic properties of metal complexes can be achieved because stability of the molecular orbitals are highly dependent on the nature of metals and ligands.

Taking advantage of their well-known photophysical, photochemical and electrochemical properties mononuclear transition metal complexes are widely used in designing and constructing multicomponent systems. They can act as photosensitizers in systems for vectorial charge separation,<sup>16,67</sup> biomimetic photocatalyst for water oxidation,<sup>68</sup> photoinduced electron collection and storage,<sup>69</sup> molecular machines performing photoinduced linear movements.<sup>70</sup> They can serve as sensors both photoluminescent<sup>71</sup> and redox-active,<sup>72</sup> as switches in energy- and electron-transfer processes.<sup>73</sup>

Polynuclear transition metal complexes have been prepared from suitable choice of mononuclear building blocks and appropriate design of the supramolecular structure allowing vectorial energy transfer, photoinduced charge separation, multielectron exchange at predetermined potentials, etc.<sup>74</sup>

In chapter 6. is reported the photophysical and photochemical characterization of transition metal complexes with ditopic ligands: (i) phosphino-aminothiazoline Pt<sup>2+</sup> complexes, synthesized

---

[67] a) Hu, Yi-Zhen; Tsukiji, Shinya; Shinkai, Seiji; Oishi, Shigero; Hamachi, Itaru., *Journal of the American Chemical Society*, 2000, 122(2), 241-253. b) Heleg-Shabtai, Vered; Gabriel, Tobias; Willner, Itamar., *Journal of the American Chemical Society*, 1999, 121(13), 3220-3221.

[68] Herrero, Christian; Lassalle-Kaiser, Benedikt; Leibl, Winfried; Rutherford, A. William; Aukauloo, Ally., *Coordination Chemistry Reviews*, 2008, 252, 456-468.

[69] S. M. Molnar, G. Nallas, J. S. Bridgewater, K. J. Brewer, *J. Am. Chem. Soc.*, 1994, 116, 5206.

[70] P.R. Ashton, R. Ballardini, V. Balzani, A. Credi, R. Dress, E. Ishow, C.J. Kleverlann, O. Kocian, J.A. Preece, N. Spencer, J.F. Stoddart, M. Venturi, S. Wenger, *Chem. Eur. J.*, 2000, 6, 3558.

[71] P. D. Beer, F. Szemes, *J. Chem. Soc. Chem. Commun.*, 1995, 2245.

[72] J. D. Carr, L. Lambert, D.E. Hibbs, *Chem. Commun.*, 1997, 1649.

[73] V. Balzani, A. Credi, M. Venturi, *Molecular Devices and Machines: Concepts and Perspectives for the Nanoworld*, Wiley-VCH, Weinheim, 2008, see chapter 4.

[74] Balzani, V.; Juris, A.; Venturi, M.; Campagna, S.; Serroni, S., *Chem. Rev.*, 1996; 96(2); 759-834.

in the Laboratoire de Chimie de Coordination by Dr. Braunstein of the Université Louis Pasteur at Strasbourg,<sup>75</sup> serve as building block in the construction of heterodimetallic coordination polymers (section 6.1.); (ii) a series of  $\text{Ru}^{2+}$  complexes bearing crown-ether moieties, prepared by Dr. Fedorov group in the Photochemistry Center, Laboratory Photochemistry of Supramolecular Systems at Moscow,<sup>76</sup> are described in section 6.2. together with their metal cation sensing properties. In section 5.1.1. is reported the formation of equilibrium mixtures of trinuclear complexes where a lanthanide metal ions is bridged by cyanide ligands of two ruthenium complexes (Figure 4.3.).

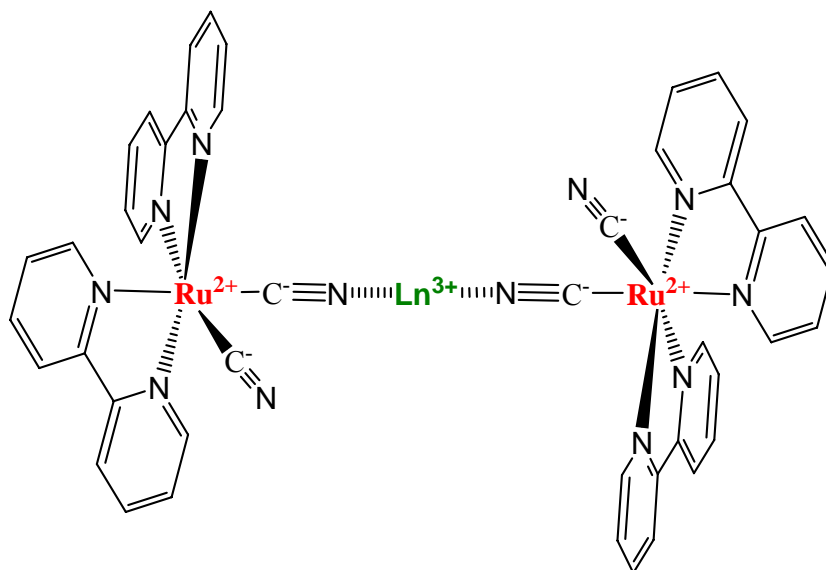


Figure 4.3. Illustration representative of the trinuclear metal complex formed in solution discussed in section 5.1.1.

[75] R. Pattacini, C. Giansante, P. Ceroni, M. Maestri, P. Braunstein., *Chemistry- An European Journal*, 2007, 13, 10117.

[76] M. Venturi, O. A. Fedorova, E. N. Andryukhina, N. E. Shepel, M. M. Mashura, Yu. V. Fedorov, M. V. Alfimov, «*Supramolecules: Design and Funcionality on a Nanomolecular Scale*»: - Prague. - Czech. - 5-9 September 2004. - P. 36.

## 4.4. Macrocycles

Numerous types of synthetic macrocycles have been developed in recent years<sup>77</sup> but, the present section does not claim reviewing this topic. An introduction to the classes of macrocyclic molecules present in next chapters has to be considered comprehensive.

Chemists usually refer to any molecule showing an arbitrarily large number of atoms arranged in a cyclic fashion as macrocycle, despite IUPAC definition of macrocycle and macromolecule.<sup>78</sup> The use of macrocycles in supramolecular chemistry and in molecular recognition phenomena has arisen from Pedersen accidental synthesis of a cyclic polyether molecule<sup>79</sup> and the subsequent elucidation of the macrocyclic effect on the binding constants with alkali metal ions. The macrocyclic effect has been attributed to the increase of both enthalpic and entropic contributions: preorganization of the binding domains achieved during synthetic process rather than self-organization of an acyclic homolog result in reduced conformational rearrangements, reduced repulsion between close lone-pairs, and reduced lone-pairs desolvation. Related examples are presented in section 5.1.1. where the core of the investigated dendrimer is constituted by a cyclam unit and in section 6.2. where crown-ether units are appended to  $\text{Ru}^{2+}$  complexes.

It is noteworthy how different classes of supramolecular species can be used in building up more complex structures so making rather blurred and arbitrary the categorisation of the resulting compounds, though academy cannot prescind from nomenclature. Figure 4.4. shows a supramolecular system, never synthesized though, that clearly illustrates such terminology problems.

---

[77] Calixarenes, clathrates, cavitands, cryptands, carcerands, coronands, spherands, cryptophanes, speleands, etc. realized by chemists clearly illustrate the great interest in this topic.

[78] IUPAC Compendium of Chemical Terminology, 2nd Edition, 1997.

[79] C. J. Pedersen, *J. Am. Chem. Soc.*, 1967, 89, 7017.

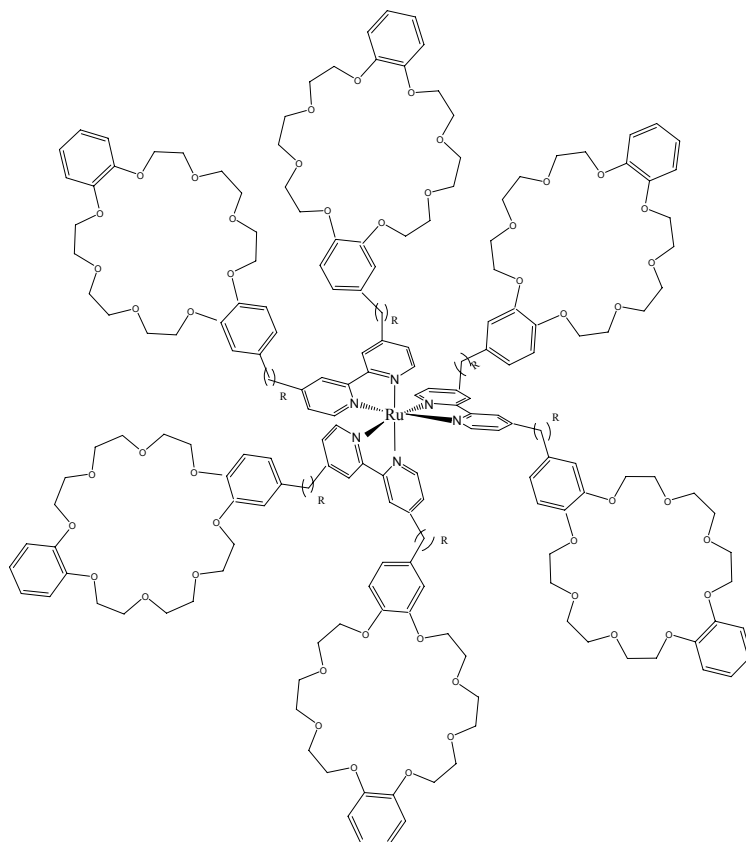


Figure 4.4. Difficult categorization evidenced by an hypothetical compound: a metal complex bearing macrocyclic units can act as the core of a dendrimer obtained hosting ammonium residues representing dendritic wedges.

In contrast to conformationally flexible cycles, shape-persistent macrocycles show rigid backbones with reduced conformational flexibility giving rise to large molecular surfaces that, heavily relying on van der Waals and hydrophobic interactions, can organize into order structures.<sup>80</sup> Shape-persistent macrocycles have an interior and an exterior at which site-specific substitution with functional groups can be accomplished. Their use as scaffolds for placing functional units at predetermined spatial positions to one another is noteworthy. This latter

[80] a) Balakrishnan, K.; Datar, A.; Zhang, W.; Yang, X.; Naddo, T.; Huang, J.; Zuo, J.; Yen, M.; Moore, J. S.; Zang, L., *J. Am. Chem. Soc.*, 2006, 128(20), 6576-6577; b) Moore, J. S., *Acc. Chem. Res.*, 1997, 30(10), 402-413; c) Dahui Zhao, Jeffrey S. Moore, *Chem. Commun.*, 2003, (7), 807-818.

aspect offers intriguing possibilities for targeting, sensing, and catalysis, but also allows energy- and electron-transfer processes to be studied on the basis of defined distance relationships. These scaffold applications require macrocycles site-specifically decorated with several different functionalities. Shape persistent macrocycles bearing photoactive units have been synthesized in the Department of Materials at the Institute of Polymers, ETH Zürich, in the laboratories directed by Prof. Schlüter<sup>81</sup> (discussion in section 7.1.)

Another widely investigated class of macrocycles is that named cyclophane, i.e., a molecule composed of an aromatic ring and an aliphatic unit which forms a bridge between two (or more) positions of the aromatic ring. Usually, cyclophanes are not at all planar molecules; they exhibit an interesting stereochemistry; molecular parts are placed and sometimes fixed in unusual orientations toward each other, and often the molecules are not rigid but conformationally flexible. Ring strain and, as a consequence, deformation of the aromatic rings out of planarity are often encountered. Electronic interactions between aromatic rings fixed face to face can take place. In addition, influence on substitution reactions in the aromatic rings result; that is, substituents in one ring induce transannular electronic effects in the other ring, often leading to unexpected products.<sup>82</sup> Cyclophanes have become important in host-guest chemistry and supramolecular chemistry as they constitute host compounds for guest species because of their cavities. For this reason, water-soluble cyclophanes have been synthesized showing the ability to include nonpolar guest molecules in aqueous solution.<sup>83</sup> Among all possible applications, the use of cyclophanes in designing materials displaying nonlinear optical phenomena is discussed in section 7.2. (investigated compounds synthesized in the group

---

[81] Junji Sakamoto, A. Dieter Schlüter, *European Journal of Organic Chemistry*, 2007, 16, 2700-2712.

[82] Voegtle, F. *Cyclophanes Chemistry*; Wiley & Sons: New York, 1993.

[83] F. Diederich, *Cyclophanes*, RSC, Cambridge, 1991.

directed by Prof. Luh, Department of Chemistry, National Taiwan University at Taipei)<sup>84</sup>. Organic molecules show large  $\pi$ -electron-mediated nonlinear optical polarizabilities and widepossibility for broad design flexibility through chemical functionalization. Literature reports are replete with examples based on the donor-conjugated bridge-acceptor design displaying intramolecular charge transfer (ICT) upon excitation. Optical polarizabilities change considerably when increasing the length of the  $\pi$ -electron bridge and the strength of the donor and acceptor groups. Despite this control, the dipolar character of D- $\pi$ -A structures retains considerable drawbacks. Dipole-dipole electrostatic interactions often result in an antiparallel molecular arrangement and a subsequent cancellation of the nonlinear response of bulk materials. Additionally, the highly anisotropic structure of an optimized material, containing aligned polar rodlike molecules, is not compatible with the polarization independent NLO response required for devices to be inserted in an optical telecommunication system. Combined group theory and quantum mechanical principles provide novel guidelines for nondipolar, molecular structures, which have become known as octupolar molecules. To take full advantage of the extended two- and three-dimensional structure of molecules bearing octupolar charge distributions, one would ideally design a three-dimensional conjugated core based on the (eventually distorted) cubic template. Electron donor and acceptor groups must be attached to this core, using a regiochemically precise synthetic methodology that keeps the desired symmetry of the target molecule. The [2.2] $\rho$ -cyclophane framework provides a suitably flexible backbone in the form of an original polarizable transmitting unit that allows for subsequent functionalization. The two aromatic units are held in close proximity, at a distance shorter than the van der Waals distance. Substitution at the 4, 7, 12, and 15 positions leads to an

---

[84] C.-F. Lee, L.-M. Yang, T.-Y. Hwu, A.-S. Feng, J.-C. Tseng, T.-Y. Luh, *J. Am. Chem. Soc.* 2000, 122, 4992-4993; b) C.-F. Lee, C.-Y. Liu, H.-C. Song, S.-J. Luo, J.-C. Tseng, H.-H. Tso, T.-Y. Luh, *Chem. Commun.* 2002, 23, 2824-2825; c) C.-Y. Liu, T.-Y. Luh, *Org. Lett.* 2002, 4, 4305-4307; d) C.-M. Chou, W.-Q. Chen, J.-H. Chen, C.-L. Lin, J.-C. Tseng, C.-F. Lee, T.-Y. Luh, *Chem. Asian J.* 2006, 1, 46-55; e) for a review, see: T.-Y. Luh, C.-F. Lee, *Eur. J. Org. Chem.* 2005, 3875-3885.

elongated cubic molecular structure with orthorhombic symmetry features enabling three-dimensional multipolar spatial arrangements, including the boundary case of octupoles.<sup>85</sup>

## 4.5. Conjugated Polymers

The insertion of such a topic in a text regarding supramolecular systems may result controversial since, as stated in section 4.1., conjugated polymers are definitely large molecules. Anyway, it has to be evidenced how conjugated polymers represent one of the most useful chemical platforms for the design of chemical sensors which tightly relies on molecular recognition phenomena. Often missing from these recognition schemes is a viable transduction mechanism and controlled conjugated polymer based supramolecular structures may effectively fill in this transduction void.<sup>86</sup>

In conjugated polymers, the chemical bonding leads to one unpaired electron (the  $\pi$  electron) per carbon atom. Moreover,  $\pi$  bonding, in which the carbon orbitals are in the  $sp^2p_z$  configuration and in which the orbitals of successive carbon atoms along the backbone overlap, leads to electron delocalization along the backbone of the polymer. This electronic delocalization provides charge mobility along the backbone of the polymer chain. As a consequence, the electronic structure in conducting polymers is determined by the chain symmetry (i.e. the number and kind of atoms within the repeat unit), with the result that such polymers can exhibit semiconducting or even metallic properties. Because band gap depends upon the molecular structure of the repeat unit, synthetic chemists are provided with the opportunity and the challenge to control the energy gap by design at the molecular level.

---

[85] a) Woo, H. Y.; Hong, J. W.; Liu, B.; Mikhailovsky, A.; Korystov, D.; Bazan, G. C., *J. Am. Chem. Soc.*, 2005, 127(3); 820-821. b) Bartholomew, G. P.; Rumi, M.; Pond, S. J. K.; Perry, J. W.; Tretiak, S.; Bazan, G. C., *J. Am. Chem. Soc.*, 2004, 126(37), 11529-11542. c) Bartholomew, G. P.; Ledoux, I.; Mukamel, S.; Bazan, G. C.; Zyss, J., *J. Am. Chem. Soc.*, 2002, 124(45), 13480-13485; d) Zyss, J.; Ledoux, I.; Volkov, S.; Chernyak, V.; Mukamel, S.; Bartholomew, G. P.; Bazan, G. C., *J. Am. Chem. Soc.*, 2000, 122(48); 11956-11962.

[86] a) McQuade, D. T.; Pullen, A. E.; Swager, T. M., *Chem. Rev.*, 2000, 100(7); 2537-2574. b) Swager, T. M., *Acc. Chem. Res.*, 1998; 31(5); 201-207.

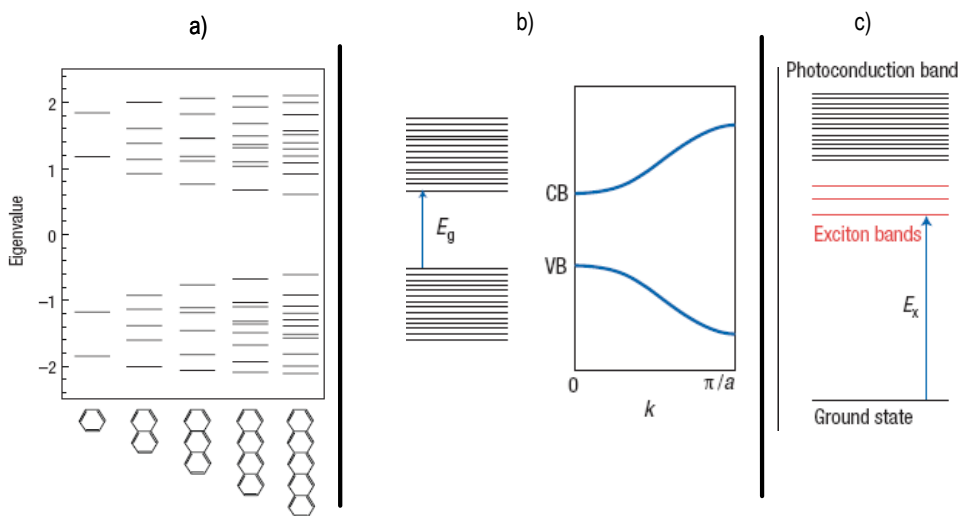


Figure 4.5. In excited states that involve transitions from a localized orbital to another localized orbital, both carriers, electron and hole, are similarly extended, and therefore spatially overlapped (molecular orbital picture in a. part). Same considerations true for excited states that have their origin in a transition from a delocalized orbital to a delocalized orbital (band theory picture in b. part). Mixing the two previous models produces a configuration-interaction description of the intrachain exciton better suitable for quasi-one dimensional systems as shown in part c.: an excited state formed by a transition from a localized orbital to a delocalized orbital, the hole is confined to a monomer, while the electron is delocalized over the chain (or vice versa).<sup>87</sup>

Reversible doping of conducting polymers, with associated control of the electrical conductivity over the full range from insulator to metal, can be accomplished either by chemical doping or by electrochemical doping. Concurrent with the doping, the electrochemical potential (the Fermi level) is moved either by a redox reaction or an acid-base reaction into a region of energy where there is a high density of electronic states; charge neutrality is maintained by the introduction of counter ions. Metallic polymers are, therefore, salts. The electrical conductivity results from the existence of charge carriers (through doping) and from

[87] A. Köhler, D. A. dos Santos, D. Beljonne, Z. Shuai, J.-L. Brédas, A. B. Holmes, A. Kraus, K. Müllen, R. H. Friend, *Nature*, 1998, 392, 903.

the ability of these charge carriers to move along the  $\pi$ -bonded chain. Consequently, doped conjugated polymers are good conductors for two main reasons: (i) doping introduces carriers into the electronic structure so, since every repeat unit is a potential redox site, conjugated polymers can be doped n-type (reduced) or p-type (oxidized) to a relatively high density of charge carriers; (ii) the attraction of an electron in one repeat unit to the nuclei in the neighbouring units leads to carrier delocalization along the polymer chain and to charge-carrier mobility, which is extended into three dimensions through interchain electron transfer. Disorder, however, limits the carrier mobility and, in the metallic state, limits the electrical conductivity. Indeed, research directed toward conjugated polymers with improved structural order and hence higher mobility is a focus of current activity in the field. Conducting polymers were initially attractive because of the fundamental interest in the doping and the doping-induced metal-insulator transition. However, the chemistry and physics of these polymers in their non-doped semiconducting state are of great interest because they provide a route to "plastic electronic" devices. Although polymer diodes were fabricated and characterized in the 1980s, the discovery of light-emitting diodes (LEDs) by Richard Friend and colleagues at Cambridge in 1990<sup>88</sup> provided the stimulus for a major push in this direction. The polymer light-emitting diode is, however, only one of a larger class of devices in the emerging class of plastic optoelectronic devices, including lasers, high sensitivity plastic photodiodes and photovoltaic cells, ultrafast image processors, thin-film transistors, and all-polymer integrated circuits; in each case these sophisticated electronic components are fabricated from semiconducting and metallic polymers.

Because the interchain electron-transfer interactions of conjugated polymers are relatively strong compared with the van der Waals and hydrogen-bonding interchain interactions typical of saturated polymers, conducting polymers tend to be insoluble and infusible. Side-chain

---

[88] J. H. Burroughes, D. D. C. Bradley, A. R. Brown, R. N. Marks, R. H. Friend, P. L. Burns, A. B. Holmes, *Nature*, 1990, 347, 539.

functionalization overcomes these drawbacks enabling the processing of semiconducting polymers from solution in organic solvents or from water by incorporating polar groups. All photonic plastic devices present a common structure: they are thin-film devices in which the active layers are fabricated by casting the semiconducting and/or metallic polymers from solution (e.g. spin-casting or ink-jet printing).<sup>89</sup>

The introduction of ionic groups, essential for increasing water solubility opened the way in using conjugated polymers (polyelectrolytes when water soluble; CPEs is the acronym) for the development of biological detection protocols that take advantage of the optical amplification afforded by CPEs. Sensing strategy takes advantage of the large optical cross section of CPEs in combination with a biomolecular recognition event that triggers fluorescence resonance energy transfer (FRET) to an acceptor dye. Electrostatic interactions are essential for controlling the average distance between optical partners and thereby the sensitivity and selectivity of the assay.

It has been possible through substantially different strategies to design assays that are specific to proteins,<sup>90</sup> DNA,<sup>91</sup> and RNA.<sup>92</sup> The overall process is complex, and there are substantial gaps in the general understanding, in particular the general shape, size, and molecular organization on the resulting aggregates. Despite the supramolecular complexity, molecular design has produced a variety of structures for optimizing assays, which allow one to control the colour of emission, the ability of the main chain to adapt to the secondary structure of biomolecules, the chain dependence of the recognition event, and the ratio of FRET vs photoinduced charge transfer. Recently, the necessity of target labelling required in traditional microarray protocols has been eliminated: DNA hybridization to immobilized PNA spots results in a change in the net charge at that particular surface leading to strong

---

[89] A. J. Heeger, *Angew. Chem., Int. Ed.*, 2001, 40(14), 2591-2611.

[90] Pinto, M. R.; Schanze, K. S. *Proc. Natl. Acad. Sci. U.S.A.* 2004, 101, 7505.

[91] Gaylord, B. S.; Heeger, A. J.; Bazan, G. C. *Proc. Natl. Acad. Sci. U.S.A.* 2002, 99, 10954.

[92] Liu, B.; Baudrey, S.; Jaeger, L.; Bazan, G. C. *J. Am. Chem. Soc.* 2004, 126, 4076.

electrostatic interactions between the cationic polymer and negatively charged DNA that bind the polymer to the hybrid DNA/PNA complex. By exciting the conjugated polymer at 488 nm on a commercial microarray scanner, the presence of the target is directly indicated by the fluorescence emission of the polymer.<sup>93</sup>

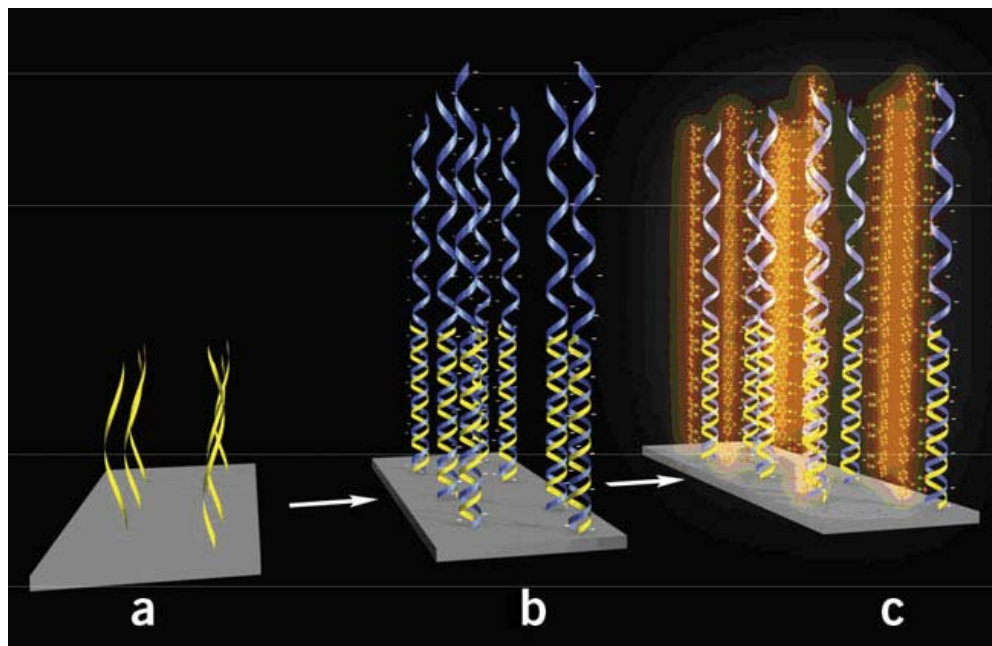


Figure 4.6. Schematic illustration of label-free ssDNA detection using immobilized PNA and cationic conjugated polymers (CCPs). (a) Surface-bound PNA (shown in yellow), (b) hybridization with ssDNA (shown in blue) and (c) electrostatic adsorption of the CCPs onto the PNA/ssDNA surface.

CPEs are demonstrated to show large two-photon cross section, as reported in chapter 8. The experimental work has been carried out at the Institute for Polymers and Organic Solids directed by Prof. Bazan in the Departments of Chemistry and Biochemistry and Materials of the University of California at Santa Barbara. It has been recently shown how two-photon induced FRET from donor CPEs drastically enhances the fluorescence of an acceptor dye intercalated in

[93] a) Cheng Jun Sun, Brent S Gaylord, Janice W Hong, Bin Liu, Guillermo C Bazan, *Nature Protocols*, 2007, 2, 2148. b) Bin Liu, Guillermo C Bazan, *Nature Protocols*, 2006, 1, 1698.

double-stranded DNA compared to direct two-photon excitation of the intercalated dye (Figure 4.7).<sup>94</sup>

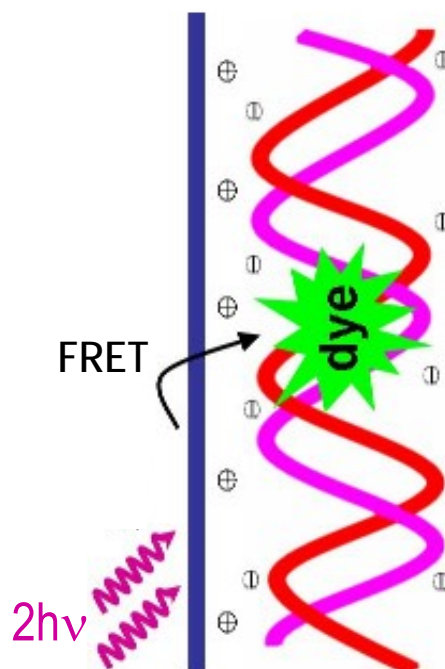


Figure 4.7. Schematic illustration of the two-photon excitation of the cationic conjugated polymer (blue line) followed by Foster-type resonance energy-transfer to the dye intercalated in dsDNA (pink and red stripes).

## 4.6. Sample Preparation

Sample solutions are prepared weighting compounds with a Mettler AT261 balance (sensitivity 0.01 mg, experimental error estimated <10%). All the organic solvents are Merck Uvasol (in spectroscopic measurements) and Romil Hi-Dry™ (in electrochemical measurements) and are used without further purification when not mentioned. The salts, acids and bases solutions are been prepared from commercial Fluka and Aldrich; products used as received. Any other reagent or model compound used is of the best purity commercial availability.

[94] Tian, Ning; Xu, Qing-Hua., *Advanced Materials*, 2007, 19(15), 1988-1991.



## 5. Dendrimers

### 5.1. Light Harvesting Dendrimers

#### 5.1.1. Recognition-mediated Intercomponent Energy-transfer

Self-assembly of molecular components by weak, non covalent interactions is a widespread concept to nature's forms and functions<sup>95</sup> and is attracting increasing interest in artificial systems.<sup>96</sup> The study of light-induced processes in artificial molecular assemblies is very promising to control mechanical movements, process information, and harvest sunlight.<sup>97</sup> Lanthanide metal ions exhibit long-lived and line-like luminescence, but direct excitation is inefficient because of the forbidden nature of their electronic transitions. Therefore, coordinating organic or inorganic chromophores are usually exploited to sensitize their luminescence (antenna effect).<sup>98</sup> Another drawback of lanthanide luminescence is the quenching of the emitting excited state by high frequency vibrational modes of the solvent,<sup>99</sup> which can be, at least in part, prevented by enclosing the metal ion in suitably designed ligands. The use

---

[95] Cramer, F. *Chaos and order*, Wiley-VCH: Weinheim, 1993.

[96] Lehn, J.-M. *Chem. Soc. Rev.* 2007, 36, 151.

[97] Balzani, V.; Venturi, M.; Credi, A. *Molecular Devices and Machines- A journey into the Nanoworld*, Wiley-VCH: Weinheim, 2008.

[98] (a) Leonard, J. P.; Nolan, C. B.; Stomeo, F.; Gunnlaugsson, T. *Top. Curr. Chem.* (Balzani, V.; Campagna, S. eds.) 2007, 281, 1. (b) Bünzli, J.-C. G.; Piguet, C. *Chem. Soc. Rev.* 2005, 34, 1048. (c) Parker, D. *Coord. Chem. Rev.* 2000, 205, 109. (d) Sabbatini, N.; Guardigli, M.; Lehn, J.-M. *Coord. Chem. Rev.* 1993, 123, 201.

[99] (a) Reisfeld, R.; Jørgensen, C. H. *Lasers and Excited States of Rare Earths*, Springer-Verlag, Berlin, 1977. (b) Gschneider Jr., K. A.; Eyring L., *Handbook on the Physics and Chemistry of Rare Earths*, North Holland, Amsterdam, 1979; Vol. 3 and Vol. 15.

of dendritic ligands may be particularly interesting because they can function both as light harvesting units and as site-encapsulating nanocontainer.<sup>100</sup>

It was previously reported that dendrimer **D** (Figure 5.1.), consisting of a 1,4,8,11-tetraazacyclotetradecane (cyclam) core with appended 12 dimethoxybenzene and 16 naphthyl units, encapsulates  $\text{Nd}^{3+}$  ions, but, when photoexcited, it is unable to transfer energy to the metal ion.

It has been then found that  $[\text{Ru}(\text{bpy})_2(\text{CN})_2]$  (Figure 5.1.) can coordinate and transfer electronic energy to  $\text{Nd}^{3+}$ .

When  $\text{Nd}^{3+}$  is added, as trifluoromethanesulfonate salt, to a  $\text{CH}_3\text{CN}:\text{CH}_2\text{Cl}_2$  solution containing **D** and  $[\text{Ru}(\text{bpy})_2(\text{CN})_2]$ , self-assembly leads to a three-component system,  $\{\text{D}\cdot\text{Nd}^{3+}\cdot[\text{Ru}(\text{bpy})_2(\text{CN})_2]\}$ , in which the luminescence of both **D** and  $[\text{Ru}(\text{bpy})_2(\text{CN})_2]$  is quenched and the luminescence of  $\text{Nd}^{3+}$  is sensitized. In this three-component system excitation of the dendrimer in the UV and of the Ru(II) complex in the VIS and UV spectral regions is indeed followed by efficient energy transfer to the lanthanide metal ion which plays the role of a light harvesting unit.

For comparison purposes, it has been also investigated the systems in which  $\text{Gd}^{3+}$  replaces  $\text{Nd}^{3+}$ . These two ions have the same charge and similar radius, but the former cannot be involved in energy transfer processes with the investigated chromophores because it does not have low-lying excited states.<sup>99</sup>

---

[100] (a) Oh, J. B.; Nah, M. K.; Kim, Y.H.; Kang, M.S.; Ka, J. W.; Kim, H. K. *Adv. Funct. Mater.* 2007, 17, 413. (b) Shen, L.; Shi, M.; Li, F.Y.; Zhang, D.; Li, X.; Shi, E.; Yi, T.; Du, Y.; Huang, C. *Inorg. Chem.* 2006, 45, 6188. (c) Baek, N. S.; Kim, Y.H.; Roh, S.G.; Kwak, B. K.; Kim, H. K. *Adv. Funct. Mater.* 2006, 16, 1873. (d) Shen, L.; Shi, M.; Li, F.; Zhang, D.; Li, X.; Shi, E.; Yi, T.; Du, Y.; Huang, C. *Inorg. Chem.* 2006, 45, 6188. (e) Ceroni, P.; Bergamini, G.; Marchioni, F.; Balzani, V. *Prog. Polym. Sci.* 2005, 30, 453. (f) Cross, J.P.; Lauz, M.; Badger, P.D.; Petoud, S. *J. Am. Chem. Soc.* 2004, 126, 16278. (g) Vicinelli, V.; Ceroni, P.; Maestri, M.; Balzani, V.; Gorka, M.; Vögtle, F. *J. Am. Chem. Soc.* 2002, 124, 6461. (h) M. Tominaga, J. Hosogi, K. Konishi, T. Aida, *Chem. Commun.* 2000, 719. (i) Kawa, M.; Fréchet, J. M. J. *Chem. Mater.* 1998, 10, 286.

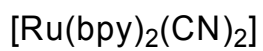
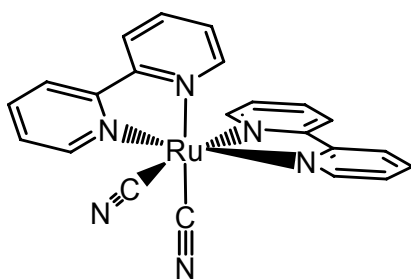
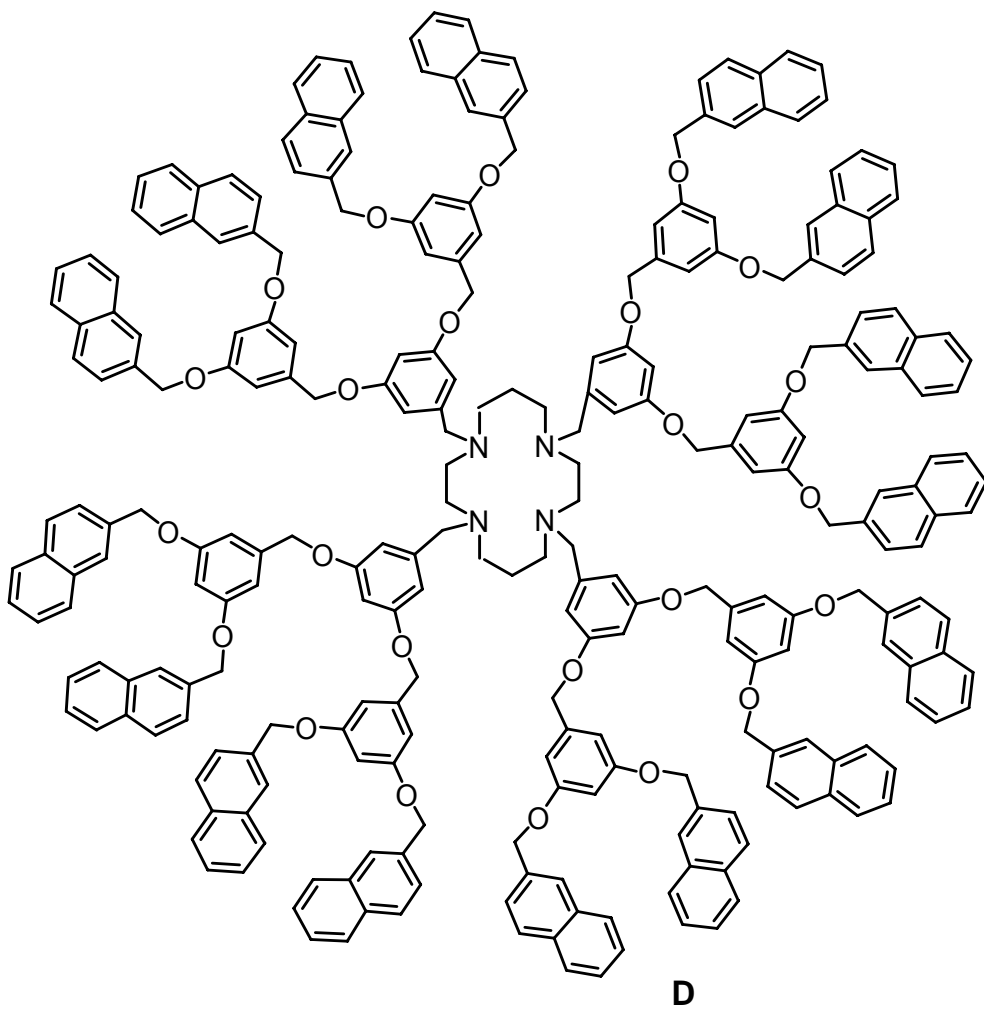


Figure 5.1. Formulae of dendrimer D and [Ru(bpy)<sub>2</sub>(CN)<sub>2</sub>] complex.

*Two-component dendrimer-Nd<sup>3+</sup> system*

The absorption and emission spectra of dendrimer **D** are displayed in Figure 5.2. (solid lines).<sup>101</sup> The three types of weak, partially overlapped, emission bands, are assigned to naphthyl-localized excited states ( $\lambda_{\text{max}}=337$  nm), naphthyl excimers ( $\lambda_{\text{max}}$  ca 390 nm), and naphthyl-amine exciplexes ( $\lambda_{\text{max}}=460$  nm).<sup>101</sup> As previously discussed, the typical naphthalene-type fluorescence at 337 nm is strongly quenched via intramolecular formation of naphthyl excimers and exciplexes with the cyclam amine units. Dendrimer **D** has a single and strong coordinating site, i.e. its cyclam core. It was previously investigated the complexation ability of this dendrimer in CH<sub>3</sub>CN:CH<sub>2</sub>Cl<sub>2</sub> 1:1 (v/v) solution with lanthanide ions (Nd<sup>3+</sup>, Eu<sup>3+</sup>, Gd<sup>3+</sup>, Tb<sup>3+</sup>, Dy<sup>3+</sup>), demonstrating that very stable complexes are formed.<sup>102</sup> This process can be followed by monitoring the changes in emission spectra upon addition of the lanthanide ion, while no significant change has been observed in the absorption spectra (Figure 5.2.a. and b.). Addition of the metal ion causes the disappearance of the exciplex band at 460 nm, with a parallel increase in the naphthyl-localised (337 nm) and excimer (ca. 390 nm) bands since its coordination to nitrogen lone pairs of the cyclam core raises the energy of the exciplex excited state above that of the naphthyl-based one. From the plots of the normalized emission intensity changes at 337 and 460 nm (inset Figure 5.2.b.) the formation of a complex with 1:2 metal to ligand stoichiometry at low lanthanide ion concentration is demonstrated.<sup>103</sup> It has been confirmed that in the Nd<sup>3+</sup> complex there is no evidence of energy transfer from either the lowest singlet (S<sub>1</sub>) or triplet (T<sub>1</sub>) excited state of the naphthyl units of the dendrimer to the metal ion.

---

[101] Saudan, C.; Balzani, V.; Ceroni, P.; Gorka, M.; Maestri, M.; Vicinelli, V.; Vögtle, F. *Tetrahedron* 2003, 59, 3845.

[102] Saudan, C.; Ceroni, P.; Vicinelli, V.; Maestri, M.; Balzani, V.; Gorka, M.; Lee, S.-K.; van Heyst, J.; Vögtle, F. *Dalton Trans.* 2004, 1597.

[103] The 1:3 metal to ligand stoichiometry reported in ref. 93 is a mistake.

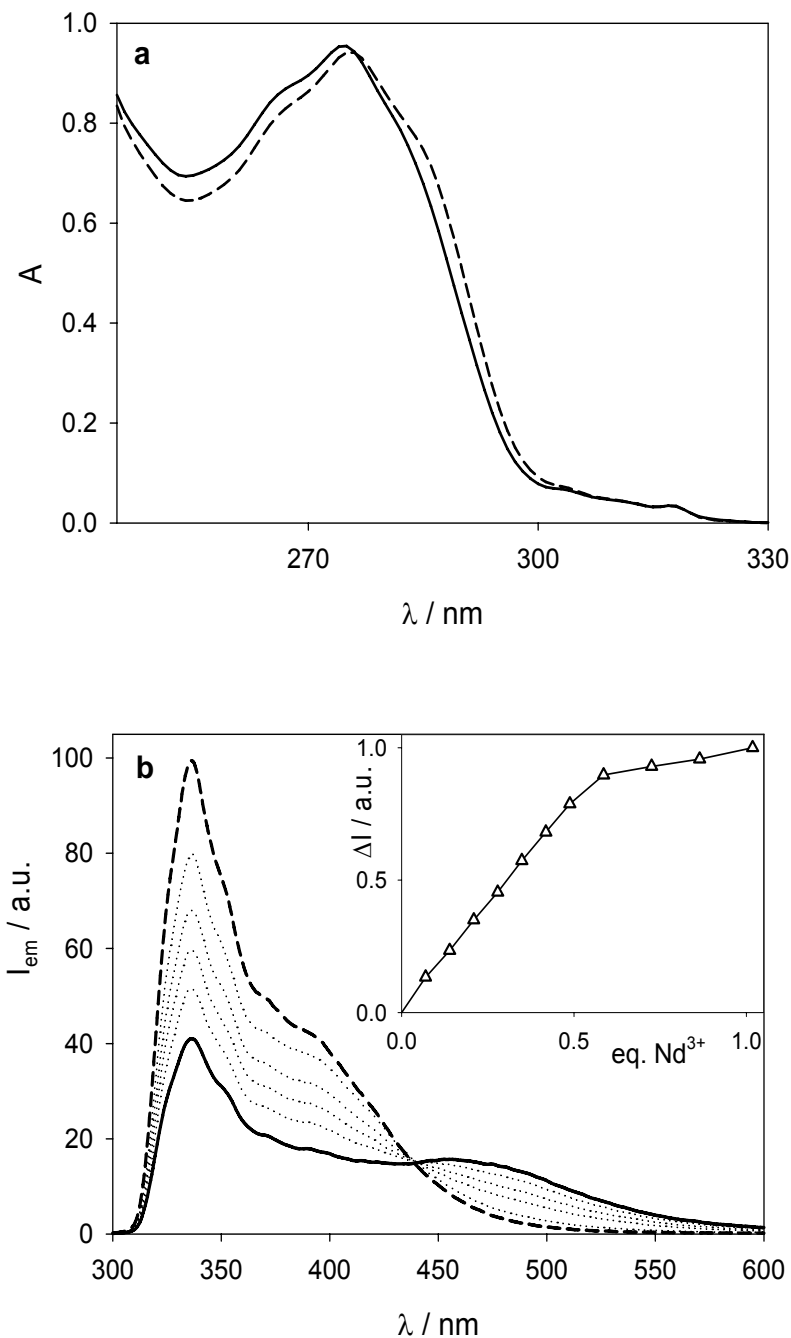


Figure 5.2. Absorption (a) and emission spectra (b) at 298 K of a  $\text{CH}_3\text{CN}:\text{CH}_2\text{Cl}_2$  1:1 (v/v) solution of dendrimer D ( $c = 7.9 \times 10^{-6} \text{ M}$ ) upon addition of  $\text{Nd}(\text{CF}_3\text{SO}_3)_3$ . The solid and dashed lines represent the spectra upon addition of 0 and 0.5 equivalent of  $\text{Nd}(\text{CF}_3\text{SO}_3)_3$ , respectively. Inset shows the normalized emission intensity ( $\lambda_{\text{ex}} = 260 \text{ nm}$ ) changes at 337 nm.

*Two-component [Ru(bpy)<sub>2</sub>(CN)<sub>2</sub>]-Nd<sup>3+</sup> system*

Heteroleptic complexes of Ru(II) containing bipyridine (bpy) and cyanide ligands, like [Ru(bpy)<sub>2</sub>(CN)<sub>2</sub>] and [Ru(bpy)(CN)<sub>4</sub>]<sup>2-</sup>, are particularly interesting because they are luminescent and can play the role of ligands giving rise to supercomplexes.<sup>104,105</sup> In particular, [Ru(bpy)<sub>2</sub>(CN)<sub>2</sub>] presents (Figure 5.3.a. and b., solid lines) low energy absorption bands and a luminescence band in the visible region which are related to metal-to-ligand (bpy) charge-transfer (MLCT) excited states (spin-allowed states for the absorption bands; the lowest spin-forbidden state for the emission band).<sup>104b,c,106</sup> The energies of these excited states are strongly dependent on the interaction of the cyanide ligands with solvent molecules,<sup>104,106</sup> protons<sup>107</sup> or metal ions.<sup>108</sup> In particular, the lowest energy band maximum shifts toward the blue when cyanide ligands are linked to a cation because of the lower electron density on the Ru(II) metal center.

Titration of a  $1.5 \times 10^{-5}$  M solution of [Ru(bpy)<sub>2</sub>(CN)<sub>2</sub>] in CH<sub>3</sub>CN:CH<sub>2</sub>Cl<sub>2</sub> 1:1 (v/v) with trifluoromethanesulfonate salts of Nd<sup>3+</sup> was performed. The expected shift towards higher energy of both MLCT absorption and emission bands (Figure 5.3.a. and b.) has been observed.

---

[104] (a) Ward, M. D. *Coord. Chem. Rev.* 2006, 250, 3128. (b) Scandola, F.; Indelli, M. T. *Pure & Appl. Chem.* 1988, 60, 973. (c) Balzani, V.; Sabbatini, N.; Scandola, F. *Chem. Rev.* 1986, 86, 319.

[105] For some recent papers, see: (a) Lazarides, T.; Easun, T. L.; Veyne-Marti, C.; Alsindi, W. Z.; George, M. W.; Deppermann, N.; Hunter, C. A.; Adams, H.; Ward, M. D. *J. Am. Chem. Soc.* 2007, 129, 4014. (b) Bernhardt, P. V.; Bozoglian, F.; Font-Bardia, M.; Martinez, M.; Meacham, A. P.; Sienna, B.; Solans, X. *Eur. J. Inorg. Chem.* 2007, 5270. (c) Davies, G. M.; Pope, S. J. A.; Adams, H.; Faulkner, S.; Ward, M. D. *Inorg. Chem.* 2005, 44, 4656. (d) Kovács, M.; Horváth, A. J. *Photochem. Photobiol. A: Chem.* 2004, 163, 13. (e) Loiseau, F.; Marzanni, G.; Quici, S.; Indelli, M. T.; Campagna, S. *Chem. Commun.* 2003, 286.

[106] Fodor, L.; Lendvay, G.; Horvath, A. *J. Phys. Chem. A* 2007, 111, 12891.

[107] (a) Peterson, S. H.; Demas, J. N. *J. Am. Chem. Soc.* 1979, 101, 6571. (b) Peterson, S. H.; Demas, J. N. *J. Am. Chem. Soc.* 1976, 98, 7880.

[108] (a) Bignozzi, C. A.; Scandola, F. *Inorg. Chem.* 1984, 23, 1540. (b) Kinnaird, M. G.; Whitten, D. G. *Chem. Phys. Lett.* 1982, 88, 275. (c) Demas, J. N.; Addington, J. W.; Peterson, S. H.; Harris, E. W. *J. Phys. Chem.* 1977, 81, 1039.

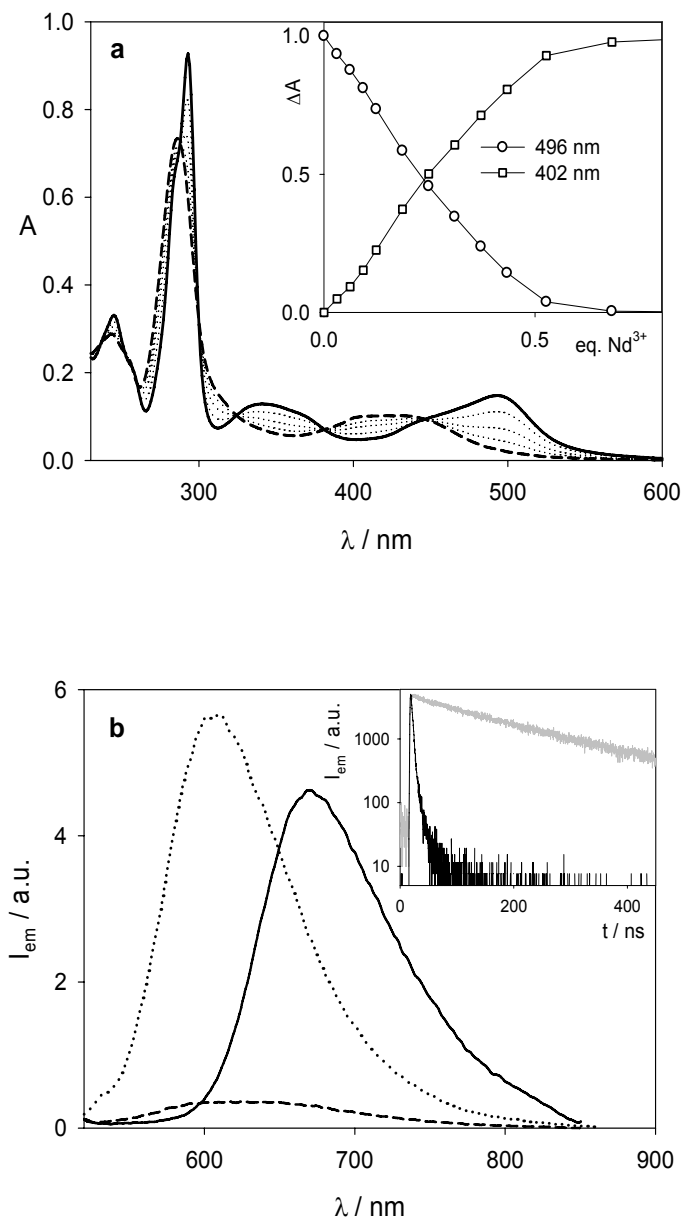


Figure 5.3. Absorption (a) and emission spectra upon excitation at 450 nm (b) of a  $\text{CH}_3\text{CN}:\text{CH}_2\text{Cl}_2$  1:1 (v/v) solution of  $[\text{Ru}(\text{bpy})_2(\text{CN})_2]$  ( $c = 1.5 \times 10^{-5}$  M) at 298 K upon addition of  $\text{Nd}(\text{CF}_3\text{SO}_3)_3$ . The solid and dashed lines represent the spectra upon addition of 0 and 1.0 equivalent of  $\text{Nd}(\text{CF}_3\text{SO}_3)_3$ , respectively. Inset of panel (a) shows the normalized absorbance changes at 402 (squares) and 496 (circles) nm. For comparison purposes, the emission spectrum upon addition of 1.0 equivalent of  $\text{Gd}(\text{CF}_3\text{SO}_3)_3$  (dotted line) is reported. Note that emission intensities are directly comparable. Inset of panel (b) shows the emission intensity decays at 607 nm upon addition of 1.0 equivalent of  $\text{Nd}^{3+}$  (black line) or  $\text{Gd}^{3+}$  (gray line).

The titration plots obtained from absorbance changes (Figure 5.3.a. inset) and emission intensity ( $\lambda_{\text{ex}} = 450 \text{ nm}$ ) are superimposed and they show linear trends that reach a plateau at ca. 0.5 equivalent of metal ion per Ru(II) complex, evidencing the formation of stable supercomplexes with 1:2 lanthanide to  $[\text{Ru}(\text{bpy})_2(\text{CN})_2]$  stoichiometry at low metal ion concentration. The trend in the appearance of  $\text{Nd}^{3+}$  sensitized emission at 1064 nm further evidences the formation of stable supercomplexes with 1:2 lanthanide to  $[\text{Ru}(\text{bpy})_2(\text{CN})_2]$  stoichiometry at low lanthanide concentration (see inset Figure 5.4.).

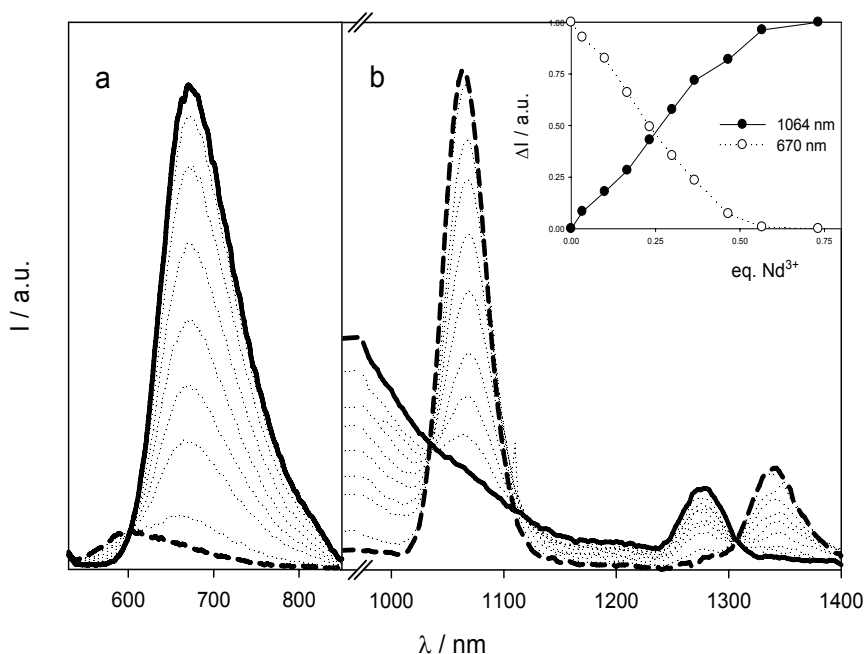


Figure 5.4. Emission spectra (a) in the 550-800 nm and (b) in the NIR spectral region upon excitation at 450 nm of a  $\text{CH}_3\text{CN}:\text{CH}_2\text{Cl}_2$  1:1 (v/v) solution of  $[\text{Ru}(\text{bpy})_2(\text{CN})_2]$  ( $c = 1.5 \times 10^{-5} \text{ M}$ ) at 298 K upon addition of  $\text{Nd}(\text{CF}_3\text{SO}_3)_3$ . The solid and dashed lines represent the spectra upon addition of 0 and 1.0 equivalent of  $\text{Nd}(\text{CF}_3\text{SO}_3)_3$ , respectively. Inset of panel (b) shows the normalized emission intensity changes at 670 nm (empty circles) and 1064 nm (filled circles) upon addition of  $\text{Nd}(\text{CF}_3\text{SO}_3)_3$ .

When  $\text{Nd}^{3+}$  is replaced by  $\text{Gd}^{3+}$ , absorption spectral changes are the same as those observed in the former case, but the emission intensity of  $[\text{Ru}(\text{bpy})_2(\text{CN})_2]$  is much higher

(Figure 5.3.b.) suggesting that in the case of  $\text{Nd}^{3+}$ , the  $[\text{Ru}(\text{bpy})_2(\text{CN})_2]$  emission band is quenched by energy transfer, as confirmed by the appearance of the  $\text{Nd}^{3+}$  emission at 1064 nm. From the quantum yields and lifetimes of the  $[\text{Ru}(\text{bpy})_2(\text{CN})_2]$  emission in the  $\text{Gd}^{3+}$  and  $\text{Nd}^{3+}$  supercomplexes ( $\Phi_{\text{em}} = 0.006$  and  $<0.0005$ ;  $\tau = 180$  and 3 ns, Figure 5.3.b. inset) and the intensity of the  $\text{Nd}^{3+}$  sensitized emission, the efficiency of energy transfer from  $[\text{Ru}(\text{bpy})_2(\text{CN})_2]$  to  $\text{Nd}^{3+}$  is estimated to be  $>90\%$ .

The luminescent excited state of  $[\text{Ru}(\text{bpy})_2(\text{CN})_2]$  sensitizes the  $^1\text{O}_2$  emission at 1270 nm (Figure 5.4.b.), as previously reported for the parent  $[\text{Ru}(\text{bpy})(\text{CN})_4]^{2-}$  complex.<sup>109</sup> When the titration experiments are carried out in air equilibrated solutions, the dioxygen emission band can be observed when  $\text{Gd}^{3+}$  is used, whereas it disappears upon titration with  $\text{Nd}^{3+}$  because of the competition of energy transfer to  $\text{Nd}^{3+}$ .

#### *Two component dendrimer- $[\text{Ru}(\text{bpy})_2(\text{CN})_2]$ system*

The absorption and emission spectra of a 1:1 mixture of dendrimer **D** and  $[\text{Ru}(\text{bpy})_2(\text{CN})_2]$  ( $c = 7.7 \times 10^{-6}$  M) in  $\text{CH}_3\text{CN}:\text{CH}_2\text{Cl}_2$  1:1 (v/v) (Figures 5.5. and 5.6., solid lines) are equal to the sum of the absorption and emission spectra of the two separated components, showing that there is no interaction.

#### *Three-component dendrimer- $[\text{Ru}(\text{bpy})_2(\text{CN})_2]$ - $\text{Nd}^{3+}$ system*

Upon titration of 1:1 mixture of dendrimer **D** and  $[\text{Ru}(\text{bpy})_2(\text{CN})_2]$  ( $c = 7.7 \times 10^{-6}$  M) in  $\text{CH}_3\text{CN}:\text{CH}_2\text{Cl}_2$  1:1 (v/v) with a 1 mM  $\text{Nd}(\text{CF}_3\text{SO}_3)_3$   $\text{CH}_3\text{CN}$  solution, the absorption spectra (Figure 5.5.) above 300 nm show a shift of the lowest energy band maximum toward the blue, as observed for the titration of  $[\text{Ru}(\text{bpy})_2(\text{CN})_2]$  in the absence of dendrimer. On a quantitative basis, however, the plots of the absorption changes at 402 and 496 nm (inset of Figure 5.5.) are substantially different from the plots obtained in the absence of dendrimer **D** (Figure 5.3.a., inset). Instead of linear plots that reach a plateau at ca. 0.5 equivalent of  $\text{Nd}^{3+}$  per

[109] Abdel-Shafi, A. A.; Ward, M. D.; Schmidt, R. *Dalton. Trans.* 2007, 2517.

Ru(II) complex, two mirror-like sigmoidal plots are observed with a plateau at ca. 1.0 equivalent. As far as emission is concerned, the changes in the shape and position of the naphthyl-based (Figure 5.6.a.) and  $[\text{Ru}(\text{bpy})_2(\text{CN})_2]$  emission bands (Figure 5.6.b.) are similar to those observed for the titration of the two separate components (Figures 5.2.b. and 5.3.b.). However, a closer look at the data reveals substantial differences.

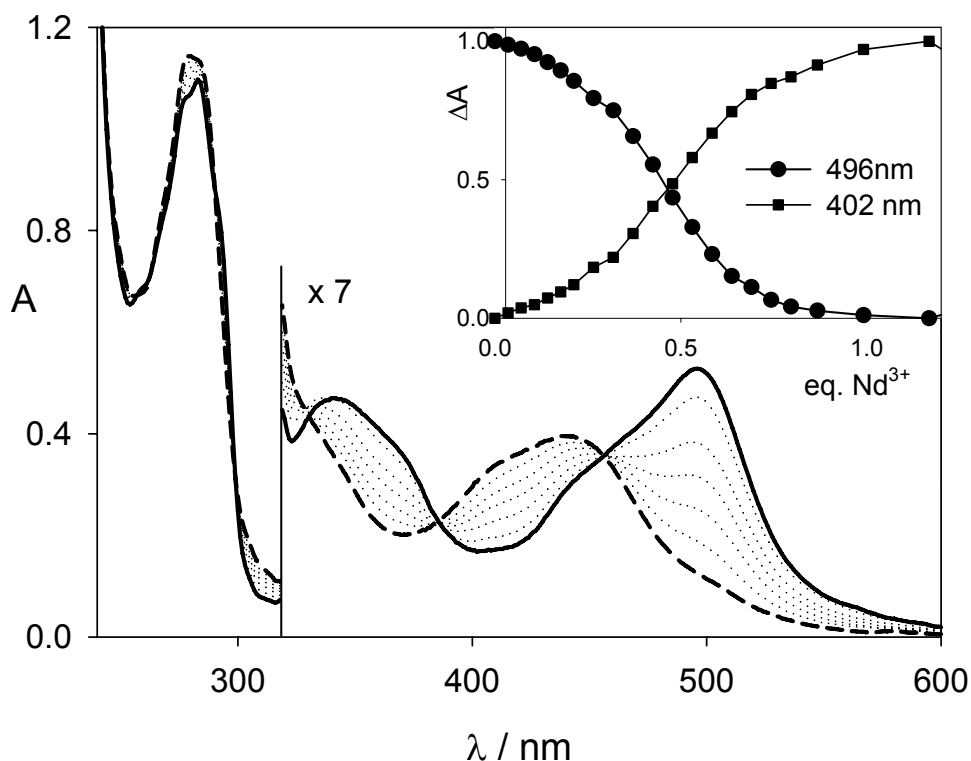


Figure 5.5. Changes observed in the absorption spectrum of a 1:1 mixture of dendrimer **D** and  $[\text{Ru}(\text{bpy})_2(\text{CN})_2]$  ( $c = 7.7 \times 10^{-6}$  M) in  $\text{CH}_3\text{CN}:\text{CH}_2\text{Cl}_2$  1:1 (v/v) solution at 298 K upon addition of  $\text{Nd}(\text{CF}_3\text{SO}_3)_3$ . The dashed and solid lines are the spectra upon addition of 0 and 1.2 equivalents of  $\text{Nd}(\text{CF}_3\text{SO}_3)_3$ . Inset shows the normalized absorbance changes at 402 (squares) and 496 nm (circles).

Upon excitation at 260 nm, where most of the light is absorbed by the **D** component, the intensity of the naphthyl monomer emission at 337 nm (Figure 5.7., solid triangles) does not show a monotonous increase, as observed in the absence of the  $[\text{Ru}(\text{bpy})_2(\text{CN})_2]$  complex

(Figure 5.7., empty triangles), reaches a maximum at 0.5 equivalent and then decreases up to about 1.0 equivalent of  $\text{Nd}^{3+}$  to rise again for higher metal ion concentration. The emission intensity at 1.0 equivalent is lower than that observed in the absence of  $[\text{Ru}(\text{bpy})_2(\text{CN})_2]$  (Figure 5.7., empty triangles).

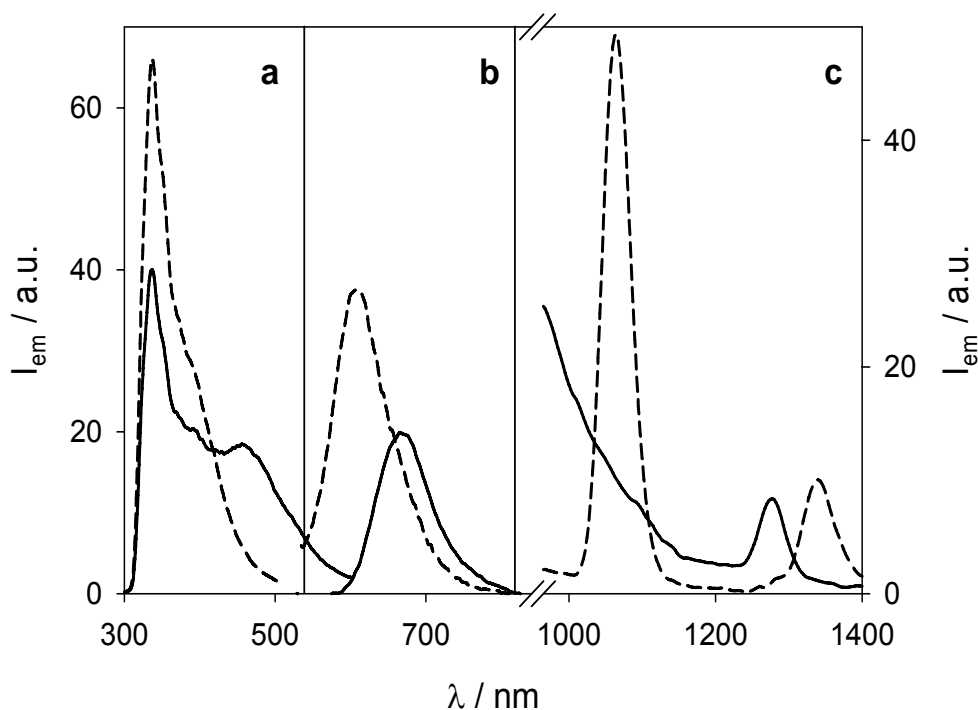


Figure 5.6. Emission spectra (a) in the 300-500 nm ( $\lambda_{\text{ex}} = 260$  nm), (b) in the 550-800 nm ( $\lambda_{\text{ex}} = 450$  nm) and (c) in the NIR spectral region of a 1:1 mixture of dendrimer **D** and  $[\text{Ru}(\text{bpy})_2(\text{CN})_2]$  ( $7.7 \times 10^{-6}$  M) in  $\text{CH}_3\text{CN}:\text{CH}_2\text{Cl}_2$  1:1 (v/v) solution at 298 K before (solid line) and after (dashed line) addition of 1.0 equivalent of  $\text{Nd}(\text{CF}_3\text{SO}_3)_3$ .

These results show that a three-component system  $\{\mathbf{D} \cdot \text{Nd}^{3+} \cdot [\text{Ru}(\text{bpy})_2(\text{CN})_2]\}$  is formed in which the dendrimer emission is quenched. Further addition of  $\text{Nd}^{3+}$  ( $> 1.1$  eq) revives the naphthyl monomer emission, as expected because excess of  $\text{Nd}^{3+}$  disassembles the three-component system into dendrimer-neodymium and  $[\text{Ru}(\text{bpy})_2(\text{CN})_2]$ -neodymium two-component species. It can be noted that for low  $\text{Nd}^{3+}$  concentrations the titration plot in the presence of  $[\text{Ru}(\text{bpy})_2(\text{CN})_2]$  is very similar to that obtained in the absence of  $[\text{Ru}(\text{bpy})_2(\text{CN})_2]$  (Figure

5.7.a.), showing that  $\text{Nd}^{3+}$  has higher affinity for **D** than for  $[\text{Ru}(\text{bpy})_2(\text{CN})_2]$ . This conclusion is confirmed by the small changes observed in the absorption band of the Ru complex at the beginning of the titration (Figure 5.4., inset). When  $\text{Nd}^{3+}$  is replaced by  $\text{Gd}^{3+}$  the titration plot of the naphthyl monomer emission intensity at 337 nm resembles that obtained with  $\text{Nd}^{3+}$ , suggesting that also in this case a three-component system  $\{\mathbf{D}\cdot\text{Gd}^{3+}\cdot[\text{Ru}(\text{bpy})_2(\text{CN})_2]\}$  is formed.

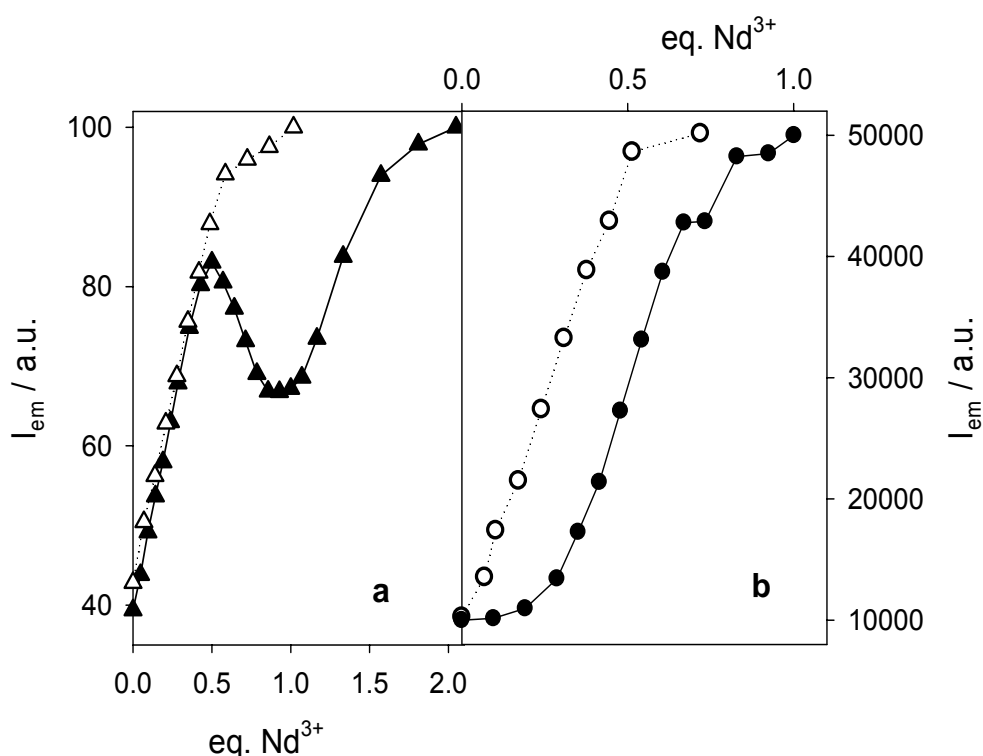


Figure 5.7. a) Emission intensity changes at 337 nm ( $\lambda_{ex} = 260$  nm) of dendrimer **D** ( $7.7 \times 10^{-6}$  M) in  $\text{CH}_3\text{CN}:\text{CH}_2\text{Cl}_2$  1:1 (v/v) solution at 298 K upon titration with  $\text{Nd}^{3+}$  in the presence (solid triangles) or in the absence (empty triangles) of  $[\text{Ru}(\text{bpy})_2(\text{CN})_2]$  ( $7.7 \times 10^{-6}$  M). (b) Emission intensity changes at 1064 nm ( $\lambda_{ex} = 450$  nm) upon titration with  $\text{Nd}^{3+}$  of  $[\text{Ru}(\text{bpy})_2(\text{CN})_2]$  ( $7.7 \times 10^{-6}$  M) in  $\text{CH}_3\text{CN}:\text{CH}_2\text{Cl}_2$  1:1 (v/v) solution at 298 K in the presence (solid circles) or in the absence (empty circles) of dendrimer **D** ( $7.7 \times 10^{-6}$  M).

In the case of  $\{\mathbf{D}\cdot\text{Nd}^{3+}\cdot[\text{Ru}(\text{bpy})_2(\text{CN})_2]\}$  system, upon excitation at 450 nm, where the light is absorbed only by the  $[\text{Ru}(\text{bpy})_2(\text{CN})_2]$  component, the MLCT emission intensity at 607

nm is much weaker (50%) than that obtained when  $\text{Nd}^{3+}$  is replaced by  $\text{Gd}^{3+}$  (Figure 5.6.b.).<sup>110</sup> Such a quenching effect can be assigned to energy transfer from the  $[\text{Ru}(\text{bpy})_2(\text{CN})_2]$  excited state to  $\text{Nd}^{3+}$ , as confirmed by the appearance of the  $\text{Nd}^{3+}$  emission at 1064 nm (Figure 5.6.c.). Instead of a linear plot that reaches a plateau at ca. 0.5 equivalent of  $\text{Nd}^{3+}$  per  $[\text{Ru}(\text{bpy})_2(\text{CN})_2]$ , a sigmoid plot with a plateau at ca. 1.0 equivalent is observed in presence of dendrimer **D** (Figure 5.7.b.). The sensitized intensity maximizes for 1:1:1 ratio of the three components confirming the formation of a  $\{\text{D}\cdot\text{Nd}^{3+}\cdot[\text{Ru}(\text{bpy})_2(\text{CN})_2]\}$  species.

As it happens for the titration of  $[\text{Ru}(\text{bpy})_2(\text{CN})_2]$  in the absence of dendrimer, the  $^1\text{O}_2$  emission at 1270 nm can be observed when  $\text{Gd}^{3+}$  is used, whereas it disappears upon titration with  $\text{Nd}^{3+}$  because of the competition of energy transfer to  $\text{Nd}^{3+}$ .

The main photophysical processes of the  $\{\text{D}\cdot\text{Nd}^{3+}\cdot[\text{Ru}(\text{bpy})_2(\text{CN})_2]\}$  adduct are summarized in Figure 5.8. which shows the energy levels of the three components. As previously reported, in the two-component dendrimer- $\text{Nd}^{3+}$  system, energy transfer from either the lowest singlet ( $\text{S}_1$ ) or triplet ( $\text{T}_1$ ) excited state of the naphthyl units of the dendrimer to the lanthanide ion does not occur. Clearly, sensitization of the  $\text{Nd}^{3+}$  emission upon dendrimer excitation in the three component system is mediated by the  $[\text{Ru}(\text{bpy})_2(\text{CN})_2]$  component. Comparison between the emission quantum yield of  $[\text{Ru}(\text{bpy})_2(\text{CN})_2]$  upon excitation at 260 nm (dendrimer absorption) and 450 nm ( $[\text{Ru}(\text{bpy})_2(\text{CN})_2]$  absorption) has allowed us to estimate that the energy transfer efficiency from the  $\text{S}_1$  excited state of the naphthyl groups to the  $^1\text{MLCT}$  excited state of  $[\text{Ru}(\text{bpy})_2(\text{CN})_2]$  is about 60% (Figure 5.8.). The energy transfer efficiency from the  $^3\text{MLCT}$  excited state of  $[\text{Ru}(\text{bpy})_2(\text{CN})_2]$  to  $\text{Nd}^{3+}$  can be assumed to be equal to the efficiency

---

[110] It is worth noting that the quantum yield of the  $[\text{Ru}(\text{bpy})_2(\text{CN})_2]$  linked to  $\text{Gd}^{3+}$  is much higher in the three-component system  $\{\text{D}\cdot\text{Nd}^{3+}\cdot[\text{Ru}(\text{bpy})_2(\text{CN})_2]\}$  than in the absence of the dendrimer ( $\Phi_{\text{em}} = 0.015$  and 0.006, respectively, see Figure 2.b. and 5.b.), although no significant change in the energy (a red shift of 3 nm) and lifetime of the corresponding  $^3\text{MLCT}$  excited state has been evidenced. Similar trend has been observed in the case of  $\text{Nd}^{3+}$ . These results can be explained by an increase of the rate constant of the radiative deactivation process of  $^3\text{MLCT}$  in the presence of **D**, brought about by slight changes in the charge density in the proximity of the  $\text{Ru}(\text{II})$  complex.

of the quenching of the  $[\text{Ru}(\text{bpy})_2(\text{CN})_2]$  emission (ca 90%) because quenching by electron transfer can be ruled out in view of the  $\text{Nd}^{3+}$  redox properties.<sup>99</sup> No evidence of energy transfer in the adduct from the naphthyl-localized  $T_1$  excited state to the lowest  $^3\text{MLCT}$  state of  $[\text{Ru}(\text{bpy})_2(\text{CN})_2]$  has been found since no change in the  $T_1$  lifetime at 77 K has been observed.

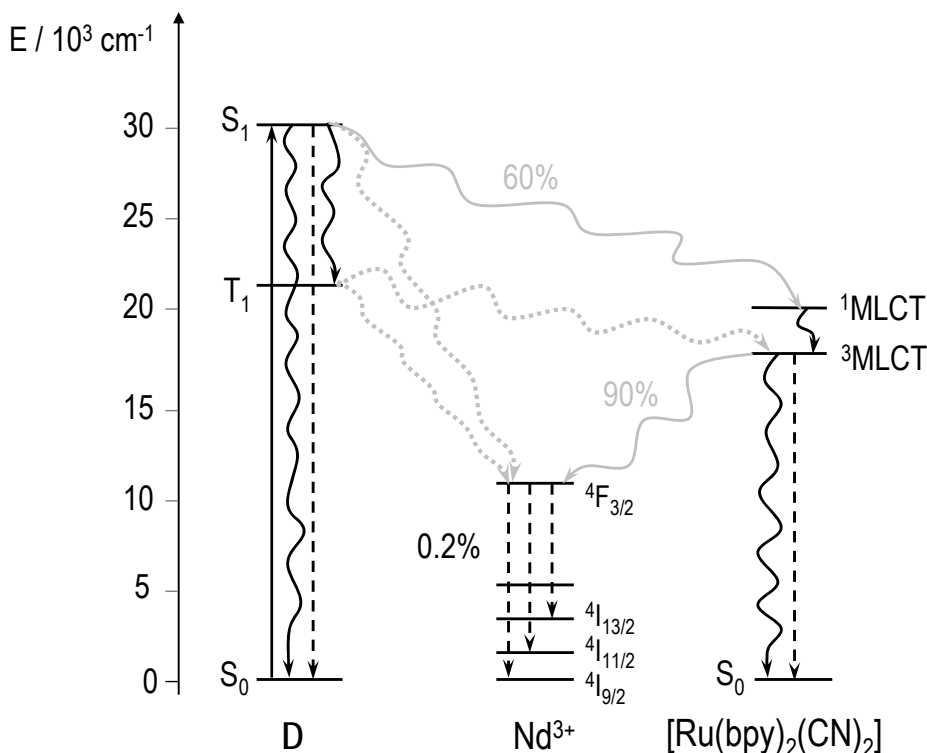


Figure 5.8. Energy level diagram showing the excited states involved in the main photophysical processes (absorption: solid line; radiative deactivation: dashed line; non-radiative deactivation process: curved line – gray solid curves indicate intermolecular energy transfer pathway, while gray dotted curves represent forbidden pathways) of the  $\{\text{D}\cdot\text{Nd}^{3+}\cdot[\text{Ru}(\text{bpy})_2(\text{CN})_2]\}$  three-component system. For the sake of clarity, naphthyl excimer energy level has been omitted.

Both quenching and sensitization maximize for a 1:1:1 ratio of the three components, indicating the presence of a self-assembled  $\{\text{D}\cdot\text{Nd}^{3+}\cdot[\text{Ru}(\text{bpy})_2(\text{CN})_2]\}$  adduct. The assembling process is reversible. The three-component system can be disassembled by addition of an excess of  $\text{Nd}^{3+}$  (Figure 5.7.a.), of **D** or  $[\text{Ru}(\text{bpy})_2(\text{CN})_2]$ , or an excess of cyclam.

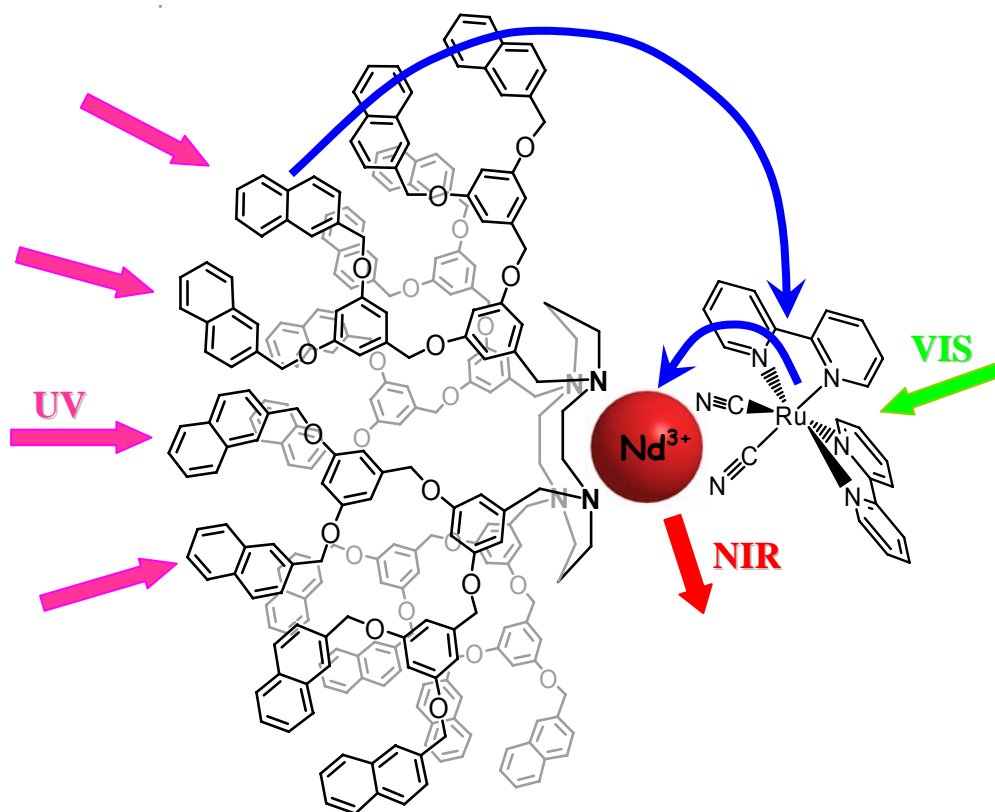


Figure 5.9. Pictorial representation of the self-assembled three component light harvesting antenna: the dendritic antenna collects UV light than efficiently funnelling excitation energy to the Ru(II) complex which in turn sensitizes lanthanide metal ion NIR emission.

In conclusion, the reversible self-assembly of a  $\{\mathbf{D} \cdot \text{Nd}^{3+} \cdot [\text{Ru}(\text{bpy})_2(\text{CN})_2]\}$  three-component system has been obtained in  $\text{CH}_3\text{CN}:\text{CH}_2\text{Cl}_2$  solution. Because of the complementary properties of the three components, new functions emerge from their self-assembly. Dendrimer **D** has a very high molar absorption coefficient in the UV spectral region because of 12 dimethoxybenzene and 16 naphthyl units; it is luminescent and presents a single coordinating site located in the core, which can strongly bind lanthanide ions, but it is unable to sensitize the coordinated  $\text{Nd}^{3+}$  ion. The  $[\text{Ru}(\text{bpy})_2(\text{CN})_2]$  complex shows absorption and emission properties highly sensitive to the presence of cations and, for the first time, we have demonstrated that it can

coordinate (by the cyanide ligands) and sensitize the emission of  $\text{Nd}^{3+}$  ions. Coupling the three species in the 1:1:1 adduct, sensitization of the  $\text{Nd}^{3+}$  ion has been achieved not only upon excitation of the Ru(II) complex, but also of the naphthyl chromophores of the dendrons. Therefore, it has been constructed a self-assembled antenna that can harvest light from the UV to the VIS region and emit in the NIR region with line-like bands. In principle, the emission wavelength can be tuned by replacing  $\text{Nd}^{3+}$  with other lanthanide ions possessing low-lying excited states. Useful applications can be envisaged in the field of bio-sensors and imaging<sup>98,111</sup> and photonic applications,<sup>112</sup> such as waveguide amplifiers, plastic lasers, light-emitting diodes.

---

[111] Escribano, P.; Julian-Lopez, B.; Planelles-Arago, J.; Cordoncillo, E.; Viana, B.; Sanchez, C. *J. Mat. Chem.* 2008, 18, 23.

[112] (a) de Bettencourt-Dias, A. *Dalton Trans.* 2007, 2229. (b) Kuriki, K.; Koike, Y.; Okamoto, Y. *Chem. Rev.* 2002, 102, 2347.

## 5.1.2. Temperature-dependent Intradendrimer Energy-transfer

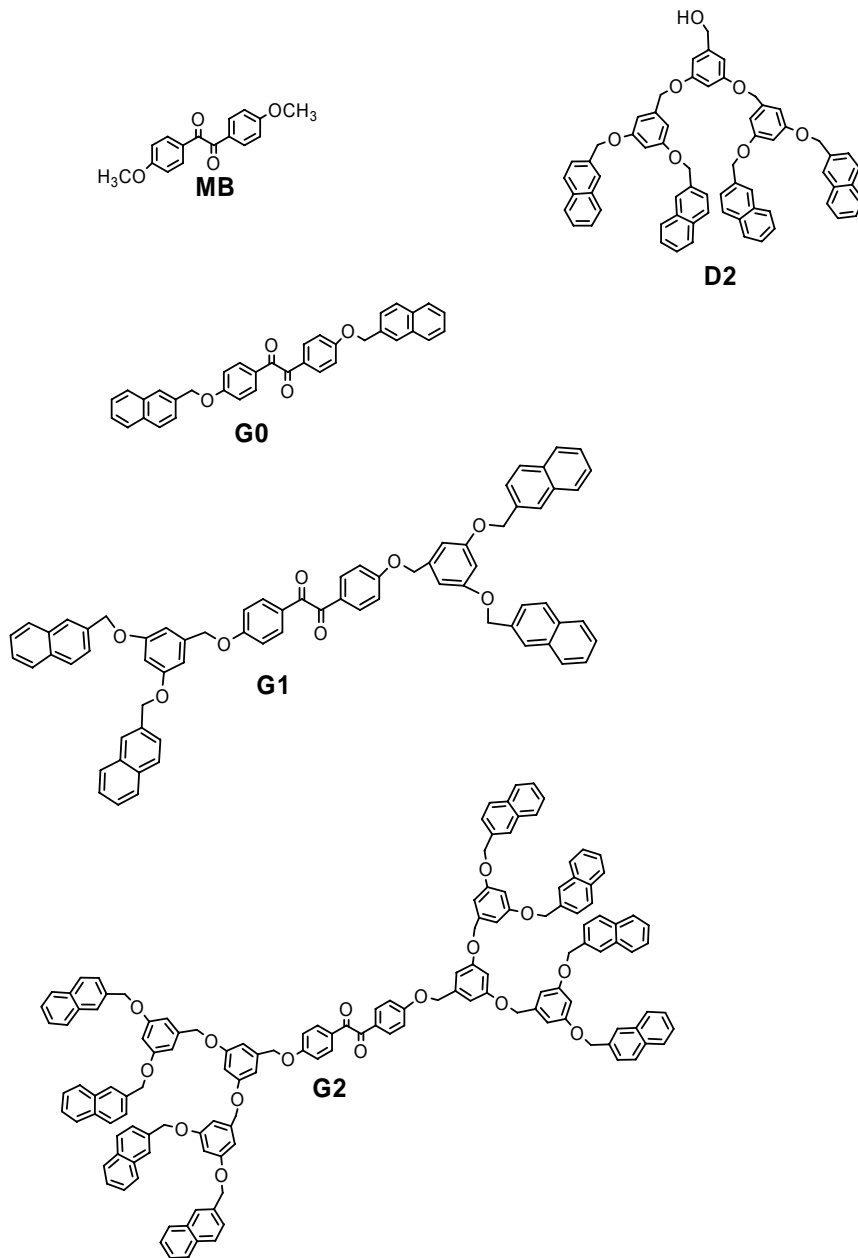


Figure 5.10. Formula of the investigated compounds.

The photophysical, photochemical, and electrochemical properties of three dendrimers consisting of a dimethoxybenzil core and branches that contain two (**G0**), four (**G1**), and eight (**G2**) naphthalene units at the periphery and zero (**G0**), two (**G1**), and six (**G2**) dimethoxybenzene units in the branches (Figure 5.10).<sup>62</sup>

### *Photophysical characterization*

Benzil, naphthalene, and dimethoxybenzene are well known luminescent species. In particular, both fluorescence and phosphorescence are exhibited by benzil<sup>113</sup> and naphthalene<sup>113</sup> in suitable experimental conditions, opening the possibility to investigate singlet-singlet and triplet-triplet energy transfer. For comparison purposes, the properties of dimethoxybenzil (**MB**), 2-methylnaphthalene, and of a dendron containing four naphthalene units and three dimethoxybenzene units (**D2**) have also been studied.

Dendron **D2** absorbs at higher energy ( $\lambda_{\max} = 275$  nm) compared to **MB** ( $\lambda_{\max} = 300$  nm) (Figure 5.11.a). In particular, the absorption spectrum of **D2** is dominated by the four naphthalene groups, since the three dimethoxybenzene moieties, that absorb in the same spectral region, have a molar absorption coefficient ( $\epsilon_{275\text{nm}} = 2200 \text{ M}^{-1} \text{ cm}^{-1}$ )<sup>114</sup> smaller than that of naphthalene ( $\epsilon_{275\text{nm}} = 6000 \text{ M}^{-1} \text{ cm}^{-1}$ ).<sup>115</sup> The absorption spectra of the dendrimers (Figure 5.11.b.) show the features of both the dimethoxybenzil core, with a shoulder at 300 nm, and the dimethoxybenzene and naphthalene units contained in the branches, with a maximum at 275 nm. The number of naphthalene and dimethoxybenzene chromophores increases on increasing dendrimer generation and, as a consequence, the absorbance at 275 nm increases while the shoulder at 300 nm is practically constant (Figure 5.11.b).

---

[113] M. Montalti, A. Credi, L. Prodi, M. T. Gandolfi, *Handbook of Photochemistry*, 3rd ed., Taylor & Francis, CRC press, 2006.

[114] This value has been estimated by the molar absorption coefficient of the second generation dendron analogous to **D2**, but terminated by benzene instead of naphthalene since at 275 nm the benzene contribution to the absorption is negligible.

[115] This value is the molar absorption coefficient of 2-methyl naphthalene.

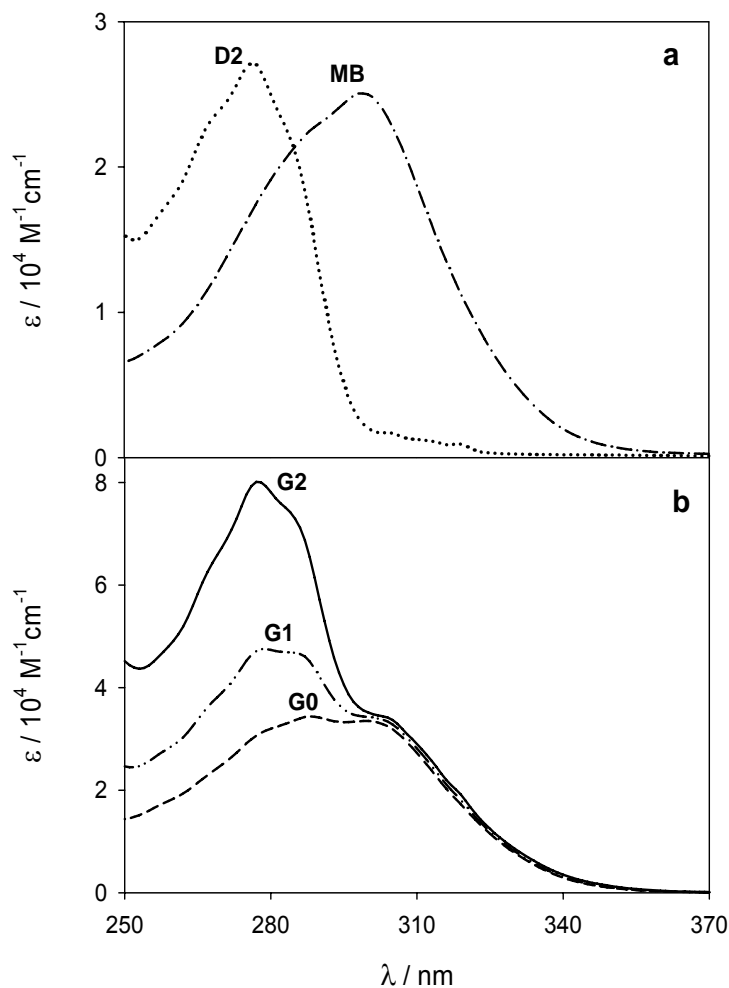


Figure 5.11. Absorption spectra of MB and D2 (a) and dendrimers G0-G2 (b) in  $\text{CH}_2\text{Cl}_2:\text{CHCl}_3$  1:1 (v/v) at 298 K.

Quantitative comparison with the spectra of the model compounds shows that there is no significant interaction in the ground state. In particular, the spectrum of **G2** is almost coincident with that obtained considering the sum of the spectra of two dendrons **D2** and a **MB** unit. Upon excitation at 277 nm, dendrimers **G0-G2** show two emission bands: the first one, with maximum at 335 nm (Figure 5.11.), is due to the fluorescence of the naphthalene

group; the second one, with maximum at 495 nm and much weaker in intensity (see, e.g., Figure 5.12.), is assigned to the dimethoxybenzil fluorescence, because of the close similarity to that recorded for **MB**. The small quantum yield of the dimethoxybenzil fluorescence is due to the close proximity of the  $S_1(n\pi^*)$  and  $T_1(n\pi^*)$  excited states that favors intersystem crossing.<sup>116</sup>

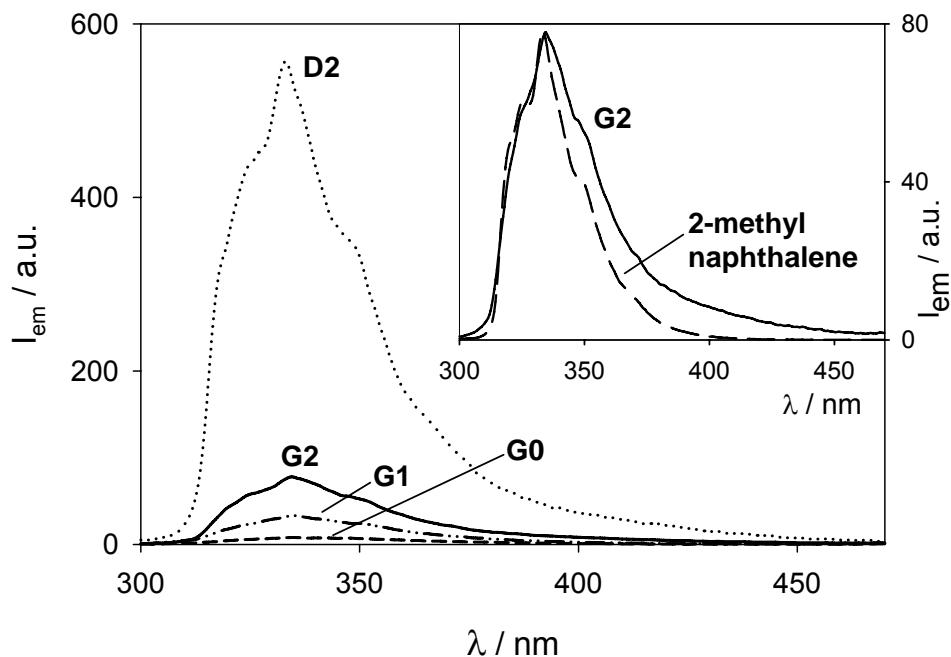


Figure 5.12. Fluorescence spectra of dendrimers G0-G2 and dendron D2 in  $\text{CH}_2\text{Cl}_2:\text{CHCl}_3$  1:1 (v/v) at 298 K with the same absorbance at the excitation wavelength.  $\lambda_{\text{ex}} = 277$  nm. Inset shows the normalized emission spectra of G2 and a model compound, 2-methyl naphthalene.

[116] (a) A. A. Lamola and G. S. Hammond, *J. Chem. Phys.*, 1965, 43, 2129. (b) D. J. Morantz and J. C. Wright, *J. Chem. Phys.*, 1971, 54, 692. (c) J. F. Arnett and S. P. McGlynn, *J. Phys. Chem.*, 1975, 79, 626. (c) T.-S. Fang, R. E. Brown, C. L. Kwan and L. A. Singer, *J. Phys. Chem.*, 1978, 82, 2489. (d) L. Flamigni, F. Barigelletti, S. Dellonte and G. Orlandi, *J. Photochem.*, 1983, 21, 237.

The emission bands centred at 335 nm of **G1**, **G2**,<sup>117</sup> and **D2** show a weak tail at lower energy, compared with that exhibited by 2-methylnaphthalene (inset of Figure 5.12.), suggesting formation of naphthalene excimers.<sup>118</sup>

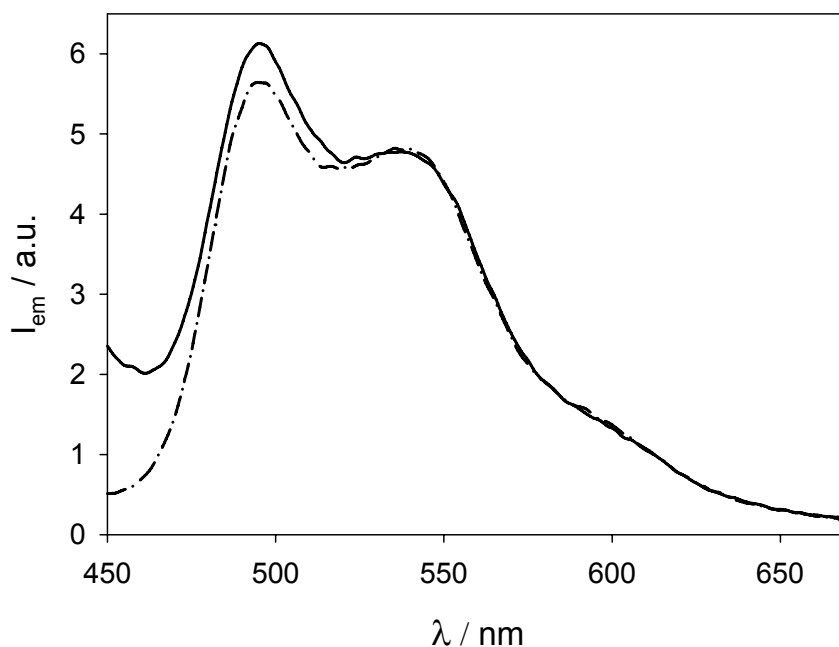


Figure 5.13. Fluorescence spectra of G2 (solid line) and MB (dashed-dotted line) in  $\text{CH}_2\text{Cl}_2:\text{CHCl}_3$  1:1 (v/v) at 298 K with the same absorbance at the excitation wavelength.  $\lambda_{\text{ex}} = 277$  nm.

It should be noticed that the naphthalene-type emission in the dendrimers is strongly quenched compared to **D2**, as evidenced by the spectra displayed in Figure 5.12. and the quantum yield data reported in Table 5.1. On the other hand, emission of the benzil core at 495 nm is sensitised. Indeed, practically coincident emission intensities at 495 nm were

[117] In the case of G0 the emission is so weak that a careful analysis of emission band shape is precluded.

[118] G. Bergamini, P. Ceroni, M. Maestri, V. Balzani, S.-K. Lee and F. Vögtle, *Photochem. Photobiol. Sci.*, 2004, 3, 898.

obtained upon excitation at 277 nm of isoabsorbing solutions of **G2** and **MB** (Figure 5.13.), although in the case of **G2** about 80% of the light is absorbed by naphthalene units at the excitation wavelength.

Therefore, an energy transfer process from the lowest excited state ( $S_1$ ) of the naphthalene units to the lower lying  $S_1$  excited state of the dimethoxybenzil core takes place with high, presumably unitary efficiency.<sup>119</sup> A further proof of a high energy transfer efficiency comes from the fact that the excitation spectra of **G0-G2** (recorded with  $\lambda_{em}=500$  nm) are practically coincident with the corresponding absorption spectra. The quantum yield of the naphthalene type emission slightly increases on increasing dendrimer generation, most likely because of the increasing distance between the donor and acceptor partners of the energy transfer process. The photoinduced energy transfer process from the  $S_1$  state of naphthalene to the  $S_1$  state of the dimethoxybenzil core is active also at 77 K (see Figure 5.14.), since a significant quenching of the naphthalene emission intensity and lifetime is observed when dendrimers **G0-G2** are compared to dendron **D2**. However, sensitization of the dimethoxybenzil has not been evidenced because its fluorescence quantum yield is so low that the corresponding band is completely covered by the much more intense phosphorescence band.

No fluorescence of the dimethoxybenzene group has been observed in dendrimers **G1** and **G2**, as expected on the basis of the behaviour of the dendron **D2** where the potentially fluorescent  $S_1$  excited state of dimethoxybenzene is quenched by energy and electron transfer processes involving the naphthalene units.<sup>119</sup> Furthermore, in the case of dendrimers **G1** and **G2** another lower-lying excited state located on the core is present, so that an additional quenching channel for the fluorescent excited state of dimethoxybenzene is available.

---

[119] A careful estimation of the emission quantum yield corresponding to the band with maximum at 495 nm in **G2** is precluded by the tail of the naphthalene emission and by the very low emission quantum yield of the dimethoxybenzil chromophore. This uncertainty is reflected in the efficiency of the energy transfer process discussed in the text.

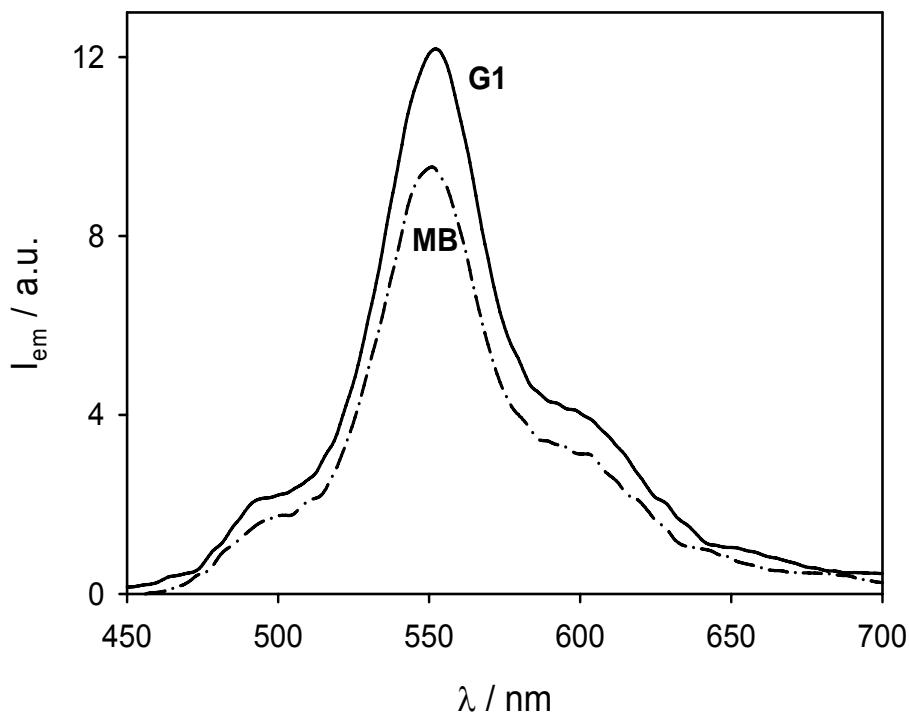


Figure 1.14. Phosphorescence spectra of MB and G1 in deaerated  $\text{CH}_2\text{Cl}_2:\text{CHCl}_3$  1:1 (v/v) solution at 298 K, under the same experimental conditions.  $\lambda_{\text{ex}} = 330$  nm.

The results obtained for **G0-G2** from fluorescence lifetime measurements are not easily interpreted because multi-exponential decays were observed due to spectral overlaps. The reference compound **MB** has a very short lifetime ( $<0.5$  ns), while **D2** shows a biexponential decay: the shorter component is the usual naphthalene-type emission, while the longer one is assigned to an excimer emission.<sup>119</sup> In the case of the dendrimers, the shorter component ( $<0.5$  ns) can be assigned to the naphthalene-type emission, that is highly quenched compared to **D2**, and the longer one to the naphthalene excimer emission (see inset of Figure 5.11.). The small emission quantum yield of the dimethoxybenzil chromophore

and the partial spectral overlap with the naphthalene excimer emission prevented a reliable estimation of the emission lifetime of the core.

The emission spectrum recorded with a 10  $\mu\text{s}$  delay for a deaerated dichloromethane/chloroform 1:1 (v/v) solution of **MB** shows a maximum at 548 nm ( $\tau = 25 \mu\text{s}$ ) and a shoulder at 495 nm (Figure 5.14.). The maximum can be attributed to the dimethoxybenzil phosphorescence. The shoulder is in the same position of the fluorescence band observed in aerated solution while it is not present in the phosphorescence spectra recorded at 77 K (vide infra) and is thus attributed to delayed fluorescence,<sup>116b</sup> i.e. to the thermal population at 298 K of the  $S_1$  excited state from  $T_1$  one. Indeed, the ratio of emission intensities at 495 and 548 nm is not dependent on the delay time used to register the emission spectrum. This result indicates that the two emission bands originate from two states with the same lifetime, i.e.  $S_1$  and  $T_1$  are in thermal equilibrium. Similar spectra have been obtained for dendrimers **G0-G2** upon selective excitation of the dimethoxybenzil chromophore at 330 nm (see e.g. **G1** in Figure 5.14.).

The phosphorescence intensity of isoabsorbing solutions at the excitation wavelength are slightly higher and the corresponding lifetimes are slightly longer in the case of the dendrimers compared to **MB** reference compound (Table 5.1.). These results demonstrate that no quenching of the  $T_1$  excited state of the dimethoxybenzil core is brought about by the naphthalene moieties and suggest that either (i) the dendritic wedges protect the dimethoxybenzil excited state by quenching from residual dioxygen or (ii) a more rigid structure of the dimethoxybenzil core in the dendrimers leads to lower non-radiative decay rate constant. On the other hand, no emission has been recorded, under the same experimental conditions, in the case of **D2**. Indeed, **D2** phosphorescence can be observed only at 77 K (vide infra) because the  $T_1$  excited state of naphthalene has a very long lifetime (Table 5.1.) that allows bimolecular quenching by impurities present even at very low concentration.

Laser-flash photolysis experiments performed on **MB** and dendrimers **G0-G2** in deaerated dichloromethane/chloroform 1:1 (v/v) solutions showed, upon excitation of the dimethoxybenzil moiety ( $\lambda_{\text{ex}} = 355$  nm), transient absorption spectra characteristic of  $T_1 \rightarrow T_n$  transitions of the dimethoxybenzil chromophore.<sup>120</sup> Time evolution of this spectral changes, e.g. at  $\lambda_{\text{max}} = 480$  nm, was not monoexponential and depended on laser intensity and chromophore concentration. The decays can be fitted by a combination of a first and second order process (see experimental section), i.e. intrinsic deactivation of  $T_1$  and bimolecular triplet-triplet annihilation:<sup>121</sup>

$$-\frac{d[*A]}{dt} = k[*A] + k'[*A]^2 \Rightarrow [*A] = \frac{[*A]_0 k}{([*A]_0 k' + k)e^{kt} - [*A]_0 k'} \quad (33)$$

where  $[*A]_0$  is the concentration of excited state ( $*A$ ) at zero time, when the laser pulse of excitation is switched on,  $k$  and  $k'$  are the rate constants of the first- and second-order processes, respectively. The triplet excited state lifetimes (first order component) are in very good agreement with data found by analysing phosphorescence intensity decays.<sup>122</sup> Triplet-triplet annihilation rate constants ( $k_{T-T}$ ), measured under the same experimental conditions ( $\lambda_{\text{ex}} = 355$  nm,  $\lambda_{\text{abs}} = 480$  nm), decreased in going from **MB** ( $k_{T-T} = 1.2 \times 10^6 \text{ M}^{-1} \text{ s}^{-1}$ ) to dendrimers (e.g., in the case of **GI**  $k_{T-T} = 0.5 \times 10^6 \text{ M}^{-1} \text{ s}^{-1}$ ). This experimental result shows that, as expected, the dimethoxybenzil core in the dendrimers is protected against self-quenching by the dendritic branches.

[120] M. V. Encinas and J. C. Scaiano, *J. Am. Chem. Soc.*, 1979, 101, 7740.

[121] N. J. Turro, *Modern Molecular Photochemistry*, University Science Book, Sausalito, CA (USA), 1991.

[122] A delayed fluorescence obtained by triplet-triplet annihilation can be excluded because of the low sample concentration and low intensity of the lamp source.

In dichloromethane/chloroform 1:1 (v/v) rigid matrix at 77 K, **MB** and **D2** show two phosphorescence bands very close in energy (Figure 5.15.a.)

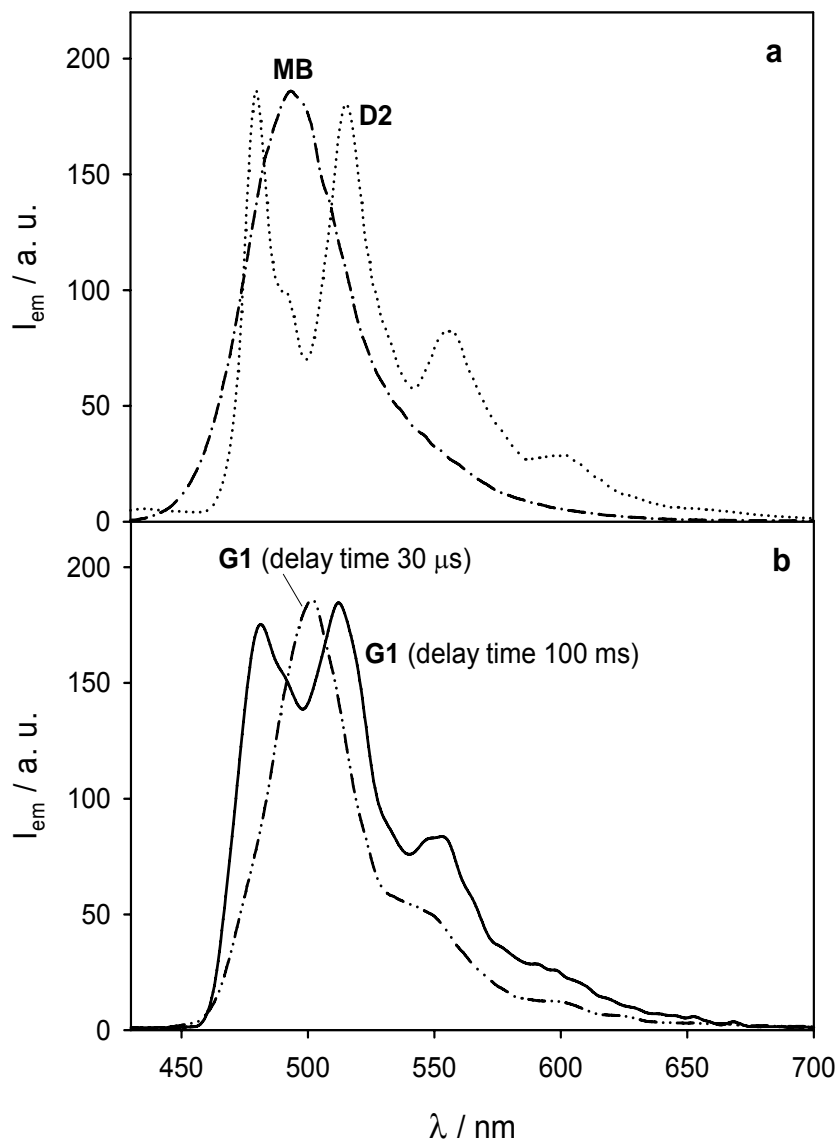


Figure 5.15. Phosphorescence spectra of MB and D2 (a) and of dendrimer G1 (b) in  $\text{CH}_2\text{Cl}_2:\text{CHCl}_3$  1:1 (v/v) at 77 K.  $\lambda_{ex} = 330$  nm.

The main differences are: (i) the vibrational structure present only in the phosphorescence of **D2**, (ii) the lifetime values: 2.7 ms for **MB** and 1.2 s for **D2** (Table 5.1.) and (iii) the phosphorescence quantum yield much lower for naphthalene than that of benzil.<sup>115</sup> The phosphorescence of **MB** is assigned to the  $n\pi^*$  triplet excited state ( $T_1$ ) of the dimethoxybenzil chromophore, and that of **D2** to the  $\pi\pi^*$   $T_1$  excited state of the naphthalene unit, as evidenced by comparison of the phosphorescence bands of 2-methylnaphthalene.<sup>118</sup> Under the same experimental conditions, dendrimers **G0-G2** show a complex behaviour: upon selective excitation of the dimethoxybenzil chromophore at 330 nm, the phosphorescence spectrum recorded with a relatively short delay (30  $\mu$ s) shows a spectral profile very similar to that observed for **MB**, while recorded with a longer delay (100 ms) is very similar to the naphthalene-type phosphorescence (see e.g., Figure 5.15.b.). Correspondingly, two lifetimes have been observed (Table 5.1.): a shorter one (ms time scale) assigned to the dimethoxybenzil chromophore, and a longer one (second time scale) due to the naphthalene moiety. The  $T_1$  excited states of naphthalene and dimethoxybenzil units are very close in energy (Figure 5.15.a.), but spectral evolution of the phosphorescence band for dendrimers **G0-G2** and observation of naphthalene phosphorescence upon selective excitation of dimethoxybenzil core are indicative of an energy transfer process from dimethoxybenzil to naphthalene chromophore (Figure 5.16.). The efficiency of this process is low, as demonstrated by the slight decrease of dimethoxybenzil triplet excited state lifetime (Table 1), and an estimation of the naphthalene sensitization efficiency and rate constant is difficult. Indeed, quantitative measurements of emission intensities at 77 K are difficult, especially in the present case since the naphthalene phosphorescence quantum yield is much lower than that of benzil.<sup>113</sup> Contrary to what happens at 77 K, at 298 K there is no evidence for energy transfer from the  $T_1$  excited state of dimethoxybenzil to that of naphthalene in dendrimers **G0-G2**. The emission quantum yield and lifetime of the  $T_1$  excited state of the dimethoxybenzil unit at room temperature is slightly higher in the case of dendrimers compared to **MB** (Table 5.1.)

and no transient absorption features typical of naphthalene (2-methyl naphthalene shows a transient absorption spectrum with  $\lambda_{\text{max}}$  at ca. 400 nm) has been observed upon selective excitation of the dimethoxybenzil core ( $\lambda_{\text{ex}} = 355$  nm).

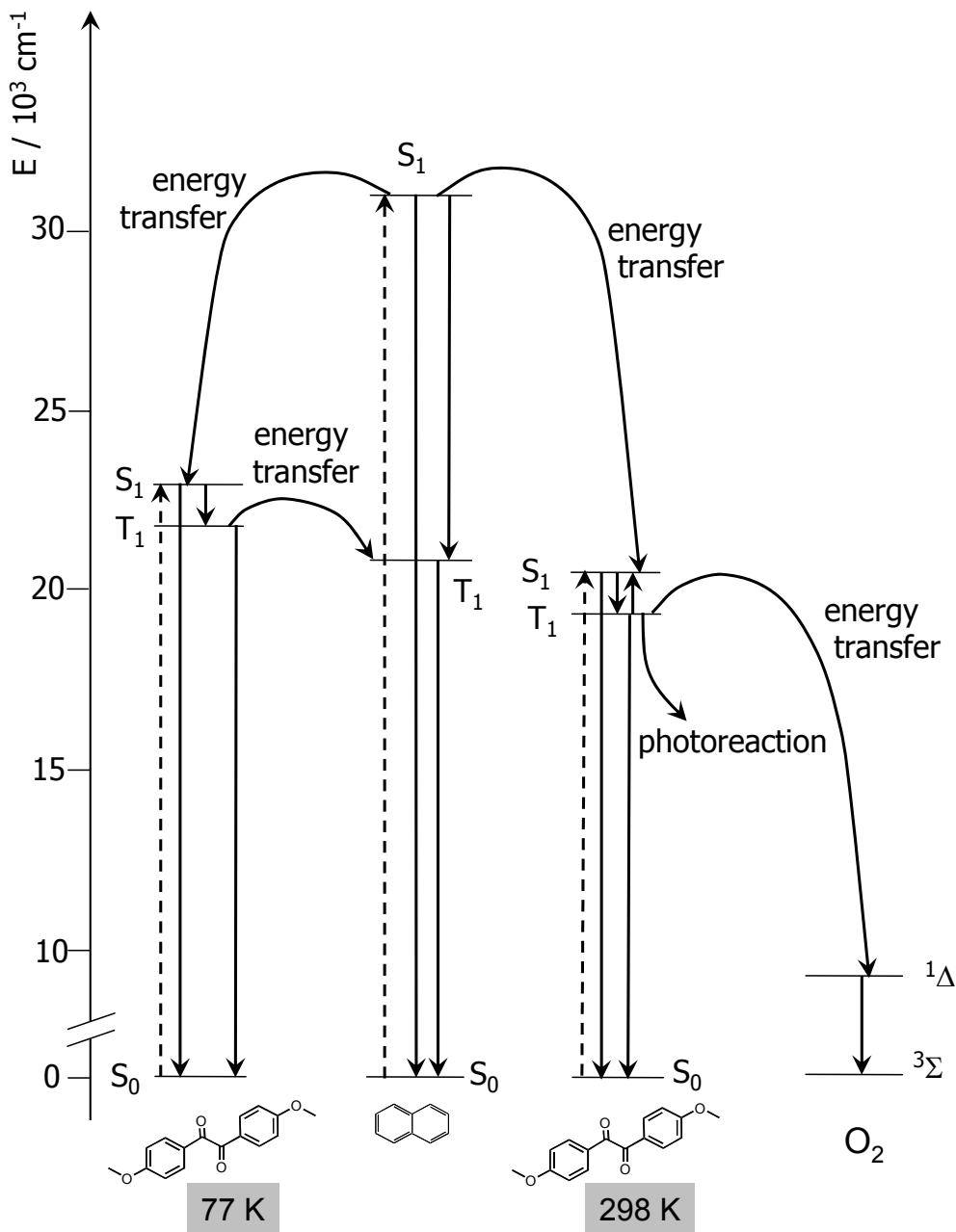


Figure 5.16. Energy diagram of the photoinduced processes in dendrimers G0-G2.

The lack of energy transfer at room temperature can be explained considering that the dimethoxybenzil phosphorescence shows a quite strong blue shift in going from 298 to 77 K, as expected for a  $n\pi^*$  transition where lack of solvent repolarization in rigid matrix leads to an increase of the corresponding excited state energy. A much less pronounced shift is expected for the naphthalene  $T_1$  excited state, because of its  $\pi\pi^*$  character. As a consequence, the lowest  $T_1$  excited state in the dendrimers is located on the dimethoxybenzil at 298 K and on the naphthalene at 77 K. Another interesting aspect of the phosphorescence bands observed for these dendrimers is that only in the case of **G2** there is a substantial solvent effect. The **G2** phosphorescence is red-shifted compared to **MB**, **G0** and **G1** in dichloromethane:methanol rigid matrix and blue-shifted in dichloromethane:chloroform (Table 5.1.). The peculiar behaviour of **G2** can be due to a different degree of back-folding of the dendrons in the two solvent mixtures, thus creating an environment of different polarity from the bulk of the solution.

In aerated solution, all the examined compounds are able to transfer energy to dioxygen with high efficiency as shown by the observation of the singlet dioxygen emission band at 1260 nm.

The results obtained for **G0**, **G1**, and **G2** in dichloromethane:chloroform 1:1 (v/v) solution show that an energy transfer process from the lowest excited state ( $S_1$ ) of the naphthalene units to the lower lying  $S_1$  excited state of the dimethoxybenzil core takes place with high efficiency, while energy transfer from the  $T_1$  excited state of the dimethoxybenzil core to the  $T_1$  excited state of the naphthalene units takes place at 77 K, but not at 298 K, where the  $T_1$  excited state of the dimethoxybenzil core moves to lower energy. It means that the lowest emitting excited state of the dendrimer is located on the dimethoxybenzil core at room temperature and on the peripheral naphthyl chromophores in rigid matrix at 77 K (Figures 5.16. and 5.17.).

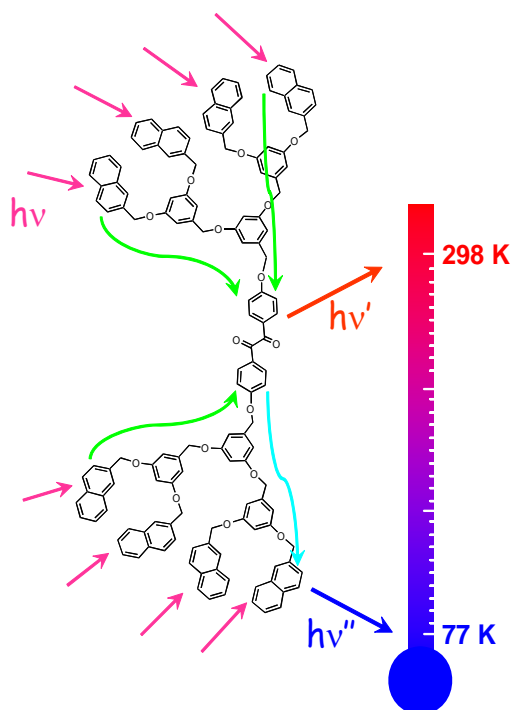


Figure 5.17. Graphical representation of the temperature dependence of the photoinduced processes in dendrimer G2.

### Photochemical characterization

Upon irradiation at 313 nm of an air-equilibrated  $\text{CH}_2\text{Cl}_2:\text{CHCl}_3$  1:1 (v/v) solution of **MB**, strong changes in the absorption spectra are observed (Figure 5.18.a.): the characteristic dimethoxybenzil band at 300 nm disappears and a new one with maximum at 255 nm increases with an isosbestic point at 273 nm. The reaction quantum yield, measured from the disappearance of the band at 300 nm, is 0.09 in air-equilibrated solution, while it is negligible ( $< 0.005$ ) in deaerated solution where no absorption change was observed for irradiation times comparable to those of the air-equilibrated experiments. Clearly, dioxygen is involved in the photochemical reaction, likely due to the formation of benzoyl peroxide, as already reported.<sup>123</sup>

[123] C. Kósa, I. Lukáč and R. G. Weiss, *Macromolecules*, 2000, 33, 4015.

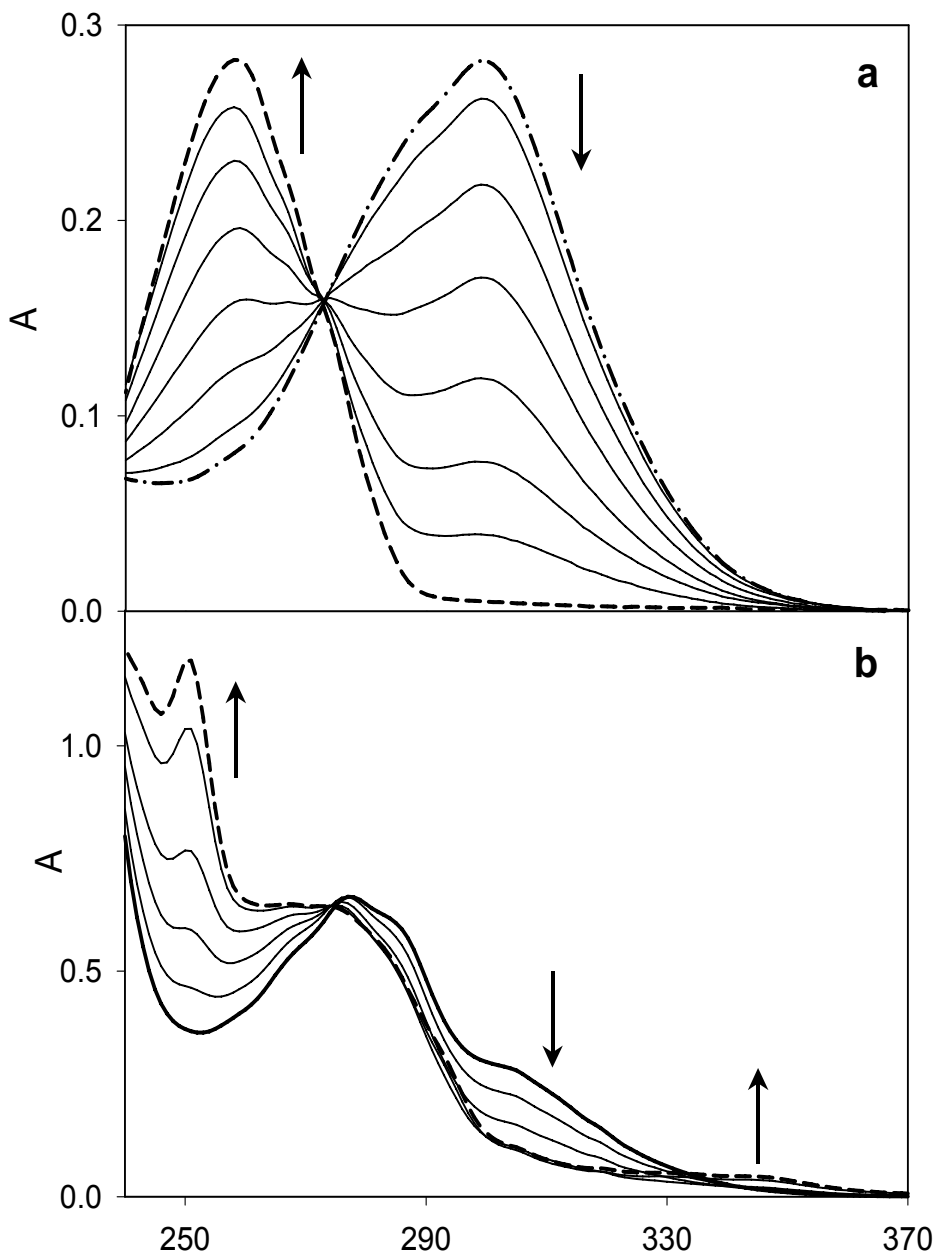


Figure 5.18. Absorption changes of MB (a) and G2 (b) in air-equilibrated  $\text{CH}_2\text{Cl}_2:\text{CHCl}_3$  1:1 (v/v) solution during irradiation at 313 nm.

Figure 5.18.b. shows the absorption changes recorded upon irradiation at 313 nm of an air-equilibrated  $\text{CH}_2\text{Cl}_2:\text{CHCl}_3$  1:1 (v/v) solution of **G2**. Although the photoreaction quantum yield is similar (0.07) to that obtained for **MB**, substantial qualitative differences from the **MB** photoreactivity can be observed: (i) two new absorption bands appear upon irradiation, one at higher energy ( $\lambda_{\text{max}}=250$  nm) compared to that of dimethoxybenzil, and one at lower energy ( $\lambda_{\text{max}} \approx 350$  nm); (ii) no effect of oxygen has been observed ( $\phi = 0.07$  both in air equilibrated and deaerated solutions).

In the case of air-equilibrated solutions of **G0** and **G1** irradiation at 313 nm caused spectral changes that, at the beginning, were similar to those observed under the same experimental conditions for **MB**, i.e. disappearance of the band at 300 nm and increase of a new one at higher energy. On going on with irradiation, however, a new band at 250 nm and a red tail ( $\lambda_{\text{max}} \approx 350$  nm) were formed, reminiscent of the photochemical reactivity of **G2**. Two different families of spectra, characterized by different isosbestic points, were indeed obtained, indicating the occurrence of two successive photochemical reactions. In deaerated solution, the photochemical reactivity of **G0** and **G1** is quite similar to that exhibited by **G2**, but with a much lower quantum yield (see Table 5.2.).

Irradiation at 313 nm of a deaerated solution containing **MB** ( $4 \times 10^{-5}$  M) and **D2** ( $4 \times 10^{-4}$  M) leads to spectral changes similar to those observed in the case of **G2**: the dimethoxybenzil band disappears and a new band at lower energy ( $\lambda_{\text{max}} \approx 350$  nm) increases.

In conclusion, the results obtained show that the dimethoxybenzil core maintains its photoreactivity toward dioxygen, and that on increasing dendrimer generation the branches perhaps protect the core towards reaction with dioxygen, but introduce a new reaction channel involving the dendron itself.

*Electrochemical characterization*

The cyclic voltammogram recorded for **MB** in dichloromethane/TBAPF<sub>6</sub> solution shows two reduction processes: the first one ( $E_{1/2} = -1.22$  V vs SCE) is completely reversible, while the second one ( $E_{1/2} = -1.47$  V vs SCE) shows some degree of chemical irreversibility. The spectroelectrochemical characterization of the monoanionic species **MB**<sup>-</sup> has been performed in an OTTE cell and evidences the appearance of new absorption bands at 370 and 600 nm.

In the cathodic region **G2** undergoes two one-electron reduction processes likely centred on the dimethoxybenzil core ( $E_{1/2(I)} = -1.19$  V  $E_{1/2(II)} = -1.66$  V vs SCE), but the second peak is cathodically shifted and presents an higher degree of chemical irreversibility. The spectroelectrochemical investigation of the monoanionic species of **G2** confirms that the first reduction process involves the dimethoxybenzil core since the absorption changes are similar to those observed for the reduction of **MB**. The spectroelectrochemistry in correspondence of the second reduction process is prevented by the narrower potential window available in the spectroelectrochemical experimental conditions.

In the anodic region the cyclic voltammogram of **G2** presents a multielectronic chemically irreversible process, that can be assigned to the oxidation of the dimethoxybenzene units of the dendrons<sup>124</sup> ( $E_{pa} = +1.93$  V vs SCE at 0.2 V/s).

In conclusion, the properties of the dendrimers in the ground state (absorption spectra and electrochemical behavior) are those expected for their dimethoxybenzil, naphthalene, and dimethoxybenzene noninteracting units. The excited state properties, however, are substantially controlled by electronic interactions between the dimethoxybenzil core and the naphthalene units contained in the branches, whereas the dimethoxybenzene units play a less important role. The results obtained from emission and transient absorption experiments in dichloromethane:chloroform 1:1 (v/v) solution at 298 and 77 K show that: (i) energy transfer

[124] P. Ceroni, V. Vicinelli, M. Maestri, V. Balzani, W. M. Müller, U. Müller, U. Hahn, F. Osswald and F. Vögtle, *New J. Chem.*, 2001, 25, 989.

from the lowest excited state ( $S_1$ ) of the naphthalene units to the lower lying  $S_1$  excited state of the dimethoxybenzil core takes place with high efficiency; (ii) energy transfer from the  $T_1$  excited state of the dimethoxybenzil core to the  $T_1$  excited state of the naphthalene units takes place at 77 K, but not at 298 K, where the  $T_1$  excited state the dimethoxybenzil core moves to lower energy. As far as the photochemical behavior is concerned, the dimethoxybenzil unit maintains its intrinsic photoreactivity toward dioxygen even when it belongs to the dendrimer core, and on increasing dendrimer generation a photoreaction between core and branches also takes place.

Table 5.1. Photophysical data in dichloromethane:chloroform 1:1 (v/v) solution, unless otherwise noted.

	Absorption		Fluorescence			Phosphorescence			
	298 K		298 K			298 K		77 K <sup>a</sup>	
	$\lambda_{\max}^1$	$\epsilon_{\max}^2$	$\lambda_{\max}^1$	$\phi_{\text{em}}$	$\tau^3$	$\lambda_{\max}^1$	$\tau^4$	$\lambda_{\max}^1$	$\tau^5$
<b>MB</b>	300	25000	495	0.0003	<0.5	550	25	494 (492)	0.0027 (0.0027)
<b>D2</b>	276	27200	335	0.028	5.4, 66	- <sup>c</sup>	- <sup>c</sup>	480 (480)	1.2 (1.5)
<b>G0</b>	288	34400	335	0.0006	<0.5 <sup>b</sup> ,3.2	550	30	502	0.0025,1
			495	0.0003	<0.5			(502)	(1.4)
<b>G1</b>	280	47500	335	0.001	<0.5 <sup>b</sup> ,3.2	550	30	502	0.0016,1
			495	0.0004	<0.5			(502)	(1.5)
<b>G2</b>	278	80100	335	0.003	<0.5 <sup>b</sup> ,3.1	550	30	492	0.0011,1
			495	0.0003	<0.5			(518)	(1.2)

## *Supramolecular Photoactive Systems*

<sup>1</sup> nm;

<sup>2</sup> M<sup>-1</sup>cm<sup>-1</sup>;

<sup>3</sup> ns;

<sup>4</sup> μs;

<sup>5</sup> s;

<sup>a</sup> data reported in parenthesis have been obtained in dichloromethane:methanol 1:1 (v/v) rigid matrix at 77 K;

<sup>b</sup> a double exponential decay has been observed, but the value of the shorter lifetime cannot be determined with the equipment used. The corresponding lifetime has not been reported since the single-photon-counting apparatus used has a time resolution of 0.5 ns;

<sup>c</sup> no emission has been observed.

Table 5.2. Photoreaction quantum yield<sup>a</sup> upon irradiation at 313 nm in dichloromethane solution at 298 K.

	$\Phi_{\text{react}}$	
	air-equilibrated solution	deaerated solution
<b>MB</b>	0.09	< 0.005
<b>G0</b>	0.11	0.007
<b>G1</b>	0.10	0.01
<b>G2</b>	0.07	0.07

<sup>a</sup> reported quantum yields were obtained by extrapolation to time zero of the initial part of the photoreaction.

## 5.2. Dendrimers Containing 4,4'-Bipyridinium Units

### 5.2.1. Aromatic Electron-Acceptors based on N-Heterocycles

The 4,4'-bipyridinium dication ( $V^{2+}$ ) (Figure 5.19.) is a commonplace among electron accepting units.<sup>125</sup> Its derivatives are widely employed in a large variety of applications, such as electron-transfer relays,<sup>126</sup> redox-active units in molecular and supramolecular systems,<sup>127</sup> molecular machines,<sup>128</sup> molecular

electronics,<sup>129</sup> electrochromic systems,<sup>130</sup> and charge-transfer salts. The prototypical species, 1,1'-dimethyl-4,4'-bipyridinium – also known as methylviologen or paraquat – was formerly used as a herbicide.<sup>131</sup>

Several other compounds based on N-heterocycles, structurally related to 4,4'-bipyridinium, have been reported in the literature, and found to behave as efficient electron acceptors. Examples are the compounds of the 1,2-bis(4-pyridinium)ethylene ( $BPE^{2+}$ )<sup>132,133</sup> and 2,7-

---

[125] P. M. S. Monk, *The Viologens – Physicochemical Properties, Synthesis and Application of the salts of 4,4'-Bipyridine*, Wiley, Chichester, 1998.

[126] V. Balzani (ed.), *Electron Transfer in Chemistry*, Vols. 1-5, Wiley-VCH, Weinheim, 2001.

[127] A. E. Kaifer, M. Gómez-Kaifer, *Supramolecular Electrochemistry*, Wiley-VCH, Weinheim, 1999.

[128] V. Balzani, A. Credi, M. Venturi, *Molecular Devices and Machines, – A Journey into the Nanoworld*, Wiley-VCH, Weinheim, 2003.

[129] Z. Li, B. Han, G. Meszaros, I. Pobelov, T. Wandlowski, A. Blaszczyk, M. Mayor, *Faraday Discuss.*, 2006, 131, 121.

[130] A. Michaelis, H. Berneth, D. Haarer, S. Kostromine, R. Neigl, R. Schmidt, *Adv. Mater.*, 2001, 13, 1825.

[131] A. Summers, *The Bipyridinium Herbicides*, Academic Press, New York, 1980.

[132] P. R. Ashton, R. Ballardini, V. Balzani, A. Credi, M. T. Gandolfi, S. Menzer, L. Pérez-García, L. Prodi, J. F. Stoddart, M. Venturi, A. J. P. White, D. J. Williams, *J. Am. Chem. Soc.*, 1995, 117, 11171.

[133] R. Ballardini, V. Balzani, A. Credi, M. T. Gandolfi, L. Prodi, M. Venturi, L. Pérez-García, J. F. Stoddart, *Gazz. Chim. Ital.*, 1995, 125, 353.

diazapyrenium ( $\text{DAP}^{2+}$ )<sup>134,135</sup> families (Figure 5.19). All these species share the nature of electron-poor  $\pi$ -systems, but possess quite distinct physicochemical properties. The peculiar feature of the first family resides in the possibility of undergoing photoinduced  $E \rightarrow Z$  isomerization, whereas the most important property of the second family is that of exhibiting strong and structured fluorescence at room temperature, and structured fluorescence and phosphorescence in rigid matrix at 77 K.

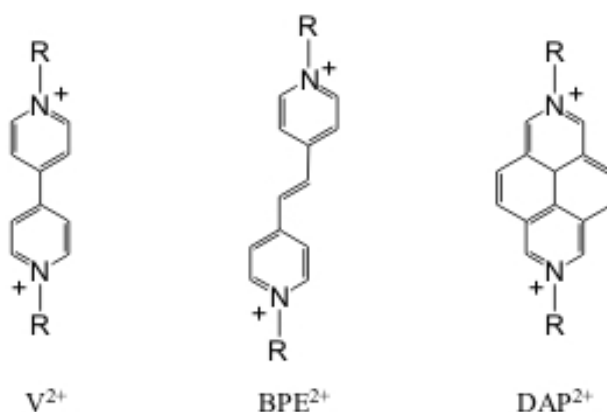


Figure 5.19. Generalized structural formulas of N,N-derivatives of 4,4'-bipyridinium ( $\text{V}^{2+}$ ),  $E$ -1,2-bis(4-pyridinium)ethylene ( $\text{BPE}^{2+}$ ), and 2,7-diazapyrenium ( $\text{DAP}^{2+}$ ) cations.

Here we report the results of photophysical, photochemical and electrochemical investigations in solution, and quantum chemical calculations, on three families of compounds based on the 4,4'-bipyridinium, 1,2-bis(4-pyridinium)ethylene, and 2,7-diazapyrenium units, respectively (Figure 5.19). Within each family, compounds bearing either alkyl or aryl

[134] (a) R. Ballardini, V. Balzani, A. Credi, M. T. Gandolfi, S. J. Langford, S. Menzer, L. Prodi, J. F. Stoddart, M. Venturi, D. J. Williams, *Angew. Chem. Int. Ed. Engl.*, **1996**, *35*, 978; (b) A. Credi, V. Balzani, S. J. Langford, J. F. Stoddart, *J. Am. Chem. Soc.*, **1997**, *119*, 2679; (c) P. R. Ashton, R. Ballardini, V. Balzani, E. C. Constable, A. Credi, O. Kocian, S. J. Langford, A. J. Preece, L. Prodi, E. R. Schofield, N. Spencer, J. F. Stoddart, S. Wenger, *Chem. Eur. J.*, **1998**, *4*, 2413; (d) A. Credi, M. Montalti, V. Balzani, S. J. Langford, F. M. Raymo, J. F. Stoddart, *New J. Chem.*, **1998**, *22*, 1061.

[135] V. Balzani, A. Credi, S. J. Langford, A. Prodi, J. F. Stoddart, M. Venturi, *Supramol. Chem.*, **2001**, *13*, 303.

substituents on the quaternarized nitrogen atoms have been examined, showing that their spectroscopic and electrochemical properties are fine tuned by the nature of the substituents.

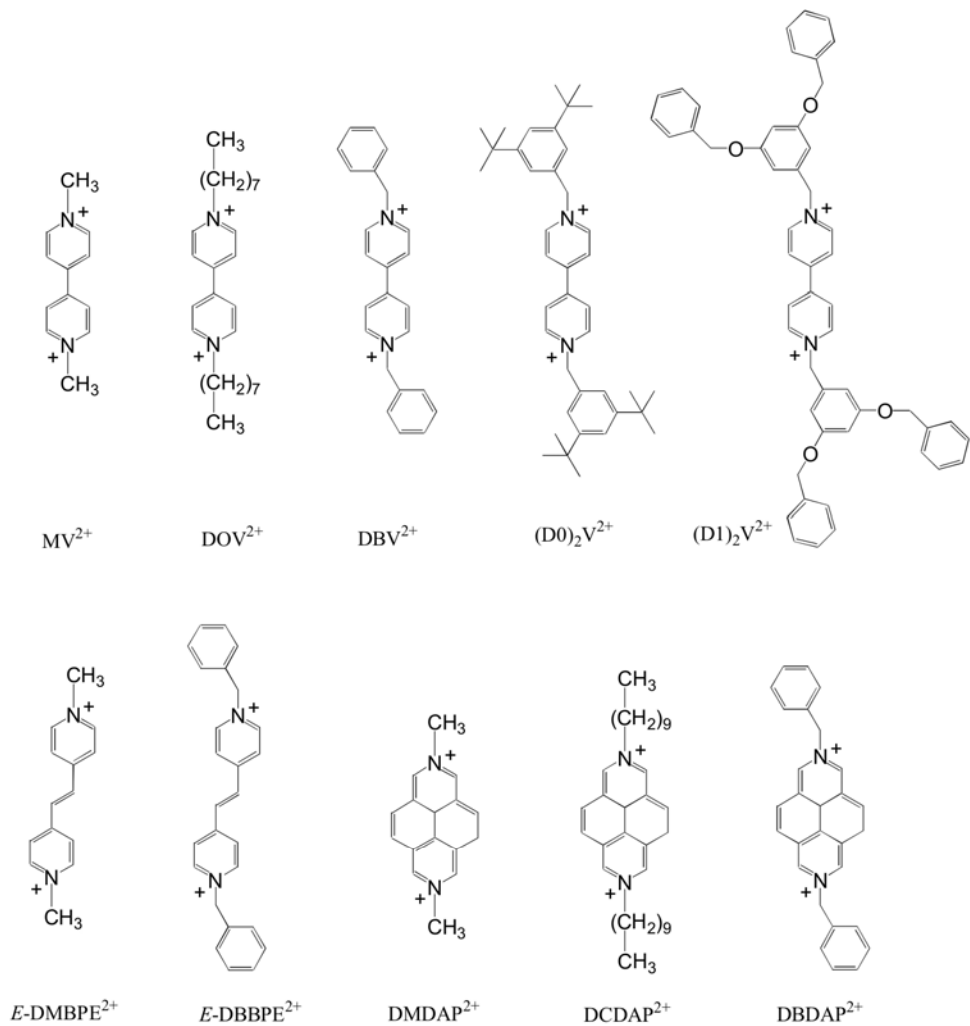


Figure 5.20. Structural formulas of the investigated compounds.

The experiments were carried out in AN solution at room temperature and in BN rigid matrix at 77 K. All the relevant data on the photophysical properties obtained in our laboratory are collected in Tables 5.3., 5.4., 5.5., together with some data selected from the

literature. Table 5.6. reports the calculated energies (ZINDO/S) of the emitting state,  $E(S_1)$ , its oscillator strength,  $f$ , the energy of the closest low-lying triplet state,  $E(T_n)$ , and the radiative,  $k_r$ , and total,  $k_t$ , deactivation rate constants.

The compounds dealt with in this paper (Figure 5.20.) exhibit very similar electrochemical behavior which in several cases has been well established for a long time. Independently on the substituents on the nitrogen atoms, in the potential window examined (from  $-1.8$  to  $+1.8$  V vs SCE) all the compounds show two consecutive reduction processes, and no oxidation process. However, the chemical nature of the substituents and the polarity of the solvent are expected to affect the values of the halfwave potentials at which the two reductions occur. Here we will discuss only the results obtained in acetonitrile solution.

#### *Derivatives of 4,4'-bipyridinium*

The absorption properties of the 1,1'-derivatives of 4,4'-bipyridinium ion have been extensively studied, while only a few, sometimes controversial data are available on their emission behaviour.<sup>136,137</sup> The UV-visible spectroscopic data on the investigated 4,4'-bipyridinium species are collected in Table 5.3.

The simplest compound of this family (Figure 5.20.) is the 1,1'-dimethyl-4,4'-bipyridinium ion ( $MV^{2+}$ ), whose absorption spectrum is reported in Figure 5.21,<sup>138</sup> together with the spectra of the dibenzyl ( $DBV^{2+}$ ) and dioctyl ( $DOV^{2+}$ ) derivatives. A comparison of the absorption band shape is shown in Figure 5.22. The absorption spectra exhibit in all cases an intense unstructured band centred at around 260 nm, attributed to a  $\pi\pi^*$  (HOMO $\rightarrow$ LUMO) transition, calculated at 259 nm for  $MV^{2+}$ .

[136] J. Peon, X. Tan, J. D. Hoerner, C. Xia, Y. F. Luk, B. Kohler, *J. Phys. Chem. A*, 2001, 105, 5768.

[137] (a) A. W.-H. Mau, J. M. Overbeek, J. W. Loder, W. H. F. Sasse, *J. Chem. Faraday Trans.*, 1986, 2, 82, 869; (b) V. Novakovic, M. Z. Hoffman, *J. Am. Chem. Soc.*, 1987, 109, 2341; (c) M. Alvaro, H. Garcia, S. Garcia, J. C. Scaiano, *J. Phys. Chem. B*, 1997, 101, 3043.

[138] P. R. Ashton, R. Ballardini, V. Balzani, M. Belohradsky, M. T. Gandolfi, D. Philp, L. Prodi, F. M. Raymo, M. V. Reddington, N. Spencer, J. F. Stoddart, M. Venturi, D. J. Williams, *J. Am. Chem. Soc.*, 1996, 118, 4931.

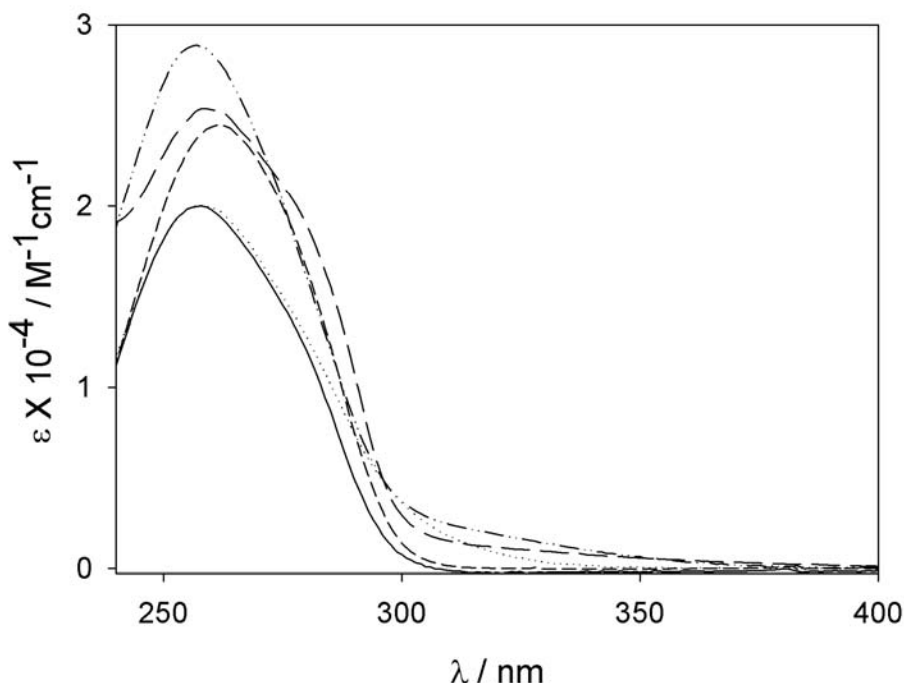


Figure 5.21. Absorption spectra of  $MV^{2+}$  (—),  $DBV^{2+}$  (·····),  $DOV^{2+}$  (----),  $(D0)_2V^{2+}$  (- · - · - ·) and  $(D1)_2V^{2+}$  (— — —) (AN, room temperature).

For  $DOV^{2+}$  the comparison shown in Figure 5.22. evidences only a slight red shift of the maximum of the band, that can be assigned to a small perturbation caused by the presence of the two long aliphatic chains as substituents. For  $DBV^{2+}$  an enlargement of the band toward longer wavelengths is present. In Figure 5.22. the spectra of the di-*tert*-butylbenzyl,  $(D0)_2V^{2+}$ , and dimethylenoxybenzyl,  $(D1)_2V^{2+}$ , derivatives of the 4,4'-bipyridinium unit (Figure 5.20.) are also reported. A modest increase in the molar absorption coefficients with respect to  $MV^{2+}$  and weak and long tails toward the visible region can be observed. In the case of  $DBV^{2+}$ , this second feature can be attributed to the presence of a couple of weak states ( $\lambda = 293$  and  $278$  nm;  $f \sim 0.01$ ) calculated below the first absorbing state. In addition, for  $(D1)_2V^{2+}$  the presence of a shoulder around  $275$  nm is due to the dimethylenoxybenzyl substituents that absorb in this region.

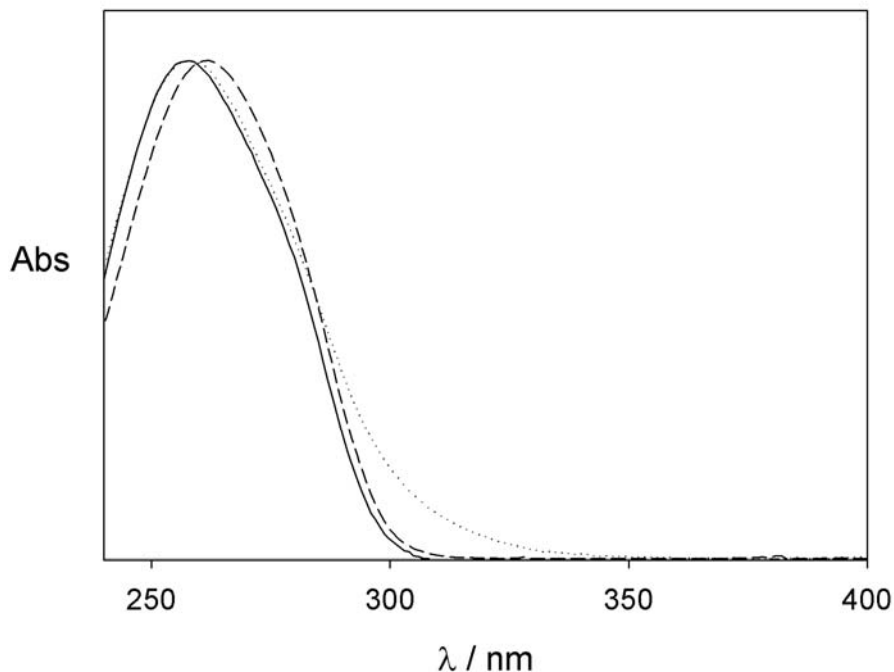


Figure 5.22. Comparison of the absorption band shape of  $MV^{2+}$  (—) and  $DBV^{2+}$  (·····),  $DOV^{2+}$  (----) (AN, room temperature).

As far as the emission properties are concerned, it has been often reported that  $MV^{2+}$  is not fluorescent in fluid solution.<sup>137</sup> On the contrary, our results agree with those reported in literature,<sup>136</sup> in which the authors have definitely stated, with detailed steady-state and time-resolved fluorimetric measurements, that  $MV^{2+}$  (as hexafluorophosphate salt) exhibits an appreciable radiative decay path from its lowest singlet excited state ( $\pi\pi^*$  in nature).

The fluorescence spectrum is reported in Figure 5.23., together with that of  $DOV^{2+}$ . As one can see, the band shape is the same, although the emission quantum yield of  $DOV^{2+}$  is about half of that of  $MV^{2+}$  (see Table 5.3.). This result can be likely attributed to the presence of the two alkyl chains, which can effectively contribute to the internal conversion deactivation process.

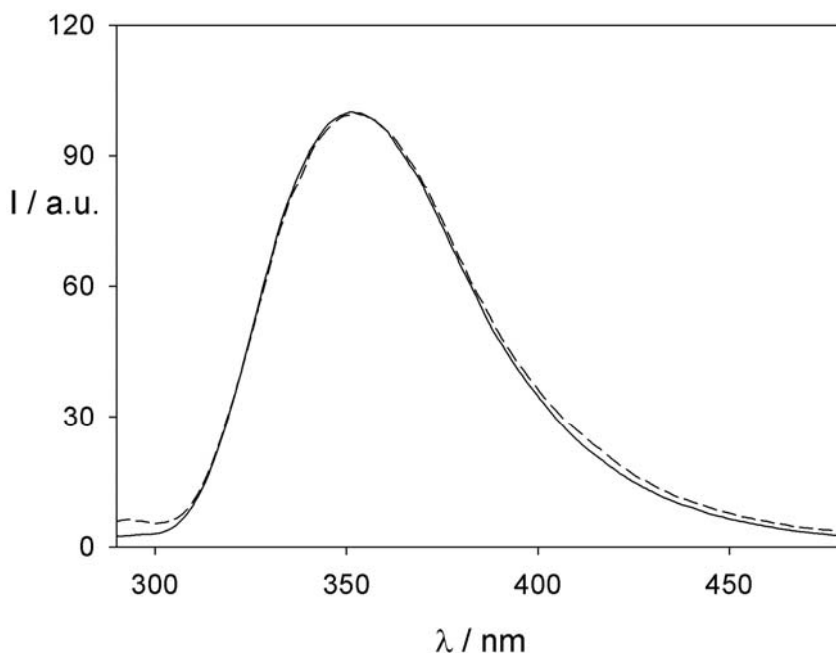


Figure 5.23. Normalized fluorescence spectra of  $MV^{2+}$  (—) and  $DOV^{2+}$  (----) (AN, room temperature,  $\lambda_{exc} = 260$  nm).

The derivatives  $DBV^{2+}$ ,  $(D0)_2V^{2+}$ , and  $(D1)_2V^{2+}$  do not show any luminescence, because the lowest singlet excited state, calculated at 424 nm for  $DBV^{2+}$  (corresponding to  $23580\text{ cm}^{-1}$ , see Table 5.6.), has a negligible oscillator strength. Contrary to what happens for  $MV^{2+}$ , the HOMO of  $DBV^{2+}$  is mainly localized on the benzyl substituents, whereas the LUMO is concentrated on the central bipyridinium ion: the promotion of electrons between  $S_0$  and  $S_1$  represents therefore a situation of intramolecular charge-transfer, accompanied, in this case, by a very effective non-radiative deactivation channel (vide infra).

The deactivation of  $S_1$  for  $MV^{2+}$  has been shown to be quite dependent on the solvent used.<sup>136</sup> In  $CH_3OH$  solution the main deactivation channel results in a photoreduction which is unequivocally detected by the presence of the monoreduced species,  $MV^{+}$ , following 265 nm excitation in a pump-probe experiment.<sup>136</sup> On the other hand in other solvents, like acetonitrile

and water, different deactivation mechanisms seem to prevail: one of these can arise from the valence isomerization to a pre-fulvenic geometry of the pyridinium ion, in analogy to what observed for pyridine in condensed phase.<sup>139</sup> In the case of DBV<sup>2+</sup>, this process appears to be further enhanced, as shown by the very large value computed for  $k$  (Table 5.6.) and the lack of phosphorescence at 77 K, although internal conversion to the ground state cannot be excluded owing to the relatively low energy of the S<sub>1</sub> state (23580 cm<sup>-1</sup>, Table 5.6.).

As already mentioned, 1,1'-dimethyl-4,4'-bipyridinium (MV<sup>2+</sup>, Figure 5.20.) is the simplest model for the bipyridinium-type dications. It exhibits two reversible and monoelectronic reduction processes at -0.43 and -0.84 V vs SCE<sup>140</sup> (Table 5.3., Figure 5.24.). The 1,1'-dioctyl derivative (DOV<sup>2+</sup>, Figure 5.20.) shows a practically identical behavior as far as reversibility, exchanged electrons, and halfwave potential values are concerned (Table 5.3.).

This result is not surprising by considering that the methyl and octyl groups are very similar alkyl substituents. In going to the 1,1'-dibenzyl derivative, DBV<sup>2+</sup>, although two reversible and monoelectronic processes are again present, a positive shift of the halfwave potential values of both the reductions is observed (Table 5.3.).<sup>132,141</sup> This finding can be explained on the basis of two slightly different viewpoints that, however, lead to the same conclusion. The first interpretation is based upon the electron withdrawing character of the benzylic group, whereas the second one takes into account hyperconjugation effects.<sup>142</sup> They allow for the electronic communication between the bipyridinium and phenyl aromatic moieties via the methylene bridge, thereby increasing the charge delocalization, hence facilitating the

---

[139] M. Chachisvillis, A. H. Zewail, *J. Phys. Chem. A*, **1999**, *103*, 7408.

[140] P. L. Anelli, P. R. Ashton, R. Ballardini, V. Balzani, M. Delgado, M. T. Gandolfi, T. T. Goodnow, A. E. Kaifer, D. Philp, M. Pietraszkiewicz, L. Prodi, M. V. Reddington, A. M. Z. Slawin, N. Spencer, J. F. Stoddart, C. Vincent, D. J. Williams, *J. Am. Chem. Soc.*, **1992**, *114*, 193.

[141] D. B. Amabilino, P.R. Ashton, V. Balzani, C. L. Brown, A. Credi, J. M. J. Fréchet, J. W. Leon, F. M. Raymo, N. Spencer, J. F. Stoddart, M. Venturi, *J. Am. Chem. Soc.*, **1996**, *118*, 12012.

[142] F. A. Carey, R. J. Sundberg, *Advanced Organic Chemistry*, Kluwer Academic/Plenum, New York, 2000.

electron uptake. The same considerations can be used to explain the behavior of  $(D0)_2V^{2+}$  and  $(D1)_2V^{2+}$  (Figure 5.20.), which show a positive shift of the halfwave potential values similar to that observed for the dibenzyl derivative (Table 5.3.).

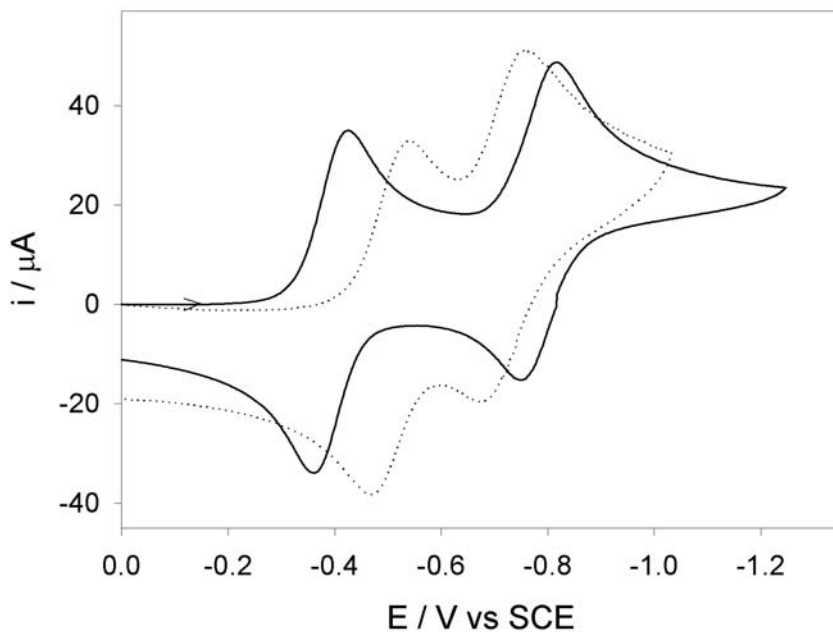


Figure 5.24. Cyclic voltammetric patterns for reduction of 1 mM  $MV^{2+}$  (—) and  $E\text{-DMBPE}^{2+}$  (·····). Conditions: argon-purged AN, room temperature,  $200\text{ mV s}^{-1}$ , glassy carbon electrode; tetraethylammonium hexafluorophosphate as supporting electrolyte.

It is also important to note that the monoreduced and doubly reduced species of most of the 1,1'-derivatives of 4,4'-bipyridinium are stable in carefully deoxygenated solution; in particular, the monoreduced species are intensely colored, owing to the presence of an unpaired electron acquired on reduction, and, depending on concentration, nature of the solvent, and temperature, can undergo dimerization.<sup>125</sup> As an example, Figure 5.25. shows the absorption spectrum of the monoreduced species of  $DBV^{2+}$ , obtained in spectroelectrochemical experiments, whose features are similar to those of  $MV^{+}$ .

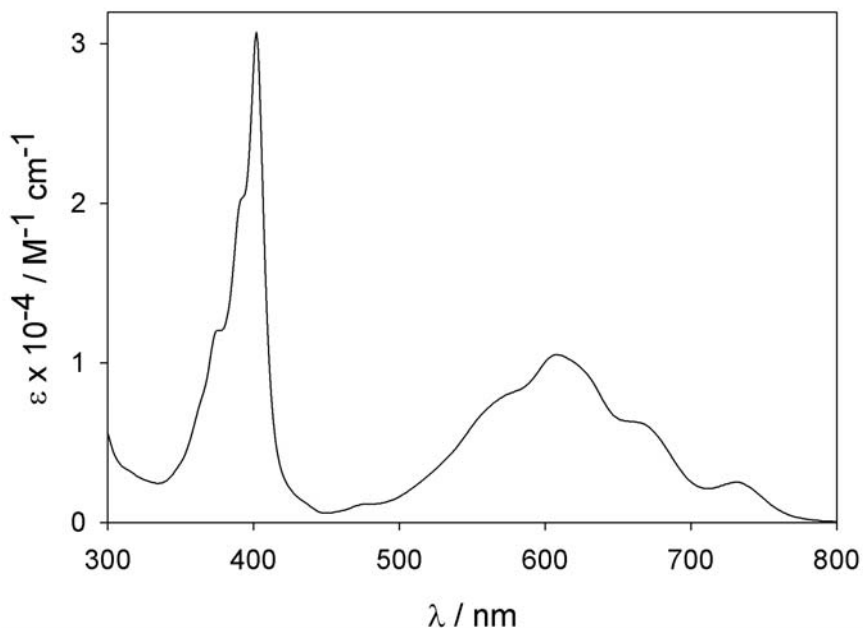


Figure 5.25. Absorption spectrum of the monoreduced  $\text{DBV}^{\bullet+}$  species (argon-purged AN, room temperature).

#### *Derivatives of 1,2-bis(4-pyridinium)ethylene*

The 1,2-bis(4-pyridinium)ethylene dications are related to the class of stilbenes, and can exist in *E* and *Z* configurational isomers.<sup>143</sup> The absorption and luminescence data reported in this section are referred to the *E* isomers which are the thermodynamically stable forms. Information on the spectra of the *Z* isomers can be found in a next section dealing with photochemical behavior.

The UV-visible spectroscopic data for the *N,N*-dimethyl and *N,N*-dibenzyl derivatives of *E*-1,2-bis(4-pyridinium)ethylene in acetonitrile solution at room temperature and in butyronitrile glass at 77 K are gathered in Table 5.4. The absorption spectrum of *E*- $\text{DBBPE}^{2+}$  is similar to that of the dimethylated species *E*- $\text{DMBPE}^{2+}$ , but slightly red-shifted (Figure 5.26.) and both

[143] H. Dürr, H. Bouas-Laurent (eds.), *Photochromism: Molecules and Systems*, Elsevier, Amsterdam, 2003.

show the typical fluorescence band of the BPE<sup>2+</sup> unit (Figure 5.26.);<sup>144</sup> however, the luminescence quantum yield of *E*-DBBPPE<sup>2+</sup> is only 4% of that of *E*-DMBPPE<sup>2+</sup>.

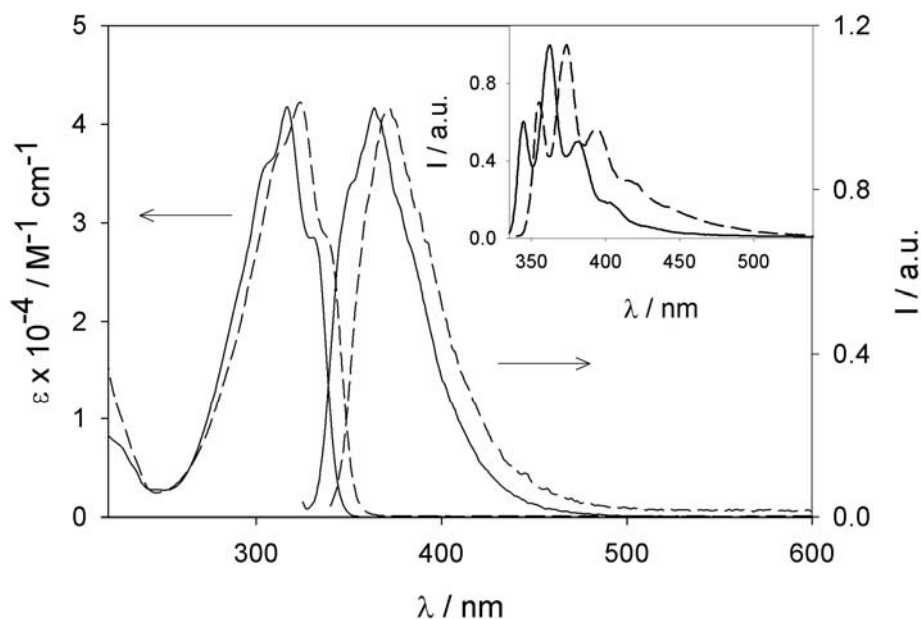


Figure 5.26. Absorption and fluorescence spectra (AN, room temperature,  $\lambda_{\text{exc}} = 320 \text{ nm}$ ) of *E*-DMBPPE<sup>2+</sup> (—) and *E*-DBBPPE<sup>2+</sup> (----). The inset shows the fluorescence spectra of *E*-DMBPPE<sup>2+</sup> (—) and *E*-DBBPPE<sup>2+</sup> (----) in BN at 77 K ( $\lambda_{\text{exc}} = 320 \text{ nm}$ ). All the fluorescence spectra are normalized at the maximum intensity.

This observation can be ascribed to the fact that the lowest singlet excited state in *E*-DBBPPE<sup>2+</sup> has a charge transfer nature, similarly to what discussed for DBV<sup>2+</sup> (vide supra). This is not unexpected because the BPE<sup>2+</sup> moiety is a good electron acceptor (vide infra) and the benzyl moiety can act as a weak reductant (the potential for the oxidation of toluene is +1.98 V vs SCE).<sup>145</sup> Such a singlet state cannot be evidenced in the absorption spectrum, most likely because the corresponding electronic transition is characterized by a weak absorption

[144] G. Favaro, G. Beggiato, *Gazz. Chim. Ital.*, 1970, 100, 326.

[145] C. K. Mann, K. K. Barnes, *Electrochemical Reactions in Non-aqueous Systems*, Dekker, New York, 1970.

coefficient (calculated  $f = 0.18$ ) compared to that exhibited by the first absorbing system ( $\epsilon_{\max} = 42000 \text{ L mol}^{-1} \text{ cm}^{-1}$ ,  $f = 0.68$ ), but can effectively deactivate non-radiatively.

In contrast to what happens for the unprotonated relative, 1,2-bis(4-pyridine)ethylene, where the  $n\pi^*$  nature of the lowest singlet excited state coupled to a close lying  $\pi\pi^*$  triplet induces an effective intersystem crossing,<sup>146</sup> the triplet way of deactivation seems to be negligible for  $E$ -DMBPE<sup>2+</sup> and  $E$ -DBBPE<sup>2+</sup>, as shown by the lack of phosphorescence at 77 K (Table 5.4.).

All the examined 4,4'-bipyridinium- and 2,7-diazapyrenium-type species are stable in solution upon irradiation with near UV light. On the contrary, the compounds containing the BPE<sup>2+</sup> moiety exhibit interesting photochemical properties. The photoreactivity of 1,2-bis(4-pyridinium)ethylene derivatives was extensively investigated in the past,<sup>147,148,149</sup> as well as that of the 1,2-bis(4-pyridyl)ethylene parent compound.<sup>150</sup> For  $E$ -DMBPE<sup>2+</sup> in AN solution, a  $E \rightarrow Z$  photoisomerization reaction was observed upon both direct excitation in the  $^1\pi\pi^*$  band<sup>132,147</sup> and triplet sensitization.<sup>132</sup>

The absorption spectral changes associated to the photoisomerization are characterized by a clean isosbestic point at 286 nm. In our investigations we found that  $E$ -DBBPE<sup>2+</sup> also undergoes a reaction in AN solution when irradiated in its  $^1\pi\pi^*$  band at 313 nm. As shown in Figure 5.27., the photoreaction causes a decrease in the intensity of such a band, and two isosbestic points (at 275 and 355 nm) are observed. After prolonged irradiation the isosbestic points are no longer maintained, and the  $\pi\pi^*$  band disappears almost completely. The

[146] G. Buntinx, R. Naskrecki, O. Poizat, *J. Phys. Chem.*, 1996, 100, 19380.

[147] T. W. Ebbesen, C. M. Previtali, T. Karatsu, T. Arai, K. Tokumaru, *Chem. Phys. Lett.*, 1985, 119, 489.

[148] T. W. Ebbesen, K. Tokumaru, M. Sumitani, K. Yoshihara, *J. Phys. Chem.*, 1989, 93, 5453.

[149] T. W. Ebbesen, R. Akaba, K. Tokumaru, M. Washio, S. Tagava, Y. Tabata, *J. Am. Chem. Soc.*, 1988, 110, 2147.

[150] D. G. Whitten, M. T. McCall, *J. Am. Chem. Soc.*, 1969, 91, 5097.

photoreaction takes place both in the presence and in the absence of oxygen, but it is slower in the latter case. The quantum yield for the disappearance of  $E$ -DBBPE $^{2+}$ , measured from the change in the absorption spectrum at 340 nm (where the absorbance of the photoproduct can be neglected) is much smaller than that for the  $E \rightarrow Z$  photoisomerization of  $E$ -DMBPE $^{2+}$  (Table 5.4.). In fact, the characteristics of the spectral changes measured for DBBPE $^{2+}$  upon 313-nm irradiation rule out the possibility that the observed photoreaction is the  $E \rightarrow Z$  isomerization about the vinylic double bond. From FABMS and  $^1\text{H}$  NMR analyses, it was found<sup>132</sup> that the photoproduct is a cyclobutene derivative, thereby excluding the presence of the  $Z$  isomer in the reaction mixture.

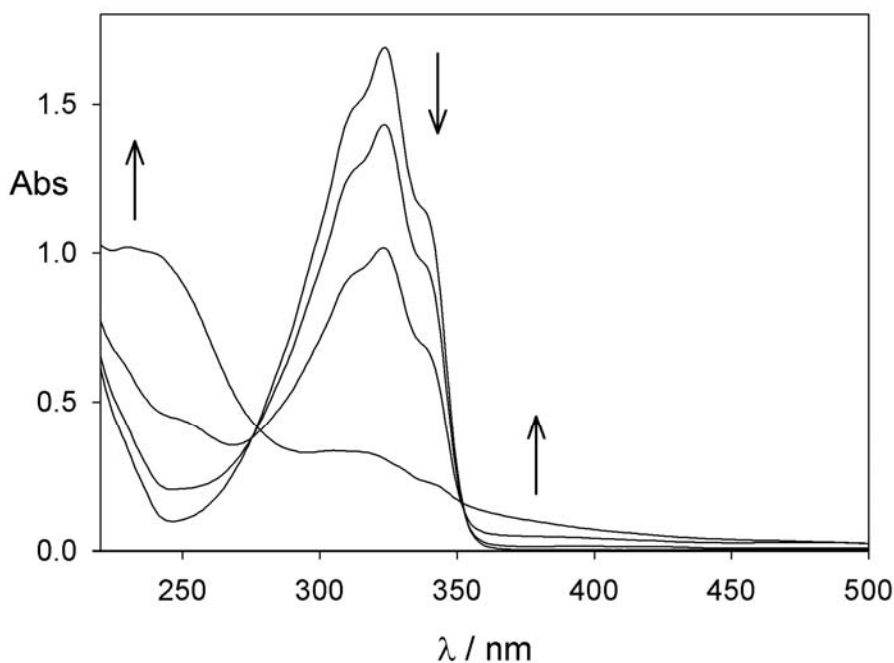


Figure 5.27. Absorption changes for a  $4.0 \times 10^{-5}$  mol  $\text{L}^{-1}$  AN solution of  $E$ -DBBPE $^{2+}$  upon direct irradiation at 313 nm at room temperature.

To explore the possibility of obtaining the photoisomerization of  $E$ -DBBPE $^{2+}$  we performed photosensitization experiments by using biacetyl (energy of the lowest triplet excited state,  $E$

$= 19700 \text{ cm}^{-1}$ ) as a triplet sensitizer. In such experiments, a degassed AN solution containing  $E\text{-DBBPPE}^{2+}$  and biacetyl is irradiated with 436-nm light, absorbed exclusively by biacetyl. The absorption spectral changes observed (after subtraction of the biacetyl absorption, constant throughout the irradiation) are shown in Figure 5.28.<sup>132</sup> As one can see, the spectral changes are different from those observed upon direct excitation (Figure 5.27.), and an isosbestic point at 286 nm is present, as expected for the  $E \rightarrow Z$  photoisomerization. The photoreaction quantum yield is 0.4; moreover, the absorption spectrum of the photoproduct is that expected for  $Z\text{DBBPPE}^{2+}$ .<sup>148</sup>

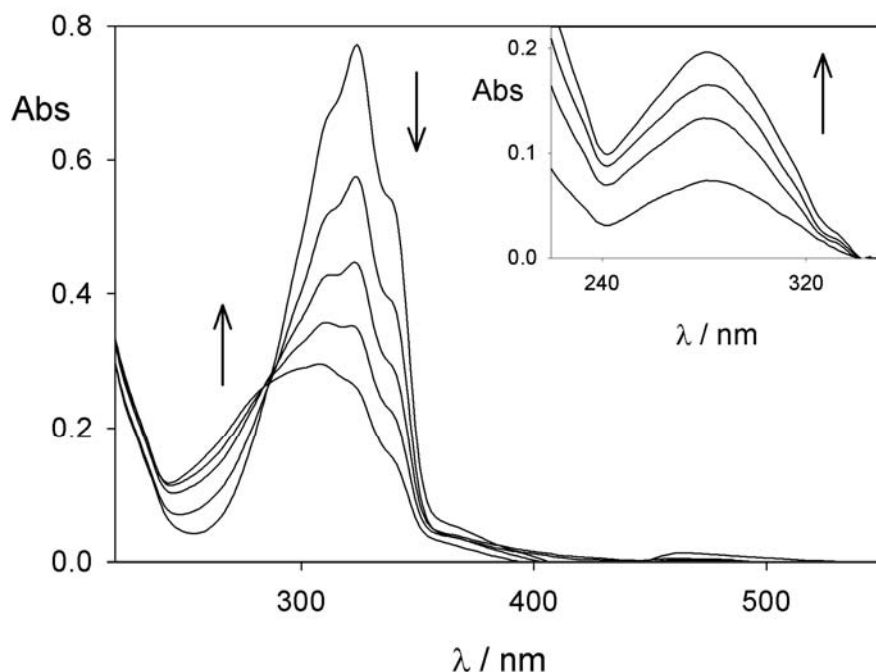


Figure 5.28. Absorption changes observed for the photoreaction of  $E\text{-DBBPPE}^{2+}$  sensitized by biacetyl (degassed AN solution, room temperature,  $2.0 \times 10^{-5} \text{ mol L}^{-1}$ ,  $\lambda_{\text{irr}} = 436 \text{ nm}$ ); the absorbance of the sensitizer has been subtracted. The inset shows the spectral changes obtained when the absorbance of the unreacted  $E\text{-DBBPPE}^{2+}$  is also subtracted.

On prolonged irradiation the solution reaches a photostationary state, which corresponds to a  $E \rightarrow Z$  conversion of 65%. When benzanthrone ( $\epsilon = 16100 \text{ cm}^{-1}$ ) is used as a triplet

sensitizer the  $E \rightarrow Z$  isomerization is again observed, with a lower quantum yield ( $\Phi = 0.2$ ) and a photostationary state less displaced to the  $Z$  isomer (18%).<sup>132</sup> On the basis of these results, the energy of the lowest triplet excited state of  $\text{DBBPE}^{2+}$  can be estimated to be around  $16000 \text{ cm}^{-1}$ .

In summary, for  $E\text{-DMBPE}^{2+}$  photoisomerization takes place by both direct ( $^1\pi\pi^*$ ) and sensitized ( $^3\pi\pi^*$ ) routes; furthermore, excitation to the  $^1\pi\pi^*$  state causes a relatively strong fluorescence. Instead, for  $E\text{-DBBPE}^{2+}$  irradiation on the  $^1\pi\pi^*$  absorption band gives rise to a very weak fluorescence, and causes a photocycloaddition reaction rather than a photoisomerization (Figure 5.29). These results can be again rationalized by considering the change in the nature of  $S_1$  in going from the methyl to the benzyl substituted compound. The  $\pi$ -electron cloud in the  $S_1$  state, owing to its CT character, is much more delocalized in  $E\text{-DBBPE}^{2+}$  than it is in  $E\text{-DMBPE}^{2+}$ . This different electronic distribution not only causes a consistent decrease of the radiative rate constant in going from  $E\text{-DMBPE}^{2+}$  to  $E\text{-DBBPE}^{2+}$  (vide supra), but also influences the non-radiative pathways. Indeed, in  $E\text{-DMBPE}^{2+}$  a direct efficient photoisomerization occurs, while irradiation on the  $^1\pi\pi^*$  absorption band of  $E\text{-DBBPE}^{2+}$  causes a cycloaddition reaction with a small quantum yield rather than isomerization (Table 5.4). In  $E\text{-DBBPE}^{2+}$  a quite efficient photoisomerization occurs via triplet sensitization. This indicates a different mechanism of  $E \rightarrow Z$  photoisomerization, i.e. a direct process through the singlet manifold for  $E\text{-DMBPE}^{2+}$  and a sensitized one through the triplet manifold for  $E\text{-DBBPE}^{2+}$ , in analogy to what observed for stilbene.<sup>151</sup>

The relevant photophysical processes concerning the compounds  $\text{DMBPE}^{2+}$  and  $\text{DBBPE}^{2+}$  in their  $E$ -isomer are shown in Figure 5.29.

The electrochemical data reported below are referred to derivatives of the 1,2-bis(4-pyridinium)ethylene in the  $E$  isomeric form, which is that stable under normal conditions.

---

[151] (a) G. Orlandi, G. Marconi, *Chem. Phys.*, 1975, 8, 458; G. Orlandi, G. Marconi, *Il Nuovo Cimento*, 1981, 63B, 332.

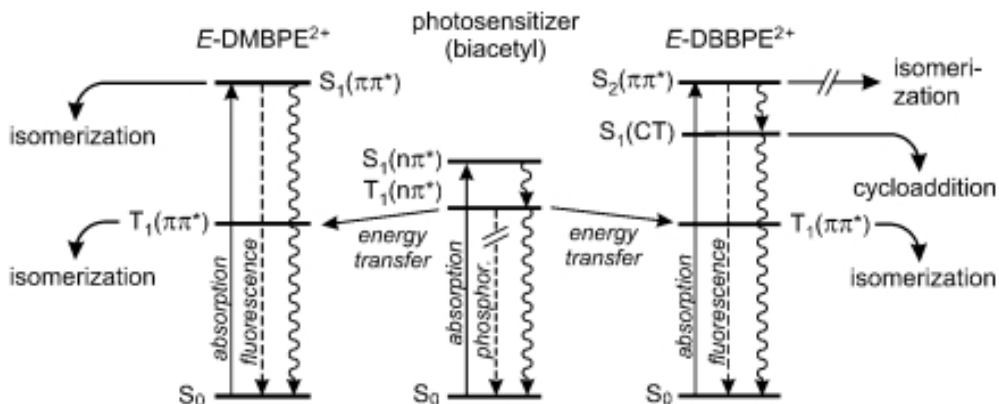


Figure 5.29. Simplified energy-level diagram of the photophysical and photochemical processes that take place in  $E\text{-DMBPE}^{2+}$  and  $E\text{-DBBPE}^{2+}$ . The wavy lines represent non radiative processes.

The electrochemical behavior of the methyl and benzyl derivatives of  $E\text{-1,2-bis(4-pyridinium)ethylene}$ , characterized by two consecutive reversible, and mono-electronic reduction processes, is very similar to that of the analogous  $4,4'$ -bipyridinium cations (Table 5.4.). It is, however, interesting to note that the first reduction takes place at potential values more negative, while the opposite occurs as far as the second reduction is concerned (Figure 5.24.). This finding can be understood by considering that in the  $E\text{-1,2-bis(4-pyridinium)ethylene}$  derivatives the two pyridinium rings, being separated by a double bond, are expected to be less electronically coupled than in the case of the  $4,4'$ -bipyridinium analogues, in which the two pyridinium rings are directly linked. As a consequence, the first electron added to the  $E\text{-1,2-bis(4-pyridinium)ethylene}$  derivatives is less delocalized than in the  $4,4'$ -bipyridinium ones, making the first reduction more difficult. For the same reason, the second electron added to the  $E\text{-1,2-bis(4-pyridinium)ethylene}$  derivatives is not much destabilized by the presence of the first electron, thereby making the second reduction easier than in the case of the  $4,4'$ -bipyridinium analogues.

As for the  $4,4'$ -bipyridinium family, the halfwave potential values of  $E\text{-DBBPE}^{2+}$ , are positively shifted in comparison to those obtained for  $E\text{-DMBPE}^{2+}$  (Table 5.4.). This positive

shift can be interpreted on the basis of the considerations made for the analogous 4,4'-bipyridinium derivative.

In the case of  $E$ -DBBPE<sup>2+</sup>, the monoreduced species has also been obtained in spectroelectrochemical experiments. This species is stable in the dark and in carefully deoxygenated solutions, and displays a very characteristic absorption spectrum that confers a pink color to the solution (Figure 5.30.).

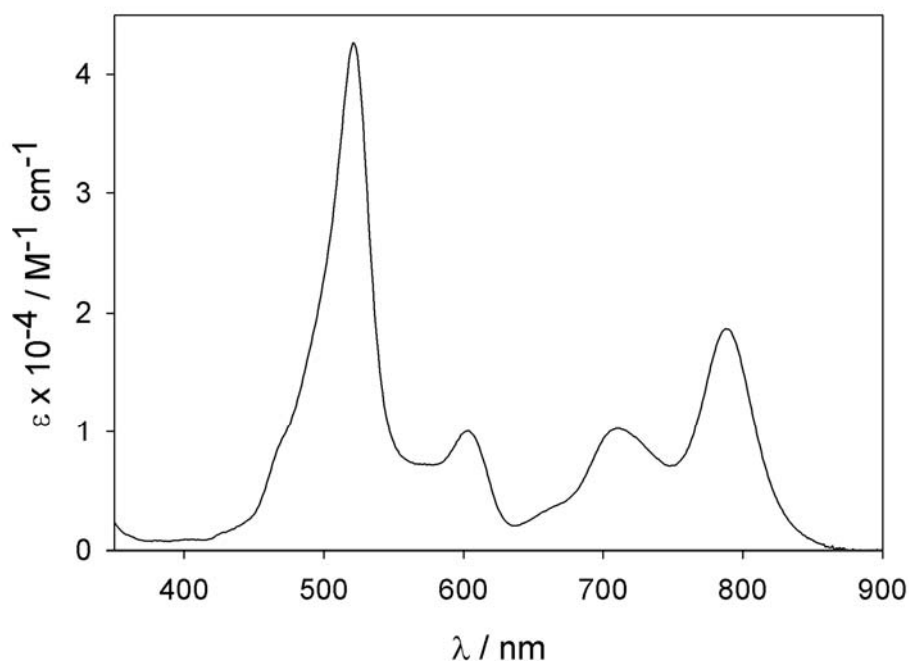


Figure 5.30. Absorption spectrum of the monoreduced  $E$ -DBBPE<sup>+</sup> species (argon-purged AN, room temperature).

#### *Derivatives of 2,7-diazapyrenium*

The UV-visible spectroscopic data for the  $N,N$ -dimethyl-, -didecanyl- and -dibenzyl derivatives of the 2,7-diazapyrenium unit in AN solution at room temperature and in BN glass at 77 K are gathered in Table 5.5.

The absorption spectra of all the investigated DAP<sup>2+</sup> derivatives exhibit (Figure 5.31.) three intense and structured bands which can be assigned to transitions to the first, second, and

third singlet  $\pi\pi^*$  excited states, respectively. The absorption bands of  $\text{DBDAP}^{2+}$  are slightly red shifted with respect to those of the parent alkyl-substituted species.

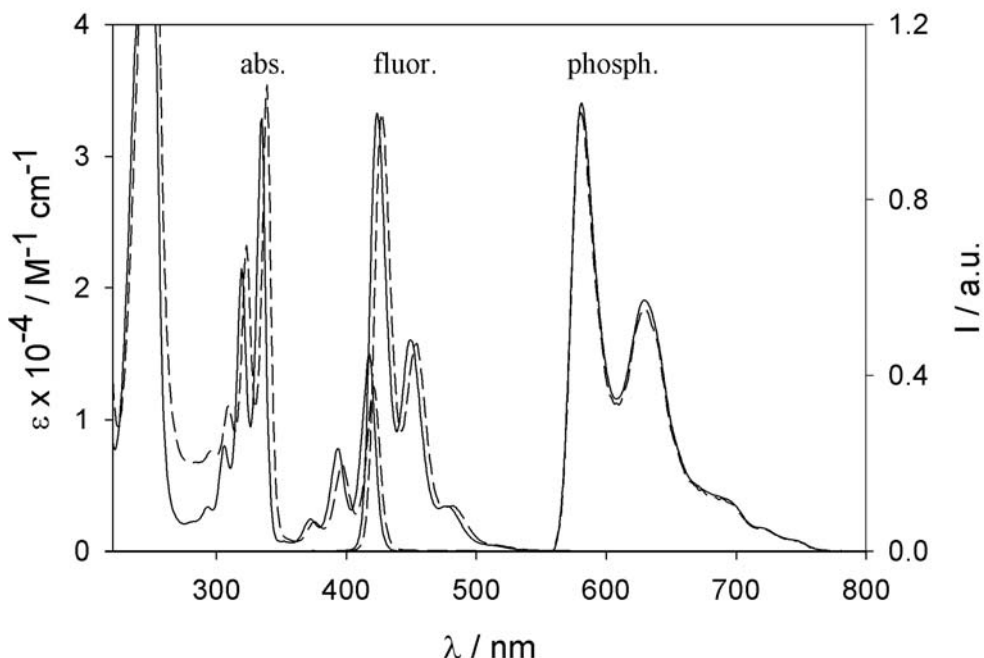


Figure 5.31. Absorption and fluorescence spectra (AN, room temperature,  $\lambda_{\text{exc}} = 390 \text{ nm}$ ), and phosphorescence spectra (BN, 77 K,  $\lambda_{\text{exc}} = 390 \text{ nm}$ ) of  $\text{DMDAP}^{2+}$  (—) and  $\text{DBDAP}^{2+}$  (---). All the luminescence spectra are normalized at the maximum intensity.

The compounds of the  $\text{DAP}^{2+}$  family are most interesting for their luminescence properties:<sup>152</sup> they exhibit a very intense and structured fluorescence band with a lifetime in the ns time scale (Table 5.5.); at 77 K, besides fluorescence, a structured phosphorescence band can also be seen (Figure 5.31.).

From an analysis of the radiative ( $k_r$ ) and total ( $k_t$ ) deactivation rate constants collected in Table 5.6., it can be noticed that for the compounds of the 4,4'-bipyridinium and  $\text{BPE}^{2+}$  families the main deactivation channel of the emitting state is due to non-radiative processes which depend essentially on the molecular structure of the compounds. This does not hold true

[152] A. M. Brun, A. Harriman, *J. Am. Chem. Soc.*, 1991, 113, 8153.

for the  $\text{DAP}^{2+}$ -based species, for which  $k_f$  is comparable with  $k_r$ . The highly condensed and rigid  $\text{DAP}^{2+}$  moiety is strongly emissive because of lack of torsion around single or double bonds — processes that represent major energy sinks for the bipyridinium- and  $\text{BPE}^{2+}$ -type species. In the case of the  $\text{DAP}^{2+}$ -based compounds a non-radiative channel may be identified with the population of a suitable  $T_n$  triplet state, followed by  $T_n \rightarrow T_1$  conversion and eventual phosphorescence. The difference in fluorescence quantum yield and lifetime values between the alkylated and benzylated compounds can be ascribed to a more efficient intersystem crossing to a  $T_n$  state in the case of  $\text{DBDAP}^{2+}$ . Indeed, for this compound the calculations show the presence of a triplet level nearly isoenergetic with  $S_1$ , and this can be taken as a hint for a very fast intersystem crossing process.

The 2,7-diazapyrenium derivatives (Figure 5.20.) are characterized by a large, flat and electron-poor surface.<sup>153</sup> While their photophysical behavior is similar to that of pyrene, the electrochemical properties resemble, but are not as nice as, those of the 4,4'-bipyridinium dications. They show indeed a first reduction process that is monoelectronic and reversible, like that exhibited by the 4,4'-bipyridinium analogues, and a second reduction process, which is irreversible and characterized by a low current intensity, most probably because of the chemical instability of the reduced species.<sup>135</sup> For this reason it has been considered only the halfwave potential values concerning the first reduction process. The data gathered in Table 5.5. show that the dimethyl,  $\text{DMDAP}^{2+}$ ,<sup>135,135</sup> and the didecanyl,  $\text{DCDAP}^{2+}$ , derivatives undergo the first reduction at a potential very similar to that of the corresponding 4,4'-bipyridinium derivatives. Moreover, in agreement with the results obtained for the two previously discussed families of compounds, and for the same reasons, in going to the dibenzyl derivative,  $\text{DBDAP}^{2+}$ , a shift of the first reduction potential towards less negative values is observed.

---

[153] (a) A. J. Blacker, J. Jazwinski, J.-M. Lehn, *Helv. Chim. Acta*, 1987, 70, 1, and references therein; (b) E. F. Lier, S. Hünig, H. Quast, *Angew. Chem. Int. Ed. Engl.*, 1968, 7, 814.

It has been attempted to obtain the monoreduced form of the 2,7-diazapyrenium derivatives by using a variety of techniques (chemical reduction, electrolysis, radiation chemistry), but the results of these bulk reduction experiments could not be rationalized because they are highly dependent on the experimental conditions (solvent, light, time, etc.), confirming that the monoreduced forms of such derivatives are extremely reactive species.

Table 5.3. Photophysical and electrochemical properties of 1,1'-derivatives of 4,4'-bipyridinium.<sup>a</sup>

compound	Absorption		fluorescence r. t.			fluorescence 77 K		phosphorescence 77 K		Electrochemistry	
	$\lambda_{\max}^1$	$\epsilon_{\max}^2$	$\lambda_{\max}^1$	$\tau^3$	$\Phi_{\text{em}}$	$\lambda_{\max}^1$	$\tau^3$	$\lambda_{\max}^1$	$\tau^4$	$E^{\text{I}}_{1/2}{}^5$	$E^{\text{II}}_{1/2}{}^5$
	MV <sup>2+</sup>	260 <sup>b</sup>	20000 <sup>b</sup>	353 <sup>c</sup>	0.9 <sup>c</sup>	0.02 <sup>c</sup>	330	7	418 <sup>d,e</sup>	3600	-0.43 <sup>f</sup>
DOV <sup>2+</sup>	264	24500	353	1	$9 \times 10^{-3}$					-0.42 <sup>g</sup>	-0.87 <sup>g</sup>
DBV <sup>2+</sup>	260	20000	—	—	—	—	—	—	—	-0.35 <sup>h</sup>	-0.78 <sup>h</sup>
(DO) <sub>2</sub> V <sup>2+</sup>	259	29000	—	—	—					-0.37	-0.79
(DI) <sub>2</sub> V <sup>2+</sup>	261	25400	—	—	—					-0.34	-0.77

<sup>1</sup> nm;

<sup>2</sup> M<sup>-1</sup>cm<sup>-1</sup>;

<sup>3</sup> ns;

<sup>4</sup> ms;

<sup>5</sup> V vs. SCE;

<sup>a</sup> absorption and fluorescence spectra were performed at room temperature on air equilibrated AN solutions. Fluorescence and phosphorescence spectra at 77 K were recorded on BN rigid matrices. Electrochemical studies were performed in argon-purged AN solution at room temperature; tetraethylammonium hexafluorophosphate as supporting electrolyte;

<sup>b</sup> from ref. [138];

<sup>c</sup> in good agreement with the data from ref. [136], where it is reported that the same results were obtained on a solution saturated with the chloride salt. The authors reported also a very weak emission in H<sub>2</sub>O with  $\lambda_{\text{max}} = 345$  nm,  $\tau < 3$  ps;

<sup>d</sup> structured band;

<sup>e</sup> highest energy feature;

<sup>f</sup> from ref. [154];

<sup>g</sup> tosylate counterion;

<sup>h</sup> from ref. [132,155].

---

[154] P. L. Anelli, P. R. Ashton, R. Ballardini, V. Balzani, M. Delgado, M. T. Gandolfi, T. T. Goodnow, A. E. Kaifer, D. Philp, M. Pietraszkiewicz, L. Prodi, M. V. Reddington, A. M. Z. Slawin, N. Spencer, J. F. Stoddart, C. Vincent, D. J. Williams, *J. Am. Chem. Soc.*, **1992**, *114*, 193.

[155] D. B. Amabilino, P.R. Ashton, V. Balzani, C. L. Brown, A. Credi, J. M. J. Fréchet, J. W. Leon, F. M. Raymo, N. Spencer, J. F. Stoddart, M. Venturi, *J. Am. Chem. Soc.*, **1996**, *118*, 12012.

Table 5.4. Photophysical, photochemical and electrochemical properties of N,N-derivatives of *E*-1,2-bis(4-pyridinium)ethylene.<sup>a</sup>

Compound	Absorption		fluorescence r. t.			Fluorescence 77 K		phosphorescence 77 K		photochemistry		electrochemistry	
	$\lambda_{\max}^1$	$\epsilon_{\max}^2$	$\lambda_{\max}^1$	$\tau^3$	$\Phi$	$\lambda_{\max}^1$	$\tau^3$	$\lambda_{\max}^1$	$\tau^4$	$\Phi_{\text{dir}}^b$	$\Phi_{\text{sens}}^b$	$E^{1/2}{}^5$	$E^{1/2}{}^5$
<i>E</i> -DMBPE <sup>2+</sup>	317	42000	365	<1 <sup>c</sup>	0.015	345 <sup>d,e</sup>	1.2	—	—	0.35 <sup>f</sup>	—	-0.50	-0.72
<i>E</i> -DBBPE <sup>2+</sup>	324 <sup>g</sup>	42000 <sup>g</sup>	372 <sup>g</sup>	<1	6×10 <sup>-4</sup> <sup>g</sup>	352 <sup>d,e</sup>	1.2	—	—	8×10 <sup>-4</sup> <sup>g,h</sup>	0.4 <sup>g,i</sup>	-0.44 <sup>g</sup>	-0.64 <sup>g</sup>

<sup>1</sup> nm;

<sup>2</sup> M<sup>-1</sup>cm<sup>-1</sup>;

<sup>3</sup> ns;

<sup>4</sup> ms;

<sup>5</sup> V vs. SCE;

<sup>a</sup> absorption and fluorescence spectra and photochemical experiments with direct irradiation were performed at room temperature on air equilibrated AN solutions. The solutions used for photosensitized reactions are degassed by the freeze-pump-thaw method. Fluorescence and phosphorescence spectra at 77 K are recorded on BN rigid matrices. Electrochemical studies are performed in argon-purged AN solution at room temperature; tetraethylammonium hexafluorophosphate as supporting electrolyte;

<sup>b</sup> quantum yield values extrapolated at  $t = 0$ ;

<sup>c</sup>  $\tau = 50$  ps reported in ref. [148].

<sup>d</sup> structured band;

<sup>e</sup> highest energy feature;

<sup>f</sup>  $E \rightarrow Z$  photoisomerization, from ref. [147];

<sup>g</sup> from ref. [132];

<sup>h</sup> the photoproduct is a cyclobutene derivative;

<sup>i</sup>  $E \rightarrow Z$  photoisomerization using biacetyl as sensitizer.

Table 5.5. Photophysical and electrochemical properties of N,N-derivatives of 2,7-diazapyrenium.<sup>a</sup>

compound	absorption		fluorescence r. t.			fluorescence 77 K		phosphorescence 77 K		electrochemistry	
	$\lambda_{\max}^1$	$\epsilon_{\max}^2$	$\lambda_{\max}^1$	$\tau^3$	$\Phi$	$\lambda_{\max}^1$	$\tau^3$	$\lambda_{\max}^1$	$\tau^4$	$E^{\text{I}}_{1/2}^5$	$E^{\text{II}}_{1/2}^5$
	DMDAP <sup>2+</sup> <sup>b</sup>	335 <sup>c</sup> 418 <sup>c</sup>	33000 15000	423 <sup>c,d</sup>	10.4	0.60	424 <sup>c,d</sup>	10.7	586 <sup>c,d</sup>	900	-0.46
DCDAP <sup>2+</sup>	336 <sup>c</sup> 418 <sup>c</sup>	20600 8300	424 <sup>c,d</sup>	9.5	0.5	428 <sup>c,d,f</sup>	7.7 <sup>f</sup>	585 <sup>c,d,f</sup>	580 <sup>f</sup>	-0.45	<i>e</i>
DBDAP <sup>2+</sup> <sup>b</sup>	341 <sup>c</sup> 421 <sup>c</sup>	35000 12500	427 <sup>c,d</sup>	4.3	0.28	427 <sup>c,d</sup>	10.5	580 <sup>c,d</sup>	750	-0.41	<i>e</i>

<sup>1</sup> nm;

<sup>2</sup> M<sup>-1</sup>cm<sup>-1</sup>;

<sup>3</sup> ns;

<sup>4</sup> ms;

<sup>5</sup> V vs. SCE;

<sup>a</sup> absorption and fluorescence spectra have been performed at room temperature on air equilibrated AN solutions. Fluorescence and phosphorescence spectra at 77 K have been recorded on BN rigid matrices. Electrochemical studies have been performed in argon-purged AN solution at room temperature; tetraethylammonium hexafluorophosphate as supporting electrolyte;

<sup>b</sup> ref. [135];

<sup>c</sup> structured band;

<sup>d</sup> highest energy feature;

<sup>e</sup> Irreversible process;

<sup>f</sup> in a 1:1 AN-BN rigid matrix.

Table 5.6. Calculated photophysical properties (ZINDO/S) for some of the investigated compounds.

compound	$E(S_1)^{1,a}$	$f^b$	$E(T_n)^{1,c}$	$k_r \times 10^{-8} \text{ s}^{-1,d}$	$k_t \times 10^{-10} \text{ s}^{-1,e}$
MV <sup>2+</sup>	34600	0.01	28410	0.02	0.1
DBV <sup>2+</sup>	23580	0.04	22570	0.2	> 45
<i>E</i> -DMBPE <sup>2+</sup>	28250	1.58	27700	8.4	5.6
<i>E</i> -DBBPE <sup>2+</sup>	24510	0.18	24210	1.3	22.7
DMDAP <sup>2+</sup>	24510	0.31	23640	0.82	0.01
DBDAP <sup>2+</sup>	24450	0.28	24390	0.74	0.03

<sup>1</sup> cm<sup>-1</sup>;

<sup>2</sup> s<sup>-1</sup>;

<sup>a</sup> energy of the lowest excited singlet state;

<sup>b</sup> S<sub>1</sub> oscillator strength;

<sup>c</sup> energy of the low-lying triplet state closest to S<sub>1</sub>;

<sup>d</sup> radiative deactivation rate constant of the emitting state;

<sup>e</sup> total deactivation rate constant of the emitting state.

### 5.2.2. Charge-Pooling Dendrimers

The dendrimers studied in this section, **B9**<sup>18+</sup> and **B21**<sup>42+</sup> (Figure 5.32.), are based on a 1,3,5-trisubstituted benzenoide core, contain 9 and 21, respectively, 4,4'-bipyridinium dication (usually called viologen) units in their branches, and 6 and 12, respectively, aryloxy groups in the periphery.<sup>156</sup> Viologen, as presented in the previous section 5.2.1., is a well known electro-active species that undergoes two successive, one-electron, reversible reduction processes and exhibits peculiar spectroscopic features in both its dicationic and radical-cationic forms. Viologen units are also known to give strong donor-acceptor complexes with electron-donor species.

Electrochemical and photosensitized reduction of dendrimers **B9**<sup>18+</sup> and **B21**<sup>42+</sup> as hexafluorophosphate salts is reported. For comparison purposes, the properties of the 1,1'-dibenzyl-4,4'-bipyridinium (**dbV**<sup>2+</sup>) and 1,1'-dioctyl-4,4'-bipyridinium (**doV**<sup>2+</sup>) mono-viologen compounds, and of dendron **B2**<sup>4+</sup>, which contains two viologen units (Figure 5.32.) have been investigated.

The results obtained are discussed in comparison with those previously reported for two analogous dendrimers (**A9**<sup>18+</sup> and **A21**<sup>42+</sup>, Figure 5.32.) terminated with tetraarylmethane bulky moieties instead of aryloxy groups.<sup>157</sup> The properties of dendron **B2**<sup>4+</sup> (Figure 5.32.), analogous of **A2**<sup>4+</sup>, have also been investigated to complete the comparison between the two families of compounds.

---

[156] C. M. Ronconi, J. F. Stoddart, V. Balzani, M. Baroncini, P. Ceroni, C. Giansante, M. Venturi, to be submitted.

[157] F. Marchioni, M. Venturi, P. Ceroni, V. Balzani, M. Belohradsky, A.M. Elizarov, H.R. Tseng, L.F. Stoddart, *Chem. Eur. J.* 2004, 10, 6361-6368.

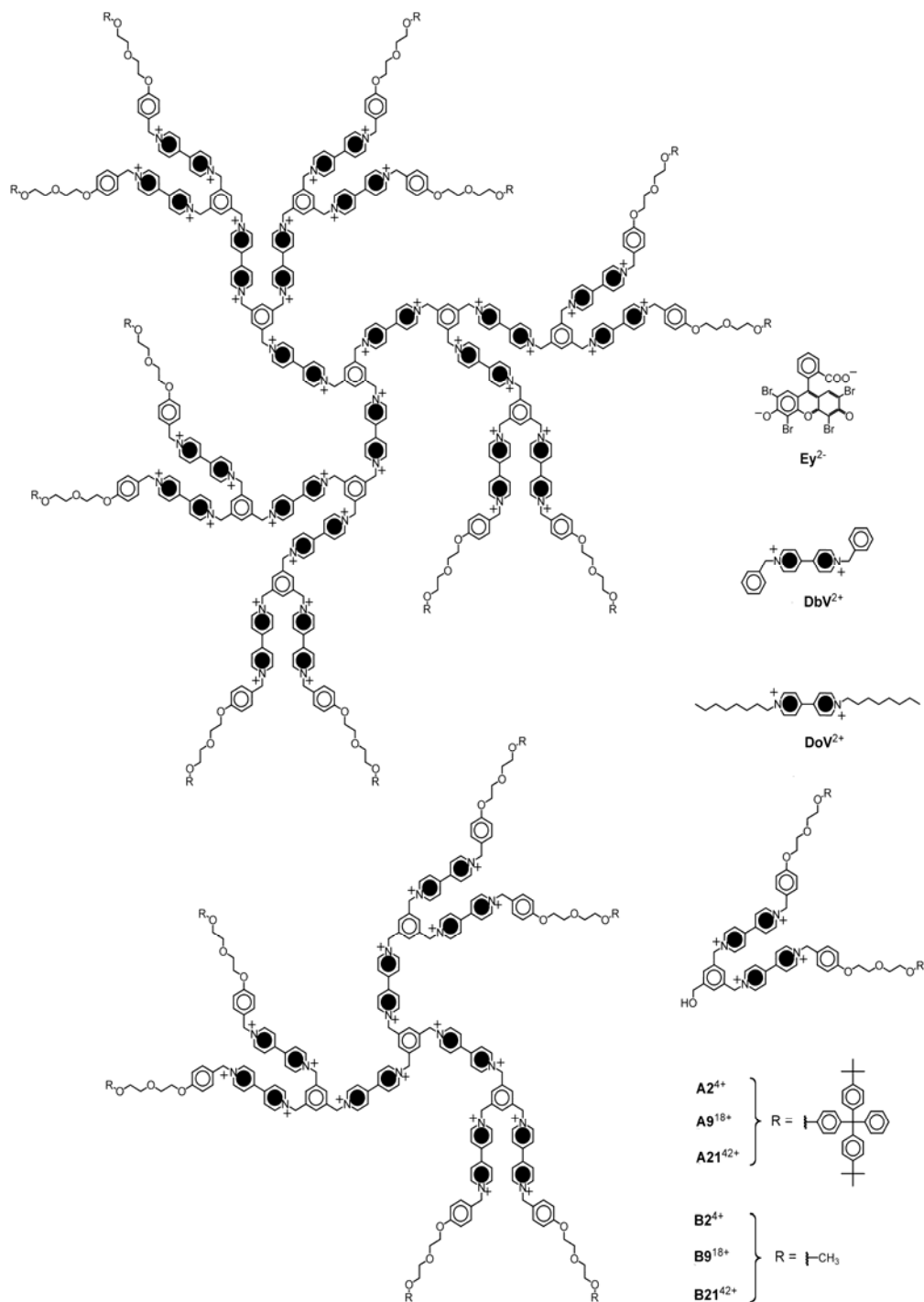


Figure 5.32. Formulas of the examined compounds. The  $A_n^{2n+}$  and  $B_n^{2n+}$  symbols used indicate the number of the viologen units contained in the dendritic structure ( $n$ ) and, as a superscript, the overall electric charge ( $2n$ ) of each compound.

*Electrochemical reduction*

Electrochemical experiments have been carried out in argon-purged MeCN solutions. The half-wave potential values, the number of exchanged electrons, and the diffusion coefficients of **dbV**<sup>2+</sup> and dendrimers **B9**<sup>18+</sup> and **B21**<sup>42+</sup> are listed in Table 5.7., where the results previously obtained<sup>157</sup> for dendrimers **A9**<sup>18+</sup> and **A21**<sup>42+</sup> are also reported for comparison purposes.

Table 5.7. Half-wave reduction potentials, numbers of exchanged electrons, and diffusion coefficients in argon-purged MeCN solution, 298 K.

	$E_{1/2}^{I,1.[a]}$	$E_{1/2}^{II,1.[a]}$	$n_{el}^{[b]}$	$n^{[c]}$	$D^2$
<b>dbV</b> <sup>2+</sup>	-0.35	-0.77	1	1	1.60
<b>B9</b> <sup>18+</sup>	-0.30	-0.78 <sup>[d]</sup>	6	9	0.45
<b>B21</b> <sup>42+</sup>	-0.30	-0.73 <sup>[d]</sup>	11	21	0.27
<b>A9</b> <sup>18+[e]</sup>	-0.29	-0.75 <sup>[d]</sup>	5	9	0.32
<b>A21</b> <sup>42+[e]</sup>	-0.30	-0.76 <sup>[d]</sup>	14	21	0.27

<sup>1</sup> V vs SCE;

<sup>2</sup>  $10^5 \times \text{cm}^2 \text{s}^{-1}$

<sup>a</sup> working electrode glassy carbon, supporting electrolyte TBAPF<sub>6</sub>;

<sup>b</sup> number of exchanged electrons obtained by chronoamperometric experiments (estimated error  $\pm$  20%);

<sup>c</sup> overall number of viologen units present in the compound as confirmed by the eosin complexation experiments;

<sup>d</sup> process affected by adsorption. half-wave potential values estimated by DPV measurements;

<sup>e</sup> from Ref. [157].

Compounds **dbV**<sup>2+</sup>, **B9**<sup>18+</sup>, and **B21**<sup>42+</sup> exhibit the two reduction processes typical of viologens. Cyclic voltammetric patterns show that the reducible viologen units of each dendrimer are equivalent and that the first reduction is reversible with nernstian behavior in all cases (Figure 5.33.), whereas the second process (particularly for **B21**<sup>42+</sup>) is affected by adsorption of the reduced species on the electrode.

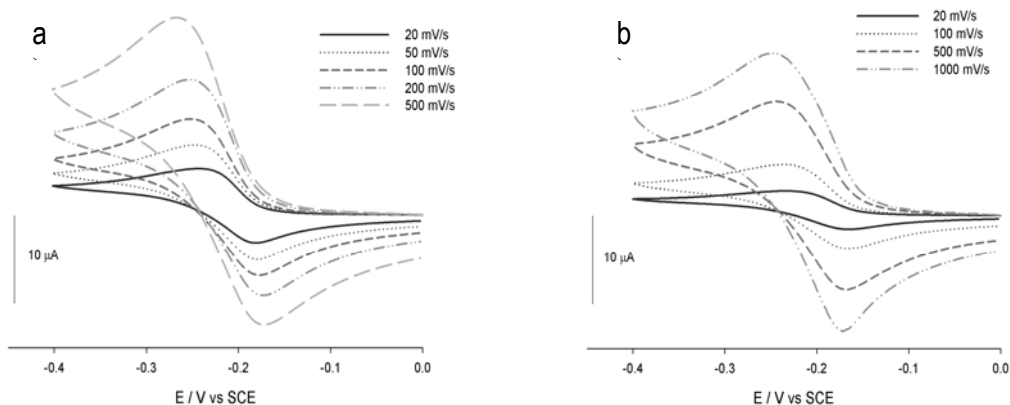


Figure 5.33. Cyclic voltammetric behavior as a function of sweep rate for the first reduction process of a) dendrimer **B9**<sup>18+</sup> ( $1.2 \times 10^{-4}$  M) and b) dendrimer **B21**<sup>42+</sup> ( $7 \times 10^{-5}$  M). Argon-purged MeCN solutions, working electrode glassy carbon, supporting electrolyte TBAPF<sub>6</sub> (0.1 M).

The diffusion coefficients and the number of exchanged electrons have been measured (Table 5.7.) from chronoamperometric experiments performed at the potential value of the first reduction process by using ultramicroelectrodes.<sup>158</sup> As expected, the diffusion coefficient of **B9**<sup>18+</sup> is larger than that of **B21**<sup>42+</sup>. For both dendrimers the number of exchanged electrons is smaller than that expected on the basis of the number of the viologens contained in the structure. Apparently, only the external viologen units, 6 for **B9**<sup>18+</sup> and 12 for **B21**<sup>42+</sup>, can be reduced in electrochemical experiments.

[158] G. Denuault, M.V. Mirkin, A.J. Bard, *J. Electroanal. Chem.* 1991, 308, 27-38.

Unfortunately spectroelectrochemical experiments aimed at obtaining the absorption spectra of the reduced compounds could not be performed because of adsorption of the reduced species on the platinum minigrad used as working electrode.

The electrochemical reduction experiments have shown that in each dendrimer, the first reduction process of all its reducible viologen units occurs at the same potential and that the first reduction process of all the reducible viologen units of all dendrimers occurs at the same potential. An interesting result is that the reduction potential of a reducible unit is not affected by the state of the other reducible units, which is an ideal property for a charge pooling system. Another result that emerges clearly from the data obtained is that the nature of the peripheral groups (tetraarylmethane and aryloxy units for the **A**-type and **B**-type families, respectively) affects neither the number of reducible viologen units nor the first reduction potential. Two concomitant effects can be taken into account to explain the lack of complete electrochemical reduction: (i) upon reduction of the external viologen shell, the structure of the dendrimer shrinks, favoured by dimerization of the reduced units, thereby preventing the internal viologen units to “see” the electrode, and (ii) the internal viologens being engaged in tight ionic couples with the hexafluorophosphate counter-anions become more difficult to reduce, thereby preventing electron-hopping from external to internal viologen units.

#### *Photosensitized reduction*

It is well known that one-electron reduction of viologen compounds can be conveniently performed by using suitable photosensitizers in the presence of sacrificial reductants. Light excitation leads the photosensitizer to a long-lived excited state that can transfer an electron to a viologen during an encounter. The back electron-transfer reaction between the oxidized photosensitizer and the reduced viologen is prevented by fast reduction of the oxidized photosensitizer by the sacrificial reductant. This kind of photoinduced processes have been

extensively exploited for photogeneration of hydrogen from aqueous solutions,<sup>159</sup> as well as to power artificial molecular devices and machines.<sup>160</sup>

Previous investigations<sup>157</sup> showed that the photochemical reduction of viologen compounds can be efficiently performed in degassed  $\text{CH}_2\text{Cl}_2$  solution by using 9-methylanthracene as a photosensitizer and triethanolamine (TEOA) as a sacrificial reductant. Pictorial representation of the photoreduction mechanism follows.

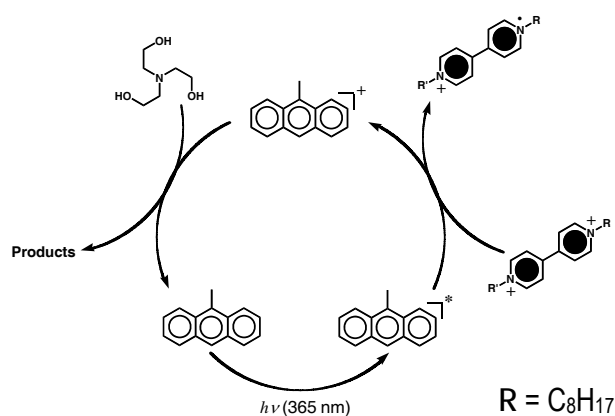


Figure 5.34. Light excitation of 9-methylanthracene in  $\text{CH}_2\text{Cl}_2$  solution in the presence of TEOA causes the reduction of  $\text{DoV}^{2+}$  to its monomeric radical cation  $\text{DoV}^{\bullet+}$  (Table 5.8., inset of Figure 5.35).

[159] See, e.g.: a) E. Amouyal, *Sol. Energy Mater. Sol. Cells* 1995, 38, 249-276; b) V. Balzani, A. Credi, M. Venturi, *Molecular Devices and Machines: Concepts and Perspectives for the Nanoworld*, Wiley-VCH, Weinheim, 2008, Ch. 7 and references therein.

[160] a) V. Balzani, A. Credi, F.M. Raymo, J.F. Stoddart, *Angew. Chem. Int. Ed.* 2000, 39, 3349-3391; b) R. Ballardini, V. Balzani, A. Credi, M.T. Gandolfi, M. Venturi, *Acc. Chem. Res.* 2001, 34, 445-455; c) V. Balzani, *Photochem. Photobiol. Sci.* 2003, 2, 459-476; d) V. Balzani, A. Credi, B. Ferrer, S. Silvi, M. Venturi, *Top. Curr. Chem.* 2005, 262, 1-27; e) V. Balzani, A. Credi, S. Silvi, M. Venturi, *Chem. Soc. Rev.* 2006, 35, 1135-1149; f) W.R. Browne, B.L. Feringa, *Nature Nanotechnology* 2006, 1, 25-35; g) R. Ballardini, A. Credi, M.T. Gandolfi, F. Marchioni, S. Silvi, M. Venturi, *Photochem. Photobiol. Sci.* 2007, 6, 345-356; h) E.R. Kay, D.A. Leigh, F. Zerbetto, *Angew. Chem. Int. Ed.* 2007, 46, 72-191; i) M.M. Pollard, M. Klok, D. Pijper, B.L. Feringa, *Adv. Funct. Mater.* 2007, 17, 718-729; j) V. Balzani, A. Credi, M. Venturi, *Molecular Devices and Machines: Concepts and Perspectives for the Nanoworld*, Wiley-VCH, Weinheim, 2008.

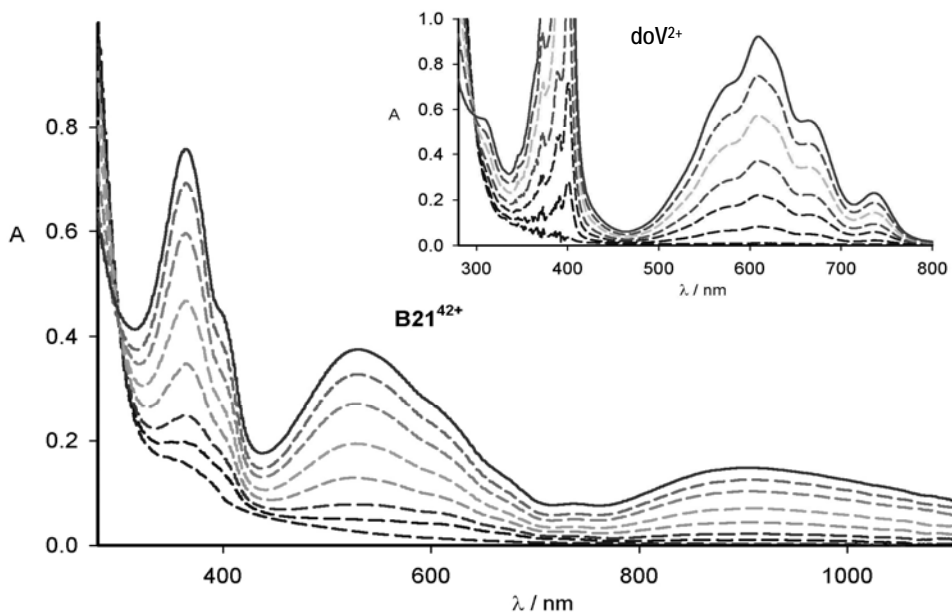


Figure 5.35: Spectral changes (optical path = 1 cm) observed upon irradiation with 365-nm light of a degassed  $\text{CH}_2\text{Cl}_2$  solution containing  $1.2 \times 10^{-4}$  M of 9-methylanthracene,  $5.0 \times 10^{-2}$  M of TEOA and  $4.0 \times 10^{-6}$  M of  $\text{B2I}^{42+}$  or (inset)  $6.7 \times 10^{-5}$  M of  $\text{doV}^{2+}$ . The solid line corresponds to the photostationary state. A solution containing  $1.2 \times 10^{-4}$  M of 9-methylanthracene was used as reference.

Figure 5.35. shows the spectral changes observed upon irradiation with 365-nm light of a degassed  $\text{CH}_2\text{Cl}_2$  solution containing 9-methylanthracene ( $1.2 \times 10^{-4}$  M), TEOA ( $5.0 \times 10^{-2}$  M), and  $\text{B2I}^{42+}$  ( $4.0 \times 10^{-6}$  M). The spectral features that arise upon irradiation are characteristics of the formation of both monomeric and dimeric reduced viologen species; similar changes are obtained for dendrimer  $\text{B9}^{18+}$ . The total number of electrons exchanged by dendrimers  $\text{B9}^{18+}$  and  $\text{B2I}^{42+}$  at the photostationary state (Table 5.8.), determined from absorbance measurements, is slightly lower than that obtained in chronoamperometric experiments. This discrepancy can be attributed to small amounts of oxidizing impurities

contained in the solvent and/or the samples used or, most probably, to underestimation of the dimer concentration because of the  $\epsilon$  values used refer to a different solvent.<sup>161</sup>

Spectra recorded at different irradiation time showed that the fraction of monomeric and dimeric reduced-viologen species changes with time (Figure 5.36.). At the photostationary state, dendrimer **B9**<sup>18+</sup> shows a prevalence of dimerized (ca. 57%) over monomeric (ca. 43%) viologen units; for dendrimer **B21**<sup>42+</sup>, the fraction of dimerized viologen units is slightly lower.

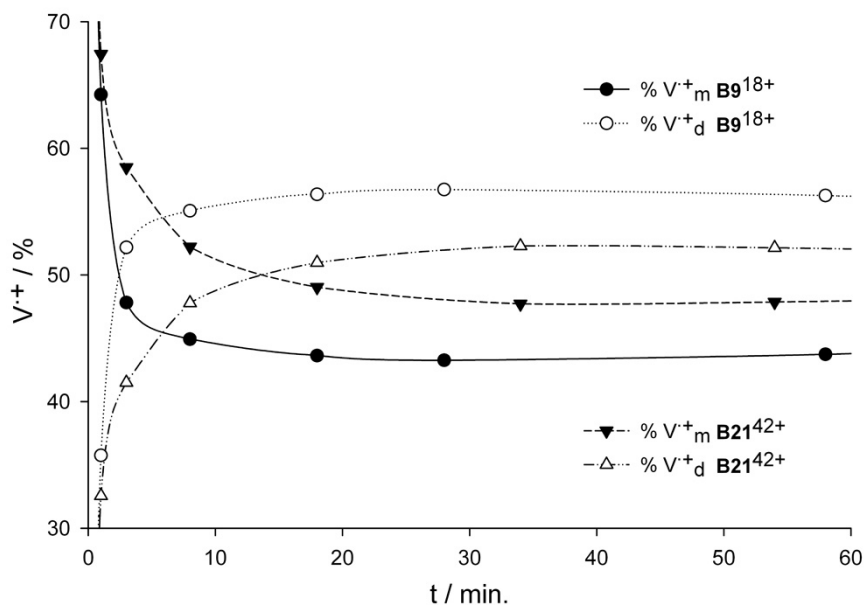


Figure 5.36: Changes in the percentages of the monomeric ( $V_m^{+}$ , solid symbols) and dimerized ( $V_d^{+}$ , open symbols) monoreduced viologen units on increasing irradiation time for the dendrimers **B9**<sup>18+</sup> (circles) and **B21**<sup>42+</sup> (triangles).

For comparison purposes we have performed the photochemical reduction of dendrons **B2**<sup>4+</sup> and **A2**<sup>4+</sup> (Table 5.8.) finding that (i) the number of reducible viologen units is slightly

[161] W. Geuder, S. Hunig, A. Suchy, *Tetrahedron* 1986, 42, 1665-1677.

lower than expected and (ii) the percentage of dimerization is low and almost unaffected by the nature of the stoppers.

Table 5.8. Ratio between dimerized ( $V_d^{+}$ ) and monomeric ( $V_m^{+}$ ) monoreduced viologen units, percentages of the total monoreduced viologen units ( $V_{tot}^{+}$ ) and numbers of exchanged electrons ( $n_{phot}$ ) at the photostationary state.<sup>a</sup>

	$V_d^{+}/V_m^{+}$	% $V_{tot}^{+}$	$n_{phot}^b$	$n^c$
<b>doV<sup>2+</sup></b>	0	100	1.0	1
<b>B2<sup>4+</sup></b>	0.15	75	1.5	2
<b>B9<sup>18+</sup></b>	1.32	53	4.7	9
<b>B2I<sup>42+</sup></b>	1.10	41	8.5	21
<b>A2<sup>4+</sup></b>	0.21	72	1.4	2
<b>A9<sup>18+[d]</sup></b>	0.85	48	4.3	9
<b>A2I<sup>42+[d]</sup></b>	0.82	60	12.6	21

<sup>a</sup> degassed  $CH_2Cl_2$  solution, irradiation with 365-nm light, 9-methylanthracene  $1.2 \times 10^{-4}$  M, TEOA  $5.0 \times 10^{-2}$  M;

<sup>b</sup> estimated error  $\pm 20\%$ ;

<sup>c</sup> overall number of viologen units present in compounds as confirmed by the eosin complexation experiments;

<sup>d</sup> adjusted from Ref. [157].

The monomer ( $\alpha$ ) and dimer ( $\omega$ ) concentrations of the monoreduced viologen units were determined from the absorbance at 605 and 537 nm ( $A_{605}$  and  $A_{537}$ , respectively) by using Equations (33) and (34):

$$\alpha = (A_{605} \varepsilon_{537} - A_{537} \varepsilon_{605}) / (\varepsilon_{605} \varepsilon_{537} - \varepsilon_{537} \varepsilon_{605}) \quad (34)$$

$$\omega = (A_{537} \varepsilon_{605} - A_{605} \varepsilon_{537}) / (\varepsilon_{605} \varepsilon_{537} - \varepsilon_{537} \varepsilon_{605}) \quad (35)$$

in which  $\varepsilon_{537}$  and  $\varepsilon_{605}$  represent the molar absorption coefficients of the dimer at the two selected wavelengths; their values have been taken from the literature<sup>161</sup> and correspond to 29000 and 2350  $\text{M}^{-1} \text{cm}^{-1}$ , respectively. For  $\varepsilon_{605}$  and  $\varepsilon_{537}$ , the molar absorption coefficients of the monomer, the values used were 14000 and 5770  $\text{M}^{-1} \text{cm}^{-1}$ , respectively, in agreement with those reported in ref. 151. The concentration of the dimerized one electron-reduced viologen units corresponds to  $2 \times \omega$ .

The electrochemical and photosensitization experiments performed on the **A**-type and **B**-type dendrimers have evidenced that (Tables 5.7. and 5.8.) in all cases only a fraction of the viologen units can be reduced. Within the experimental error, this fraction corresponds to the number of the viologen units present in the outer shell (6 for **A9**<sup>18+</sup> and **B9**<sup>18+</sup>, 12 for **A21**<sup>42+</sup> and **B21**<sup>42+</sup>).

The fact that the number of reducible viologen units is smaller than expected cannot be attributed to lack of branches in the structures of the dendrimers because the results obtained for eosin complexation (see next Section) clearly show that the examined compounds do contain 9 (**A9**<sup>18+</sup> and **B9**<sup>18+</sup>) and 21 (**A21**<sup>42+</sup> and **B21**<sup>42+</sup>) viologen units, in agreement with the NMR and mass spectra characterization.

The photosensitized reduction experiments have shown that the numbers of viologen units reducible under the photochemical conditions are in fair agreement with those obtained by

chronoamperometric experiments, confirming that only the viologens of the external shell can be reduced. The photosensitized experiments have also revealed that formation of the one-electron reduced viologen units is accompanied by their dimerization reaction. The lack of reduction of all the viologen units in such experiments can be explained considering that (i) the uncharged photosensitizer cannot displace the counter-ions assembled in proximity of the highly charged core of the dendrimer, and (ii) the interaction between the photosensitizer and the internal viologen units can be prevented by the dimerization of the external reduced units that shrinks the dendrimer structure. It has been also evidenced that dimerization is not a strongly favoured process as shown by the fact that it does not occur for the monoviologen  $\text{doV}^{2+}$  species and leads to only 15-20 % of associated species in the case of dendrons  $\text{B2}^{4+}$  and  $\text{A2}^{4+}$  which are structurally preorganized to give dimerization (Table 5.8.). In the case of the dendrimers, the fraction of dimerized viologen units is higher (about 45% and 57% for the **A**-type and **B**-type families, respectively), as expected because of the possibility to give dimers also between reduced units belonging to different dendrons. The results also show that the bulky tetraarylmethane peripheral moieties disfavour formation of dimers compared with the smaller aryloxy groups.

In principle, polyviologen dendrimers can behave as molecular batteries<sup>157,162,163</sup> being potentially capable of storing at easy accessible potential values a number of electrons twice

---

[162] a) S. Heinen, L. Walder, *Angew. Chem. Int. Ed.* 2000, 39, 806-809; b) S. Heinen, W. Meyer, L. Walder, *J. Electroanal. Chem.* 2001, 498, 34-43.

[163] a) N. Ardoin, D. Astruc, *Bull. Soc. Chim. Fr.* 1995, 132, 875-909; b) M.R. Bryce, W. Devonport, in *Advances in Dendritic Macromolecules* (Ed.: G.R. Newkome), JAI Press, London, 1996, Vol. 3, p. 115-149; c) C. Gorman, *Adv. Mater.* 1998, 10, 295-309; d) V. Balzani, S. Campagna, G. Denti, A. Juris, S. Serroni, M. Venturi, *Acc. Chem. Res.* 1998, 31, 26-34; e) I. Cuadrado, M. Morán, C.M. Casado, B. Alonso, J. Losada, *Coord. Chem. Rev.* 1999, 193-195, 395; f) M.B. Nielsen, C. Lomholt, J. Becher, *Chem. Soc. Rev.* 2000, 29, 153-164; g) D. Astruc, *Acc. Chem. Res.* 2000, 33, 287-298; h) S. Serroni, S. Campagna, F. Puntotiero, C. Di Pietro, N.D. McClenaghan, F. Loiseau, *Chem. Soc. Rev.* 2001, 30, 367-375; i) B. Alonso, D. Astruc, J.-C. Blais, S. Nlate, S. Rigaut, J. Ruiz, V. Sartor, C. Valério, *C.R. Acad. Sci. Paris, Chimie* 2001, 4, 173-180; j) A. Juris, M. Venturi, P. Ceroni, V. Balzani, S. Campagna, S. Serroni, *Collect. Czech. Chem. Commun.*, 2001, 66, 1-32; k) A. Juris, in *Electron Transfer in Chemistry* (Ed.: V. Balzani),

that of the viologen units. Although it has been reported that in dendrimers very similar to those here described all the viologen units are reducible,<sup>162</sup> our results clearly show that only a fraction of such units can be reduced and throw light on the reasons why charge-pooling is incomplete and on the role played by the terminal groups.

The fact that the number of reducible viologen units is smaller than expected cannot be attributed to lack of branches in the structures of the dendrimers because the results obtained for eosin complexation clearly show that the examined compounds do contain 9 (**A9**<sup>18+</sup> and **B9**<sup>18+</sup>) and 21 (**A21**<sup>42+</sup> and **B21**<sup>42+</sup>) viologen units.

Photosensitized reduction experiments evidence that for both the **A**-type and **B**-type families of dendrimers a fraction of the monoreduced viologen units undergoes dimerization and that such a process prevails for the dendrimers in which the bulky tetraarylmethane terminal groups have been removed.

Moreover, it has been evidenced a clear dendrimer effect on the dimerization process involving the reduced viologen units. The dendritic structure of compounds **B9**<sup>18+</sup>, **B21**<sup>42+</sup>, **A9**<sup>18+</sup>, and **A21**<sup>42+</sup> provides an environment capable of favouring dimerization because it forces the reduced viologen units to occupy close positions and is flexible enough to enable the interactions not only between the reduced units belonging to the same branch (intra-dendron interactions), but also between the reduced units contained in different branches (inter-dendron interactions).

---

Wiley-VCH, Weinheim, 2001, Vol. 3, p. 655-714; l) D. Astruc, F. Chardac, *Chem. Rev.* 2001, 101, 2991-3031; m) C.B. Gorman, *C.R. Acad. Sci. Paris, Chimie*, 2003, 6, 911-918.

### 5.2.3. Dendrimers as Hosts

As mentioned in section 5.2.1., 4,4'-bipyridinium units are also known to give strong donor-acceptor complexes with electron-donor species: 4,4'-bipyridinium dications strongly interact with the dianionic form of eosin, **Ey**<sup>2-</sup> (Figure 5.32. in the previous section) to yield charge-transfer (CT) complexes.<sup>164,165</sup> It has been previously observed that addition of **DoV**<sup>2+</sup> as hexafluorophosphate salt (shown in Figure 5.32.), to a CH<sub>2</sub>Cl<sub>2</sub> solution of **Ey**<sup>2-</sup>, as tetrabutylammonium salt, causes (i) noticeable perturbations in the visible absorption band of **Ey**<sup>2-</sup>, and (ii) complete quenching of its fluorescence because of the formation of a strong 1:1 complex ( $K_{\text{ass}} > 10^6 \text{ M}^{-1}$ ).<sup>164</sup>

At first, dendrimers spectroscopic properties have been analyzed. Figure 5.37. shows the absorption spectra in acetonitrile of dendrimers **B9**<sup>18+</sup> and **B21**<sup>42+</sup> compared with the spectra of **DoV**<sup>2+</sup> (also shown in Figure 5.32.) taken as model compound of the dendrimer viologen units, at concentrations respectively 9 and 21 times higher than those of **B9**<sup>18+</sup> and **B21**<sup>42+</sup>. It is evident that the absorption spectra of the dendrimers are not identical to that of the model compound, and that the differences are much more pronounced in the case of **B21**<sup>42+</sup>. In particular, its spectrum is less intense than that of the model compound in the spectral region around the maximum and shows broad and weak absorption features, also present to a minor extent in the spectrum of **B9**<sup>18+</sup>, that emerge from the low-energy tail of the intense UV band.

Investigated dendrimers do not exhibit luminescence as discussed in section 5.2.1.

---

[164] F. Marchioni, M. Venturi, A. Credi, V. Balzani, M. Belohradsky, A.M. Elizarov, H.R. Tseng, J.F. Stoddart, *J. Am. Chem. Soc.* 2004, 126, 568-573.

[165] I. Willner, Y. Eichen, M. Rabinovitz, R. Hoffman, S. Cohen, *J. Am. Chem. Soc.* 1992, 114, 637-644.

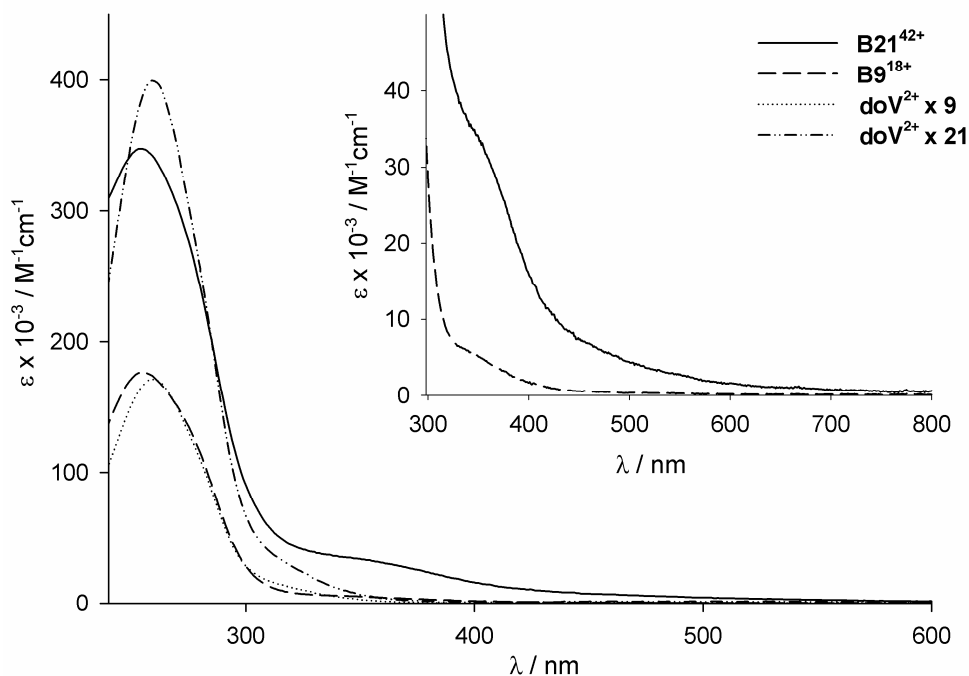


Figure 5.37. Absorption spectra in MeCN of dendrimers **B9<sup>18+</sup>** (dashed line) and **B21<sup>42+</sup>** (solid line) compared with the spectra of 9 (dotted line) and 21 (dashed and dotted line) **DoV<sup>2+</sup>** units. Inset: enlarged view ( $\lambda$  above 300 nm) of the spectra of the dendrimers.

The results obtained in this section will now be discussed and compared with those previously reported<sup>164</sup> for similar dendrimers terminated with bulky tetraarylmethane groups (compounds **A9<sup>18+</sup>** and **A21<sup>42+</sup>**).

The absorption spectra of dendrimers **B9<sup>18+</sup>** and **B21<sup>42+</sup>** are different, particularly in the case of **B21<sup>42+</sup>**, from the spectrum of **DoV<sup>2+</sup>**. The differences can derive from the fact that (i) **DoV<sup>2+</sup>** is not a fully satisfactory model, at least from a spectroscopic viewpoint, for the viologen units contained in the dendritic structure (it has to be noticed that **DbV<sup>2+</sup>** represents an even worst model compound than **DoV<sup>2+</sup>**). Each unit in the dendrimer, in fact, shares benzyl groups with other units (Figure 5.32.) and some benzyl groups carry bismethyleneoxy substituents, and (ii) charge-transfer (CT) interactions originate between the

electron-acceptor viologen units and the proximate (through bond) or remote (through space) electron-donor aryloxy units, as suggested by the appearance of an absorption tail for  $\lambda > 320$  nm.

The previously studied dendrimers **A9**<sup>18+</sup> and **A21**<sup>42+</sup> exhibited a similar behavior; a quantitative analysis shows, however, that **A21**<sup>42+</sup> has an absorption derived by CT interactions that is less intense (about one half) and shifted towards lower energy compared to **B21**<sup>42+</sup>. These results show that the terminal stoppers play some role in determining the spectroscopic properties of such dendrimers.

Fluorescent titration experiments have been performed to study the interaction between **Ey**<sup>2-</sup> and dendrimers **B9**<sup>18+</sup> and **B21**<sup>42+</sup>. The experimental data obtained by titrating CH<sub>2</sub>Cl<sub>2</sub> solutions of **B9**<sup>18+</sup> and **B21**<sup>42+</sup> (each containing ca.  $1 \times 10^{-5}$  M viologen units) with a solution of **Ey**<sup>2-</sup> (Figure 5.38.) show that the eosin fluorescence signal appears only when the number of added **Ey**<sup>2-</sup> exceeds the number of viologen units contained in each dendrimer. These results demonstrate that compounds **B9**<sup>18+</sup> and **B21**<sup>42+</sup> are capable of quenching the fluorescence of 9 and 21 eosin dianions, respectively, which means that each viologen unit of the dendrimers associates with one eosin dianion. Titration of dendron **B2**<sup>4+</sup> ( $9.0 \times 10^{-6}$  M viologen units) confirms the stoichiometric formation of 1:1 complexes between the viologen units and eosin (Figure 5.38.). The quenching of the eosin fluorescence by association with the quencher (static mechanism) is confirmed by the fact that dynamic quenching can be ruled out considering the short lifetime ( $\tau = 3.8$  ns) of the eosin excited state and the low concentration ( $< 5 \times 10^{-5}$  M) of the quencher.

It has been found that both the **A**-type and **B**-type dendrimers are able to host a number of eosin dianions equal to the number of viologen units present in their branches. This result shows that neither the dendrimer generation nor the nature of the peripheral groups plays a role in the formation of the complexes between viologen and eosin moieties. Clearly, eosin

anions can penetrate in the interior of the positively charged dendrimers, replacing the  $\text{PF}_6^-$  counter ions. The dendrimers can be viewed as polyvalent scaffolds with a well-defined number of independent seats where single eosin dianions can be hosted.

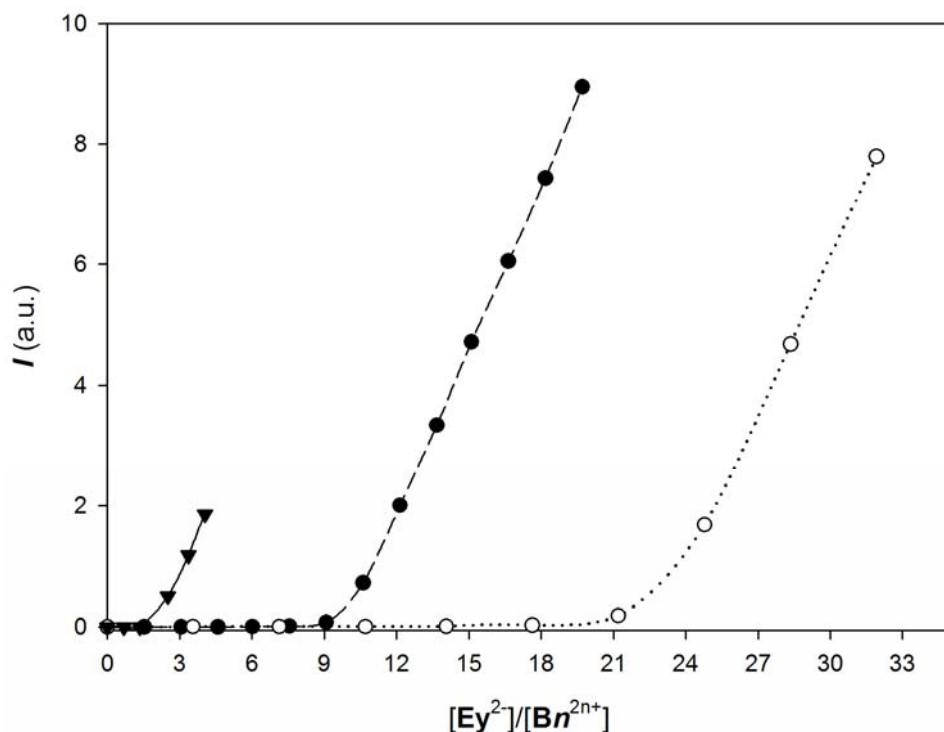


Figure 5.38. Fluorescent titration experiments performed in  $\text{CH}_2\text{Cl}_2$  solutions. Diagram of the intensity of the eosin  $\text{Ey}^{2-}$  fluorescence band ( $\lambda_{\text{ex}} = 500 \text{ nm}$ ;  $\lambda_{\text{em}} = 560 \text{ nm}$ ) as a function of the  $[\text{Ey}^{2-}]/[\text{Bn}^{2n+}]$  ratio:  $\text{B2}^{4+}$  (solid triangles);  $\text{B9}^{18+}$  (solid circles);  $\text{B21}^{42+}$  (open circles).

Continuing the work on polyviologen dendrimers it has been found that these compounds independently of the nature and bulkiness of the terminal groups ( $\text{A9}^{18+}$ ,  $\text{A21}^{42+}$ ,  $\text{B9}^{18+}$ , and  $\text{B21}^{42+}$ ) can act as polytopic receptors toward electron-donor substrates hosting a number of eosin dianions equal to the number of viologen units present in their branches (Figure 5.39.). The data obtained clearly show that the host-guest interactions, that drive complex formation in low polar medium, are not affected by either the steric hindrance of the

terminal groups or the electronic interactions that such groups establish with the viologen units. These results are of interest for the design and construction of dendrimers capable of performing functions related to drug delivery or sensing applications.

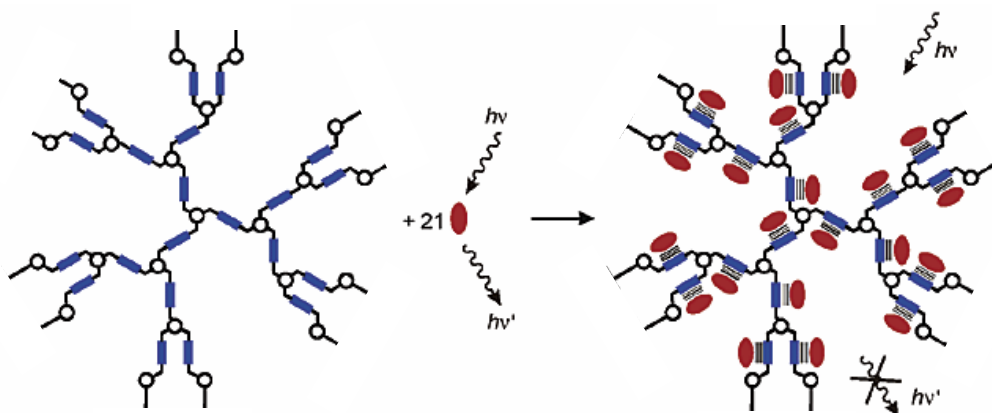


Figure 5.39. Graphical representation of B21<sup>42+</sup> as a polytopic receptor in CH<sub>2</sub>Cl<sub>2</sub> solutions: each viologen unit (blue rectangle) interact with an eosin E<sub>y</sub><sup>2-</sup> molecule (red oval) quenching the latter luminescence.

### 5.2.4. Dendrimers as Guests

Because of their constitutional order, dendrimers can contain selected chemical units in predetermined sites of their structure (core, branches, periphery). Dendrimers containing redox-active<sup>166</sup> units are currently attracting much attention for a variety of applications which include electrochemical sensors,<sup>167</sup> redox catalysts<sup>168</sup> and molecular batteries.<sup>169</sup> Dendrimers with a single redox site as a core are the simplest examples of systems with an encapsulated redox center<sup>170</sup> and their redox properties are usually modulated by the size and nature of the dendritic branches.<sup>171</sup>

Because of their large structures, dendrimers are extensively used as host molecules for a variety of metal ions<sup>172</sup> (section 5.1.1.) or molecules<sup>173</sup> (section 5.2.3.). This concept has been

- 
- [166] (a) Astruc, D.; Daniel, M.-C.; Ruiz, J. *Chem. Commun.* 2004, 2637; (b) Astruc, D. *Pure Appl. Chem.* 2003, 75, 461; (c) Venturi, M.; Ceroni, P. *C. R. Chimie* 6 2003, 935; (d) Cameron, C. S.; Gorman, C. B. *Adv. Funct. Mat.* 2002, 12, 17; (e) Campagna, S.; Di Pietro, C.; Loiseau, F.; Maubert, B.; McClenaghan, N. D.; Passalacqua, R.; Puntoriero, F.; Ricevuto, V.; Serroni, S. *Coord. Chem. Rev.* 2002, 229, 67.
- [167] (a) Daniel, M.-C.; Ruiz, J.; Astruc, D. *Inorg. Chem.* 2004, 43, 8649; (b) Daniel, M.-C.; Ruiz, J.; Blais, J.-C.; Daro, N.; Astruc, D. *Chem. Eur. J.* 2003, 9, 4371; (c) Daniel, M.-C.; Ruiz, J.; Astruc, D. *J. Am. Chem. Soc.* 2003, 125, 1150.
- [168] Kim, E.; Kim, K.; Yang, H.; Kim, Y. T.; Kwak, J. *Anal. Chem.* 2003, 75, 5665.
- [169] (a) Ruiz, J.; Pradet, C.; Varret, F.; Astruc, D. *Chem. Commun.* 2002, 1108; (b) Nlate, S.; Ruiz, J.; Sartor, V.; Navarro, R.; Blais, J.-C.; Astruc, D. *Chem. Eur. J.* 2000, 6, 2544.
- [170] (a) Gorman, C. B.; Smith, J. C. *Acc. Chem. Res.* 2001, 34, 60; (b) Cardona, C.M.; Mendoza, S.; Kaifer, A. E. *Chem. Soc. Rev.* 2000, 29, 37.
- [171] See, e.g.: (a) Chasse, T. L.; Gorman, C. B. *Langmuir* 2004, 20, 8792; (b) Marchioni, F.; Venturi, M.; Credi, A.; Balzani, V.; Belohradsky, M.; Elizarov, A. M.; Tseng, H.-R.; Stoddart, J. F. *J. Am. Chem. Soc.* 2004, 126, 568; (c) McClenaghan, N. D.; Passalacqua, R.; Loiseau, F.; Campagna, S.; Verheyde, B.; Hameurlaine, A.; Dehaen, W. *J. Am. Chem. Soc.* 2003, 125, 5356; (d) Rio, Y.; Accorsi, G.; Armaroli, N.; Felder, D.; Levillain, E.; Nierengarten, J.-F. *Chem. Commun.* 2002, 2830.
- [172] See, e.g.: (a) Cross, J. P.; Lauz, M.; Badger, P. D.; Petoud, S. *J. Am. Chem. Soc.* 2004, 126, 16278; (b) Nakajima, R.; Tsuruta, M.; Higuchi, M.; Yamamoto, K. *J. Am. Chem. Soc.* 2004, 126, 1630; (c) Vögtle, F.; Gorke, M.; Vicinelli, V.; Ceroni, P.; Maestri, M.; Balzani, V. *ChemPhysChem* 2001, 12, 769; (d) Zhou, L.; Russell, D. H.; Zhao, M.; Crooks, R. M. *Macromol.* 2001, 34, 3567.

further elaborated by incorporating single specific binding sites within the dendrimer, e.g. a cyclophane<sup>174</sup> or a cyclam<sup>175</sup> unit as a core. Dendrimers that can host metal ions or small molecules mimic in some way the behavior of proteins.

In spite of their large structures, dendrimers can also be involved as guests in molecular recognition phenomena.<sup>176</sup> In such cases, the host species does not interact with the whole dendritic structure, but only with specific component units. Usually, the dendrimer-guest behavior is connected with the threading of dendritic branches by ring-shaped molecules.<sup>177,178,179</sup> Particularly active in this field is the group of Kaifer and co-workers who have prepared several dendrimers containing a single site as potential guest unit and have investigated their adducts with  $\beta$ -cyclodextrin, cucurbituril, and bis-para-phenylene-34-crown-10.<sup>180</sup>

---

[173] See e.g.: (a) Broeren, M. A. C.; van Dongen, J. L. J.; Pittelkow, M.; Chrisensen, J. B.; van Genderen, M. H. P. Meijer, E. W. *Angew. Chem. Int. Ed.* 2004, 43, 3557; (b) Yamaguchi, T.; Ishii, N.; Tashiro, K.; Aida, T. *J. Am. Chem. Soc.* 2003, 125, 13934; (c) Morgan, M. T.; Carnahan, M. A.; Immoos, C. E.; Ribeiro, A. A.; Finkelstein, S.; Lee, S. J.; Grinstaff, M. W. *J. Am. Chem. Soc.* 2003, 125, 15485; (d) Balzani, V.; Ceroni, P.; Gestermann, S.; Gorka, M.; Kauffmann, C.; Vögtle, F. *Tetrahedron* 2002, 58, 629; (e) Dykes, G. M.; Brierley, L. J.; Smith, D. K.; McGrail, P. T.; Seeley, G. *Chem. Eur. J.* 2001, 7, 4730.

[174] Diederich, F.; Felber, B. *Proc. Nat. Acad. Sci.* 2002, 99, 4778.

[175] (a) Bergamini, G.; Ceroni, P.; Balzani, V.; Cornelissen, L.; van Heyst, J.; Lee, S.-K.; Vögtle, F. *J. Mater. Chem.* 2005, 15, 2959; (b) Saudan, C.; Balzani, V.; Gorka, M.; Lee, S.-K.; van Heyst, J.; Maestri, M.; Ceroni, P.; Vicinelli, V.; Vögtle, F. *Chem. Eur. J.* 2004, 10, 899; (c) Saudan, C.; Balzani, V.; Gorka, M.; Lee, S.-K.; Maestri, M.; Vicinelli, V.; Vögtle, F. *J. Am. Chem. Soc.*, 2003, 125, 4424; (d) Enoki, O.; Imaoka, T.; Yamamoto, K. *Org. Lett.* 2003, 5, 2547.

[176] Ong, W.; Gómez-Kaifer, M.; Kaifer, A. E. *Chem. Commun.* 2004, 1677.

[177] Gibson, H. W.; Yamaguchi, N.; Hamilton, L.; Jones, J. W. *J. Am. Chem. Soc.* 2002, 124, 4653.

[178] van Bommel, K. J. C.; Metselaar, G. A.; Verboom, W.; Reinhoudt, D. N. *J. Org. Chem.* 2001, 66, 5405.

[179] Lee, J. W.; Ko, Y. H.; Park, S.-H.; Yamaguchi, K.; Kim, K. *Angew. Chem., Int. Ed.* 2001, 40, 746.

[180] (a) Ong, W.; Grindstaff, J.; Sobransingh, D.; Toba, R.; Quintela, J. M.; Peinador, C.; Kaifer, A. E. *J. Am. Chem. Soc.* 2005, 127, 3353; (b) Moon, M.; Grindstaff, J.; Sobransingh, D.; Kaifer, A. E. *Angew. Chem. Int. Ed.* 2004, 43, 5496; (c) Ong, W.; Kaifer, A. E. *Angew. Chem. Int. Ed.* 2003, 42, 2164; (d) Toba, R.; Quintela, J. M.; Peinador, C.; Román, E.; Kaifer, A. E. *Chem. Commun.* 2002, 1768.

When the potential guest unit constitutes the core of a symmetric dendrimer, host-guest formation requiring threading of ring-shaped hosts cannot take place. It has been recently shown<sup>181</sup> that in such a case suitable tweezer-shaped molecules can be used to clip the dendritic core in dichloromethane solution.<sup>182</sup>

Investigations have been extended to the host-guest systems obtained upon complexation of a tweezer-shaped receptor with two families of dendrimers. The tweezer-shaped molecule used (**T** in Figure 5.40.) comprises a naphthalene and four benzene components bridged by four methylene units and exhibits electron donating properties.<sup>183</sup> The investigated dendrimers (Figure 5.40.) consist of an electron acceptor 4,4'-bipyridinium core with appended one (unsymmetric dendrimers,  $\text{DnB}^{2+}$ )<sup>184</sup> or two (symmetric dendrimers,  $(\text{Dn})_2\text{B}^{2+}$ )<sup>185</sup> first, second, and third generation 1,3-dimethyleneoxybenzene (Fréchet-type) dendrons. Association is thermodynamically driven by electron donor-acceptor interactions.

The assembling process has been investigated by NMR and UV/VIS absorption and fluorescence spectroscopy and electrochemical measurements. Association constants have been measured, demonstrating that the assembling/disassembling process can be controlled by redox stimulation, and obtaining some interesting information on the structure of the host-guest species and the dynamics of their formation.

---

[181] Balzani, V.; Ceroni, P.; Giansante, C.; Vicinelli, V.; Klärner, F.-G.; Verhaelen, C.; Vögtle, F.; Hahn, U. *Angew. Chem. Int. Ed.* 2005, 44, 4574.

[182] For a somewhat related gas-phase study of these systems, see: Schalley, C.A.; Verhaelen, C.; Klärner, F.-G.; Hahn, U.; Vögtle, F. *Angew. Chem. Int. Ed.* 2005, 44, 477.

[183] (a) Klärner, F.-G.; Kahlert, B. *Acc. Chem. Res.* 2003, 36, 919; (b) Marchioni, F.; Juris, A.; Lobert, M.; Seelbach, U. P.; Kahlert, B.; Klärner, F.-G. *New J. Chem.* 2005, 29, 780.

[184] V. Balzani, H. Bandmann, P. Ceroni, C. Giansante, U. Hahn, Frank-Gerrit Klärner, W. M. Müller, U. Müller, C. Verhaelen, V. Vicinelli, F. Vögtle, *J. Am. Chem. Soc.*, 2006, 128, 637.

[185] Ceroni, P.; Vicinelli, V.; Maestri, M.; Balzani, V.; Müller, W. M.; Müller, U.; Hahn, U.; Osswald, F.; Vögtle, F. *New J. Chem.* 2001, 25, 989.

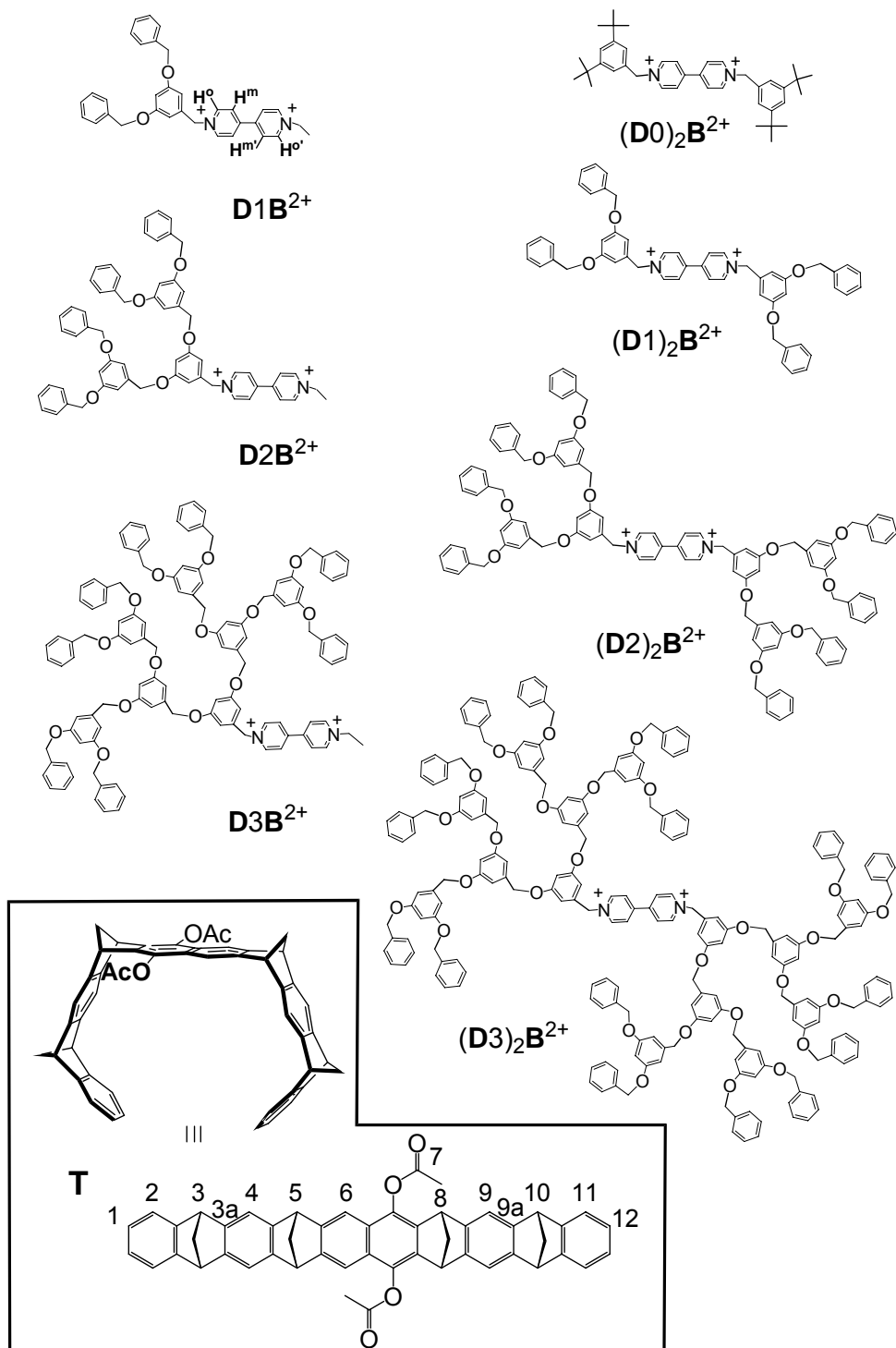


Figure 5.40. Formulas of the investigated compounds: D stays for dendron, n indicates the dendron generation ( $n=1,2,3$ ), and  $B^{2+}$  stays for the 4,4'-bipyridinium core.

The absorption and emission spectra of the host **T** in dichloromethane solution are shown in Figure 5.41. The relatively weak, low energy absorption bands are typical of the naphthalene chromophoric group.

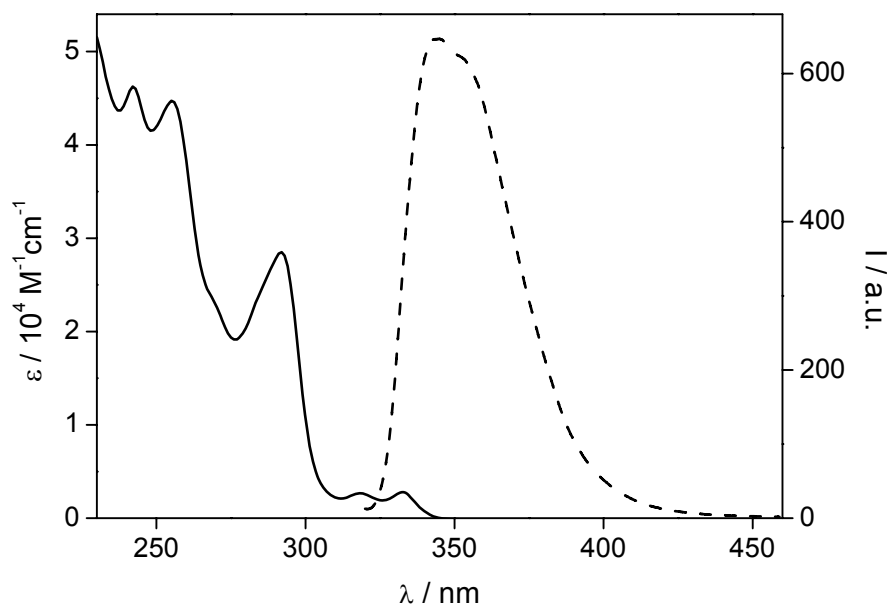


Figure 5.41.. Absorption (solid line) and emission (dashed line,  $\lambda_{\text{ex}} = 280 \text{ nm}$ ) spectra of an air-equilibrated solution of the tweezer-shaped receptor **T** at room temperature.

The strong fluorescence band with  $\lambda_{\text{max}} = 344 \text{ nm}$ ,  $\tau = 9.5 \text{ ns}$ ,  $\Phi = 0.53$  can also be assigned to the naphthalene unit.

In dichloromethane/acetonitrile 9:1 solution, tweezer-shaped molecule **T** shows an irreversible oxidative process at +1.6 V, whereas no reduction process has been observed in the potential window of the solvent used (up to -2.0 V vs. SCE).

The investigated dendrimers contain three types of chromophoric groups, namely 4,4'-bipyridinium, 1,3-dimethylenedioxybenzene, and benzene. The ratios among these three types of groups are different in each dendrimer: the two limiting cases are 1:1:1 for **DIB**<sup>2+</sup> and

1:14:16 for  $(\mathbf{D3})_2\mathbf{B}^{2+}$ . The 4,4'-bipyridinium species exhibit a strong absorption band around 260 nm (4,4'-dimethylbipyridinium:  $\lambda_{\max} = 259$  nm,  $\epsilon = 20700$  M<sup>-1</sup> cm<sup>-1</sup>; 4,4'-dibenzylbipyridinium:  $\lambda_{\max} = 259$  nm,  $\epsilon = 22700$  M<sup>-1</sup> cm<sup>-1</sup>), while 1,3-dimethylenedioxybenzene shows a relatively weak absorption band around 275 nm ( $\epsilon = 2200$  M<sup>-1</sup> cm<sup>-1</sup>)<sup>186</sup> and benzene a very weak band at 255 nm ( $\epsilon = 250$  M<sup>-1</sup> cm<sup>-1</sup>). As previously reported for the symmetric  $(\mathbf{D}_n)_2\mathbf{B}^{2+}$  dendrimers,<sup>185</sup> the absorption spectra of the unsymmetric ones (see, e.g.,  $\mathbf{D1B}^{2+}$  in Figure 5.42.) do not coincide with the summation of the spectra of the component units, particularly because of the presence of a broad and weak absorption tail above 300 nm that is assigned to a charge-transfer (CT) transition from 1,3-dimethylenedioxybenzene electron-donor units to the 4,4'-bipyridinium electron-acceptor core.

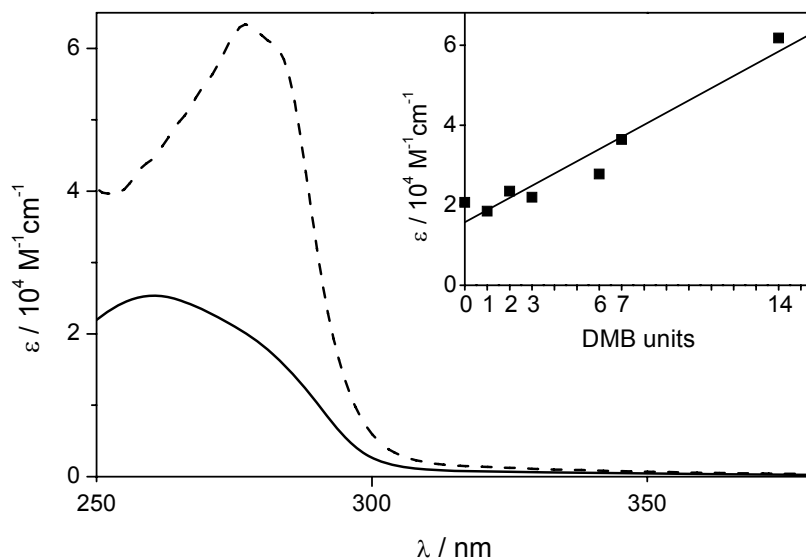


Figure 5.42. Absorption spectra of  $\mathbf{D1B}^{2+}$  (solid line) and of  $(\mathbf{D3})_2\mathbf{B}^{2+}$  (dashed line) in air-equilibrated acetonitrile/dichloromethane 1:1 v/v solution at room temperature. Inset shows molar absorption coefficients of the dendrimers at 280 nm versus the number ( $n$ ) of dimethylenedioxybenzene units. For  $n = 0$  the  $\epsilon$  value for 4,4'-dimethylbipyridinium is reported.

[186] The value of the molar absorption coefficient for the dimethoxybenzene unit was obtained from the absorption spectrum of dendron D2.

The inset of Figure 5.42. shows the variation of the molar absorption coefficients at 280 nm, where only 4,4'-bipyridinium and 1,3-dimethylenedioxybenzene absorb, versus the number  $n$  of 1,3-dimethylenedioxybenzene units. The linear fit is not fully satisfactory, likely because of the above mentioned CT interactions among the chromophoric units both in the symmetric and unsymmetric dendrimers.

Dimethylenedioxybenzenes and, accordingly, Fréchet-type dendrons<sup>187</sup> are known to exhibit fluorescence ( $\lambda_{\text{max}} = 350$  nm and  $\tau < 1$  ns). Such a band is no longer present in both the symmetric<sup>185</sup> and unsymmetric dendrimers. This result shows that the fluorescent excited state of the 1,3-dimethylenedioxybenzene units ( $E_{00} \sim 4.1$  eV) is quenched by the 4,4'-bipyridinium core via a fast electron-transfer process, as expected from the negative free energy change ( $\Delta G \sim -2$  eV).<sup>188</sup>

The investigated dendrimers contain the well known 4,4'-bipyridinium electroactive unit,  $\mathbf{B}^{2+}$ . Such a unit undergoes two successive, reversible, one-electron reduction processes at easily accessible potentials that correspond to the formation of a cation radical ( $\mathbf{B}^{2+} \rightarrow \mathbf{B}^+$ ) and a neutral ( $\mathbf{B}^+ \rightarrow \mathbf{B}$ ) species. The monoreduced species  $\mathbf{B}^+$  shows a characteristic, very strong absorption in the visible region. Because of their electron-acceptor properties, 4,4'-bipyridinium species can interact with electron-donor compounds to form adducts in a variety of structures, including pseudorotaxanes, rotaxanes and catenanes.<sup>189</sup>

In agreement with these expectations, the  $\mathbf{D}_n\mathbf{B}^{2+}$  unsymmetric dendrimers, as well as the  $(\mathbf{D}_n)_2\mathbf{B}^{2+}$  symmetric ones<sup>190</sup> show two reversible one-electron transfer processes. The half-wave potential values ( $E_{1/2}$ ) observed for reduction of the six dendrimers are gathered in Table 5.9.

---

[187] Stewart, G. M.; Fox, M. A. *J. Am. Chem. Soc.* 1996, 118, 4354.

[188] Balzani, V.; Scandola, F. *Supramolecular photochemistry*; Ellis Horwood: Chichester, England, 1991.

[189] Balzani, V.; Credi, A.; Raymo, F. M.; Stoddart, J. F. *Angew. Chem. Int. Ed.* 2000, 39, 3348.

[190] Toba, R.; Quintela, J. M.; Peinador, C.; Román, E.; Kaifer, A. E. *Chem. Commun.* 2001, 857.

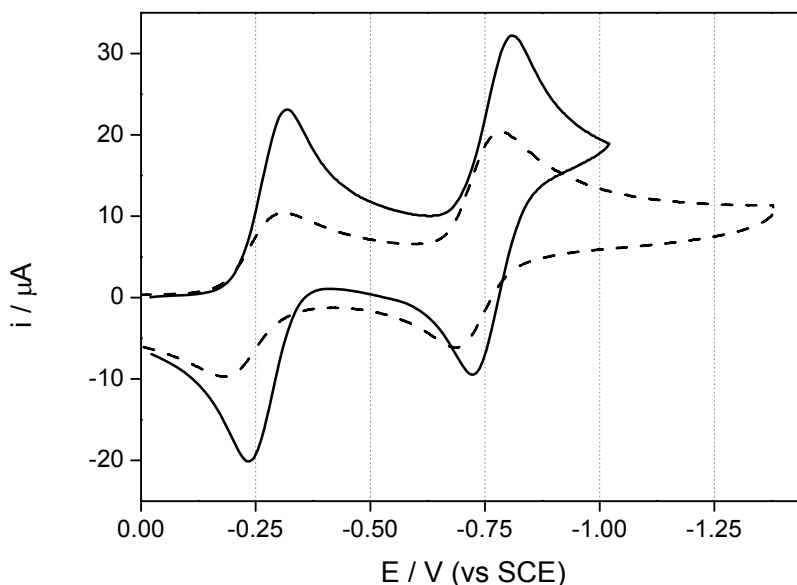


Figure 5.43. Cyclic voltammetric curves for  $D1B^{2+}$  (solid line) and of  $(D3)_2B^{2+}$  (dashed line) 1.1 mM in MeCN/ $CH_2Cl_2$  1:9 v/v- $[NBu_4]PF_6$  (0.1 M) solution. Scan rate  $v = 0.2$  V/s $^{-1}$ .

The cyclic voltammetric curves recorded, under the same experimental conditions, for two equimolar solution of  $D1B^{2+}$  and  $(D3)_2B^{2+}$  are shown in Figure 5.43.; the higher current intensities for  $D1B^{2+}$  compared to  $(D3)_2B^{2+}$  reflect its higher diffusion coefficient, as expected on the basis of the lower molecular mass.

As to the  $E_{1/2}$  values, the diagram of Figure 5.44. shows that (i) reduction potentials are slightly negatively shifted (30-40 mV) for the unsymmetric compared to the symmetric ones, and (ii), within each family, the first generation dendrimer shows a slight negative shift of both the reduction processes compared to the second and third generation ones.<sup>191</sup> The  $E_{1/2}$  values reported in Table 5.9. show that the 4,4'-bipyridinium core is easily accessible to the electrode surface and slightly affected by the presence of the dendritic branches.

[191] Kaifer et al.180a reported a very small positive shift of the first reduction process in acetonitrile solution upon increasing the generation from 1 to 3 in a series of dendrimers differing from the present  $DnB^{2+}$  one for the substituent on the apical position of the bipyridinium residue.

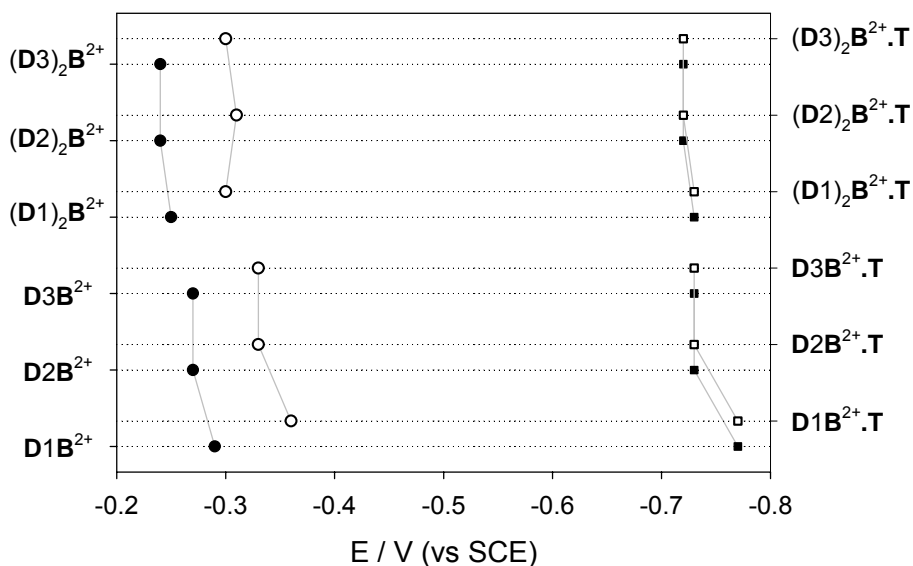


Figure 2.44. Half-wave potentials for the reduction processes of the symmetric and unsymmetric dendrimers and for their adduct with **T**.

The rate of electron transfer to the electrode surface is high for all the dendrimers (see Figure 5.43.). For example, in the case of  $(\mathbf{D}3)_2\mathbf{B}^{2+}$  the two reduction processes show a Nernstian behavior at scan rates up to 5 V/s, thus indicating no significant inhibition or site isolation effect on the dendrimer core by the dendrons.

As mentioned above, the concave host **T** exhibits a strong fluorescence band with  $\lambda_{\max} = 344$  nm. When a ca.  $10^{-5}$  M air-equilibrated dichloromethane solution of **T** has been titrated with each one of the dendrimers, small changes have been observed in the absorption spectrum of the solution with respect to the mere summation of the two components spectra. On the other hand, the fluorescence band of the tweezer-shaped molecule is strongly (but not completely, vide infra) quenched, as shown in Figure 5.45. for the case of  $(\mathbf{D}3)_2\mathbf{B}^{2+}$ . Since dynamic quenching can be ruled out because of the short (9.5 ns) excited state lifetime of **T**, these results indicate that tweezer-shaped receptor and dendrimers give rise to adducts. It has

been also verified that the fluorescence of **T** is not quenched upon addition to the solution of the dendrons used to build up the dendrimers. Therefore, one conclude that adduct formation must involve an interaction between the tweezer and the bipyridinium dendritic cores.

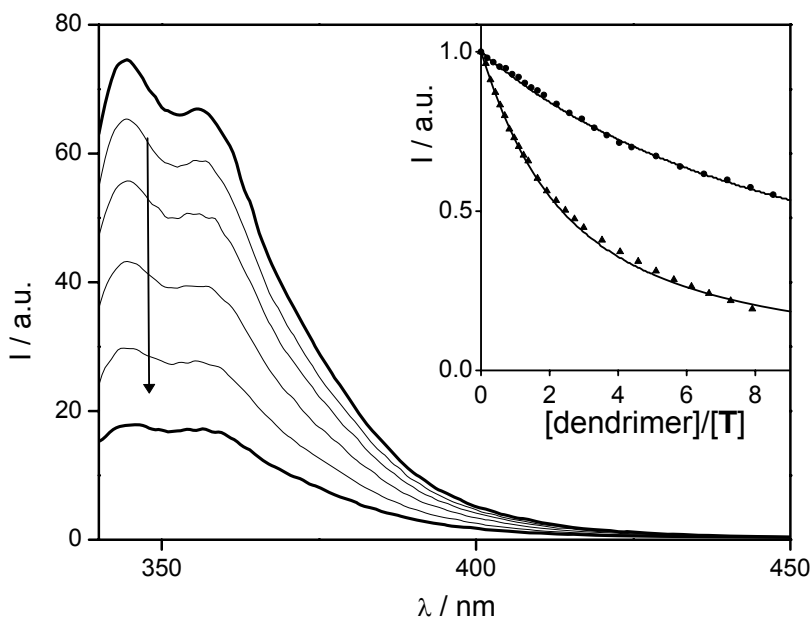


Figure 5.45. Changes in the fluorescence spectra of a  $1.6 \times 10^{-5}$  M solutions of **T** upon titration with  $(D3)_2B^{2+}$ ; experimental conditions: dichloromethane solution, room temperature, excitation at 334 nm. The inset shows the titration curve obtained by plotting the emission intensity at 356 nm as a function of the equivalents of  $D1B^{2+}$  (triangles) and of  $(D3)_2B^{2+}$  (circles). The points have been corrected for the fraction of light absorbed by **T**. The solid line shows the fitting based on formation of a 1:1 complex.

This conclusion is fully confirmed by electrochemical experiments. It has been found that the CV pattern for reduction of the dendritic cores is affected by the addition of tweezer. In particular, both the cathodic and anodic peaks corresponding to the first one-electron reduction process of a dendritic core progressively move to more negative values upon addition of tweezer, whereas the peaks corresponding to the second reduction process are practically unaffected (see Table 5.9. and Figure 5.46.).

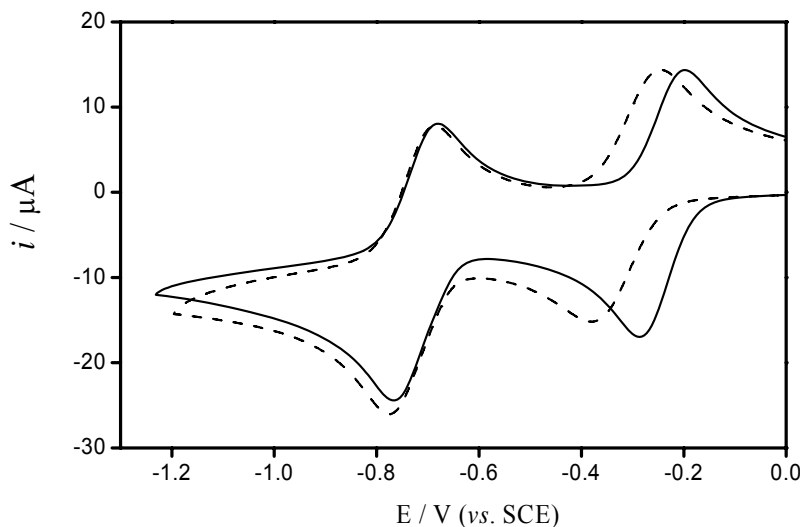


Figure 5.46. Cyclic voltammetric curves for a  $1.0 \times 10^{-3}$  M dichloromethane/acetonitrile 9:1 solution of  $(D2)_2B^{2+}$  in the absence (full line) and in the presence (dashed line) of  $3.2 \times 10^{-3}$  M **T**. Under such conditions, the association constant shows that about 98% of the species are associated. Scan rate:  $0.2 \text{ V s}^{-1}$ ,  $[NBu_4]PF_6$  0.1 M.

In order to elucidate the stoichiometry and the strength of adduct formation (Table 5.10.), fluorescence titration experiments have been performed taking into account<sup>192</sup> the fraction of light absorbed by the dendrimer. The titration plot obtained for  $1.6 \times 10^{-5}$  M solutions of **T** upon addition of  $D1B^{2+}$  and  $(D3)_2B^{2+}$  are shown in the inset of Figure 5.45.

From a qualitative viewpoint, the behavior of the titration plots (see, e.g., inset to Figure 5.45.) could be interpreted in two different ways: (i) if the fluorescence intensity of the **T** molecules involved in adduct formation is completely quenched, the results indicate that a significant fraction of host molecules remain free; (ii) if all the tweezer-shaped molecule are involved in adduct formation, in such an adduct the fluorescence intensity of the receptor **T** is

[192] Credi, A.; Prodi, L. *Spectrochimica Acta A*, 1998, 54, 159.

only partly quenched. This problem can be solved by measuring the fluorescence lifetime of **T** in the absence and presence of dendrimers. In case (i), the fluorescence lifetime should be the same; in case (ii), the fluorescence lifetime should decrease by a factor comparable to that of emission intensity quenching. It has been found that the lifetime of the host **T** fluorescence is 9.5 ns both in the absence and in the presence of dendrimers (up to ten equivalents) and that there is no evidence of a double exponential decay. Therefore, one concludes that the complexed species do not show any appreciable fluorescence and that even after addition of an excess of dendrimer a significant fraction of tweezer-shaped receptor molecules remain uncomplexed.

In order to calculate the thermodynamic constants of the inclusion complexes formation, a 1:1 model is used (eq. 36.) where the host **T** concentration is  $[H]$  and the concentration of the added dendritic guests is  $[G]$  leading to the adducts HG,

$$K_{ass} = \frac{[HG]}{[H] \cdot [G]} = \frac{[HG]}{([H]_0 - [HG]) \cdot ([G]_0 - [HG])} \quad (36)$$

The observed luminescence intensity arising from excited free host molecules, after being corrected for geometrical and inner filter effects,<sup>192</sup> is related (eq. 37.) to the concentration of supermolecule  $[HG]$  formed in solution,

$$I_{obs} = I_H * [H]_0 + (I_{HG} - I_H) * [HG] \quad (37)$$

where  $I_H$  represents an absolute parameter of H fluorescence intensity, while  $I_{HG} = 0$  as revealed by fluorescence lifetime measurements, and  $[HG]$  are related to the association constants by eq. 38.:

$$[HG] = \frac{1}{2 * K_{ass}} \cdot \left( a - \sqrt{a^2 - 4 * K_{ass} * [H]_0 * [G]_0} \right) \quad (38)$$

$$\text{where } a = (K_{ass} * [H]_0 + K_{ass} * [G]_0 + 1) \quad (39)$$

The conclusions drawn from the spectrofluorimetric titration experiments are fully confirmed by NMR investigations. The complex formation between **T** and 4,4'-bipyridinium guest molecules could be detected by the characteristic upfield shifts of the <sup>1</sup>H NMR signals of the guest protons. The maximum complexation-induced <sup>1</sup>H NMR shifts,  $\Delta\delta_{max}$ , the association constants,  $K_a$ , and hence the Gibbs energies of association,  $\Delta G_{ass}$ , have been determined for the formation of the complexes of receptor **T** with the unsymmetric dendrimers of first, and second generation **D<sub>n</sub>B<sup>2+</sup>** (n = 1,2) and the symmetric dendrimers **(D0)<sub>2</sub>B<sup>2+</sup>**, **(D1)<sub>2</sub>B<sup>2+</sup>** by the use of <sup>1</sup>H NMR titrations (Table 5.10. and 5.11.). In the other cases, the signals of the dendrimer protons in the presence of **T** are very broad and could not be assigned. In addition to the thermodynamic parameters, the stoichiometry is determined through Job plot analysis to be (1:1) for the complex between **T** and **(D0)<sub>2</sub>B<sup>2+</sup>**.

The binding constants,  $K_a$ , obtained by <sup>1</sup>H NMR titrations are in good agreement with those determined by spectrofluorimetric measurements (Table 5.10.). In dichloromethane solution receptor **T** forms highly stable complexes with the symmetric and unsymmetric dendrimers with values of the binding constants in the order of 10<sup>4</sup> M<sup>-1</sup> which decrease with increasing dendrimer generation. The complexes of the unsymmetric dendrimers are more stable than those of the corresponding symmetric dendrimers of the same generation. A similar dependence of the complex stability on the size of the dendrimer was observed in the gas phase by mass spectroscopy.<sup>182</sup> Apparently, even in solution (but only in a non-polar solvent) the bipyridinium core is stabilized by “intramolecular solvation”, which results from the back-folding of the electron-donor branches, an effect that increases with increasing dendrimer generation. In

acetone the complex stabilities are much lower than in dichloromethane indicating that the bipyridinium dication is substantially stabilized by solvation with the polar solvent.

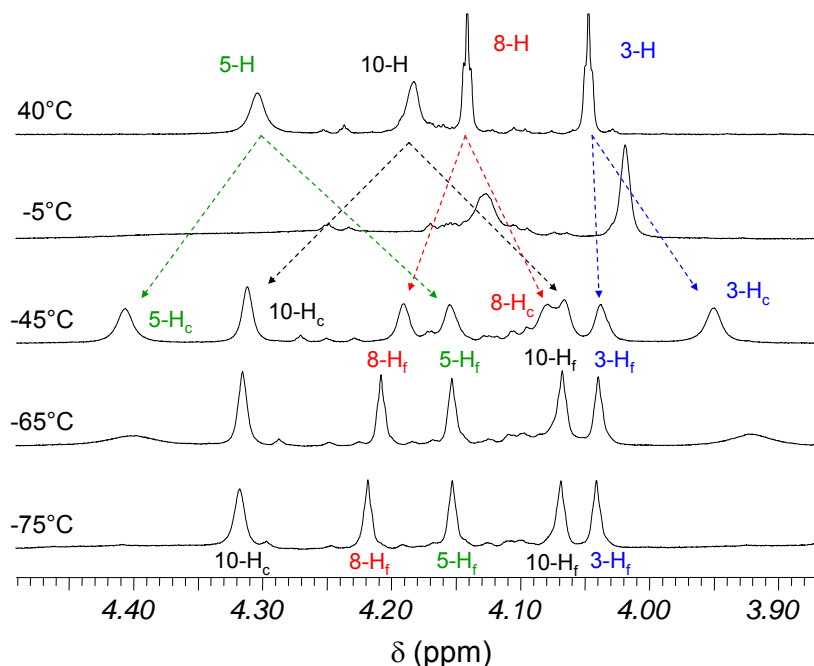


Figure 5.47.  $^1\text{H}$  NMR spectra of a 2:1 mixture of **T** and  $(\text{D}0)_2\text{B}^{2+}$  in  $\text{CDCl}_3/d_6\text{-acetone}$  1:2 at various temperatures. In the spectrum at  $-45^\circ\text{C}$  the  $^1\text{H}$  NMR signals at  $\delta = 4.191, 4.155, 4.066$  and  $4.038$  ppm could be assigned to protons  $8\text{-H}_f, 5\text{-H}_f, 10\text{-H}_f$  and  $3\text{-H}_f$  of the free tweezer by comparison with the  $^1\text{H}$  NMR spectrum of **T**. The  $^1\text{H}$  NMR signals at  $\delta = 4.407, 4.312, 4.079$  and  $3.950$  were assigned to the corresponding protons  $5\text{-H}_c, 10\text{-H}_c, 8\text{-H}_c$  and  $3\text{-H}_c$  of complex  $(\text{D}0)_2\text{B}^{2+}\cdot\text{T}$  by 2D NMR experiments. At temperatures lower than  $-45^\circ\text{C}$  the signals assigned to  $3\text{-H}_c, 5\text{-H}_c,$  and  $8\text{-H}_c$  of the complex are broadened and coalesce at  $-75^\circ\text{C}$  because of “freezing” out the shuttle process. The signal assigned to  $10\text{-H}_c$  remains sharp at lower temperatures apparently due to an accidental equivalence of  $10\text{-H}_c$  (in) and  $10\text{-H}_c$  (out) in the frozen complex  $(\text{D}0)_2\text{B}^{2+}\cdot\text{T}$  (see Figure 5.51.).

The large  $\Delta\delta_{\text{max}}$  values observed for the protons at the bipyridinium core in the complexes of the dendrimers with receptor **T** and the temperature dependence of the  $^1\text{H}$  NMR spectra (vide infra) provide good evidence that one of the pyridinium rings is positioned inside and the other one outside the cavity of the receptor and that **T** shuttles from one to the other pyridinium ring. At room temperature, the shuttling as well as the complex

dissociation/association processes are fast and lead to an averaging of the  $^1\text{H}$  NMR signals of the free and complexed guest and host protons.

The kinetics of the dissociation/association process could be analyzed by the temperature dependence of the  $^1\text{H}$  NMR spectra of 2:1 mixtures of receptor **T** with  $(\text{D0})_2\text{B}^{2+}$ ,  $(\text{D1})_2\text{B}^{2+}$ , or  $\text{D1B}^{2+}$ . In the  $^1\text{H}$  NMR spectrum of a 2:1 mixture of **T** and  $(\text{D0})_2\text{B}^{2+}$  dissolved in  $\text{CDCl}_3/d_6\text{-acetone}$  1:2 (Figure 5.48.) the four  $^1\text{H}$  NMR signals (assigned to the bridgehead protons of **T**) are broadened by lowering the temperature and finally at  $-45^\circ\text{C}$  each signal is split into two signals which could be assigned to free and complexed **T** by comparison with the  $^1\text{H}$  NMR spectrum of isolated **T** and by HH-COSY 2D NMR experiments. The specific rate constants of the exchange between free and complexed tweezer-shaped molecule **T** are determined from the line-shape analysis of the temperature-dependent signals assigned to the bridgehead protons 5-H and 10-H which show the largest splitting at low temperature. The temperature dependence of the rate constants allows one to calculate the activation parameters of the exchange between complexed and free receptor which are a measure for the dissociation parameters (Figure 5.48.).<sup>193</sup> Similar temperature-dependent NMR spectra were observed for the 2:1 mixture of **T** and  $(\text{D1})_2\text{B}^{2+}$  dissolved in  $\text{CD}_2\text{Cl}_2/d_6\text{-acetone}$  1:2 (Figure 10). In this case only the line-shapes of the temperature-dependent signals assigned to 5-H could be analyzed because of the partial overlap of the other signals at  $-55^\circ\text{C}$  (in the range of slow exchange). Although the exchange between complexed and free tweezer-shaped host is again slow in the  $^1\text{H}$  NMR spectrum of the 2:1 mixture of **T** and  $\text{D1B}^{2+}$  dissolved in  $\text{CD}_2\text{Cl}_2/d_6\text{-acetone}$  1:2 at  $-75^\circ\text{C}$ , no line-shape analysis could be performed because the signals

---

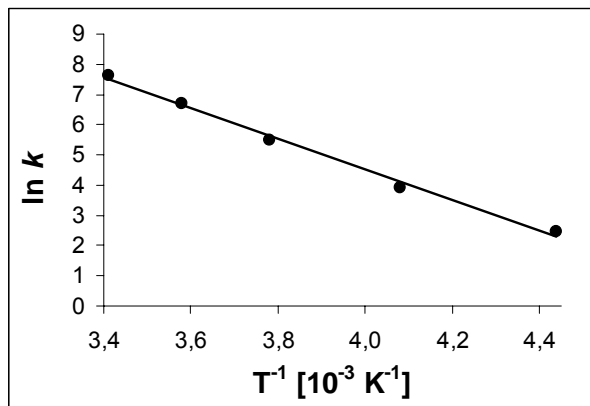
[193] Two processes – the dissociation/association and a less likely  $\text{SN}_2$ -like transfer of the guest molecule from the complex to the empty tweezer has to be taken into consideration for the observed exchange. Therefore, the observed activation enthalpy is either equal to or smaller than the dissociation enthalpy. The dynamics in the host-guest complexes are discussed in more detail for the complexes between tweezer **T** and 1,2,4,5-tetracyanobenzene or tropylium tetrafluoroborate as examples: M. Lobert, H. Bandmann, U. Burkert, U. P. Büchele, V. Podsadlowski, F.-G. Klärner, *Chem. Eur. J.* in press.

of the host bridgehead protons show a stronger overlap at low temperature than the corresponding signals in the other spectra discussed above.

<b>(D0)<sub>2</sub>B<sup>2+</sup>•T<sup>a</sup></b>				<b>(D1)<sub>2</sub>B<sup>2+</sup>•T<sup>b</sup></b>	
	<b>5-H</b>	<b>10-H</b>	<b>Average</b>	<b>5-H</b>	
<b>T [°C]</b>	<b>k [s<sup>-1</sup>]</b>	<b>k [s<sup>-1</sup>]</b>	<b>k [s<sup>-1</sup>]</b>	<b>T [°C]</b>	<b>k [s<sup>-1</sup>]</b>
25	2200	1900	2050	25	3000
10	800	800	800	10	1300
- 5	240	240	240	- 5	570
- 25	50	50	50	-15	310
- 45	12	12	12	-25	190
				-35	76
				-45	40
				- 55	24

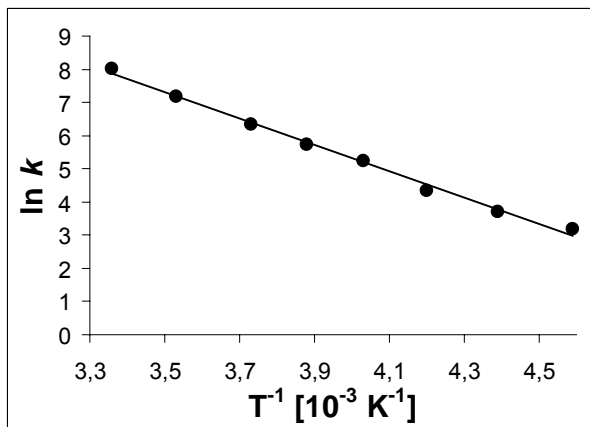
Figure 5.48. Determination of the activation parameters (free enthalpy of activation,  $\Delta G^\ddagger$ , enthalpy of activation,  $\Delta H^\ddagger$ , and entropy of activation,  $\Delta S^\ddagger$ ) from the temperature dependence of the specific rate constants  $k$  of the dissociation of complex (D0)<sub>2</sub>B<sup>2+</sup>•T (a, see next page) and (D1)<sub>2</sub>B<sup>2+</sup>•T (b, see next page) in CDCl<sub>3</sub>/d<sub>6</sub>-acetone 1:2 and CD<sub>2</sub>Cl<sub>2</sub>/d<sub>6</sub>-acetone 1:2, respectively.

a)



$A [s^{-1}]$	$4.23 \cdot 10^{+10}$
$E_a [kcal \cdot mol^{-1}]$	$(10.04 \pm 0.44)$
$T_m [K]$	263.00
$r^2$	0.9942
$\Delta H^\ddagger [kcal \cdot mol^{-1}]$	$(9.51 \pm 0.44)$
$\Delta G^\ddagger [kcal \cdot mol^{-1}]$	$(12.58 \pm 0.63)$
$\Delta S^\ddagger [cal \cdot mol^{-1} \cdot K^{-1}]$	$-(11.65 \pm 1.70)$

b)



$A [s^{-1}]$	$1.74 \cdot 10^{+9}$
$E_a [kcal \cdot mol^{-1}]$	$(7.9 \pm 0.2)$
$T_m [K]$	258.00
$r^2$	0.9946
$\Delta H^\ddagger [kcal \cdot mol^{-1}]$	$(7.4 \pm 0.2)$
$\Delta G^\ddagger [kcal \cdot mol^{-1}]$	$(12.0 \pm 0.3)$
$\Delta S^\ddagger [cal \cdot mol^{-1} \cdot K^{-1}]$	$-(18.0 \pm 0.9)$

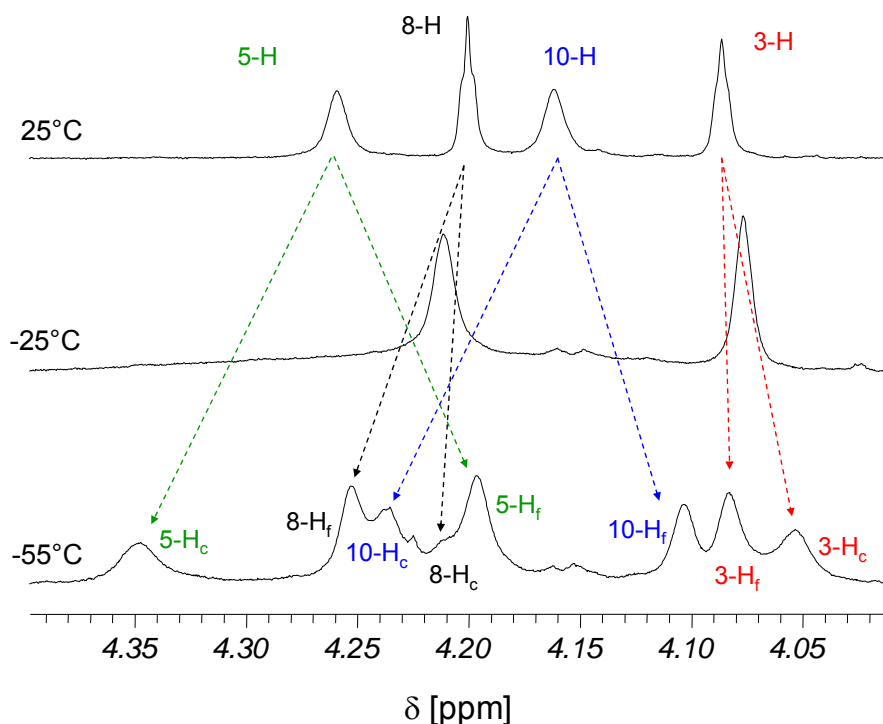


Figure 5.49.  $^1\text{H}$  NMR spectra of a 2:1 mixture of **T** and  $(\text{D}1)_2\text{B}^{2+}$  in  $\text{CD}_2\text{Cl}_2/d_6\text{-acetone}$  1:2 at various temperatures. In the spectrum at  $-55^\circ\text{C}$  the  $^1\text{H}$  NMR signals at  $\delta = 4.253$ ,  $4.196$ ,  $4.103$  and  $4.083$  ppm were assigned to protons  $8\text{-H}_f$ ,  $5\text{-H}_f$ ,  $10\text{-H}_f$  and  $3\text{-H}_f$  of the free tweezer by comparison with the  $^1\text{H}$  NMR spectrum of **T**. The  $^1\text{H}$  NMR signals at  $\delta = 4.347$ ,  $4.235$ ,  $4.196$  and  $4.053$  were assigned to the corresponding protons  $5\text{-H}_c$ ,  $10\text{-H}_c$ ,  $8\text{-H}_c$  and  $3\text{-H}_c$  of complex  $(\text{D}1)_2\text{B}^{2+}\cdot\text{T}$  by comparison with the  $^1\text{H}$  NMR spectrum of  $(\text{D}0)_2\text{B}^{2+}\cdot\text{T}$  at  $-45^\circ\text{C}$ .

In this case the specific rate constant,  $k$ , and hence the Gibbs energy of activation,  $\Delta G^\ddagger$ , could be estimated from the difference in the resonance frequencies  $\delta\nu = \nu(5\text{-H}_c) - \nu(5\text{-H}_f) = 57.5$  Hz to be  $k = 2.22 \cdot \delta\nu = 127.7$   $\text{s}^{-1}$  and  $\Delta G^\ddagger = 10.5$   $\text{kcal mol}^{-1}$  at the temperature of coalescence ( $-55^\circ\text{C}$ ).<sup>194</sup> Similar results have been obtained for the complex formation between **T** and  $(\text{D}0)_2\text{B}^{2+}$  dissolved in pure  $\text{CD}_2\text{Cl}_2$ . Due to the partial overlap of the signals of the bridgehead protons of free and complexed receptor only the specific rate constant and

[194] Günther, H. *NMR-Spektroskopie*, 1. Auflage, Georg Thieme Verlag, Stuttgart, 1973, S. 248.

the Gibbs activation energy could be estimated here to be  $k = 2.22 \cdot \delta\nu = 222 \text{ s}^{-1}$  and  $\Delta G^\ddagger = 13.0 \text{ kcal mol}^{-1}$  at the temperature of coalescence ( $0^\circ\text{C}$ ).

Beside dissociation/association, two “intramolecular” dynamic processes have to be considered to explain the  $^1\text{H}$  NMR spectra of the complexes at low temperature: (i) the already mentioned shuttling process and (ii) the guest rotation inside the tweezer-shaped host cavity around the long axis of the bipyridinium core. The shuttling process leads to an averaging of the protons  $\text{H}^o/\text{H}^o'$  and  $\text{H}^m/\text{H}^m'$  at the bipyridinium unit which are non equivalent in the complexes even of the symmetric dendrimers  $(\text{D}_n)_2\text{B}^{2+}$  ( $n = 0 - 3$ ), and the rotation causes the averaging of the protons  $\text{H}^o/\text{H}^o'$  and  $\text{H}^m/\text{H}^m'$  or  $\text{H}^o'/\text{H}^o$  and  $\text{H}^m'/\text{H}^m$  at one and the same pyridinium ring which are non equivalent in the complexes due to the acetoxy substituents at the central naphthalene spacer-unit of the host. In the  $^1\text{H}$  NMR spectra of the complex  $(\text{D}_0)_2\text{B}^{2+} \cdot \text{T}$  at temperatures lower than  $-45^\circ\text{C}$  (i.e., when dissociation/association proceeds slowly with respect to the NMR time scale) the signals at  $\delta = 8.61, 5.83,$  and  $4.81$  assigned to the bipyridinium protons  $\text{H}^o, \text{H}^m, \text{N}^+-\text{CH}_2$  are broadened, but no splitting into separate peaks can be detected. The signal broadening is an indicator for the occurrence of “intramolecular” processes but does not allow to establish which of these processes is “frozen out on the NMR timescale”. However, the specific broadening of the signals assigned to the bridgehead protons 3-, 5-, and 8- $\text{H}_c$  of complexed **T** in the  $^1\text{H}$  NMR spectrum of a 2:1 mixture of **T** and  $(\text{D}_0)_2\text{B}^{2+}$  at temperatures lower than  $-45^\circ\text{C}$  (Figure 5.47.) can only be the result of “freezing out” the shuttling process. The rotational process does not affect the position of these signals. With the assumption that the splitting of signal 5- $\text{H}_c$  is  $\delta\nu \approx 100 \text{ Hz}$  in the range of slow exchange, the Gibbs activation energy is of the order of  $\Delta G^\ddagger \approx 9.3 \text{ kcal mol}^{-1}$  at  $-75^\circ\text{C}$ , the temperature of coalescence. Similar results have been obtained for the complex  $(\text{D}_1)_2\text{B}^{2+} \cdot \text{T}$ . In the  $^1\text{H}$  NMR spectrum of a 1.2:1 mixture of  $(\text{D}_1)_2\text{B}^{2+}$  and **T** in  $\text{CD}_2\text{Cl}_2/d_6$ -acetone at  $-105^\circ\text{C}$  (Figure 5.50.) the bridgehead protons of complexed host give rise to eight signals. From the splitting of the 5- $\text{H}_c$  signals,  $\delta\nu = 125 \text{ Hz}$ , the Gibbs activation energy of

the shuttle process can be calculated to be  $\Delta G^\ddagger = 9.2 \text{ kcal mol}^{-1}$  at  $-75^\circ\text{C}$ , the temperature of coalescence.<sup>195</sup>

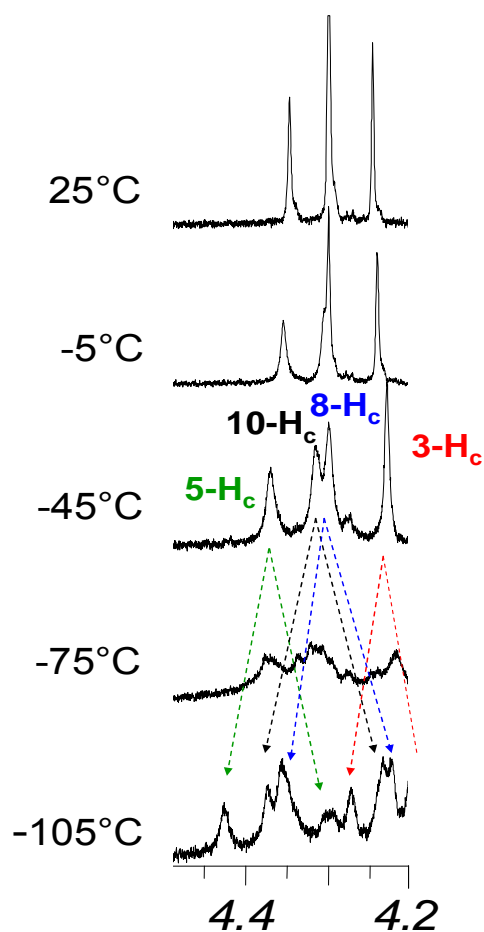


Figure 5.50.  $^1\text{H}$  NMR spectra of a 1.2:1 mixture of  $(\text{D1})_2\text{B}^{2+}$  and T in  $\text{CD}_2\text{Cl}_2/d_6\text{-acetone}$  1:2 at various temperatures, representing the shuttling process. Each of the signals in the spectrum at  $-45^\circ\text{C}$  at  $\delta = 4.339, 4.230, 4.198$  and  $4.058$  assigned to protons 5- $\text{H}_c$ , 10- $\text{H}_c$ , 8- $\text{H}_c$ , and 3- $\text{H}_c$  of the complexed T is split into two signals by lowering the temperature to  $-105^\circ\text{C}$ . At the coalescence temperature of  $-75^\circ\text{C}$  the specific rate constant and the Gibbs activation energy were calculated from the splitting of the signals of 5- $\text{H}_c$  ( $\delta v = 125 \text{ Hz}$ ) to be  $k_{(\text{coalescence})} = \pi \cdot \delta v / \sqrt{2} = 2.22 \delta v = 277$  and  $\Delta G^\ddagger = 9.2 \text{ kcal/mol}$ .

[195] The fact that the averaged signal of each proton (observed in the range of fast exchange) has to be the center of the two signals (observed for each proton in the range of slow exchange), allows the assignment of all bridgehead protons in the spectrum at  $-105^\circ\text{C}$ .

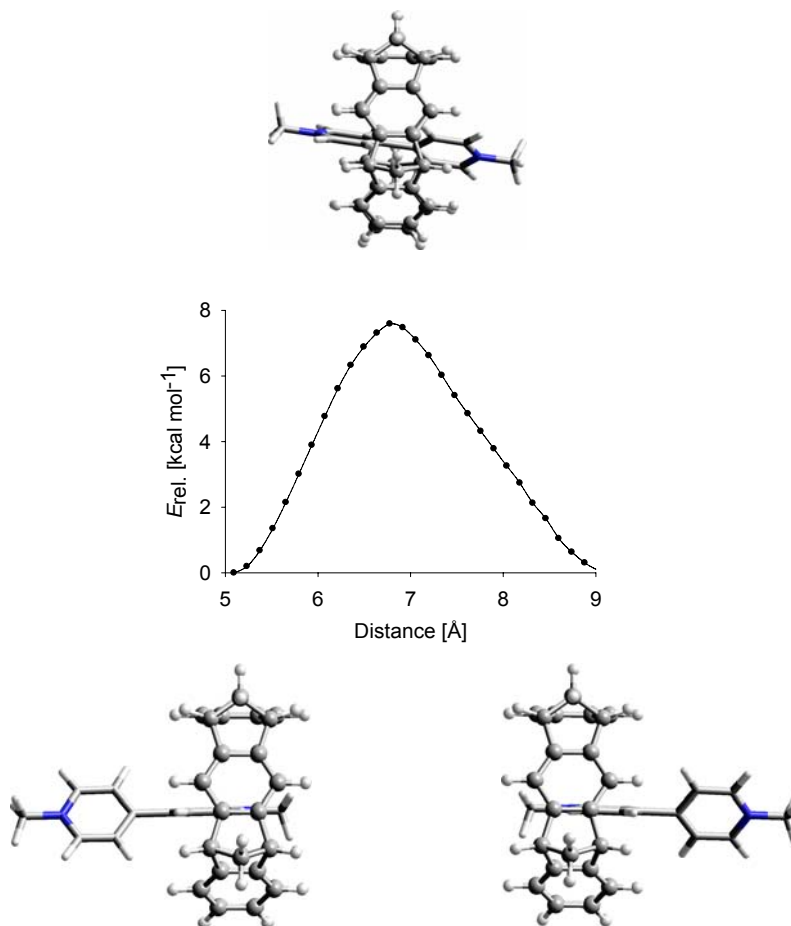


Figure 5.51. The change in energy  $E_{rel.}$  calculated for the shuttling process of **T** along the axis of the *N,N*-dimethyl-bipyridinium dication by force-field MMFF 94. The “Distance” is given between the *N*-methyl-C-atom of the bipyridinium dication and the benzene C atom fused with the norbornadiene unit of the sidewall of **T** (C-3a). The unsymmetric plot results from the computational method. Thirty structures (which are not completely symmetric) were optimized by force-field calculation with constraints of the distance between 5 and 9 Å given in the plot.

The experimentally determined Gibbs activation energies agree well with the energy barrier calculated by force-field MMFF94 for the shuttling process in the complex of the concave host **T** with *N,N*-dimethyl-4,4'-bipyridinium dication (Figure 5.51).<sup>196</sup>

[196] SPARTAN 04, Wavefunction, Inc., 18401 Von Karman Ave., Suite 370, Irvine, CA 92715, USA.

The complex structures (Figure 5.52.), which are calculated for the complexes  $(\mathbf{D0})_2\mathbf{B}^{2+}\cdot\mathbf{T}$  and  $(\mathbf{D1})\mathbf{B}^{2+}\cdot\mathbf{T}$  as representative examples by force field (MMFF 94),<sup>196</sup> are in good accord with the experimental data.

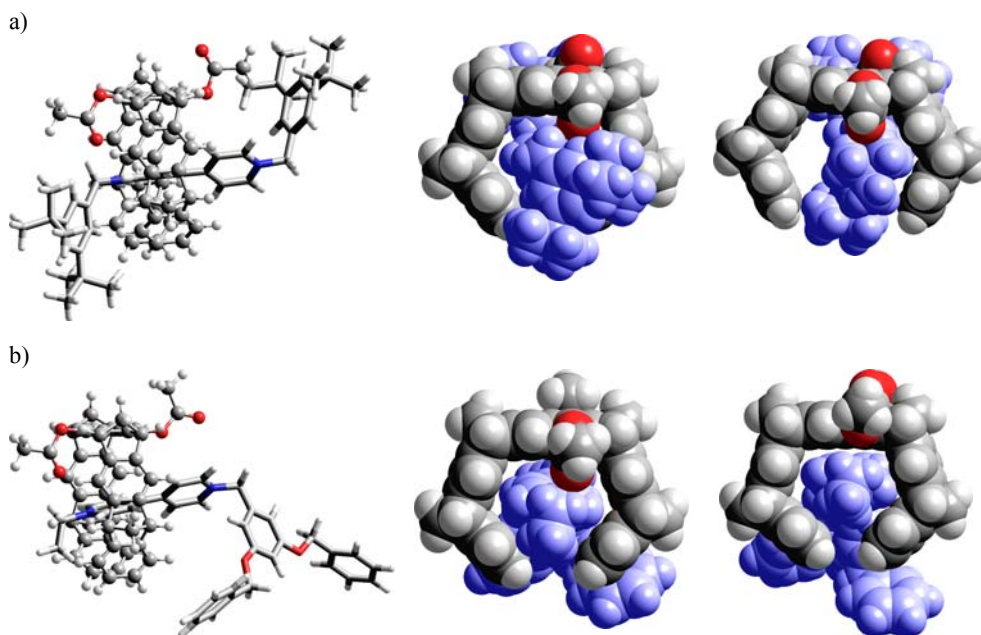


Figure 5.52. The structures of the complexes a)  $(\mathbf{D0})_2\mathbf{B}^{2+}\cdot\mathbf{T}$  and b)  $\mathbf{D1B}^{2+}\cdot\mathbf{T}$ . Left: side view (ball and stick); center: top view (space filling); right: top view on the transition state of dissociation by threading (space filling). The sidearms of tweezer  $\mathbf{T}$  have to be substantially expanded in the transition state of dissociation of  $(\mathbf{D0})_2\mathbf{B}^{2+}\cdot\mathbf{T}$  whereas the dissociation of  $\mathbf{D1B}^{2+}\cdot\mathbf{T}$  can proceed without significant distortion of the tweezer geometry.

At room temperature these structures are, however, highly dynamic. The tweezer-shaped molecule  $\mathbf{T}$  shuttles quickly from one to the other pyridinium ring of the guest molecule and the guest molecule undergoes a rapid rotation around the long axis of the bipyridinium core inside the tweezer cavity. In the complexes of unsymmetric dendrimers  $(\mathbf{D1})\mathbf{B}^{2+}$  and  $(\mathbf{D2})\mathbf{B}^{2+}$  the  $^1\text{H}$  NMR signals in  $\text{CD}_2\text{Cl}_2$  assigned to the protons at the *N*-ethyl-substituted

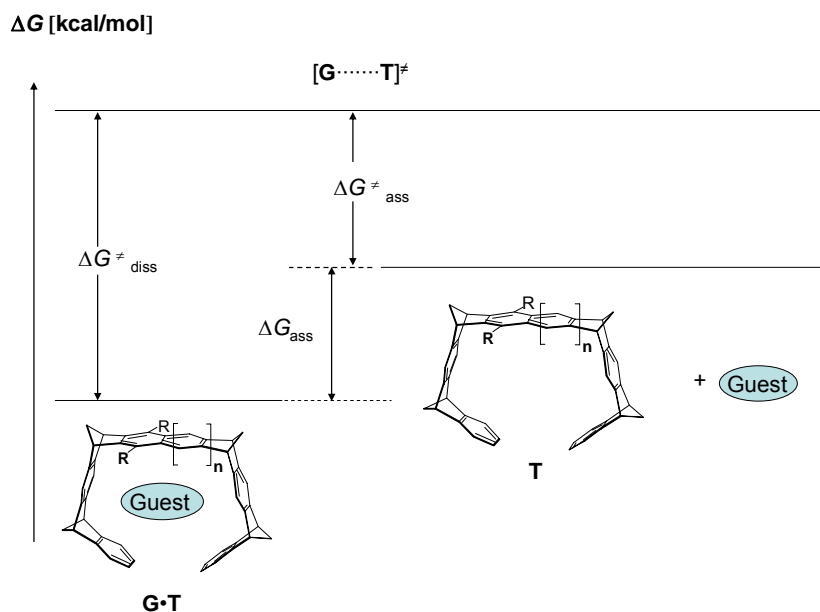
pyridinium ring exhibit larger complexation-induced shifts than those of the corresponding protons at the pyridinium ring substituted with the dendron whereas in *o*-acetone these differences in the complexation-induced shifts are small (Table 5.11.). These findings suggest that in the non-polar solvent, dichloromethane, the *N*-ethyl-substituted pyridinium ring of **D1B<sup>2+</sup>** and **D2B<sup>2+</sup>** is preferentially positioned inside the host cavity whereas in the polar solvent, acetone, such a preference does not exist. This observation is further evidence that in acetone the “intermolecular solvation” can successfully compete with the “intramolecular solvation” resulting from the back-folding of the dendron branches.

The complex formation between the dendrimers and host **T** can be further characterized by the construction of complete Gibbs energy diagrams for the complex dissociation/association by means of the now available thermodynamic and kinetic data (Figure 5.53.).

From these diagrams it becomes evident that the formation of the complexes observed here has substantial activation barriers, comparable to the complex between host **T** and 1,2,4,5-tetracyanobenzene (TCNB,  $\Delta G_{\text{ass}}^{\ddagger} = 7.8 \text{ kcal mol}^{-1}$ ).<sup>193</sup> These barriers are much higher than the barrier expected for diffusion-controlled processes (1-2 kcal mol<sup>-1</sup> depending on the viscosity of the solution). The Gibbs activation energies determined for the dissociation of the complexes of the symmetric guest molecules (**D0**)<sub>2</sub>**B<sup>2+</sup>•T** and (**D1**)<sub>2</sub>**B<sup>2+</sup>•T** are of similar size, whereas the dissociation barrier of the complex of the unsymmetric dendrimer **D1B<sup>2+</sup>•T** is smaller by about 2 kcal mol<sup>-1</sup>. The same trend is found for activation barriers calculated for the association.

The stopper groups attached to the bipyridinium core in (**D0**)<sub>2</sub>**B<sup>2+</sup>** and (**D1**)<sub>2</sub>**B<sup>2+</sup>** are, evidently, too bulky. Thus, the complex formation and dissociation cannot occur by threading of these guest molecules through the open tweezer face without severe deformation of the tweezer topology (Figure 5.52.). In these cases the complex is formed by moving the guest molecule through the receptor’s tips inside the cavity, as it happens for the association of **T** and TCNB.<sup>193</sup>

Figure 5.53. Gibbs activation energy diagram of association and dissociation for the complex formation between host T and guest molecules (D0)<sub>2</sub>B<sup>2+</sup>, (D1)<sub>2</sub>B<sup>2+</sup>, and D1B<sup>2+</sup>.



Complex	$\Delta G^{\ddagger}_{\text{diss}}$	$\Delta G_{\text{ass}}$	$\Delta G^{\ddagger}_{\text{ass}}$
<b>(D0)<sub>2</sub>B<sup>2+</sup>·T</b>	12.6 <sup>b,f</sup>	-3.9 <sup>b</sup>	8.7 <sup>b</sup>
	13.0 <sup>c,e</sup>	-5.4 <sup>c</sup>	7.6 <sup>c</sup>
<b>(D1)<sub>2</sub>B<sup>2+</sup>·T</b>	12.0 <sup>d,f</sup>	-4.4 <sup>d</sup>	7.6 <sup>d</sup>
<b>D1B<sup>2+</sup>·T</b>	10.5 <sup>d)</sup>	-4.3 <sup>d</sup>	6.2 <sup>d</sup>
<b>(D0)<sub>2</sub>B<sup>2+</sup>·T</b> (n=0, R=H)	12.0 <sup>b,e</sup>	-2.4 <sup>b</sup>	9.6 <sup>b</sup>

<sup>a</sup>  $\Delta G^{\ddagger}_{\text{ass}} = \Delta G^{\ddagger}_{\text{diss}} + \Delta G_{\text{ass}}$ ;

<sup>b</sup> in CDCl<sub>3</sub>/ *d*<sub>6</sub>-acetone 1:2;

<sup>c</sup> in CD<sub>2</sub>Cl<sub>2</sub>;

<sup>d</sup> in CD<sub>2</sub>Cl<sub>2</sub>/ *d*<sub>6</sub>-acetone 1:2;

<sup>e</sup> calculated from the differences in resonance frequencies at the coalescence temperature;

<sup>f</sup> determined by line shape analysis.

A further example is the formation of the complex between the benzene-spaced host (Figure 5.53., **T**,  $n = 0$  and  $R = H$ ) and the bipyridinium salt  $(\mathbf{D0})_2\mathbf{B}^{2+}$ .<sup>197</sup> This complex is thermodynamically much less stable than the corresponding complex of the naphthalene-spaced host **T** ( $n = 1$ ) because the inclusion of the guest molecule into the smaller cavity requires a larger expansion of the receptor sidearms increasing the strain energy. This strain effect is also responsible for the larger activation barrier of association. The finding of negative entropies of activation for the dissociation of the complexes of **T** with  $(\mathbf{D0})_2\mathbf{B}^{2+}$ ,  $(\mathbf{D1})_2\mathbf{B}^{2+}$  (Figure 5.48.), and TCNB ( $\Delta S^\ddagger = -10.6 \text{ cal mol}^{-1} \text{ K}^{-1}$ )<sup>193</sup> suggests that the guest molecule is still clipped between the host's tips in the transition state. The restriction of rotational and translation degrees of freedom in the transition state contributes negative terms to the entropy of activation. The smaller Gibbs activation energies determined for the dissociation/association of the complex with unsymmetric dendrimer  $\mathbf{DIB}^{2+} \cdot \mathbf{T}$  indicates that this complex is formed by a different route than the other complexes, most likely by threading the *N*-ethyl-substituted pyridinium ring of  $\mathbf{DIB}^{2+}$  through the open concave receptor face, which can proceed according to force-field calculations (Figure 5.52.) without significant distortion of the receptor topology.

---

[197] Kamieth, M.; Klärner F.-G. , *J. Prakt. Chem.* 1999, 341, No. 3, 245.

The investigation of the spectroscopic and electrochemical behavior of the symmetric and unsymmetric first, second, and third generation dendrimers  $(\mathbf{D}_n)_2\mathbf{B}^{2+}$  and  $\mathbf{D}_n\mathbf{B}^{2+}$  ( $n = 1, 2, 3$ ) and their host-guest complexes with host  $\mathbf{T}$  allows the following conclusions. The quite strong fluorescence of the 1,3-dimethyleneoxybenzene units of the dendrons is completely quenched as a result of through-bond or through-space donor-acceptor interactions that are also evidenced by a low energy tail in the absorption spectrum. In dichloromethane solution the 4,4'-bipyridinium cores of the investigated dendrimers are hosted by the tweezer-shaped molecule  $\mathbf{T}$ . Host-guest formation causes the quenching of the receptor fluorescence. The association constants, as measured from fluorescence and  $^1\text{H}$  NMR titration plots are of the order of  $10^4 \text{ M}^{-1}$ , decrease on increasing dendrimer generation, and are slightly larger for the unsymmetric than for the symmetric dendrimer of the same generation. The association constants are strongly solvent-dependent and decrease by more than one order of magnitude when the non-polar solvent, dichloromethane, is replaced by more polar acetone. The large complexation-induced shifts and the temperature dependence of the  $^1\text{H}$  NMR signals of the host and guest protons provide insight into the structures and dynamics of the host-guest complexes. Accordingly, the bipyridinium core is positioned inside the host cavity with a fast shuttling of the host from one to the other pyridinium ring ( $\Delta G^\ddagger < 10 \text{ kcal/mol}$ ). In the case of the unsymmetric dendrimers the *N*-ethyl-substituted pyridinium ring is preferentially complexed. The Gibbs activation barriers of the host-guest complex dissociation is in the range of 10.5-13.0 kcal/mol indicating that the complexation of the bipyridinium dications, which are symmetrically substituted with two bulky stopper groups, proceeds by clipping the guest molecule between the host's tips in the transition state, whereas the complexes of the unsymmetric dendrimers are formed by threading the *N*-ethyl-substituted pyridinium ring through the open receptor face. Host-guest formation is also found to cause a displacement of the first reduction wave of the 4,4'-bipyridinium unit towards more negative potential values, whereas the second reduction wave was unaffected.

These results show that the host-guest complexes between the tweezer-shaped receptor and the dendrimers are stabilized by electron donor-acceptor interactions and that they can be reversibly assembled/disassembled by electrochemical stimulation.

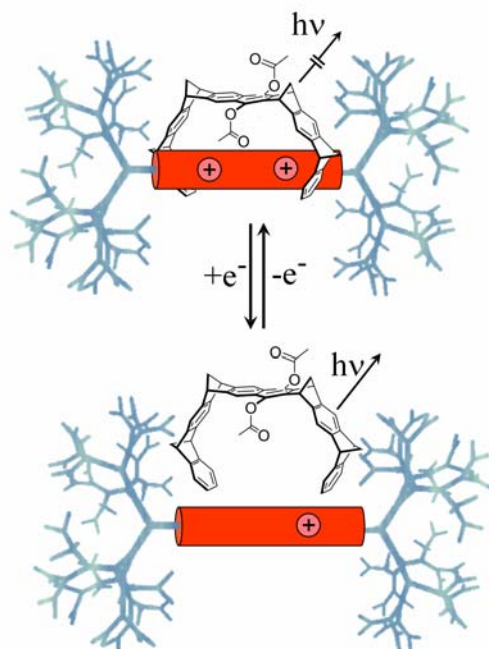


Figure 5.54. Graphical representation for the complex formation between host T and dendritic guest molecule  $(Dn)_2B^{2+}$ ; reversible dissociation can be achieved by electrochemical stimuli restoring host fluorescence.

Table 5.9. Half-wave potentials (V vs. SCE) in dichloromethane/ acetonitrile 9:1 v/v, [NBu<sub>4</sub>]PF<sub>6</sub> 0.1 M, except otherwise noted.

	$B^{2+} \rightarrow B^+$	$B^+ \rightarrow B$
<b>D1B<sup>2+</sup></b>	-0.29	-0.77
<b>D1B<sup>2+</sup>•T<sup>b</sup></b>	-0.36	-0.77
<b>D2B<sup>2+</sup></b>	-0.27	-0.73
<b>D2B<sup>2+</sup>•T<sup>b</sup></b>	-0.33	-0.73
<b>D3B<sup>2+</sup></b>	-0.27	-0.73
<b>D3B<sup>2+</sup>•T<sup>b</sup></b>	-0.33	-0.73
<b>(D1)<sub>2</sub>B<sup>2+</sup><sup>a</sup></b>	-0.25	-0.73
<b>(D1)<sub>2</sub>B<sup>2+</sup>•T<sup>a,b</sup></b>	-0.30	-0.73
<b>(D2)<sub>2</sub>B<sup>2+</sup></b>	-0.24	-0.72
<b>(D2)<sub>2</sub>B<sup>2+</sup>•T<sup>b</sup></b>	-0.31	-0.72
<b>(D3)<sub>2</sub>B<sup>2+</sup></b>	-0.24	-0.72
<b>(D3)<sub>2</sub>B<sup>2+</sup>•T<sup>b</sup></b>	-0.30	-0.72

<sup>a</sup> dichloromethane/acetonitrile 3:1 v/v.;

<sup>b</sup> under the experimental conditions used more than 95% of the electroactive species is in the complexed form.

Table 5.10. Association constants,  $K_a$  [ $M^{-1}$ ] of the complexes between host T and various bipyridinium salts.

	$K_a$ [ $10^3 M^{-1}$ ]	
<b>D1B</b> <sup>2+</sup>	34 <sup>a</sup>	29 <sup>b</sup>
	-	1.5 <sup>c</sup>
<b>D2B</b> <sup>2+</sup>	22 <sup>a</sup>	16 <sup>b</sup>
<b>D3B</b> <sup>2+</sup>	16 <sup>a</sup>	-
<b>(D0)<sub>2</sub>B</b> <sup>2+</sup>	-	8.4 <sup>b,e</sup>
	-	0.7 <sup>d,e</sup>
<b>(D1)<sub>2</sub>B</b> <sup>2+</sup>	27 <sup>a,e</sup>	-
	-	1.6 <sup>c</sup>
<b>(D2)<sub>2</sub>B</b> <sup>2+</sup>	18 <sup>a,e</sup>	-
<b>(D3)<sub>2</sub>B</b> <sup>2+</sup>	9 <sup>a,e</sup>	-

<sup>a</sup> spectrofluorimetric titration in  $CH_2Cl_2$  at room temperature. Experimental error, 10%;

<sup>b</sup> <sup>1</sup>H NMR titration at 25 °C, experimental error  $\leq$  20% in  $CD_2Cl_2$ ;

<sup>c</sup> as above in  $CD_2Cl_2$ /acetone- $d_6$  1:2;

<sup>d</sup> as above in  $CDCl_3$ /acetone- $d_6$  1:2;

<sup>e</sup> reported in ref. [181]

Table 5.11. Complexation-induced  $^1\text{H}$  NMR shifts of the bipyridinium guest protons at 25 °C.

Complex	H <sup>o</sup>	H <sup>o'</sup>	H <sup>m</sup>	H <sup>m'</sup>	N <sup>+</sup> -CH <sub>2</sub>	N <sup>+</sup> -CH <sub>2</sub> CH <sub>3</sub>
<b>D1B<sup>2+</sup>•T</b>	0.79 <sup>a</sup>	2.93 <sup>a</sup>	2.41 <sup>a</sup>	3.19 <sup>a</sup>	0.19 <sup>a</sup>	1.23 <sup>a</sup>
	1.47 <sup>d</sup>	1.60 <sup>d</sup>	2.99 <sup>d</sup>	3.59 <sup>d</sup>	0.29 <sup>d</sup>	0.51 <sup>d</sup>
	0.4 <sup>b</sup>	0.35 <sup>b</sup>	0.8 <sup>b</sup>	0.8 <sup>b</sup>	0.06 <sup>b</sup>	0.09 <sup>b</sup>
<b>D2B<sup>2+</sup>•T</b>	0.61 <sup>a</sup>	- <sup>c</sup>	- <sup>c</sup>	- <sup>c</sup>	0.13 <sup>a</sup>	0.72 <sup>a</sup>
	0.4 <sup>b</sup>	0.52 <sup>b</sup>	1.0 <sup>b</sup>	1.0 <sup>b</sup>	0.09 <sup>b</sup>	0.08 <sup>b</sup>
<b>(D1)<sub>2</sub>B<sup>2+</sup>•T</b>	1.35 <sup>d</sup>			- <sup>c</sup>	0.28 <sup>d</sup>	
<b>(D0)<sub>2</sub>B<sup>2+</sup>•T</b>	0.91 <sup>a</sup>			3.22 <sup>a</sup>	0.17 <sup>a</sup>	

<sup>a</sup>  $\Delta\delta_{\text{max}}$  in CD<sub>2</sub>Cl<sub>2</sub>;<sup>b</sup>  $\Delta\delta_{\text{obs}}$  in *d*<sub>6</sub>-acetone with [T] = 7.1 · 10<sup>-4</sup> M and [D1B<sup>2+</sup>] = 7.4 · 10<sup>-4</sup> M or [D2B<sup>2+</sup>] = 7.6 · 10<sup>-4</sup> M;<sup>c</sup> not detectable because of the signal broadening;<sup>d</sup>  $\Delta\delta_{\text{max}}$  in CD<sub>2</sub>Cl<sub>2</sub>/*d*<sub>6</sub>-acetone 1:2.

The aforementioned involvement in molecular recognition phenomena of dendrimers with a 4,4'-bipyridinium core either symmetrically and asymmetrically bearing polyaryl-ether dendrons<sup>181,184</sup> will be further discussed. Molecular recognition has been defined (section 1.2.) by the information and the energy involved in selection and binding of substrate(s) by a given receptor molecule.<sup>1</sup> Molecular recognition phenomena imply formation of supramolecular species characterized by peculiar structural, thermodynamic and kinetic features determined by molecular information stored in receptor and substrate(s) and their mutual interactions leading to selective binding.

When the core of the dendritic structure constitutes an electron-acceptor guest unit (4,4'-bipyridinium moiety in the asymmetric  $\mathbf{DnB}^{2+}$  and symmetric  $(\mathbf{Dn})_2\mathbf{B}^{2+}$  dendrimers as hexafluorophosphate salts shown in Figure 5.40.) its inclusion into a hosting structure, requiring both shape and size either interactional complementarity, allows to use as host a concave molecule comprising a naphthalene and four benzene components bridged by four methylene groups and exhibiting electron-donor properties (tweezer-shaped molecule  $\mathbf{T}$  also shown in the Figure 5.40.). Matching such double complementarity requirements, inclusion complex formation occurs. Replacing the tweezer-shaped molecule  $\mathbf{T}$  with a ring-shaped host like a dinaphtho-crown ether molecule, in fact, geometrical complementarity between receptor and substrate (at least towards symmetric  $(\mathbf{Dn})_2\mathbf{B}^{2+}$  dendrimers) is not achieved so preventing mutual recognition, while one-electron reduction of the 4,4'-bipyridinium dendritic core hinders interactional complementarity of receptor  $\mathbf{T}$  towards monoreduced  $\mathbf{DnB}^{\cdot+}$  and  $(\mathbf{Dn})_2\mathbf{B}^{\cdot+}$  substrates leading to supramolecular adducts dissociation as already shown by cyclic voltammetric patterns. Nor geometrical neither interactional complementarity are, instead, achieved replacing flat aromatic cations with alkyl cations such as  $\text{Et}_4\text{N}^+$ .

Furthermore, stability and selectivity of the supermolecule depend on the medium and result from a subtle balance between solvation (of both receptor and substrate) and

complexation (i.e. 'solvation' of the substrate by the receptor). Consequently, binding properties might markedly be affected by the medium.

In the present case, host-guest complex formation between the dendrimers  $\mathbf{D}_n\mathbf{B}^{2+}$  and  $(\mathbf{D}_n)_2\mathbf{B}^{2+}$  and the tweezer-shaped molecule  $\mathbf{T}$  is essentially driven by an electrostatic interaction between the electron-acceptor core of the dendrimers and the electron-donor host cavity. Clear evidence is given by both cathodic and anodic peaks, corresponding to the first one-electron reduction process of the dendritic core, moving toward more negative potential values upon host addition (Figure 5.46.). So is not surprising that association constants values obtained by fluorescence titration experiments in  $\text{CH}_3\text{CN}$  solution decrease more than one order of magnitude compared to those found in  $\text{CH}_2\text{Cl}_2$  solution; similar trend in the binding constants has been also found comparing results obtained by  $^1\text{H-NMR}$  measurements in pure  $\text{CD}_2\text{Cl}_2$  and  $\text{CD}_2\text{Cl}_2/\text{acetone-d}_6$  (1:2) and  $\text{CDCl}_3/\text{acetone-d}_6$  (1:2). Increasing solvent polarity electrostatic interactions are partially screened and solvation of the dicationic 4,4'-bipyridinium core by solvent molecules competes with 'intermolecular solvation' by the host cavity.

Yet, a relevant role in adduct formation when the guest is a divalent species is known to be played by ion pairing,<sup>198</sup> when the formation of inclusion complexes in low dielectric media involves previous ion-pair dissociation, apparent stability constants are known to be concentration dependent.<sup>199</sup> Concerning the  $\mathbf{D}_n\mathbf{B}^{2+}$  and  $(\mathbf{D}_n)_2\mathbf{B}^{2+}$  dendrimers and the molecular receptor  $\mathbf{T}$ , complexes formation does not involve the dissociated dications resulting in ion-paired adducts with concentration independent values of the binding constants. Within experimental error, in fact, close thermodynamic constant values have been obtained by independent titration experiments performed in air-equilibrated  $\text{CH}_2\text{Cl}_2$  or  $\text{CD}_2\text{Cl}_2$  solutions at

---

[198] F. Huang, J. Jones, C. Slebodnick, H. W. Gibson, *J. Am. Chem. Soc.*, 2003, 125, 47.

[199] In the case that the apparent  $K_{\text{ass}}$  for inclusion complexes formation is concentration dependent is imperative to specify either host and guest concentrations.

298 K at concentration values ranging between  $10^{-5}$  –  $10^{-4}$  M using spectrofluorimetric technique and 0.5 – 4 mM in  $^1\text{H-NMR}$  measurements.

The hexafluorophosphate salts of dendrimers  $\text{D}_n\text{B}^{2+}$  and  $(\text{D}_n)_2\text{B}^{2+}$  possess hydrophilic 4,4'-bipyridinium core surrounded by hydrophobic 1,3-dimethylenedioxybenzene-based dendrons. As a result of such an amphiphilic character, the medium may affect the shape of the dendritic substrates themselves.

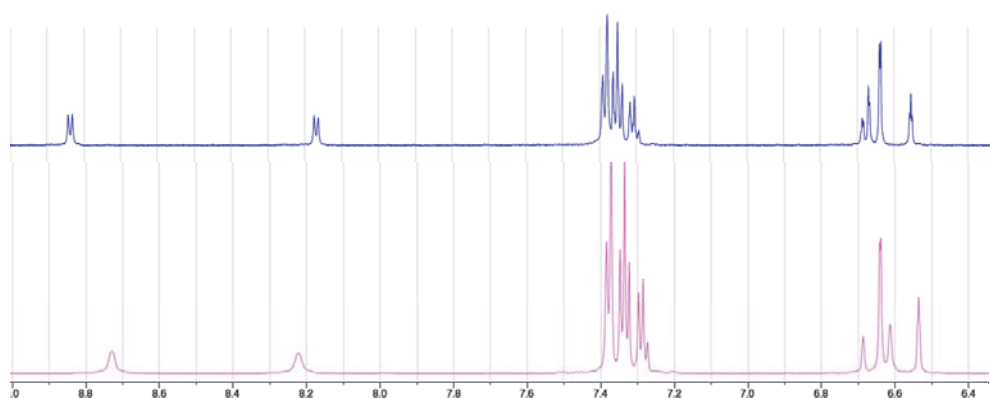


Figure 5.55.  $^1\text{H-NMR}$  spectra of  $(\text{D}_2)_2\text{B}^{2+}$  0.4 mM in  $\text{CD}_3\text{CN}$  (blue line) and  $\text{CD}_2\text{Cl}_2/\text{CD}_3\text{CN}$  9:1 (purple line) at 295 K.

The  $^1\text{H-NMR}$  spectra of  $(\text{D}_2)_2\text{B}^{2+}$  0.4 mM recorded in  $\text{CD}_3\text{CN}$  at  $22.3^\circ\text{C}$  (blue spectrum in Figure 5.55.) and in  $\text{CD}_3\text{COCD}_3$  at room temperature<sup>185</sup> show sharp and well-resolved resonances, while the  $^1\text{H-NMR}$  spectrum recorded in  $\text{CD}_2\text{Cl}_2/\text{CD}_3\text{CN}$  9:1 (purple spectrum in Figure 5.55.) shows broad resonances and up to twenty times faster nuclear relaxation times. These findings suggest that relatively low degree of solvation is achieved in low polarity medium such as dichloromethane. Consequently, dendrimers and their counteranions would likely rearrange their conformation in order to create a less hydrophobic nanoenvironment

surrounding dicationic cores. Self-protection of the dendritic core driven by solvophobic effects might occur through either back-folding of the dendrons<sup>200</sup> and formation of aggregates.

In addition, conformational rearrangements related to substrates structure have been deduced by analyzing electron-withdrawing properties of the dendrimers. With regard to the  $E_{1/2}$  values assigned to the first one-electron reduction process on the 4,4'-bipyridinium dendritic cores, it has been found that reduction potentials, in  $\text{CH}_2\text{Cl}_2/\text{MeCN}$  (9:1 v/v)  $\text{NBu}_4\text{PF}_6$  (0.1 M) solution, are negatively shifted (30 – 40 mV) for the asymmetric dendrimers compared to the symmetric ones and within each family, the first-generation dendrimer shows a slight negative shift compared to the second- and third-generation ones (Table 5.9.). Increasing the number of electron-donor 1,3-dimethylenedioxybenzene units in dendritic structure might lead to decrease electron-acceptor character of the core. These experimental results, instead, indicate that growing dendrimer generation and even more, adding a dendron as in symmetric dendrimers results in an increase of the electron-withdrawing character of the dendritic core. Two larger dendrons would likely force the two pyridinium rings, constituting the electro-active site, in a more planar conformation leading to a better delocalization of the added electron. The rate of electron transfer to the electrode surface is high for all the dendrimers and the two reduction processes show a Nernstian behaviour at scan rates up to 5 V/s, thus indicating no significant inhibition or site isolation effect on the dendrimer core by the dendrons.

Dendrimer conformational arrangements deduced by  $^1\text{H-NMR}$  and electrochemical techniques are contrasting. In order to rationalize such divergent findings,  $^1\text{H-NMR}$  measurements have been performed in presence of increasing quantity of the supporting electrolyte used in electrochemical measurements. Titration of a 0.4 mM  $\text{CD}_2\text{Cl}_2/\text{CD}_3\text{CN}$  9:1 solution of  $(\text{D}2)_2\text{B}^{2+}$

---

[200] The symmetric second generation dendrimer, although without counteranions, being in gas-phase, and bearing naphthalene instead of benzene units at its periphery, undergoes backfolding, see: C.A. Schalley, C. Verhaelen, F.-G. Klärner, U. Hahn, F. Vögtle, *Angew. Chem.* 2005, 117, 481; *Angew. Chem. Int. Ed.* 2005, 44, 477.

with  $\text{NBu}_4\text{PF}_6$  results in a gradual sharpening (Figure 5.56.) of the resonances of the  $^1\text{H-NMR}$  spectra and in an increase of the nuclear relaxation times till reaching those values found in  $\text{CD}_3\text{CN}$ .  $^1\text{H-NMR}$  spectra of dendrimers in acetonitrile- $d_3$  solution have been found insensitive to  $\text{NBu}_4\text{PF}_6$  addition. Following previous considerations, dendrons unfolding and more likely, aggregates dismembering occur upon salt addition.

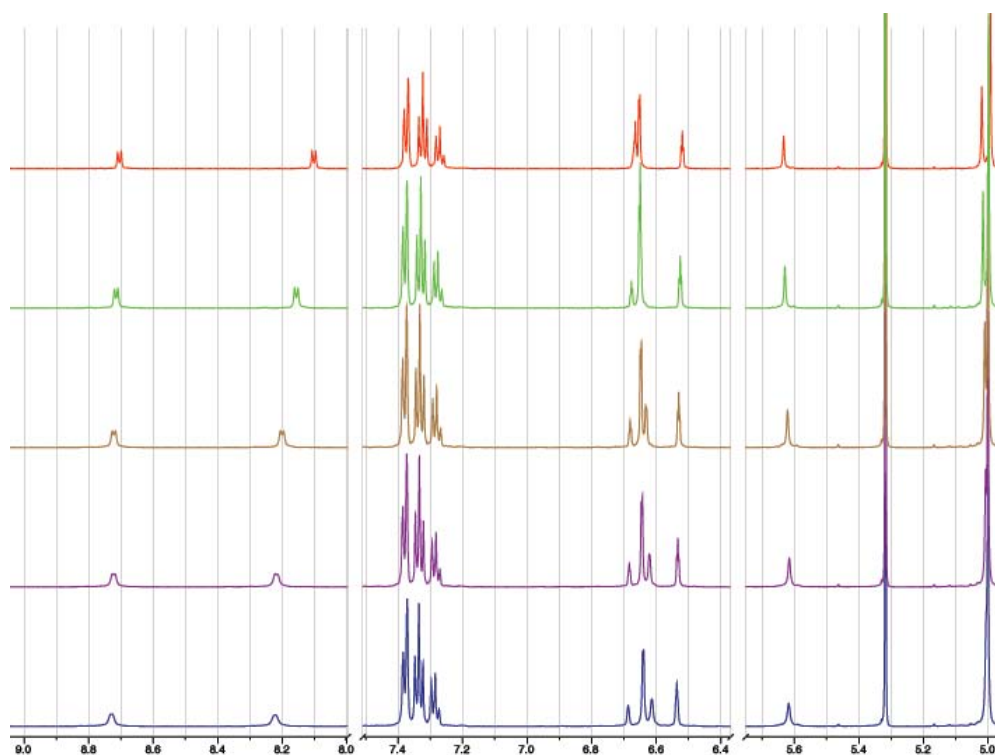


Figure 5.56.  $^1\text{H-NMR}$  spectra of  $(\text{D}_2)_2\text{B}^{2+}$  0.4 mM in  $\text{CD}_2\text{Cl}_2/\text{CD}_3\text{CN}$  9:1 (blue line) at 295 K upon increasing  $\text{NBu}_4\text{PF}_6$  concentration (4 mM purple line, 17 mM brown line, 65 mM green line, 0.15 M red line).

Consequently, salt addition effect on dendrimers inclusion complexes with **T** receptor molecule has been investigated. Thermodynamic and kinetic constants have been found very sensitive to the ionic composition of the solution.

Titrating a ca. 10  $\mu\text{M}$  dichloromethane air-equilibrated solution of **T** with  $\text{DnB}^{2+}$  and  $(\text{Dn})_2\text{B}^{2+}$ , tweezer-shaped molecule fluorescence is quenched; time-resolved fluorescence

measurements support a static quenching mechanism due to host-guest complexes formation. Adding  $\text{NBu}_4\text{PF}_6$  to a host **T** solution, a higher quenching efficiency of its fluorescence has been observed upon dendrimer  $(\text{D}3)_2\text{B}^{2+}$  addition (Figure 5.57).

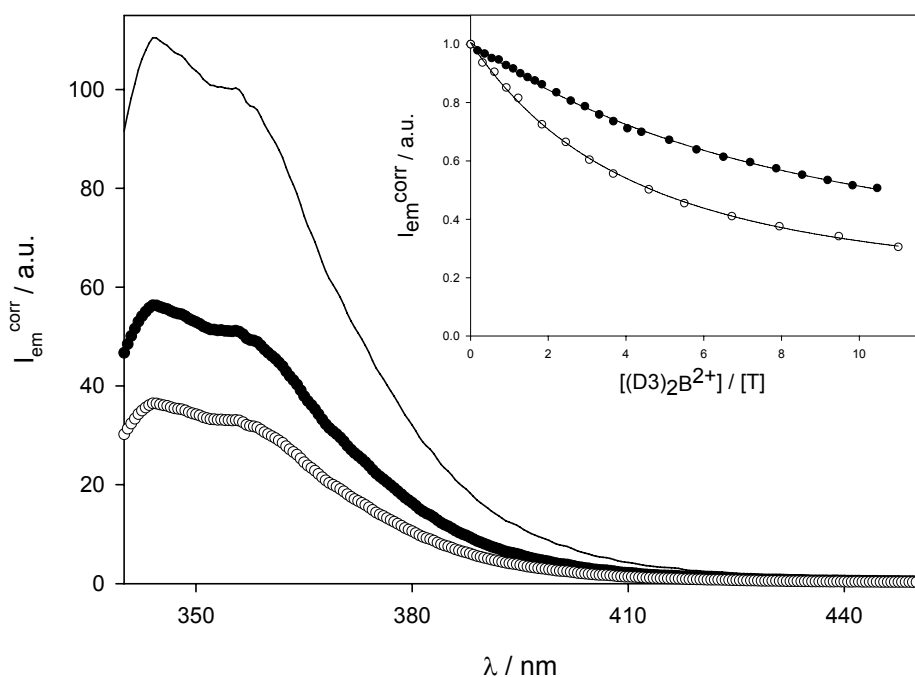


Figure 5.57. Solid line represents fluorescence spectrum of a 16  $\mu\text{M}$  air-equilibrated dichloromethane solution of **T**;  $\lambda_{\text{exc}} = 334$  nm, room temperature. Filled circles line represents fluorescence spectrum of the same **T** solution upon addition of 10 equivalents of  $(\text{D}3)_2\text{B}^{2+}$ . Open circles line shows fluorescence spectrum of **T** solution in presence of  $[\text{Bu}_4\text{NPF}_6]=0.14$  M upon addition of 10 equivalents of  $(\text{D}3)_2\text{B}^{2+}$ . Inset shows the titration curves obtained by plotting the emission intensity at 356 nm as a function of the equivalents of added  $(\text{D}3)_2\text{B}^{2+}$ , after correction for the fraction of light absorbed by **T**. Solid lines show the fitting based on formation of a 1:1 complex. Filled circles, no added salt; open circles,  $[\text{Bu}_4\text{NPF}_6]=0.14$  M.

$\text{NBu}_4\text{PF}_6$  does not interact with the mere host molecule since no changes in its absorption and emission spectra have been detected, so enabling to assume no cation competition<sup>201</sup> for the **T** hosting cavity by the quat  $\text{Bu}_4\text{N}^+$ . Furthermore, stoichiometry indicates no ion assisted

[201] W. Ong, A. E. Kaifer, *J. Org. Chem.*, 2004, 69, 4.

complexation.<sup>202</sup> Nonetheless, similar quantitative results have been obtained adding  $\text{NEt}_4\text{PF}_6$ ,  $\text{NEt}_4\text{ClO}_4$ ,  $\text{NBu}_4\text{BF}_4$ ,  $\text{NBu}_4\text{BPh}_4$ ,  $\text{NBu}_4\text{Br}$  salts to dichloromethane solutions of **T** then titrated with  $(\text{D}3)_2\text{B}^{2+}$  dendrimer. It clearly emerges how salt, as either dissociated ions and ionic couples, exerts its role on the bulk rather than directly affecting complexation.

The higher quenching of the concave receptor **T** fluorescence upon  $(\text{D}3)_2\text{B}^{2+}$  substrate addition achieved in presence of salt in solution accounts for increased stability of the endo-recognition process (see inset of Figure 5.57.). Thermodynamic constant for inclusion complex formation between **T** and  $(\text{D}3)_2\text{B}^{2+}$  in dichloromethane raises from  $9300 \text{ M}^{-1}$  when no salt is present in solution to  $22300 \text{ M}^{-1}$  at  $[\text{NBu}_4\text{PF}_6] = 0.14 \text{ M}$ . Contrarily to previous observations,<sup>203</sup> increasing salt concentration in solution weakening in receptor-substrate electrostatic interactions does not prevail in such a host-guest system.

To further elucidate salt effects on inclusion complexes formation in solution, spectrofluorimetric titrations of ca.  $10 \mu\text{M}$  dichloromethane air-equilibrated solutions of **T** at different  $\text{NBu}_4\text{PF}_6$  concentrations with  $\text{doV}^{2+}$ ,  $(\text{D}1)_2\text{B}^{2+}$ ,  $\text{D}3\text{B}^{2+}$ , and  $(\text{D}3)_2\text{B}^{2+}$ , so taking into account dendron number and generation, have been performed. Figure 5.58. shows how salt addition (approximately till the same salt concentration in those solutions used in electrochemical measurements) affects the thermodynamic stability of the host-guest complexes depending on dendrimer structure.

Association constant values ratio at different salt concentrations evidences how, within symmetric dendrimers, the third generation species is almost unaffected till millimolar  $\text{NBu}_4\text{PF}_6$  concentration, while increasing salt content in solution it undergoes more marked changes compared to the first generation dendrimer.<sup>204</sup> Nonetheless, within third generation dendrimers,

---

[202] Few equivalents of salt does not influence complex formation. J. W. Jones, L. N. Zakharov, A. L. Rheingold, H. W. Gibson, *J. Am. Chem. Soc.*, 2002, 124, 45.

[203] S. Kubik, *J. Am. Chem. Soc.*, 1999, 121, 25.

[204]  $K_{\text{ass}}([\text{NBu}_4\text{PF}_6] \approx 10^{-3} \text{ M}) / K_{\text{ass}}([\text{NBu}_4\text{PF}_6] = 0)$  for the dendrimers  $(\text{D}1)_2\text{B}^{2+}$  and  $(\text{D}3)_2\text{B}^{2+}$  is 1.20 and 1.02 respectively, while  $K_{\text{ass}}([\text{NBu}_4\text{PF}_6] \approx 10^{-1} \text{ M}) / K_{\text{ass}}([\text{NBu}_4\text{PF}_6] = 0)$  is 2.15 and 2.40.

asymmetric functionalization of the 4,4'-bipyridinium core results in an increased sensitivity to low  $\text{NBu}_4\text{PF}_6$  concentration.<sup>205</sup> Dendrons folding might be taken into account only in higher generations symmetric dendrimers as confirmed by analyzing  $\text{NBu}_4\text{PF}_6$  effects on inclusion complex formation between the host **T** and the 1,1'-dioctyl-4,4'-bipyridinium as  $\text{PF}_6^-$  salt (**DoV**<sup>2+</sup> is shown in the Figure 5.32.); in such a case, while unfolding of alkyl non electron-donor apolar branches is unlikely to occur, association constant values increase with increasing  $\text{NBu}_4\text{PF}_6$  concentration.<sup>206</sup>

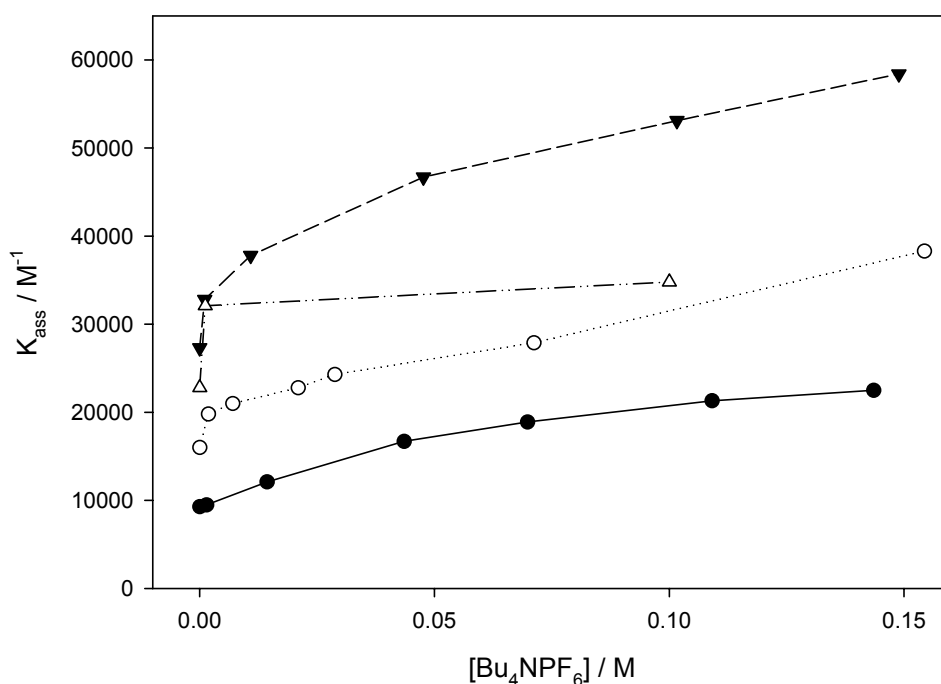


Figure 5.58. Plot of the association constants,  $K_{\text{ass}}$ , for  $(\text{D3})_2\text{B}^{2+}$  (filled circles),  $\text{D3B}^{2+}$  (open circles),  $(\text{D1})_2\text{B}^{2+}$  (filled triangles) **doV**<sup>2+</sup> (open triangles) vs.  $\text{Bu}_4\text{NPF}_6$  concentration in solution.

[205]  $K_{\text{ass}}([\text{NBu}_4\text{PF}_6] \approx 10^{-3} \text{ M}) / K_{\text{ass}}([\text{NBu}_4\text{PF}_6] = 0)$  for the dendrimers **D3B**<sup>2+</sup> and  $(\text{D3})_2\text{B}^{2+}$  is 1.24 and 1.02 respectively, while  $K_{\text{ass}}([\text{NBu}_4\text{PF}_6] \approx 10^{-1} \text{ M}) / K_{\text{ass}}([\text{NBu}_4\text{PF}_6] = 0) = 0$  is 2.40 for both dendrimers.

[206]  $K_{\text{ass}}([\text{NBu}_4\text{PF}_6] \approx 10^{-3} \text{ M}) / K_{\text{ass}}([\text{NBu}_4\text{PF}_6] = 0)$  for the model compound **doV**<sup>2+</sup> is 1.41, while  $K_{\text{ass}}([\text{NBu}_4\text{PF}_6] \approx 10^{-1} \text{ M}) / K_{\text{ass}}([\text{NBu}_4\text{PF}_6] = 0)$  is 1.53.

These findings support the idea that solvophobic interactions lead to aggregates formation whose size, shape, and stability are determined by the branches appended to the 4,4'-bipyridinium core. Salt (as both ionic couples and ions) in solution provides higher degree of solvation of the dendritic substrates resulting in aggregates dismembering and, consequently, favouring 'intermolecular solvation' of the dendritic core by the host cavity.

Through temperature-dependent  $^1\text{H-NMR}$  analysis, complexation has been found to proceed by threading in asymmetric dendrimers while by clipping in symmetric ones. Stopped-flow spectrophotometric measurements show that host **T** fluorescence decay upon addition of  $(\text{Dn})_2\text{B}^{2+}$  is slower than that observed upon  $\text{DnB}^{2+}$  addition (see Table 5.12.). The rate constants for the formation of inclusion complexes between receptor and symmetric dendritic guests are lower than those found with asymmetric dendrimers. These results may account for higher steric hindrance of two larger dendrons so the resulting clipping mechanism of complexation is slower than threading.

Also kinetic behaviour has been found to be affected by salt presence in solution: the higher is the salt content in a 14  $\mu\text{M}$  dichloromethane air-equilibrated solution of **T** at 293 K, the slower is its fluorescence decay upon addition of one equivalent of  $(\text{D3})_2\text{B}^{2+}$  dendrimer (Figure 5.59. and Table 5.13.) resulting in lower complex formation rate constants. This may account for dendrimer aggregates dismembering besides not quantified slower diffusion of the dendrimer and the tweezer-shaped receptor in solution in presence of  $\text{NBu}_4\text{PF}_6$ . Note that also decomplexation rate constants decrease with almost the same trend (inset in Figure 5.59. and Table 5.13.) maybe confirming no ions direct cooperation in inclusion complex formation.

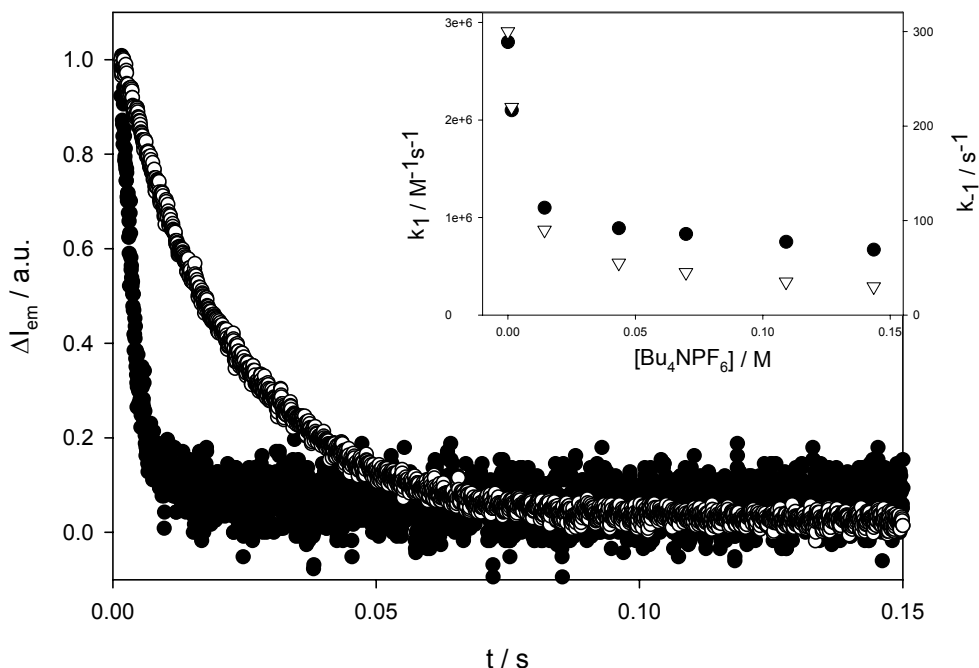


Figure 5.59. Fluorescence decay of 14  $\mu\text{M}$  T air-equilibrated dichloromethane solution at 293 K, upon addition of one equivalent of  $(\text{D}3)_2\text{B}^{2+}$ ;  $\lambda_{\text{exc}} = 297$  nm. Filled circles represent fluorescence decay when no salt is added; open circles, instead, when  $[\text{Bu}_4\text{NPF}_6] = 0.14$  M. Inset shows kinetics constants for association ( $k_1$ , filled circles) and dissociation ( $k_{-1}$ , open triangles) processes for T and  $(\text{D}3)_2\text{B}^{2+}$  plotted versus  $\text{Bu}_4\text{NPF}_6$  concentration in solution.

In conclusion, increasing electrolyte content in low dielectric medium, an increase in thermodynamic constants and a decrease in kinetic constants for inclusion complexes formation between the tweezer-shaped receptor **T** and 4,4'-bipyridinium core dendrimers bearing polyaryl ether dendrons  $\text{D}_n\text{B}^{2+}$  and  $(\text{D}_n)_2\text{B}^{2+}$  has been observed. Such features characterizing the supramolecular adducts have been attributed to the dendritic components and their structural and conformational rearrangements upon salt addition in solution.

These salt effects must be taken into account when studying host-charged guest complexes in apolar solvents with techniques that require presence of supporting electrolytes such as

voltammetry. In such cases salt addition in electrochemical experiments may modify the electrophore's nanoenvironment in a hard to predict way.

Furthermore, because salt presence in the medium affects dendrimers structure and conformation (as happens in many proteins folding<sup>207</sup>) it should be considered when designing dendrimers for gene carrier and drug delivery purposes or sensing applications.<sup>208</sup>

These salt-induced structural and conformational rearrangements in dendrimers have been speculated rather than definitively demonstrated. Anyway, the construction of the investigation and its presentation leads to verisimilar (to me) conclusions. Anyway, the concept of verisimilitude rather than the concept of true is opposed to the concept of lie, someone said. Further analysis should be performed, but both complexity of the problem and lack of interest on these salted topics suggest to give up the investigation.

---

[207] T. Beringhelli, I. Eberini, M. Galliano, A. Pedoto, M. Perduca, A. Sportiello, E. Fontana, H. L. Monaco, E. Gianazza, *Biochemistry*, 2002, 41, 51.

[208] a) A. Verma, J. M. Simard, V. M. Rotello, *Langmuir*, 2004, 20, 10; b) M. Ballauff, C. N. Likos, *Angew. Chem.* 2004, 116, 23; *Angew. Chem. Int. Ed.* 2004, 43, 23.

Table 5.12. Thermodynamic and kinetic parameters for inclusion complex formation between tweezer-shaped host T and dendritic guests  $(Dn)_mB^{2+}$ , 14  $\mu\text{M}$  in air-equilibrated dichloromethane solution at 293 K.

<b>T+(Dn)<sub>m</sub>B<sup>2+</sup></b>	<b>K<sub>eq</sub> / M<sup>-1</sup></b>	<b>k<sub>i</sub> / M<sup>-1</sup> s<sup>-1</sup></b>	<b>k<sub>-i</sub> / s<sup>-1</sup> <sup>a</sup></b>
<b>(D1)<sub>2</sub>B<sup>2+</sup></b>	27300	$1.9 \cdot 10^7$	700
<b>(D2)<sub>2</sub>B<sup>2+</sup></b>	18000	$7.7 \cdot 10^6$	430
<b>(D3)<sub>2</sub>B<sup>2+</sup></b>	9300	$2.8 \cdot 10^6$	300
<b>D1B<sup>2+</sup></b>	33600	$\geq 10^8$	$\geq 10^3$
<b>D2B<sup>2+</sup></b>	21900	$\geq 10^8$	$\geq 10^3$
<b>D3B<sup>2+</sup></b>	16000	$\geq 10^8$	$\geq 10^3$

<sup>a</sup>  $k_{-i} = k_i / K_{eq}$ .

Table 5.13. Thermodynamic and kinetic parameters for inclusion complex formation between tweezer-shaped host T and dendritic guests (D3)<sub>2</sub>B<sup>2+</sup>, 14 μM in air-equilibrated dichloromethane solution at 293 K, at different Bu<sub>4</sub>NPF<sub>6</sub> concentration.

[NBu <sub>4</sub> PF <sub>6</sub> ] / M	K <sub>eq</sub> / M <sup>-1</sup>	k <sub>1</sub> / M <sup>-1</sup> s <sup>-1</sup>	k <sub>-1</sub> / s <sup>-1</sup> <sup>a</sup>
0	9300	2.8*10 <sup>6</sup>	300
1.5 x 10 <sup>-3</sup>	9700 <sup>b</sup>	2.1*10 <sup>6</sup>	220
1.4 x 10 <sup>-2</sup>	12300 <sup>b</sup>	1.1*10 <sup>6</sup>	90
4.4 x 10 <sup>-2</sup>	16300 <sup>b</sup>	8.9*10 <sup>5</sup>	55
7.0 x 10 <sup>-2</sup>	19200 <sup>b</sup>	8.3*10 <sup>5</sup>	45
1.1 x 10 <sup>-1</sup>	21900 <sup>b</sup>	7.5*10 <sup>5</sup>	35
1.4 x 10 <sup>-1</sup>	22300 <sup>b</sup>	6.7*10 <sup>5</sup>	30

<sup>a</sup> k<sub>-1</sub> = k<sub>1</sub> / K<sub>eq</sub>;

<sup>b</sup> values extrapolated fitting the trend in K<sub>eq</sub> upon salt addition represented in Figure 5.58. with an exponential function growing to a maximum.

## 6. Metal Complexes

### 6.1. Phosphino-Aminothiazoline Pt(II) Complexes

Phosphino-aminothiazolines can exist in solution in two tautomeric forms, in which the N-H proton involves the endo-cyclic or exo-cyclic nitrogen atom. The two tautomers show different reactivities toward alcoholysis, the imino form being more rapidly degraded. Their bischelated platinum complexes have been studied in the solid state by single crystal X-ray diffraction, revealing the unique stereoelectronic features of the [Pt(PN<sub>th</sub>)] (PN<sub>th</sub> = diphenylphosphino-aminothiazoline) moiety. The complex *cis*-[Pt(PN<sub>th</sub>)<sub>2</sub>] reacts with gold(I) salts to yield dimetallic compounds, whose molecular structures have been determined by X-ray diffraction. Solid *cis*-[Pt(PN<sub>th</sub>)<sub>2</sub>] shows vapoluminescent properties when exposed to alcohol vapors. A combined photophysical and crystallographic investigation has been carried out in order to clarify the unprecedented rigidochromic role of the alcohol in this phenomenon.

The reaction of PPh<sub>2</sub>Cl with primary amines in the presence of NEt<sub>3</sub> represents a simple and efficient synthetic method for the preparation of  $\alpha$ -aminophosphines.<sup>209</sup> The commercial availability of a large number of functionalized amines facilitates the fine tuning of the stereoelectronic properties of this class of ligands. A systematic study of their coordination properties becomes then easier, as well as that of the catalytic and physical properties of their metal complexes.<sup>210</sup> It was recently reported the synthesis of the new ligand diphenylphosphino-2-amino-2-thiazoline (**I**), the formation of which follows a non-trivial

[209] Z. Fei, P. J. Dyson, *Coord. Chem. Rev.* 2005, 249, 2056-2074.

[210] See e.g. (a) P. Braunstein, *Chem. Rev.* 2006, 106, 134-159; (b) P. Braunstein, F. Naud, *Angew. Chem.* 2001, 113, 702-722; *Angew. Chem., Int. Ed.* 2001, 40, 680-699; (c) G. Helmchen, A. Pfaltz, *Acc. Chem. Res.* 2000, 33, 336-345; (d) C. S. Slone, D. A. Weinberger, C. A. Mirkin, *Prog. Inorg. Chem.* 1999, 48, 233-350.

reaction pathway involving the intermediacy of the diphosphine  $\text{Ph}_2\text{PN}=\overline{\text{CN}}(\text{PPh}_2)\text{CH}_2\text{CH}_2\text{S}$  and phosphoryl migrations, as summarized in Figure 6.1.<sup>[211]</sup>

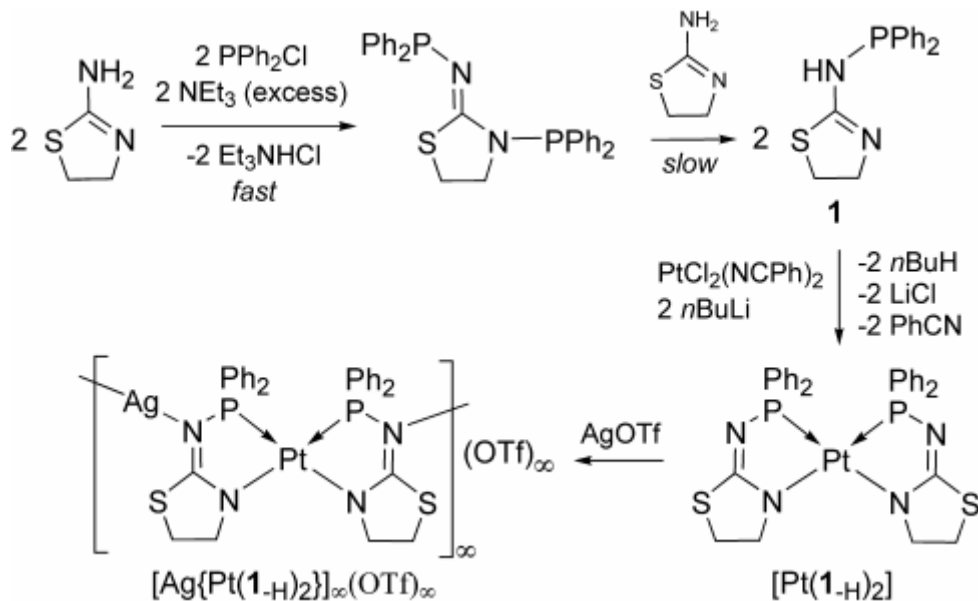


Figure 6.1. Synthesis of the phosphino-aminothiazoline Pt(II) complex as precursor of the heterodimetallic coordination polymer.

Ligand **1** readily leads to stable bischelated platinum(II) complexes featuring its deprotonated form, *cis*- $[\text{Pt}(\mathbf{1-H})_2]$  (Figure 6.1.). Access to this complex can result from ligand deprotonation prior to chelation (Figure 6.1.), or from deprotonation of a dicationic bischelated complex, by taking advantage of the enhanced acidity of the NH moiety upon P-coordination, which allows the use of bases weaker than  $n\text{BuLi}$ , such as  $\text{NEt}_3$ . Despite its remarkable stability, *cis*- $[\text{Pt}(\mathbf{1-H})_2]$  easily reacts with electrophilic metal centers, giving rise, for instance, to

[211] G. Margraf, R. Pattacini, A. Messaoudi, P. Braunstein, *Chem. Commun.* 2006, 3098-3100.

the formation of the heterodimetallic Pt/Ag coordination polymer  $[Ag\{Pt(1-H)_2\}]_\infty(OTf)_\infty$  (Figure 6.1.,  $OTf = CF_3SO_3^-$ ).<sup>211</sup>

Investigation of the coordination properties of phosphino-aminothiazole ligands has been performed in order to study and compare their solution behavior and the reactivity of their transition metal complexes. Herein is reported a comparative study on a series of bischelated platinum(II) complexes which revealed that minor structural differences may result in remarkably different chemical and photophysical properties.

When two equivalents of aminophosphines **1** are reacted with  $[PtCl_2(NCPh)_2]$  in the presence of  $NEt_3$ , *cis*- $[Pt(1-H)_2]$  is obtained, in almost quantitative yields.

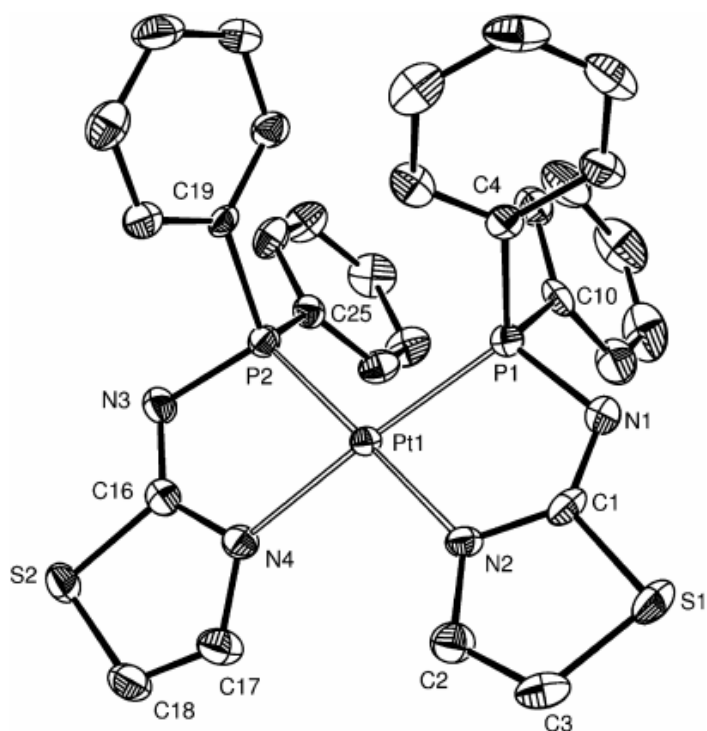


Figure 6.2. View of the molecular structure of compound *cis*- $[Pt(1-H)_2]$  in *cis*- $[Pt(1-H)_2] \cdot 2 CH_3OH \cdot CH_3CN$  (Displacement parameters include 50 % of the electron density).

The poor solubility of this neutral, bischelated complex in MeCN facilitates their purification. Their X-ray molecular structures are depicted in Figure 6.2. and selected bond distances and angles are compared in Table 6.1. In these complexes, two deprotonated ligands **1** chelate the metal center through the phosphorous and the endo-cyclic nitrogen atoms. Although they display similar geometrical parameters (Table 6.1.), some structural details deserve comments.

<i>cis</i> -[Pt( <b>1-H</b> ) <sub>2</sub> ]	
av. P-Pt	2.238(1)
av. N-Pt	2.095(3)
av. N-P	1.663(3)
av. C1-N1	1.326(5)
av. C1-N2	1.322(5)
C1-S	1.765(4)
C3-S	1.799(4)
N2-C2	1.472(4)

Table 6.1. Selected bond distances [Å] for compound *cis*-[Pt(**1-H**)<sub>2</sub>].

In complex *cis*-[Pt(**1-H**)<sub>2</sub>], the C=N double bond is more delocalized over the N-C-N unit compared to other phosphino-aminothiazole Pt(II) complexes (not shown here because they are not luminescent<sup>212</sup>). The average S-C3 and N2-C2 distances are longer in *cis*-[Pt(**1-H**)<sub>2</sub>] than in

[212] For a detailed discussion see: R. Pattacini, C. Giansante, P. Ceroni, M. Maestri, P. Braunstein, *Chem. Eur. J.*, 2007, 13, 10117. \*

the other three complexes, as a result of the non-aromaticity of the thiazole ring. The value of the latter influences the bond order C1-N2.

Complex  $cis-[Pt(\mathbf{I-H})_2]$  co-crystallizes with two molecules of  $CH_3OH$  and one of  $CH_3CN$ . The  $CH_3OH$  molecules form hydrogen bonds with the exo-cyclic nitrogen atoms of the complex to form  $CH_3OH \cdots cis-[Pt(\mathbf{I-H})_2] \cdots HOCH_3$  entities [O1 $\cdots$ N1 and O2 $\cdots$ N3 separations: 2.813(5) and 2.809(5) respectively] (Figure 6.3.). The acetonitrile methyl groups connect the  $CH_3OH \cdots cis-[Pt(\mathbf{I-H})_2] \cdots HOCH_3$  moieties through H $\cdots$ O contacts, in such a way that infinite chains of formula  $cis-[Pt(\mathbf{I-H})_2] \cdot 2CH_3OH \cdot CH_3CN$  are formed. These chains are furthermore interconnected by H $\cdots$ Pt contacts between  $\mathbf{I}$  and the remaining methyl hydrogen of  $CH_3CN$ s are 9.8673(2) and 16.0880(3) Å respectively.

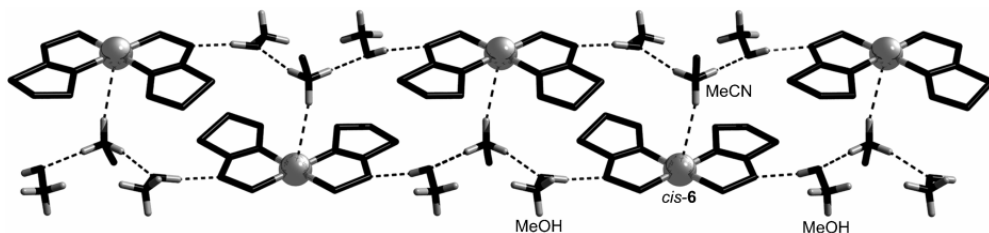


Figure 6.3. View of the crystal structure of  $cis-[Pt(\mathbf{I-H})_2] \cdot 2 CH_3OH \cdot CH_3CN$ . Phenyl groups omitted for clarity. Symmetry operation generating equivalent molecules:  $-x, -y, -z$ ;  $-x, 1/2+y, 1/2-z$ .

While for other complexes form **b** (Figure 6.4.) is more appropriate, on the basis of structural parameters, resonance form **a** gives significant contribution to the bonding in  $cis-[Pt(\mathbf{I-H})_2]$ , which should result in a more nucleophilic character for the two exocyclic nitrogen atoms and consequently, in their enhanced reactivity toward electrophilic metal centers.

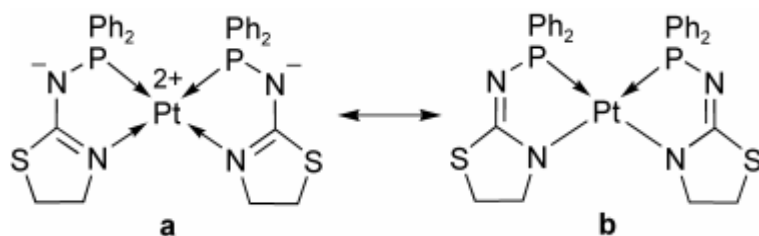


Figure 6.4. Resonance forms of *cis*-[Pt(1-H)<sub>2</sub>].

As already mentioned, the C1-N2 bond of *cis*-[Pt(1-H)<sub>2</sub>] is shorter than in the other complexes, which results in a larger contribution of form **a** to the bonding (Figure 6.4.) and thus in a higher nucleophilicity of the nitrogen atom in  $\alpha$  position to phosphorus. Reactions with electrophilic metal centers are indeed faster with *cis*-[Pt(1-H)<sub>2</sub>] than with other complexes.

Complexes *cis*-[Pt(1-H)<sub>2</sub>] has been reacted with [AuCl(tht)] (tht = tetrahydrothiophene) in 1:1 and 1:2 ratios. Although coordination of AuCl fragments is observed for all the metalloligands, the reactions with the not shown complexes resulted in unstable compounds which quickly decomposed with formation of gold mirrors.

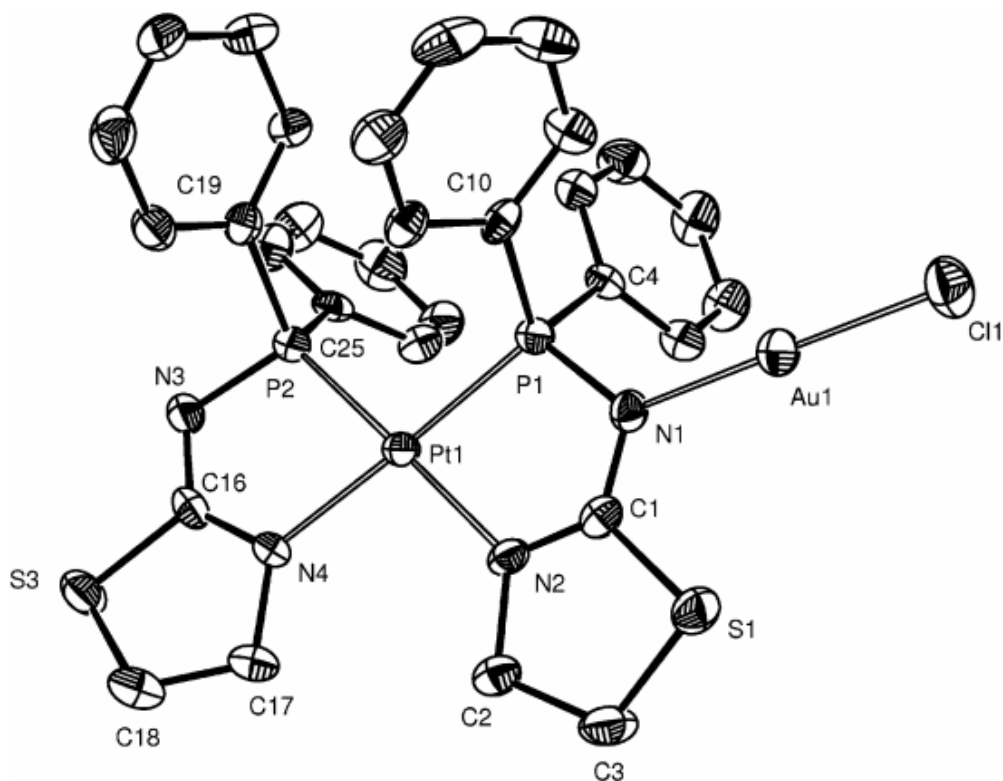


Figure 6.5. View of the molecular structure of compound **10** in 10·3 CHCl<sub>3</sub> (Displacement parameters include 50 % of the electron density).

Only in the case of *cis*-[Pt(**1**-H)<sub>2</sub>] stable compounds have been isolated, namely [*cis*-[Pt(**1**-H)<sub>2</sub>](AuCl)] (**10**) and [*cis*-[Pt(**1**-H)<sub>2</sub>](AuCl)<sub>2</sub>] (**11**). ORTEP views of **10** in 10·3CHCl<sub>3</sub> and **11** in 11·2CH<sub>2</sub>Cl<sub>2</sub> are shown in Figures 6.5. and 6.6., respectively. Selected bond distances and angles are reported in Table 6.2.

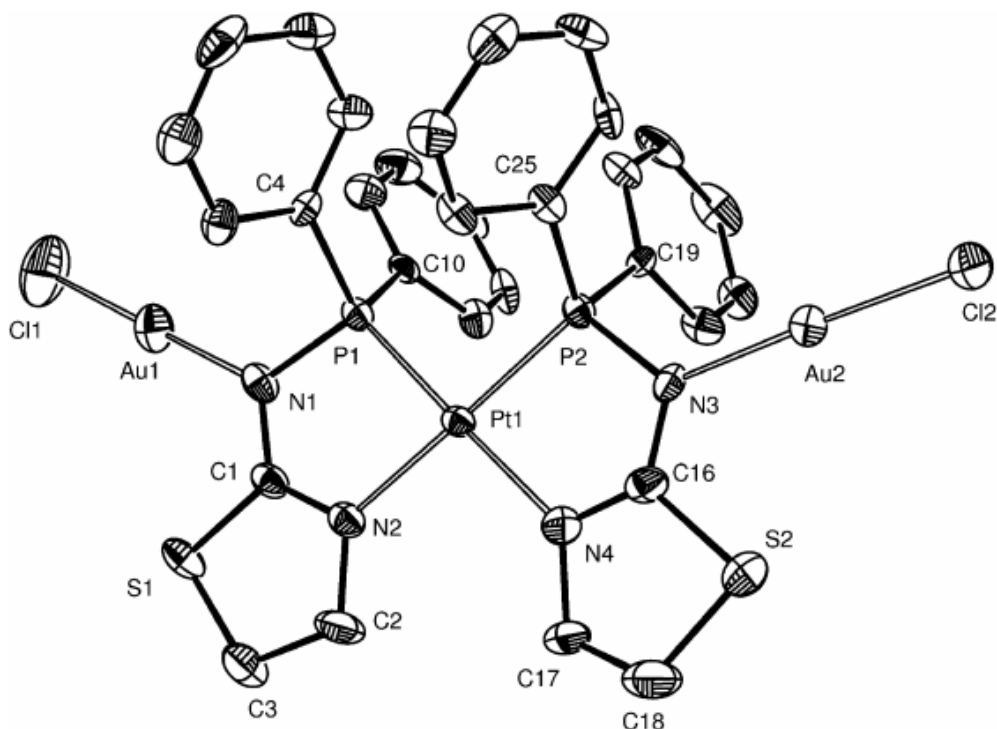


Figure 6.6. View of the molecular structure of compound 11 in 11.2 CH<sub>2</sub>Cl<sub>2</sub> (Displacement parameters include 50 % of the electron density).

Both **10** and **11** are neutral dimetallic complexes. In **10** only one of the exo-cyclic nitrogen atoms of *cis*-[Pt(**1-H**)<sub>2</sub>] is coordinated to an AuCl group whereas in **11**, each exo-cyclic N atom is coordinated to an AuCl group as a 2e donor. Coordination of the neutral Au<sup>I</sup> fragments to *cis*-[Pt(**1-H**)<sub>2</sub>] leaves the geometrical parameters of the latter almost unchanged, with only a small change on the N-C distances in the NCN groups. In **10**, the N1-Cl distance (1.346(7) Å) is only slightly longer than N3-Cl16 (1.322(7) Å) and than N1-Cl in *cis*-[Pt(**1-H**)<sub>2</sub>] (1.326(5) Å), while shortening of the N2-Cl distance is observed (1.305(7) Å) compared to N4-Cl16 (1.335(7) Å) and to N2-Cl in *cis*-[Pt(**1-H**)<sub>2</sub>] (1.327(5) Å). **11** behaves in the same way.

distance	10	11	angle	10	11
Au1-Cl1	2.2542(16)	2.242(3)	N2-Cl	1.305(7)	1.324(11)

Au2-Cl2	-	2.249(2)	N3-Cl6	1.322(7)	1.346(10)
Au1-N1	2.032(4)	2.028(7)	N4-Cl6	1.335(7)	1.302(12)
Au2-N3	-	2.027(7)	Cl1-Au1-N1	179.23(14)	178.4(2)
P1-N1	1.676(5)	1.680(7)	Cl2-Au2-N3	-	178.0(2)
P2-N3	1.665(5)	1.689(7)	P1-Pt1-N2	80.61(13)	80.9(2)
P1-Pt1	2.2353(14)	2.236(2)	P2-Pt1-N4	79.69(13)	81.3(2)
P2-Pt1	2.2501(15)	2.233(2)	P1-N1-Cl1	114.2(4)	115.3(6)
N2-Pt1	2.094(4)	2.093(7)	P2-N3-Cl6	111.6(4)	113.5(6)
N4-Pt1	2.080(4)	2.115(7)	N1-Cl1-N2	124.2(5)	122.1(8)
N1-Cl1	1.346(7)	1.354(11)	N3-Cl6-N4	126.8(5)	126.2(8)

Table 6.2. Selected bond distances [Å] and angles [°] for compounds **10** in 10-3 CHCl<sub>3</sub> and **11** in 11-2 CH<sub>2</sub>Cl<sub>2</sub>.

The Pt/Au complexes **10** and **11** are stable and no degradation has been observed upon exposure to air or moisture for days. Although **10** has been obtained in good yields, traces of compound **11** were always observed, even when [AuCl(tht)] is used in default. This implies that the addition of a second equivalent of AuCl to *cis*-[Pt(**11**-H)<sub>2</sub>] is only slightly slower than that of the first. Compound **10** could be easily separated from **11** by fractional crystallization. It is noticed that when cycles of dissolution in common solvents followed by evaporation of the solvent to dryness are applied to **10** and **11**, the quantity of complex dissolved gradually decreased, without appreciable decomposition. Compounds **10** and **11**

slowly and almost quantitatively crystallize from their freshly prepared saturated  $\text{CHCl}_3$  and  $\text{CH}_2\text{Cl}_2$  solutions, respectively.

Although typical for terminal AuCl moieties, no close Au...Au contacts are present in the crystal structures of **10** and **11** (minimum Au...Au separations: 6.3842(4) Å for **10** and 6.824(2) Å for **11**). The chlorine atoms of **10** are in fact involved in multiple H...Cl contacts, in particular with the solvent and the thiazole protons (Figure 6.7.).

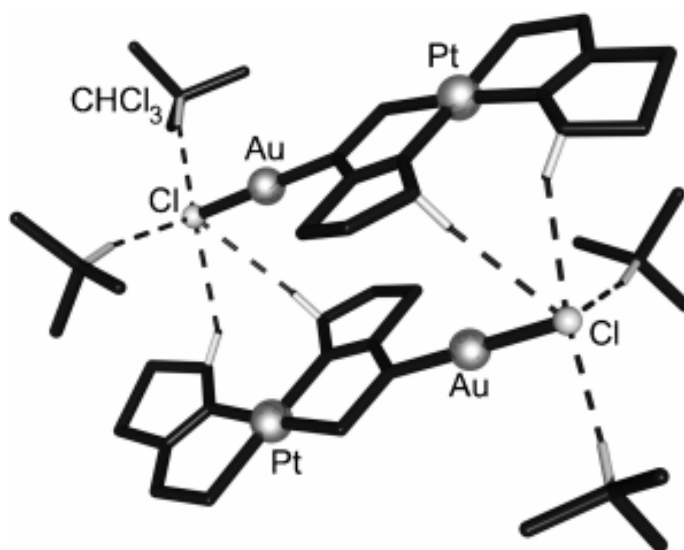


Figure 6.7. View of the crystal structure of 10-3  $\text{CHCl}_3$ , representing a pair of complexes, interconnected by H...Cl contacts and interacting with the solvent through the AuCl moiety. Dashed lines represent H...Cl contacts. White sticks represent the hydrogen atoms involved in these contacts. Protons and phenyls omitted for clarity.

Pairs of molecules adopt a head to tail arrangement and are disposed parallel to each other, forming layers of complex molecules which are in turn separated by layers of solvent (Figure 6.8.).

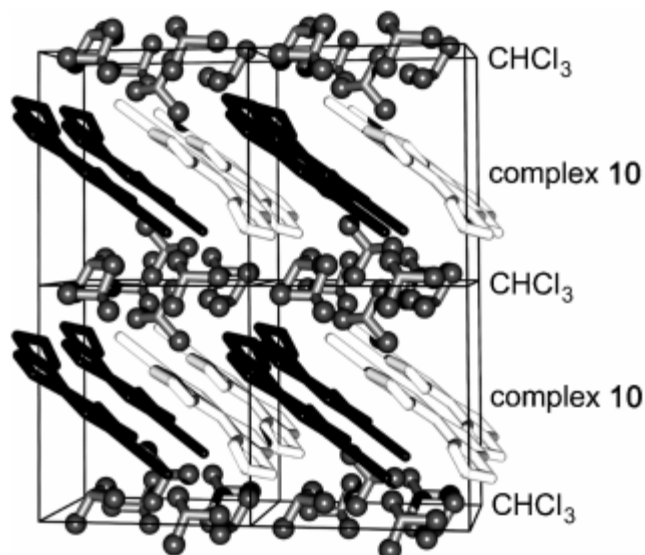


Figure 6.8. View of the crystal structure of 10·3 CHCl<sub>3</sub> along axis *c*, representing layers of parallel complex molecules separated by layers of solvent. Molecules of 10 oriented in the same direction are depicted with the same color. Figure 6.7.

Similar features are present in the crystal structure of **11**. In this case each CH<sub>2</sub>Cl<sub>2</sub> molecule bridges two adjacent complexes and interacts with the AuCl groups through H···Cl contacts (Figure 6.9).

Examples of polynuclear compounds containing  $\alpha$ -phosphino-amines and -imines bonded to two transition metal centers with both phosphorus and  $\alpha$ -N have been reported in the literature. They include complexes featuring mutually interacting metal centers,<sup>213</sup> dinuclear species bearing deprotonated Ph<sub>2</sub>PNHPPH<sub>2</sub> (dppa)<sup>214</sup> or Ph<sub>2</sub>PNHC<sub>6</sub>H<sub>4</sub>NHPPH<sub>2</sub>,<sup>215</sup> phosphine

[213] a) H. Nagashima, T. Sue, T. Oda, A. Kanemitsu, T. Matsumoto, Y. Motoyama, Y. Sunada, *Organometallics* 2006, 25, 1987-1994; b) Y. Sunada, T. Sue, T. Matsumoto, H. Nagashima, *J. Organomet. Chem.* 2006, 691, 3176-3182; c) D. Fenske, B. Maczek, K. Maczek, *Z. Anorg. Allg. Chem.* 1997, 623, 1113-1120; d) A. M. Baranger, R. G. Bergman, *J. Am. Chem. Soc.* 1994, 116, 3822-3835.

[214] a) R. Uson, A. Laguna, M. Concepcion Gimeno, *J. Chem. Soc., Dalton Trans.* 1989, 1883-1886; b) R. Uson, A. Laguna, M. Laguna, M. C. Gimeno, P. G. Jones, C. Fittschen, G. M. Sheldrick, *Chem. Commun.* 1986, 509-510; c) J. Ellermann, W. Wend, *Nouv. J. Chim.* 1986, 10, 313-320.

[215] P. A. Bella, O. Crespo, E. J. Fernandez, A. K. Fischer, P. G. Jones, A. Laguna, J. M. Lopez-de-Luzuriaga, M. Monge, *J. Chem. Soc., Dalton Trans.* 1999, 4009-4017.

functionalized macrocycles bridging transition metals<sup>216</sup> and metal carbonyl clusters.<sup>217</sup> At variance with their preparation, the strategy consisted in the reaction of an isolated mononuclear, difunctional metalloligand, whose connectivity is fully maintained in the heterodimetallic product.

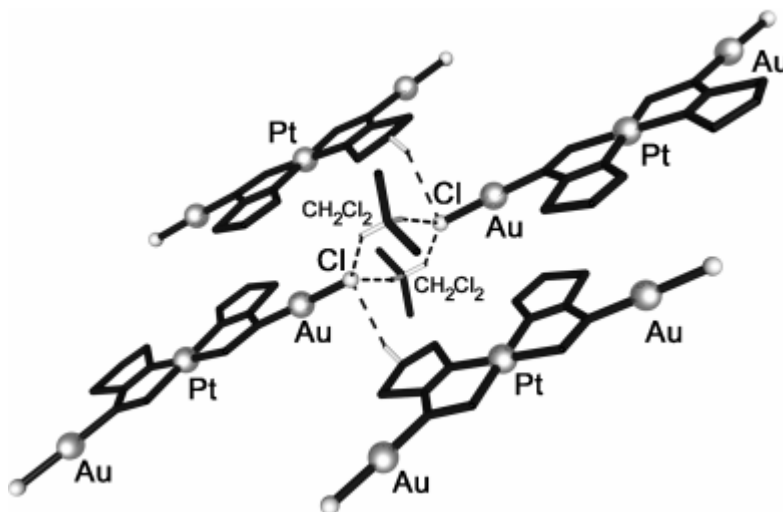


Figure 6.9. View of the crystal structure of 11-2 CH<sub>2</sub>Cl<sub>2</sub>. Dashed lines represent H...Cl contacts. White sticks represent the hydrogen atoms involved in these contacts. Protons and phenyls omitted for clarity.

This procedure has been used previously,<sup>218</sup> e.g. with  $[\text{Pd}(\text{dmba})\{\text{Ph}_2\text{PN}\cdots\text{C}(\cdots\text{O})\text{Me}\}]$  (dmba = *o*-C<sub>6</sub>H<sub>4</sub>CH<sub>2</sub>NMe<sub>2</sub>) to afford the metal-metal bonded I-D heterodimetallic coordination polymer  $[\text{Ag}\{\text{Pd}(\text{dmba})[\text{Ph}_2\text{PN}\cdots\text{C}(\cdots\text{O})\text{Me}]\}]_\infty$ .<sup>219</sup>

[216] J. Powell, C. J. May, *J. Am. Chem. Soc.* 1982, 104, 2636-2637.

[217] A. M. Z. Slawin, M. B. Smith, J. D. Woollins, *Chem. Commun.* 1996, 2095-2096.

[218] N. Oberbeckmann-Winter, P. Braunstein, R. Welter, *Organometallics* 2005, 24, 3149-3157.

[219] P. Braunstein, C. Frison, N. Oberbeckmann-Winter, X. Morise, A. Messaoudi, M. Bénard, M.-M. Rohmer, R. Welter, *Angew. Chem.* 2004, 116, 6246-6251; *Angew. Chem. Int. Ed.* 2004, 43, 6120-6125.

*Photophysical properties of cis-[Pt(1-H)<sub>2</sub>]*

Complex *cis*-[Pt(1-H)<sub>2</sub>] is the only one in the series that, upon exposure of the solid to CH<sub>3</sub>OH vapors, displays a luminescence visible to the naked eye under excitation with a conventional UV lamp for TLC analysis. Moreover, crystals of *cis*-[Pt(1-H)<sub>2</sub>] $\cdot$ 2CH<sub>3</sub>OH $\cdot$ CH<sub>3</sub>CN also displayed a visible luminescence, unlike those of *cis*-[Pt(1-H)<sub>2</sub>] $\cdot$ C<sub>6</sub>H<sub>5</sub>CH<sub>3</sub>.

This luminescent sensor property of *cis*-[Pt(1-H)<sub>2</sub>] led to a detailed investigation of the photophysical properties of this complex, both in solution and in the solid state, in the presence or not of alcohol vapors, and as a function of temperature.

Complex *cis*-[Pt(1-H)<sub>2</sub>] absorbs only in the UV region of the spectrum with a maximum at 300 nm (Figure 6.10.).

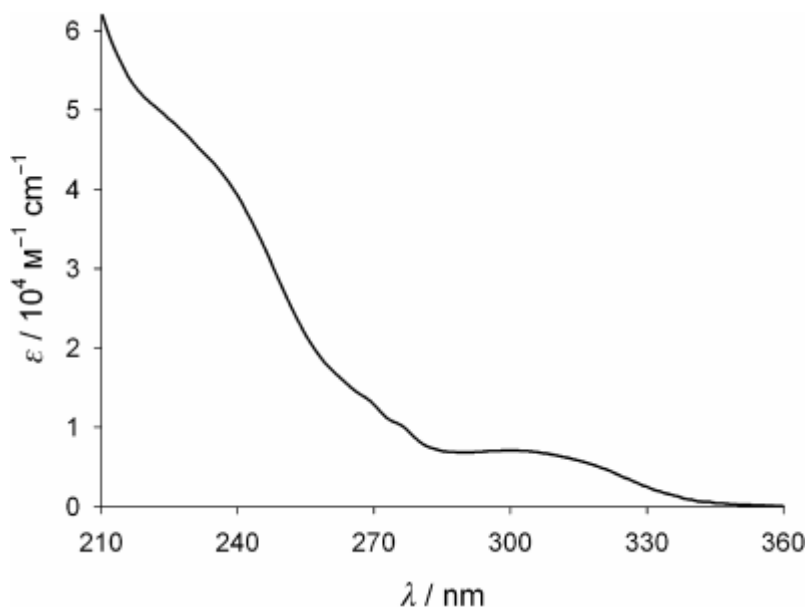


Figure 6.10. Absorption spectrum of complex *cis*-[Pt(1-H)<sub>2</sub>] in CH<sub>3</sub>OH solution at 298 K.

At 298 K solutions of *cis*-[Pt(1-H)<sub>2</sub>] in alcohols (C<sub>2</sub>H<sub>5</sub>OH:CH<sub>3</sub>OH 4:1 v/v), 2-methyltetrahydrofuran, chlorinated solvents (CH<sub>2</sub>Cl<sub>2</sub>:CHCl<sub>3</sub> 1:1 v/v) or butyronitrile do not exhibit

luminescence, either in air-equilibrated or in argon-saturated conditions, while in rigid matrix at 77 K a strong luminescence occurs (Figure 6.11.).

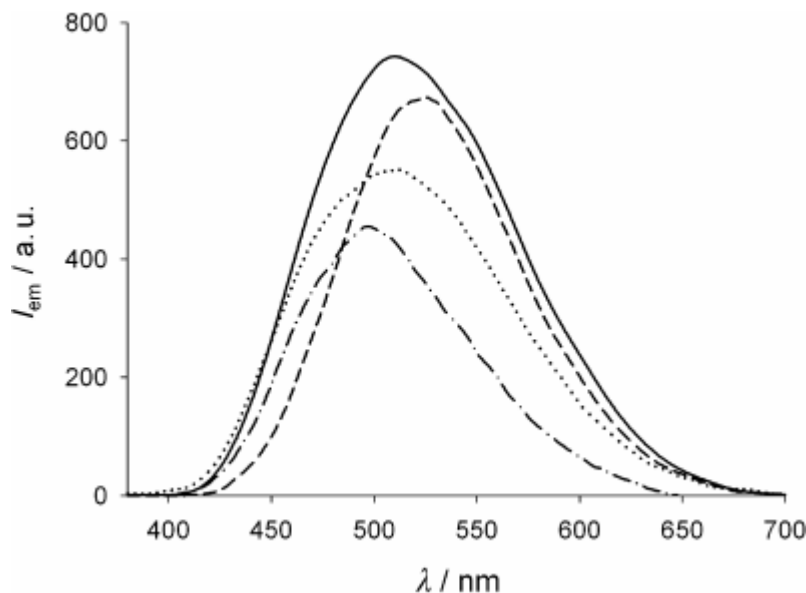


Figure 6.11. Emission spectra of complex *cis*-[Pt(1-H)<sub>2</sub>] in rigid matrix at 77 K of C<sub>2</sub>H<sub>5</sub>OH:CH<sub>3</sub>OH, 4:1 v/v (solid line), CH<sub>2</sub>Cl<sub>2</sub>:CHCl<sub>3</sub>, 1:1 v/v (dashed line), butyronitrile (dotted line), and 2-methyl tetrahydrofuran (dashed-dotted line). Emission intensities are directly comparable since these solutions have the same absorbance at the excitation wavelength ( $\lambda_{\text{ex}} = 315 \text{ nm}$ ).

Slight changes in the band maximum, shape and excited-state lifetimes (Table 6.3.) and more pronounced differences in the relative emission intensities were observed as a function of solvent.

The nature of the emitting excited state is not easy to ascertain. A simplified classification based on a localized molecular orbital approach<sup>220</sup> (metal- or ligand-centered, metal-to-ligand or ligand-to-metal charge transfer) is not satisfactory for this platinum(II) complex as states of

[220] V. Balzani, V. Carassiti, *Photochemistry of Coordination Compounds*, Academic Press, London, New York, 1970, p. 432 pp.

mixed nature are likely to exist.<sup>221</sup> The rather long lifetime and the large energy difference between absorption and emission bands suggest that this excited state is formally a triplet.

matrix	$\lambda_{\max}/\text{nm}$	$I_{\text{rel}}/\text{a.u.}$	$\tau/\mu\text{s}$
C <sub>2</sub> H <sub>5</sub> OH:CH <sub>3</sub> OH 4:1 v/v	510	100	25
CH <sub>2</sub> Cl <sub>2</sub> :CHCl <sub>3</sub> 1:1 v/v	525	90	15
butyronitrile	510	75	20
2-methyl tetrahydrofuran	495	60	20

Table 6.3. Photophysical properties of complex *cis*-[Pt(1-H)<sub>2</sub>] in rigid matrix at 77 K. Relative intensities are directly comparable since the investigated solutions have the same absorbance at the excitation wavelength ( $\lambda_{\text{ex}} = 315\text{ nm}$ ).

Free ligand **1** in a butyronitrile rigid matrix shows an unstructured and very weak phosphorescence band with a maximum at 440 nm, insensitive to solvent polarity and with a longer lifetime ( $\tau = 5\text{ ms}$ ) compared to complex *cis*-[Pt(**1-H**)<sub>2</sub>]. The phosphorescence band maximum of complex *cis*-[Pt(**1-H**)<sub>2</sub>] is red-shifted compared to that of free ligand **1** and is quite sensitive to solvent nature and temperature (see Table 6.3.), suggesting that the corresponding transition is not merely ligand centred, but has a charge-transfer character.

Because of the huge increase of luminescence intensity for complex *cis*-[Pt(**1-H**)<sub>2</sub>] upon lowering the temperature from 298 to 77 K, the luminescence intensity and excited-state lifetimes as a function of temperature have been investigated in more detail. Figure 6.12. shows the changes in emission lifetime and band maximum for butyronitrile solution (similar results have been obtained in a CH<sub>2</sub>Cl<sub>2</sub>:CH<sub>3</sub>OH mixture) from 85 to 125 K. A strong

[221] J. A. Williams, *G. Top. Curr. Chem.*, in press.

discontinuity is present in the temperature range 100-120 K, where the band maximum shifts strongly to the red (from 495 to 550 nm), the luminescence intensity decreases by a factor of ca. 20 and the excited-state lifetime slightly decreases (about 1.5 time). At temperatures above 125 K, no substantial change in the emission band shape and position is observed in comparison to those recorded at 120 K, but the emission intensity decreases and complete loss of luminescence occurs above 160 K. In this temperature range, butyronitrile becomes completely fluid ( $T_f = 161$  K) and deactivation by non-radiative processes becomes faster.

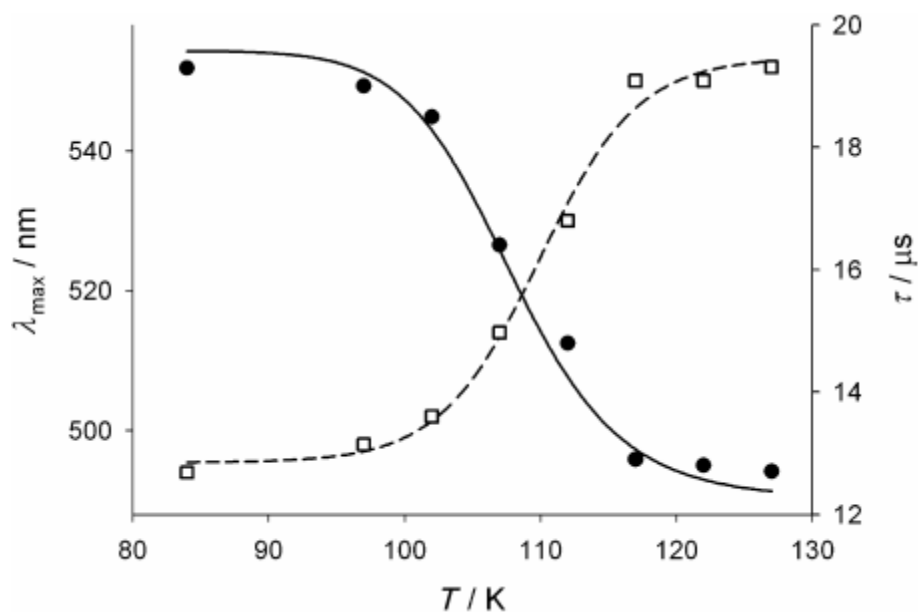


Figure 6.11. Emission lifetime (solid circles, right axis) and emission band maximum (empty squares, left axis) as a function of temperature for complex *cis*-[Pt(1-H)<sub>2</sub>] in butyronitrile.  $\lambda_{\text{ex}}=315$  nm. The solid line represents the fitted curve according to eq. 40.

Red-shifts of the emission bands upon increasing temperature have been reported for other complexes, in which the emitting excited state has a charge transfer character.<sup>222,223</sup> This

[222] See e.g.: (a) F. Barigelletti, A. Juris, V. Balzani, P. Belser, A. von Zelewsky, *J. Phys. Chem.* 1987, 91, 1095-1098; (b) F. Barigelletti, P. Belser, A. von Zelewsky, A. Juris, V. Balzani, *J. Phys. Chem.* 1985, 89, 3680-3684.

phenomenon is a rigidochromic effect,<sup>224</sup> i.e. a large color change of an emission as a function of the rigidity (viscoelasticity) of the medium. Matrix softening may remove viscosity-dependent potential barriers presented by the solvent cage, thus enabling the complex to relax to lower energy nuclear configurations corresponding to smaller equilibrium distances between the metal center and the ligands, not accessible in a rigid matrix.<sup>223</sup> According to this model, decrease of lifetimes ( $\tau$ ) can be accounted for by an additional radiationless decay process of the emitting excited state as the temperature increases. In particular, values of  $\tau$  can be fitted (solid line in Figure 6.11.) according to the following empirical equation:<sup>222</sup>

$$\frac{1}{\tau} = \frac{k_0 + B}{\{1 + \exp[C(1/T - 1/T_B)]\}} \quad (40)$$

which describes a stepwise behavior centered at temperature  $T_B$  ( $k_0$  is a temperature-independent term,  $B$  is the value attained by  $1/\tau$  at  $T \gg T_B$  and  $C$  is a temperature related to the smoothness of the step). At low temperatures (85-100 K in the present case), vibrational motions of the complex occur much faster than reorientational and translational rearrangements of the solvent molecules, so that the solvent medium behaves as a rigid cage and some radiationless processes, in particular the low-frequency ones, are inhibited. The fitting of the data with this model in the temperature range 85-125 K is good and leads to a value of  $T_B = 110$  K.

To better understand the aforementioned effect of  $\text{CH}_3\text{OH}$  on the luminescence of complex  $\text{cis}[\text{Pt}(\text{I-H})_2]$ , the emission properties of a solid sample obtained by evaporation from toluene solution before and after exposure to  $\text{CH}_3\text{OH}$  vapors at room temperature have been

---

[223] a) P. J. Giordano, S. M. Fredericks, M. S. Wrighton, D. L. Morse, *J. Am. Chem. Soc.* 1978, 100, 2257-2259; (b) R. J. Watts, J. S. Harrington, J. van Houten, *J. Am. Chem. Soc.* 1977, 99, 2179-2187.

[224] M. Wrighton, D. L. Morse, *J. Am. Chem. Soc.* 1974, 96, 998-1003.

investigated. In the presence of CH<sub>3</sub>OH a much stronger luminescence<sup>225</sup> is observed (Figure 6.12.) with a maximum shifted to the blue (Table 6.4.).

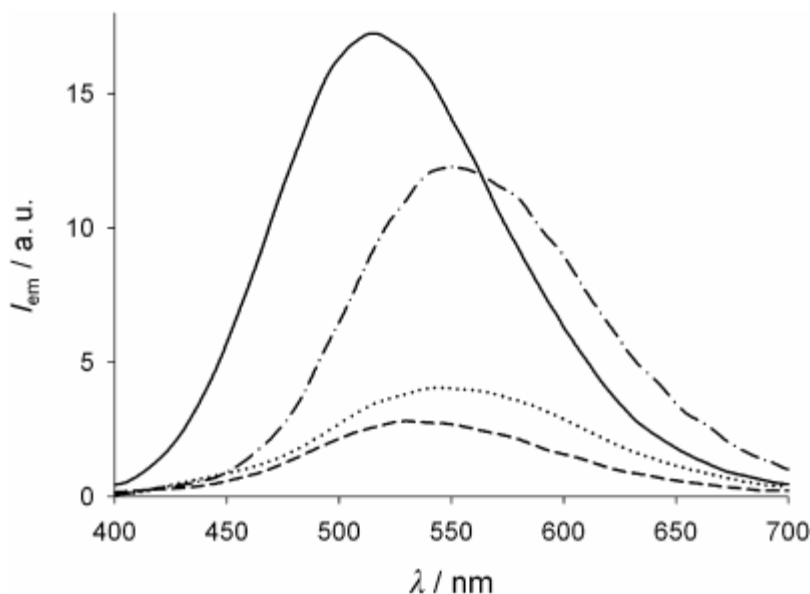


Figure 6.12. Emission spectra of complex *cis*-[Pt(1-H)<sub>2</sub>] crystallized from toluene (dashed line) or exposed to CH<sub>3</sub>OH (solid line), CH<sub>3</sub>CH<sub>2</sub>OH (dashed-dotted line), or (CH<sub>3</sub>)<sub>2</sub>CHOH (dotted line) at room temperature.  $\lambda_{\text{ex}}=313\text{nm}$ .

This vapoluminescence effect observed upon exposure to CH<sub>3</sub>OH vapours of complex *cis*-[Pt(1-H)<sub>2</sub>] crystallized from toluene, cannot be attributed to a disruption of intermolecular Pt...Pt interactions, as in the case of previously reported Pt<sup>II</sup> complexes.<sup>226</sup>

[225] Emission quantum yields cannot be measured with our experimental equipment, but the data reported correspond to an average of multiple emission spectra recorded without moving the sample from the spectrofluorimeter. Therefore, the different emission intensities of the solid sample in different experimental conditions are meaningful within the large experimental error (20%).

[226] For some examples, see: (a) W. Lu, M. C. W. Chan, N. Zhu, C.-M. Che, Z. He, K.-Y. Wong, *Chem. Eur. J.* 2003, 9, 6155-6166. (b) C. E. Buss, K. R. Mann, *J. Am. Chem. Soc.* 2002, 124, 1031-1039. (c) S. M. Drew, D. E. Janzen, C. E. Buss, D. I. MacEwan, K. M. Dublin, K. R. Mann, *J. Am. Chem. Soc.* 2001, 123, 8414-8415.

Table 6.4. Photophysical properties of complex  $cis\text{-[Pt(1-H)}_2]$  at 298 and 77 K for solid samples exposed to different alcohol vapors.  $\lambda_{\text{ex}} = 315 \text{ nm}$ .

vapour	298 K		77 K	
	$\lambda_{\text{max}}/\text{nm}$	$\tau/\mu\text{s}$	$\lambda_{\text{max}}/\text{nm}$	$\tau/\mu\text{s}$
- <sup>a</sup>	530	0.2, 1.0	520	20
CH <sub>3</sub> OH	520	0.2, 1.0	505	20
CH <sub>3</sub> CH <sub>2</sub> OH	550	0.2, 1.0	540	20
(CH <sub>3</sub> ) <sub>2</sub> CHOH	540	0.2, 1.0	530	20

<sup>a</sup> crystals obtained by toluene solutions without exposure to any alcohol vapour.

Indeed, the single crystal X-ray diffraction analysis of complex  $cis\text{-[Pt(1-H)}_2]$  crystallized from toluene, i.e.  $cis\text{-[Pt(1-H)}_2]\cdot\text{C}_6\text{H}_5\text{CH}_3$ , revealed a molecular structure almost identical to that found in  $cis\text{-[Pt(1-H)}_2]\cdot 2\text{CH}_3\text{OH}\cdot\text{CH}_3\text{CN}$ , with a shorter minimum Pt...Pt intermolecular distance: 5.9267(2) Å for  $cis\text{-[Pt(1-H)}_2]\cdot\text{C}_6\text{H}_5\text{CH}_3$  and 8.9268(2) Å for  $cis\text{-[Pt(1-H)}_2]\cdot 2\text{CH}_3\text{OH}\cdot\text{CH}_3\text{CN}$ . The crystal data for  $cis\text{-[Pt(1-H)}_2]\cdot\text{C}_6\text{H}_5\text{CH}_3$  are reported in the CIF file deposited in the CCDC database (CCDC code: 653227). In the solid state structure of  $cis\text{-[Pt(1-H)}_2]\cdot 2\text{CH}_3\text{OH}\cdot\text{CH}_3\text{CN}$ , a CH<sub>3</sub>OH molecule forms a hydrogen bond with each exo-cyclic nitrogen atoms of the complex (Figures 6.3. and 6.13.).

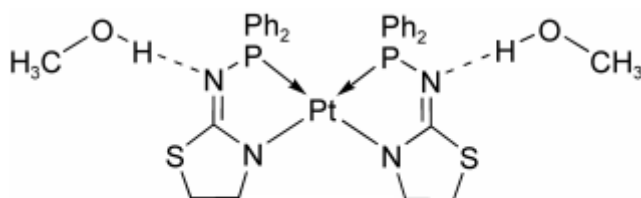


Figure 6.13. Graphical representation of  $cis\text{-[Pt(1-H)}_2]$  forming hydrogen bond with two methanol molecules.

Because of the *structural* effect of the N...HOCH<sub>3</sub> hydrogen bonding, complex *cis*-[Pt(II-H)<sub>2</sub>]-2CH<sub>3</sub>OH·CH<sub>3</sub>CN has a more rigid structure than *cis*-[Pt(II-H)<sub>2</sub>]-C<sub>6</sub>H<sub>5</sub>CH<sub>3</sub>. This may explain the increase of emission quantum yield because deactivation by non-radiative decays is slower in a more rigid structure. Remarkable electronic effects of this hydrogen bonding on *cis*-[Pt(II-H)<sub>2</sub>] and therefore on the luminescence properties are unlikely. The NMR spectroscopic data of *cis*-[Pt(II-H)<sub>2</sub>] in CH<sub>3</sub>OH solutions are in fact very similar to those in CDCl<sub>3</sub> and the molecular structures of *cis*-[Pt(II-H)<sub>2</sub>] in *cis*-[Pt(II-H)<sub>2</sub>]-2CH<sub>3</sub>OH·CH<sub>3</sub>CN and in *cis*-[Pt(II-H)<sub>2</sub>]-C<sub>6</sub>H<sub>5</sub>CH<sub>3</sub> are almost identical. In the crystals of *cis*-[Pt(II-H)<sub>2</sub>]-2CH<sub>3</sub>OH·CH<sub>3</sub>CN molecules of acetonitrile were also present. On the other hand, acetonitrile vapours do not lead to luminescent properties for dry *cis*-[Pt(II-H)<sub>2</sub>].

A vapoluminescent effect was also observed upon exposure of solid *cis*-[Pt(II-H)<sub>2</sub>] to CH<sub>3</sub>CH<sub>2</sub>OH (Figure 6.12.), but the increase in the luminescence intensity is lower and the band maximum is more shifted to the red (Table 6.4.). (CH<sub>3</sub>)<sub>2</sub>CHOH has a very modest effect (Figure 6.12.): slight increase in emission intensity and small red-shift of the band maximum (Table 6.4.), while CH<sub>3</sub>(CH<sub>2</sub>)<sub>3</sub>OH does not lead to any significant increase in luminescence or change in the emission band maximum. Luminescence intensity decays of these solid samples are multiexponential and they can be fitted by using two families of lifetimes ( $\tau_1 = 0.2 \mu\text{s}$ ,  $\tau_2 = 1.0 \mu\text{s}$ ) in which the percentage of the longer lifetime increases upon increasing emission quantum yield.

The solid samples discussed above show a much stronger luminescence at 77 K, a lifetime of 20  $\mu\text{s}$ , and a significantly blue-shifted emission maximum compared to the corresponding values at room temperature (Table 6.4.), confirming the charge transfer character of the corresponding electronic transition. The emission bands recorded under these experimental conditions are very similar in shape and position to those recorded in the corresponding rigid matrix. Therefore, the emission in the solid state is of the same nature as that observed for

diluted solutions (ca.  $5 \times 10^{-5}$  M) at 77 K, i.e. it is a property of the isolated molecule, thus confirming that Pt...Pt interactions do not play any role in the luminescence properties of these solid samples.

By analogy with complexes containing a coordinated P,O-phosphanyl enolate ligand,<sup>210a</sup> which react with softer electrophiles such as transition metal centers at the enolate carbon  $\alpha$  to P, it has been provided here further examples showing that complexes containing an isoelectronic P,N-phosphanyl iminolate chelate can also lead to heterodimetallic complexes in a controlled way. With the latter systems, the advantage is that the coordination geometry of the P-N nitrogen atom remains planar upon metalation, which simplifies the stereochemical issues one encounters with the corresponding P-C system since upon metalation, the carbon atom becomes a  $sp^3$ -hybridized stereogenic center.

It has been found that rather minor stereoelectronic differences in the ligands may significantly affect the chemical and physical properties of the related complexes. The vapoluminescence properties of *cis*-[Pt(II-H)] prompts the study of the coordination properties of ligand II toward less precious metals, in order to fine tune their potential activity as sensors. The rationalization of the unprecedented H-bonding rigidochromic effect of the alcohol will enable better tuning these structural and physical properties. .

## 6.2. Crown Ether containing Ru(II) Complexes

In order to evaluate the possibility of constructing optical sensors capable of detecting metal cations in biochemical, environmental and industrial analysis, the properties of cage-type ligands acting as ditopic receptors have been initially studied. All the measurements on the benzo-crown ether 4-styrylpyridine (**2**), benzo-crown ether 2-styrylphenanthroline (**3**), and benzo-crown ether 2-azastyrylpyridine (**4**) ligands (shown in Figure 6.14.) have been carried out in air-equilibrated MeCN solution at room temperature.

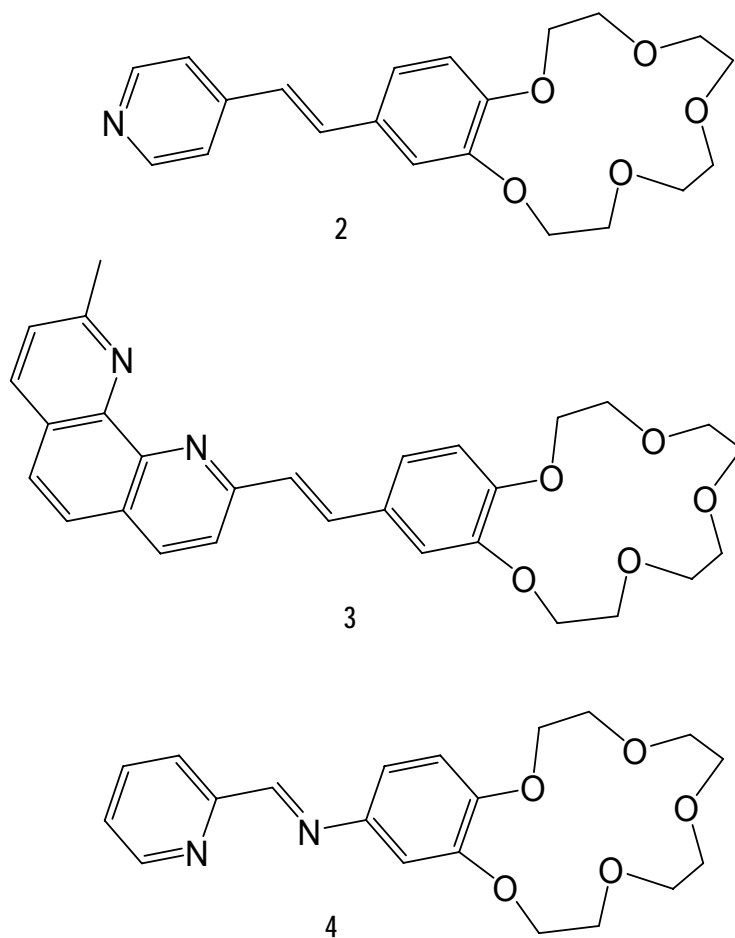


Figure 6.14. Formulas of the investigated ditopic receptors.

The absorption spectra of the ditopic ligands, shown in Figure 6.15., exhibit a relatively intense band in the near UV region ( $\lambda_{\text{max}}$  around 350 nm) that can be roughly attributed to  $\pi-\pi^*$  transitions.

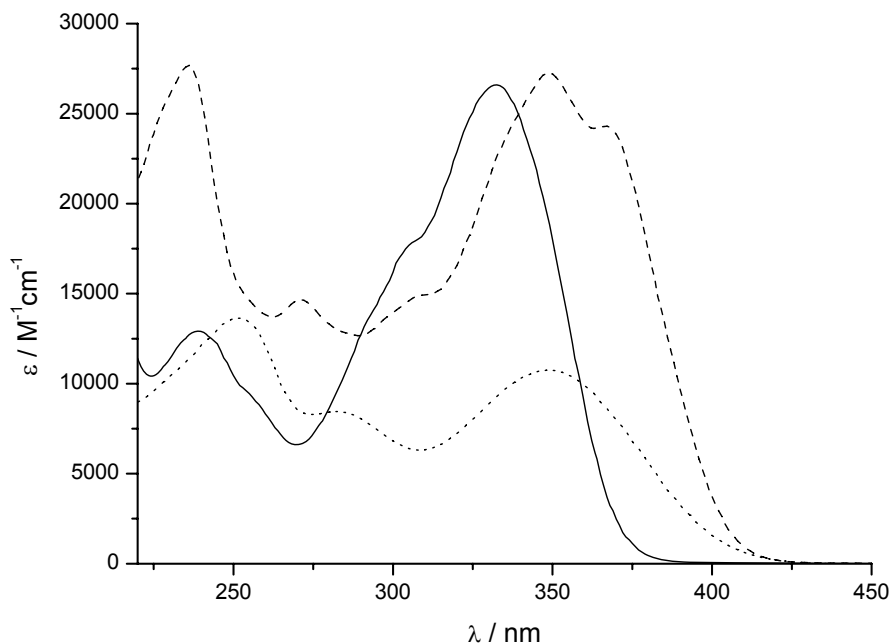


Figure 6.15. Absorption spectra of the ligands (2, solid line; 3 dashed line, 4 dotted line).

Upon irradiation with UV light, compounds **2** and **3** undergo a *trans-cis* photoisomerization process reaching a photostationary state. Laziness prevents investigation of the photoisomerization of ligand **4**. Since the absorption spectrum of the *cis* isomer is not known because the photoisomerization process does not reach completeness, an elegant method is used to obtain the absorption spectrum of the *cis* isomer.<sup>227</sup> For a photoreversible system, in absence of side reactions, and assuming that the ratio of the quantum yields of *trans-cis* photoisomerization and *cis-trans* photoisomerization at any wavelength is constant, such as within the same absorption band, the absorption spectrum of the *cis* isomer can be calculated

[227] E. Fischer, *J. Phys. Chem.*, 1967, 71, 3704.

mixing the photostationary states reached irradiating at two different wavelengths (see Figures 6.16. and 6.17.).

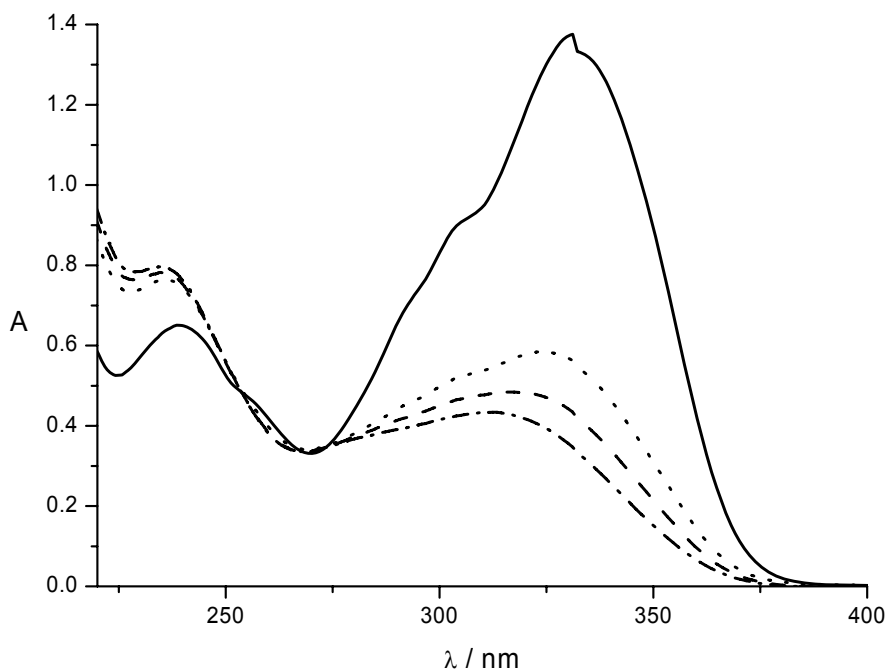


Figure 6.16. Absorption spectra of *trans*-2 (black line) and the photostationary states reached irradiating at 313 nm (dotted line) and at 365 (dashed line); the calculated *cis*-1 absorption spectrum is shown in dot-dashed line style.

The performed experiments seem to indicate that the quantum yield of the photoreaction is higher for ligand **2** compared to ligand **2** since the former photostationary states are closer to *cis*-**2**. From a qualitative view point, the considerable changes in the absorption spectrum are induced by very short exposure (few seconds) to solar light or to the excitation light of the spectrofluorimeter accounting for high quantum yields of photoisomerization.

The photostationary states reached in this way are stable in the dark; however, upon irradiation with 235-nm light, reaching a higher excited state, a different photostationary state is obtained.

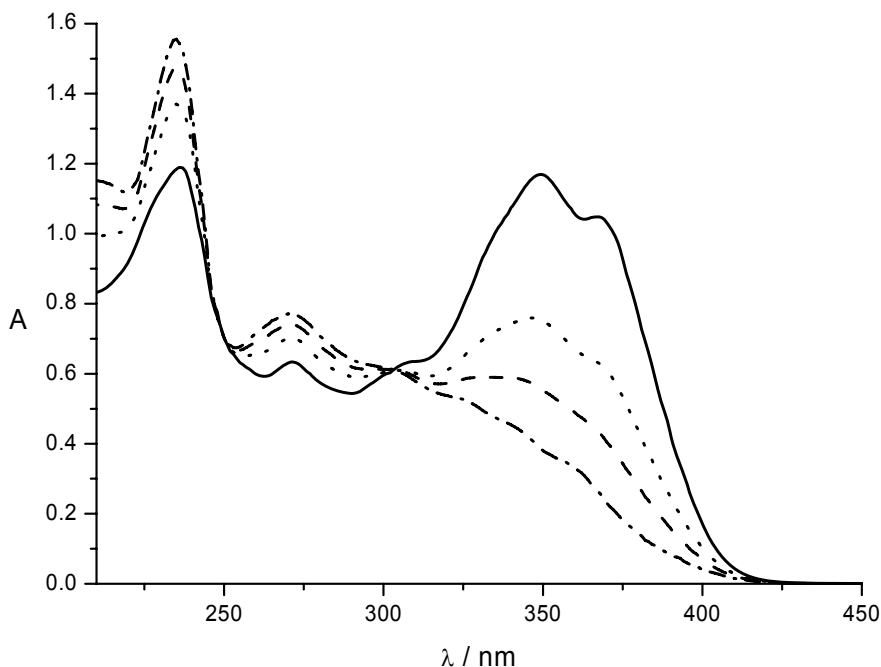


Figure 6.17. Absorption spectra of *trans*-**3** (black line) and the photostationary states reached irradiating at 313 nm (dotted line) and at 365 (dashed line); the calculated *cis*-**3** absorption spectrum is shown in dot-dashed line style.

As far as the emission properties are concerned, ditopic receptors **2** and **3** show weak emission bands with  $\lambda_{\text{max}}$  around 450 nm that decrease during the photoisomerization reaction.

In order to provide quantitative informations on ligands as ditopic receptors, titration experiments have been performed with protons and metal cations selectively bound to the aromatic amine units and to the crown ether moieties. It is expected a bathochromic shift of the absorption spectrum of the ligands upon cation recognition by the aromatic amine units, while a hypsochromic shift is instead expected upon cation interaction with the crown ether units. Protons and transition metal ions are expected to interact with aromatic amine units, while alkali and alkaline earth metal ions are expected to coordinate crown ether units.

In fact, titration with triflic acid leads to stoichiometric protonation of the pyridine moiety of compound **2**. As shown in Figure 6.18, the maximum of the absorption band exhibits a bathochromic shift of about 60 nm. The protonated form of compound **2** undergoes photoisomerization upon UV light irradiation and does not show any emission.

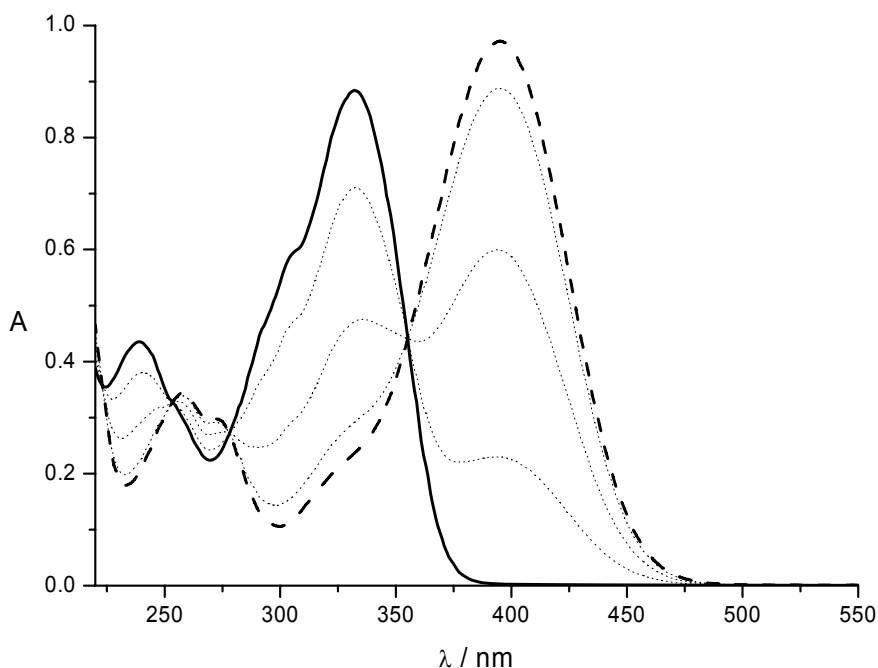


Figure 6.18. Absorption spectra of *trans*-**2** (solid line) that undergoes stoichiometric protonation (*trans*-**2**H<sup>+</sup> is the dashed line).

The receptor properties of the crown ether moiety of compound **2** have also been investigated. As shown in Figures 6.19., titration of compound **2** with Mg(ClO<sub>4</sub>)<sub>2</sub> causes absorption changes upon addition of an excess of Mg<sup>II</sup> ions, as expected by known high selectivity of benzo-crown with five oxygen towards small (K<sup>+</sup> or Na<sup>+</sup>) alkali and alkaline earth metal ions. Anyway, resulting hypsochromic shift of the maximum of the absorption band of **2** because of the lowered electron-donor ability of the heteroatoms of the crown ether moiety is

observed. Furthermore the data seem to indicate that complexes with different stoichiometry are present in solution.

Possible changes in the receptor capability of the crown ether moiety induced by protonation and/or *trans-cis* isomerization should be under investigation.

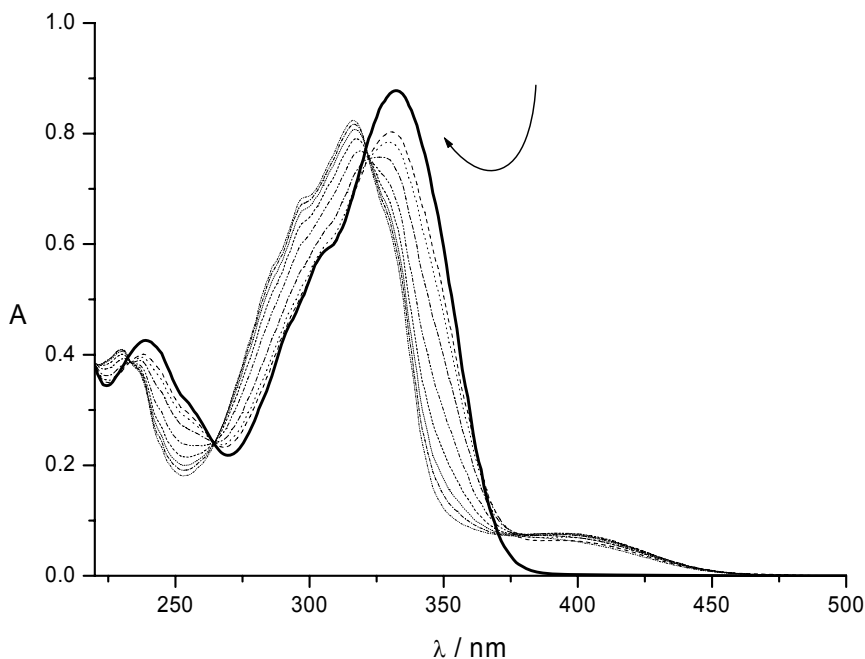


Figure 6.19. Absorption spectra of *trans*-2 (solid line) changing upon addition of  $\text{Mg}(\text{ClO}_4)_2$ .

The receptor properties of the crown ether moiety of compound **3** have been investigated upon titration with  $\text{Mg}(\text{ClO}_4)_2$ . The changes observed (Figure 6.20.) indicate again the low affinity of the used crown ether for  $\text{Mg}^{\text{II}}$ .

Because the phenanthroline moiety of compound **3** can compete with the crown ether for the  $\text{Mg}^{\text{II}}$  ion complexation, the titration experiments have been repeated by using the protonated form of compound **3** in which the phenanthroline is engaged with the proton. As shown in Figure 6.21. clear isosbestic points are obtained. The complexation stoichiometry, as

well as possible changes in the receptor property of the crown moiety induced by photoisomerization, are under investigation.

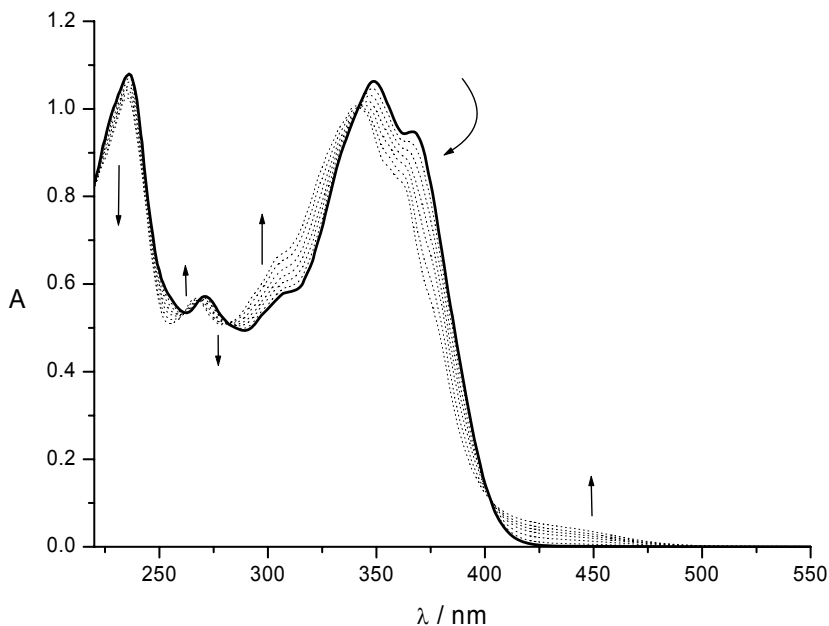


Figure 6.20. Absorption spectra of *trans*-3 (solid line) changing upon addition of  $\text{Mg}(\text{ClO}_4)$ .

Because it is known that the phenanthroline is complexed by the  $\text{Zn}^{\text{II}}$  ions, compound **3** has been also titrated with a solution of  $\text{Zn}^{\text{II}}$  ions. As shown in Figure 6.22, clear isosbestic points are obtained upon addition of one half equivalent of  $\text{Zn}^{\text{II}}$ , according to the high coordination number of  $\text{Zn}^{\text{II}}$ , forming the  $\text{Zn}^{\text{II}}\mathbf{3}_2$  equilibrium mixture then disrupted for further addition of  $\text{Zn}^{\text{II}}$  ions.

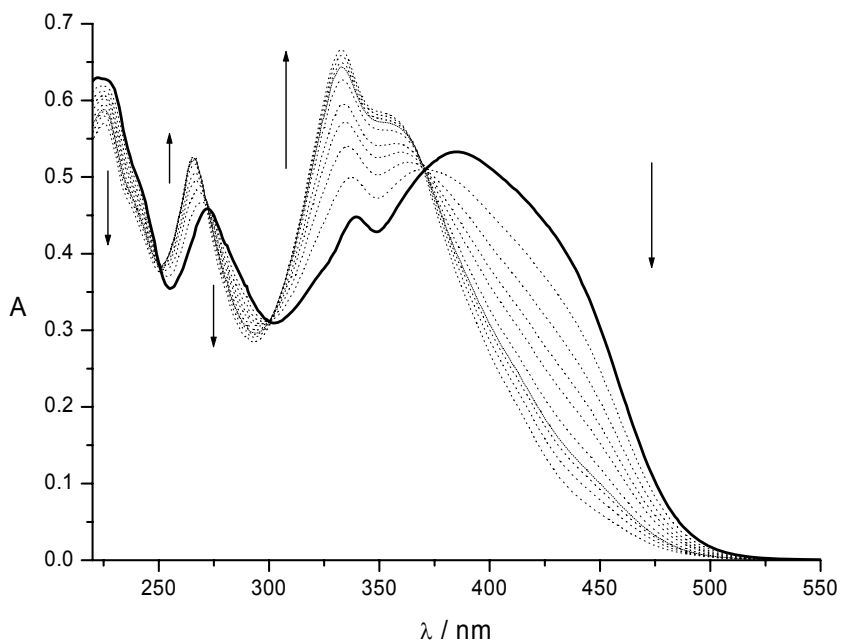


Figure 6.21. Absorption spectra of *trans*-3H<sup>+</sup> (solid line) changing upon addition of Mg(ClO<sub>4</sub>).

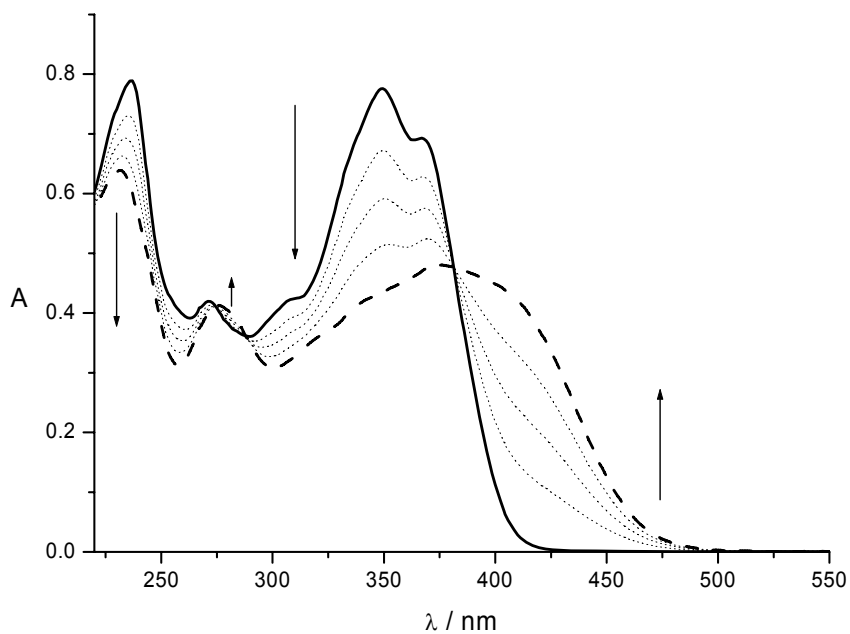


Figure 6.22. Absorption spectra of *trans*-3 (solid line) coordinated by Zn<sup>II</sup> ions (dashed line represents absorption spectrum of Zn<sup>II</sup>3<sub>2</sub>).

The same considerations can be done in the case of ligand **4**. A bathochromic shift of its absorption spectrum follows proton coordination by the N lone pairs in the aromatic residue while hypsochromic shift occurs upon alkali and alkaline earth metal ions coordination of the crown ether unit as shown in Figure 6.23. titrating with  $\text{Mg}(\text{ClO}_4)_2$ . The binding constant calculated using a 1:1 binding process model is  $10^{5.5}$ , close to the values obtained for the other two ligands previously discussed. These results account for negligible effect played by the aromatic residue attached to the crown ether on the latter binding properties.

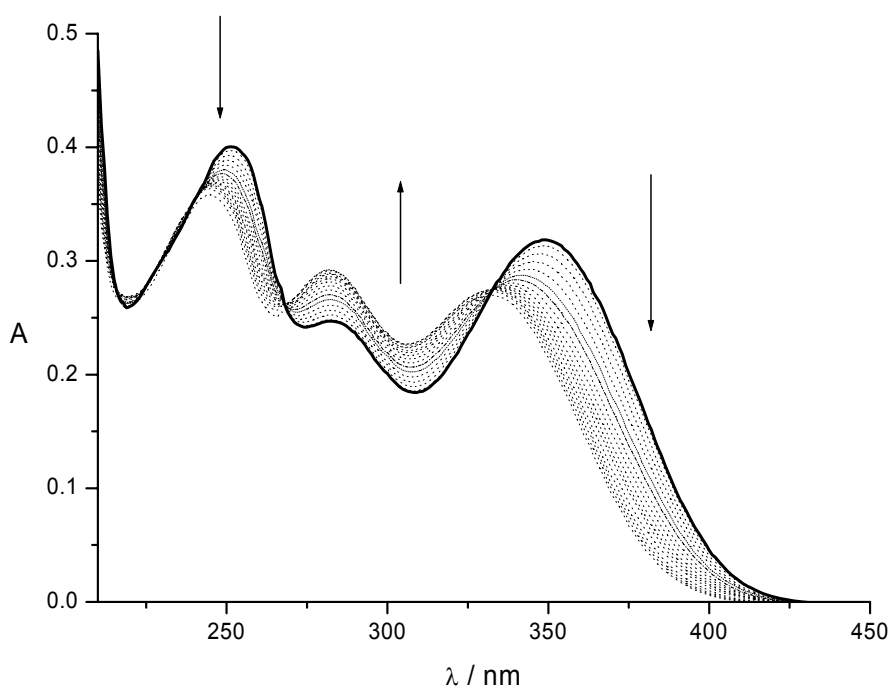


Figure 6.23. Absorption spectra of *trans*-4 (solid line) upon addition of an excess of  $\text{Mg}(\text{ClO}_4)_2$ .

It has to be noted how two of benzo-crown-15-ether-5 units can coordinate bigger ions such as  $\text{Ba}^{\text{II}}$  producing absorption spectral changes analogous to those observed for the smaller  $\text{Mg}^{\text{II}}$  through the formation of sandwich complexes. Moreover, binding constants calculated using a two ligands per metal ion model coincide with the product of two successive 1:1 binding events accounting for lack of selectivity towards  $\text{Mg}^{\text{II}}$  and  $\text{Ba}^{\text{II}}$ .

The aforementioned ditopic ligands **2**, **3**, and **4** are then attached to Ru<sup>II</sup> metal ions containing two 2,2'-bipyridyl ligands through the aromatic amine residue leading to metal complexes that can be used as photoluminescence compounds capable of drastically changing their luminescence upon interaction of the free crown ether residue with alkali and alkaline earth metal ions, excited state reactants in energy and electron transfer processes. More precisely, Ru<sup>II</sup> complex luminescence is expected to be quenched because of charge-transfer interaction with the electron donor crown ether moieties. So alkali and alkaline earth metal ions can be detected through recovering Ru<sup>II</sup> complex luminescence.

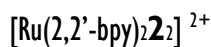
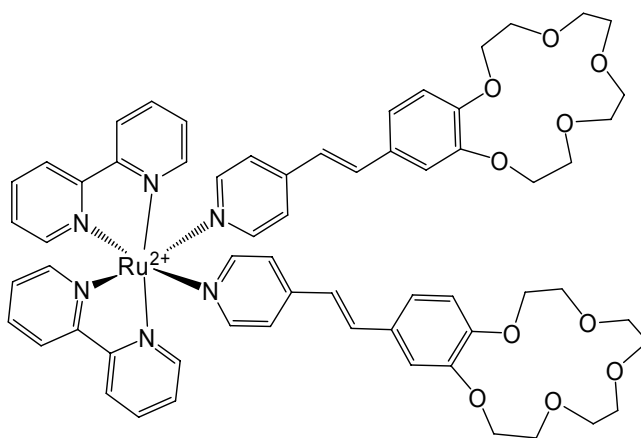
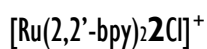
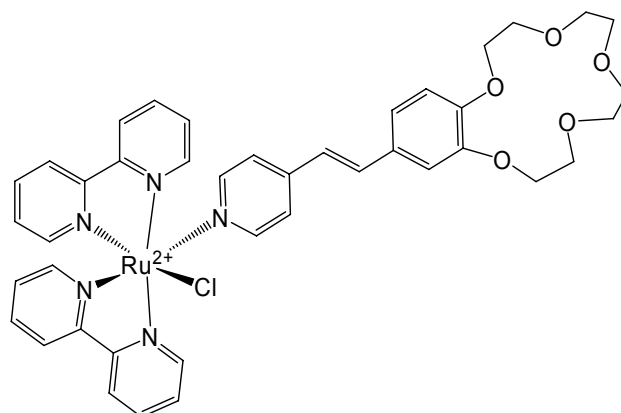


Figure 6.24. Formula of  $[\text{Ru}(2,2'\text{-bpy})_2\text{Cl}]^+$  and  $[\text{Ru}(2,2'\text{-bpy})_2]^{2+}$  complexes as hexafluorophosphate salts.

$\text{Ru}^{\text{II}}$  complexes containing two 2,2'-bipyridyl ligands and one or two **2** ditopic ligands have been synthesized and are shown in Figure 6.24.

The absorption spectra of solution of  $[\text{Ru}(2,2'\text{-bpy})_2\mathbf{2}\text{Cl}]^{2+}$  and  $[\text{Ru}(2,2'\text{-bpy})_2\mathbf{2}_2]^{2+}$  as hexafluorophosphate salts are shown in Figure 6.25. They exhibit a characteristic absorption band in the visible region of the spectrum confidently assigned to metal to ligand charge transfer (MLCT,  $d \rightarrow \pi^*$ ), and other two absorption bands localized on the two different ligands (LC,  $\pi \rightarrow \pi^*$ ) where the spike at higher energy is characteristic of bipyridyl ligand one the other one resembling the absorption spectrum of ligand **2**. The presence of two ligands **2** doubles the molar absorption coefficient compared to the  $[\text{Ru}(2,2'\text{-bpy})_2\mathbf{2}\text{Cl}]^+$  complex.

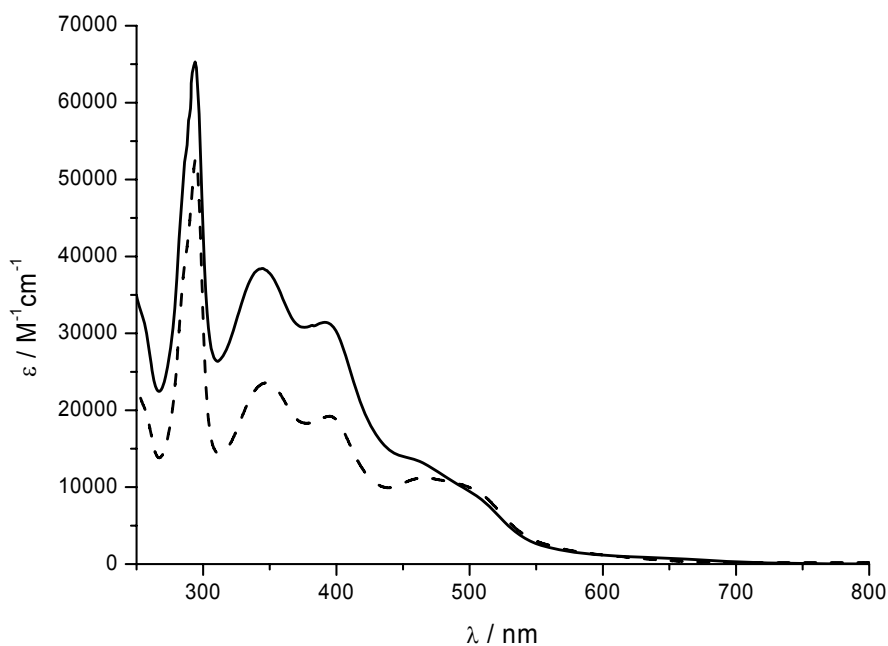


Figure 6.25. Absorption spectra of  $[\text{Ru}(2,2'\text{-bpy})_2\mathbf{2}\text{Cl}]^+$  (dashed line) and  $[\text{Ru}(2,2'\text{-bpy})_2\mathbf{2}_2]^{2+}$  (solid line) in acetonitrile solution at room temperature.

In both cases, the emission of the complex is completely quenched because of the charge-transfer interaction between  $\text{Ru}^{\text{II}}$  and **2** at the ground state.

Upon irradiation  $[\text{Ru}(2,2'\text{-bpy})_2\text{2Cl}]^+$  shows a wavelength-dependent behaviour; in fact, irradiation with 365-nm light generates a pseudo-photostationary state (Figure 6.26.), that is different from that obtained upon irradiation with 436-nm light (Figure 6.27.).

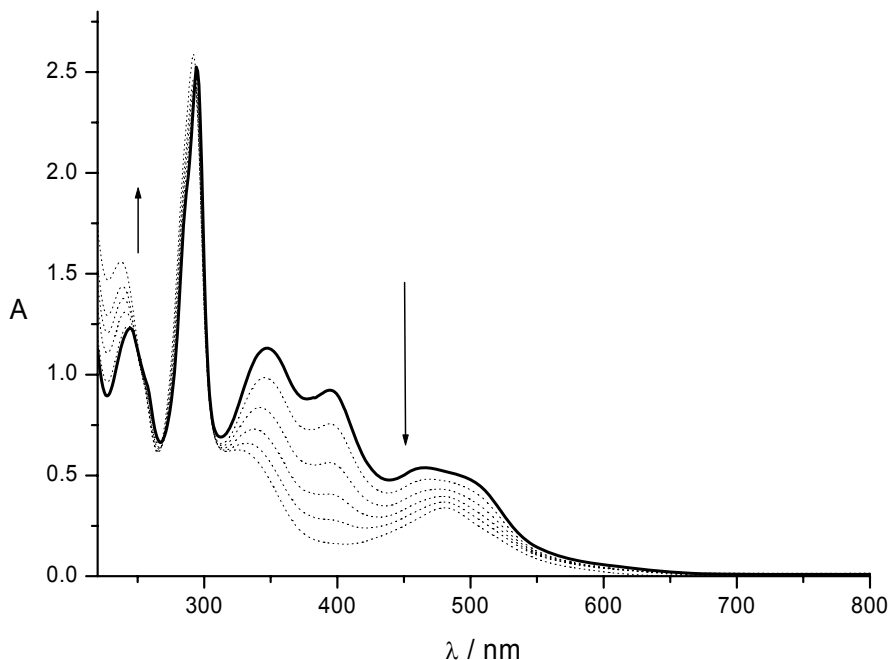


Figure 6.26. Spectral changes of  $[\text{Ru}(2,2'\text{-bpy})_2\text{2Cl}]^+$  (solid line) upon irradiation at 365 nm.

Upon irradiation with 365-nm light, the spectral changes observed for  $[\text{Ru}(2,2'\text{-bpy})_2\text{2Cl}]^+$  (Figure 6.26.) are similar to those obtained for free compound **2** (Figure 6.16.), suggesting that irradiation causes *trans-cis* isomerization of the styryl moiety of **2**.

When the complex is irradiated with 436-nm light, the observed spectral changes have been attributed to a photodissociation process; the hypsochromic shift of the absorption band (Figure 6.27.) characteristic of **2** suggests, indeed, that the pyridine moiety of the ligand is no more coordinated to Ru(II) ions. Direct population of the charge-transfer state probably lowers the electron-withdrawing ability of the Ru<sup>II</sup> metal ion leading to substitution of ligand **2** with a solvent molecule.

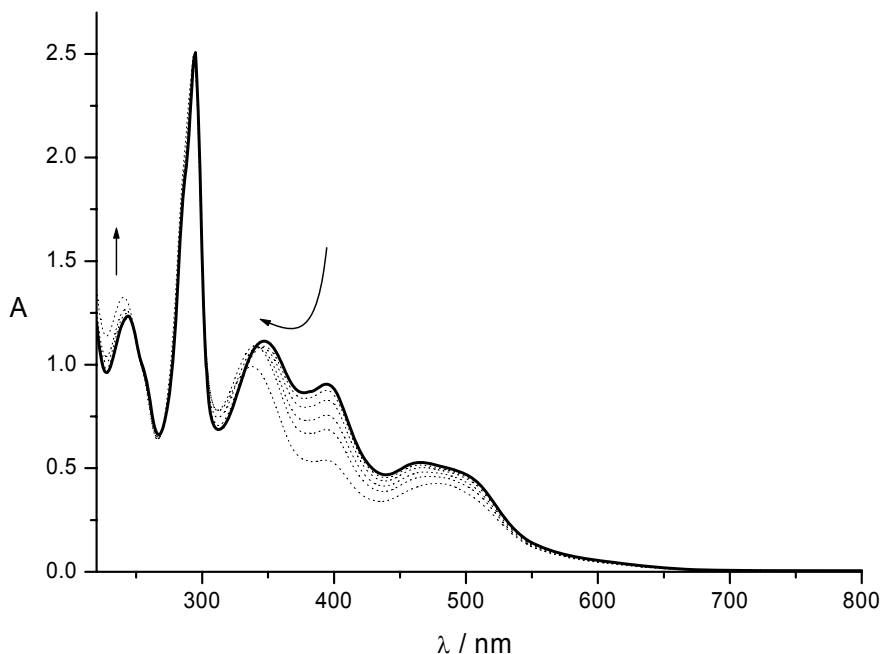


Figure 6.26. Spectral changes of  $[\text{Ru}(2,2'\text{-bpy})_2\text{Cl}]^+$  (solid line) upon irradiation at 436 nm.

Similar results have been obtained in anhydrous dichloromethane solution.

Similar results have been obtained on  $[\text{Ru}(2,2'\text{-bpy})_2\mathbf{2}_2]^{2+}$  air-equilibrated anhydrous acetonitrile and dichloromethane solutions. Anyway, solutions of  $[\text{Ru}(2,2'\text{-bpy})_2\mathbf{2Cl}]^{2+}$  and  $[\text{Ru}(2,2'\text{-bpy})_2\mathbf{2}_2]^{2+}$  are thermally stable and do not undergo ligand substitution.

An investigation on the ability of  $[\text{Ru}(2,2'\text{-bpy})_2\mathbf{2Cl}]^+$ , and  $[\text{Ru}(2,2'\text{-bpy})_2\mathbf{2}_2]^{2+}$  in selectively binding metal cations has also been performed; the absorption changes observed upon titration with  $\text{Mg}^{\text{II}}$  ions are in agreement with those observed with free ligand (compare Figures 6.27. and 6.19.). It has to be remarked how the binding constants are two order of magnitude lower than those found for the free ligand.

Yet,  $[\text{Ru}(2,2'\text{-bpy})_2\mathbf{2}_2]^{2+}$  complex has been conceived to give complexes in which two crown ether moieties bind large alkali and alkaline earth metal ions so arranged in a sandwich- type fashion.

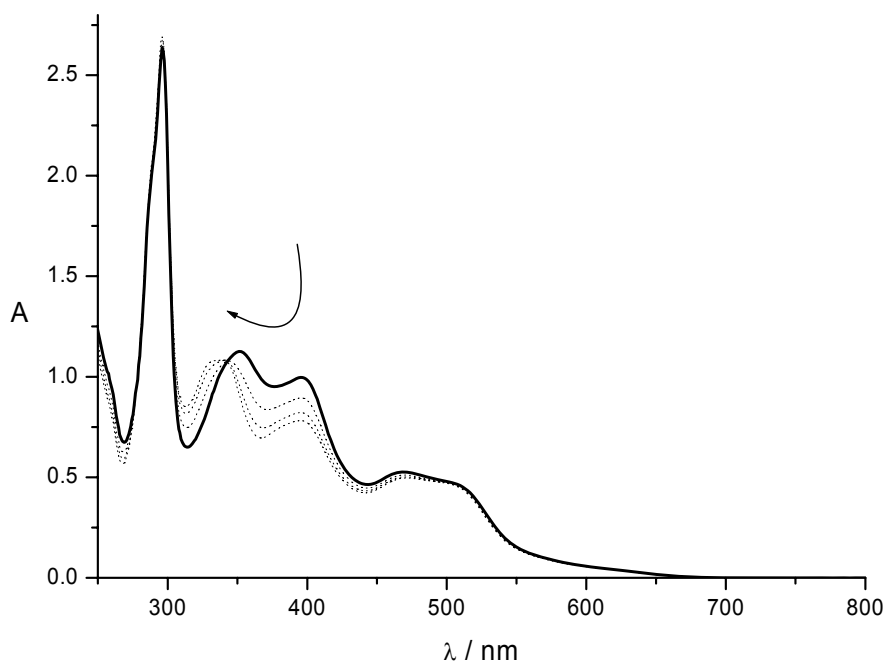


Figure 6.27. Spectral changes of  $[\text{Ru}(2,2'\text{-bpy})_2\text{Cl}]^+$  (solid line) upon addition of  $\text{Mg}(\text{ClO}_4)_2$ .

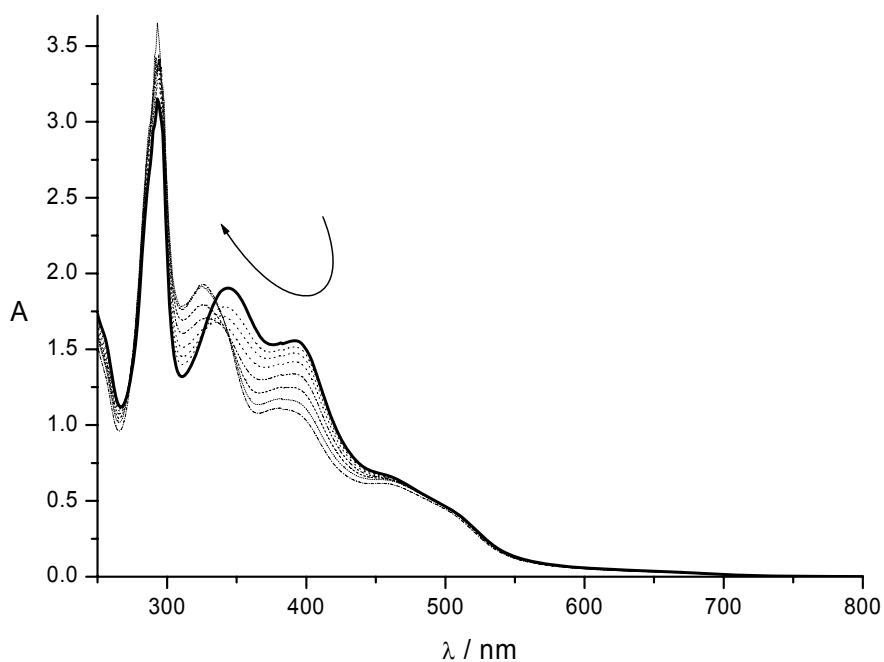


Figure 6.28. Spectral changes of  $[\text{Ru}(2,2'\text{-bpy})_2]^{2+}$  (solid line) upon addition of  $\text{Ba}(\text{ClO}_4)_2$ .

Binding constant (derived from spectral changes shown in Figure 6.28.) with  $\text{Ba}^{\text{II}}$  is lower than that found in the case of the sandwich complex between two free ligand **2** and  $\text{Ba}^{\text{II}}$  but an order of magnitude higher than the binding constant for the sandwich complex formed between  $\text{Ba}^{\text{II}}$  and two  $[\text{Ru}(2,2'\text{-bpy})_2\text{2Cl}]^+$  complexes revealing higher selectivity of  $[\text{Ru}(2,2'\text{-bpy})_2\text{2}]^{2+}$  compared to  $[\text{Ru}(2,2'\text{-bpy})_2\text{2Cl}]^+$ .

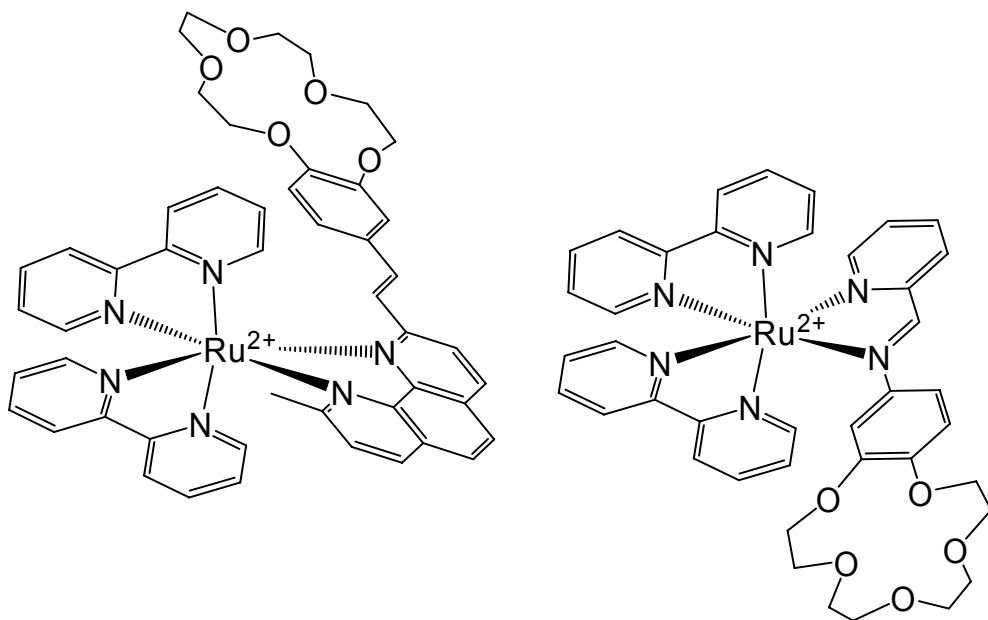


Figure 6.29. Formula of  $[\text{Ru}(2,2'\text{-bpy})_2\text{3}]^{2+}$  (left complex) and  $[\text{Ru}(2,2'\text{-bpy})_2\text{4}]^{2+}$  (right complex) as hexafluorophosphate salts.

The complexes  $[\text{Ru}(2,2'\text{-bpy})_2\text{3}]^{2+}$  and  $[\text{Ru}(2,2'\text{-bpy})_2\text{4}]^{2+}$  are expected to do not undergo ligand photosubstitution as expected for the presence of two binding sites on phenanthroline and azastyril-pyridine units that should be less labile than pyridine. However, complex  $[\text{Ru}(2,2'\text{-bpy})_2\text{4}]^{2+}$  shows lability as evidenced by the recovery of the luminescence peculiar of the free ligand **4** upon irradiation with visible light. Unfortunately, also  $[\text{Ru}(2,2'\text{-bpy})_2\text{3}]^{2+}$  shows stability problems. A complete characterization of the metal complexes is so prevented.

Anyway, this kind of compounds is definitely interesting since they can be used as building blocks for the construction of supramolecular systems, besides analytic purposes. Through

simple modification of the crown ether moiety, for example, the Ru<sup>II</sup> complex might act as stopper and/ or photosensitizer in proton-driven self-assembled (pseudo)rotaxanes (Figure 6.30).

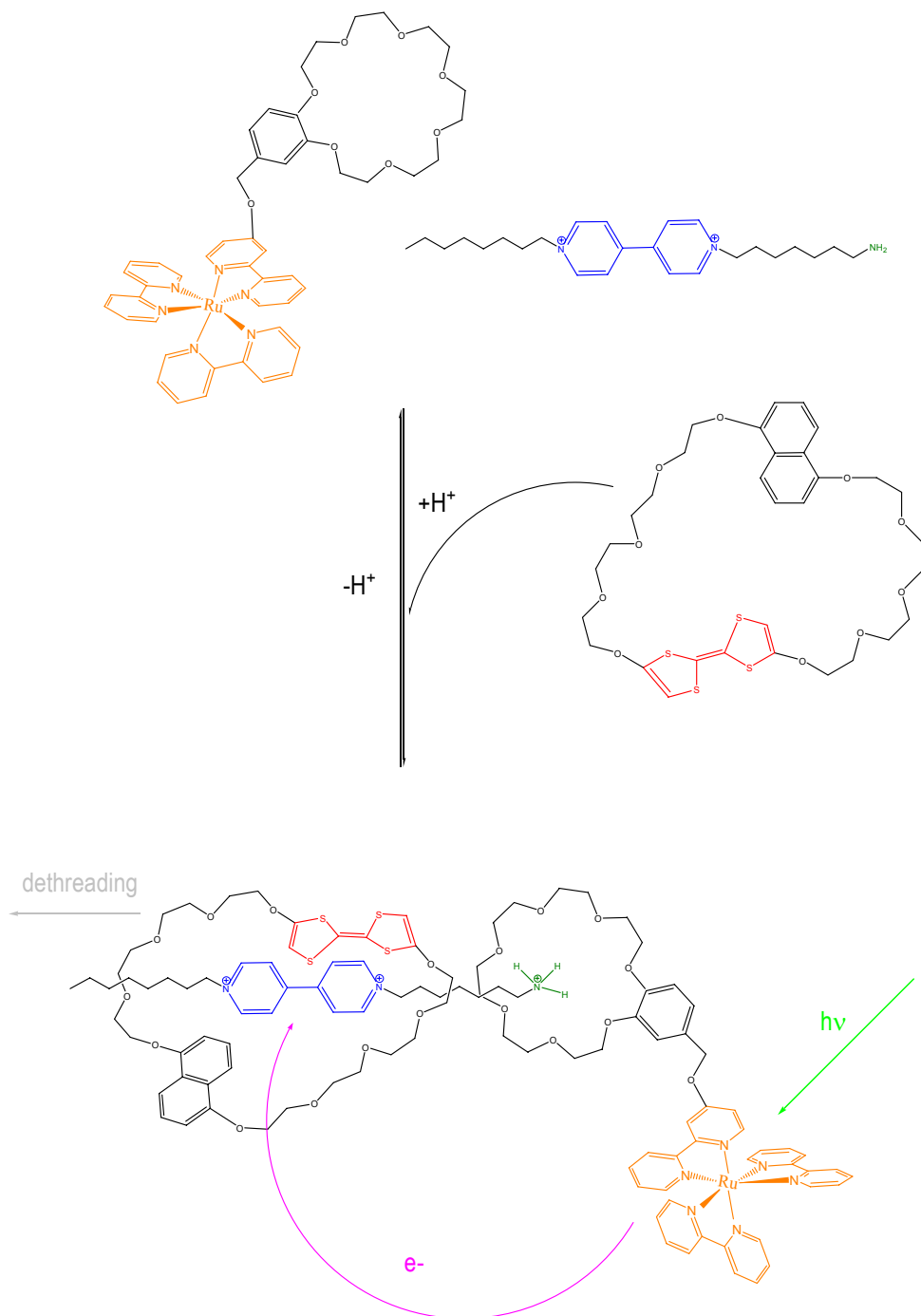


Figure 6.30. Self-assembled light-driven hypothetical example of pseudorotaxane.

## 7. Macrocycles

### 7.1. Shape-Persistent Macrocycles

Their rigid backbones with reduced conformational flexibility give rise to large molecular surfaces, that, heavily relying on van der Waals and hydrophobic interactions, can organize into order structures. The shape-persistent macrocycles here presented have a tendency to avoid face-to-face stacking: crystallization gives rise to layered structures where every third layer only lies directly on the top of each other so preventing the formation of one-dimensional tubular assemblies.<sup>228</sup> Sol-gel approach has been tried in order to obtain nano-channel formation without reaching appreciable results.

Anyway, the use of shape-persistent macrocycles as scaffolds for placing functional units at predetermined spatial positions to one another has been pursued. Particularly interesting are shape-persistent macrocycles incorporating coordination units such as 2,2'-bipyridines (bpy). *Endo*-cyclic metal-ion coordination may be exploited to generate nanowires,<sup>229</sup> whereas *exo*-cyclic coordination can be used to construct large arrays of polynuclear metal complexes.<sup>230</sup>

Shape-persistent macrocycles incorporating 2,2'-bipyridine units with reactive substituents has been conceived to yield supramolecular systems undergoing protonation and metallation besides intercomponent energy and/ or electron transfer processes (molecular components shown in Figure 7.1.).

---

[228] O. Henze, D. Lentz, and A. Dieter Schlüter, *Chem. Eur. J.*, 2000, 6, 2362-2367.

[229] L. T. Scott, G. J. DeCicco, G. Reinhardt, *J. Am. Chem. Soc.* 1985, 107, 6546-6555.

[230] a) O. Henze, D. Lentz, A. Schäfer, P. Franke, A. D. Schlüter, *Chem. Eur. J.* 2002, 8, 357-365; b) M. Venturi, F. Marchioni, V. Balzani, D. M. Opris, O. Henze, A. D. Schlüter, *Eur. J. Org. Chem.* 2003, 21, 4227-4233; c) M. Venturi, F. Marchioni, B. F. Ribera, V. Balzani, D. M. Opris, A. D. Schlüter, *ChemPhysChem*, 2006, 7, 229-239.

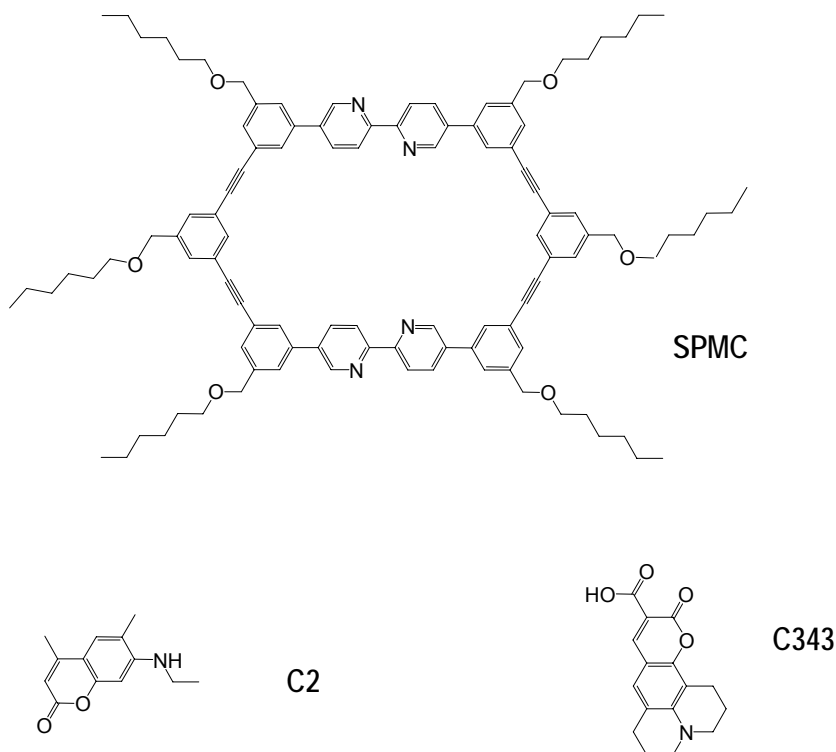


Figure 7.1. Formulas of the model compounds, building blocks of the investigated multicomponent systems see (Figures 7.12., 7.19., and 7.26.).

The photophysical and electrochemical properties of the unsubstituted macrocycle (**SPMC** in Figure 7.1.) has been analyzed together with its behaviour upon protonation.

**SPMC** shows a strong structured absorption band in the UV spectral region (solid line in Figure 7.2.,  $\lambda_{\max} = 308 \text{ nm}$ ,  $\epsilon_{308} = 190000 \text{ M}^{-1}\text{cm}^{-1}$ ) and an intense blue emission (solid spectrum in Figure 7.3.,  $\lambda_{\max} = 381 \text{ nm}$ ,  $\phi_{381} = 0.9$ ;  $\tau = 750 \text{ ps}$ , black decay in Figure 7.5.).

Upon acid addition, 2,2'-bipyridine units undergo almost stoichiometric protonation (3.3 equivalents of acid are necessary to reach a plateau in spectral changes; see Figure 7.4.). The observed changes in absorption spectra (Figure 7.2.) are similar to those already published,<sup>230</sup> showing clear isosbestic points that account for clean chemical processes occurring, that is monoprotection of each of the two 2,2'-bipyridine residues.

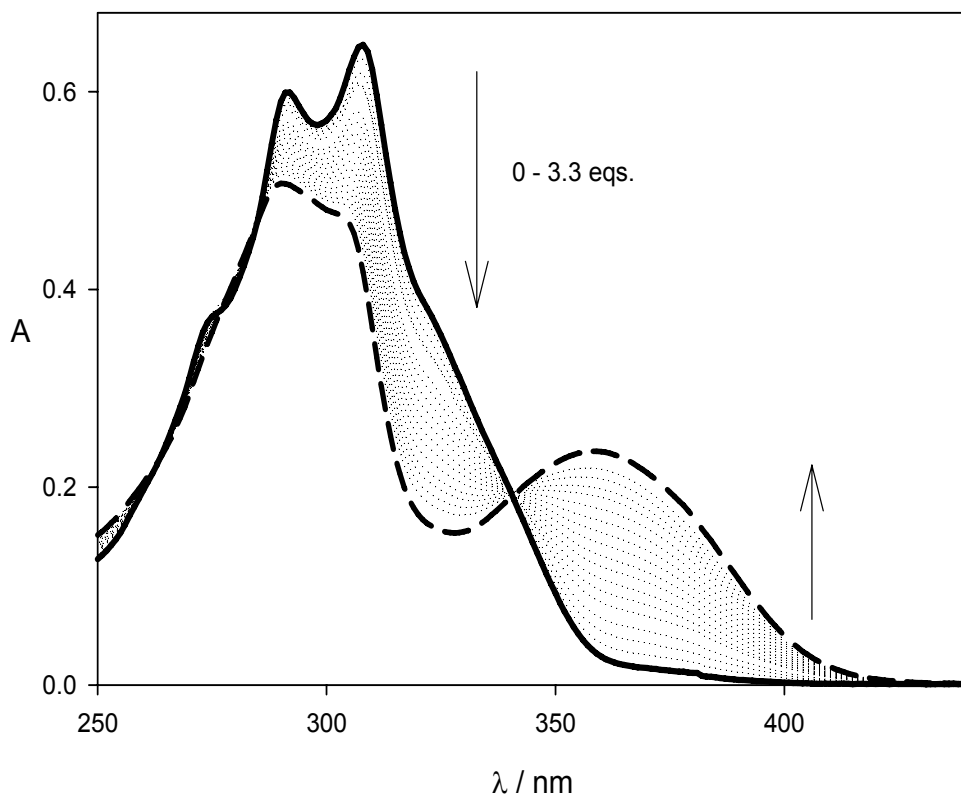


Figure 7.2. Absorption spectra of a  $\text{CH}_2\text{Cl}_2$  air-equilibrated solution of SPMC ( $c = 3.4 \times 10^{-6}$  M) at 298 K upon addition of  $\text{CF}_3\text{SO}_3\text{H}$  (triflic acid). Solid spectrum is SPMC, dashed spectrum is  $\text{SPMC}\cdot 2\text{H}^+$ .

To monitor the spectral changes in emission during the titration experiments, **SPMC** has been excited at 278 nm, a wavelength which, also in the case of the coumarin-functionalized macrocycles (*vide infra*), is practically absorbed only by the macrocyclic unit independently of its protonation state. Emission spectra changes upon protonation coherently with previous findings,<sup>230</sup> and again a clear isosbestic point is observed while forming  $\text{SPMC}\cdot 2\text{H}^+$  species. Dashed spectra in Figures 7.2. and 7.3. represents, respectively, absorption ( $\lambda_{\text{max}} = 360$  nm,  $\epsilon_{360} = 67000 \text{ M}^{-1}\text{cm}^{-1}$ ) and emission ( $\lambda_{\text{max}} = 514$  nm,  $\phi_{514} = 0.12$ ;  $\tau = 11.5$  ns dark grey decay in Figure 7.5.) spectra of  $\text{SPMC}\cdot 2\text{H}^+$ .

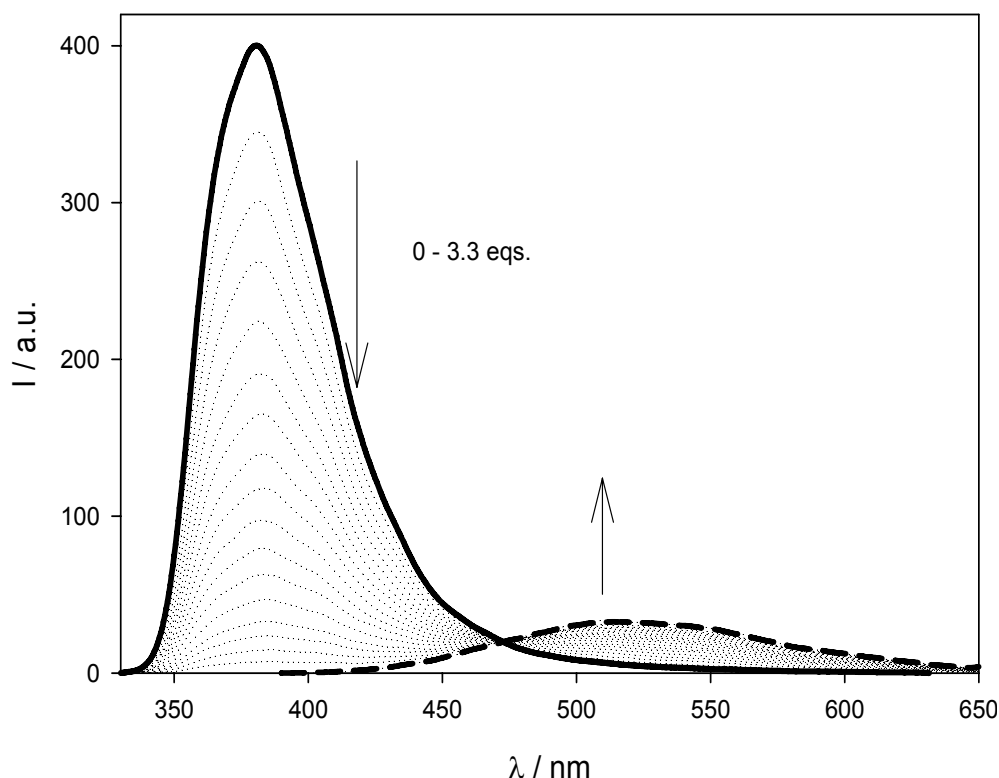


Figure 7.3. Emission spectra upon excitation at 278 nm of a  $\text{CH}_2\text{Cl}_2$  air-equilibrated solution of SPMC ( $c = 3.4 \times 10^{-6}$  M) at 298 K upon addition of  $\text{CF}_3\text{SO}_3\text{H}$  (triflic acid). Solid spectrum is SPMC, dashed spectrum is  $\text{SPMC}\cdot 2\text{H}^+$ .

However, a closer look at the titration plots (Figure 7.4.) provides interesting information on the evolution from **SPMC** to **SPMC·2H<sup>+</sup>**. It has been found out the statistical nature of the protonation process, what means that the double protonation of the macrocycle starts simultaneously with the monoprotection, or, in other words, that the two 2,2'-bipyridine units behave independently. This behaviour can be easily understood by looking at the situation obtained when half of the protons needed to diprotonate the macrocycle are added. At this point the absorption of the protonated species (empty squares in Figure 7.4.) is half of the final value, whereas the emission at 381 nm (characteristic of the unprotonated macrocycle, filled circles in Figure 7.4.) is almost 25% of the initial value. This result is

consistent with a quadratic probability distribution where 50% of the macrocycle is present in its monoprotonated form, 25% in its diprotonated form, and 25% in the unprotonated form; in mono- and diprotonated macrocycles emission at 381 nm is completely quenched, while remaining **SPMC** still emits at 381 nm.

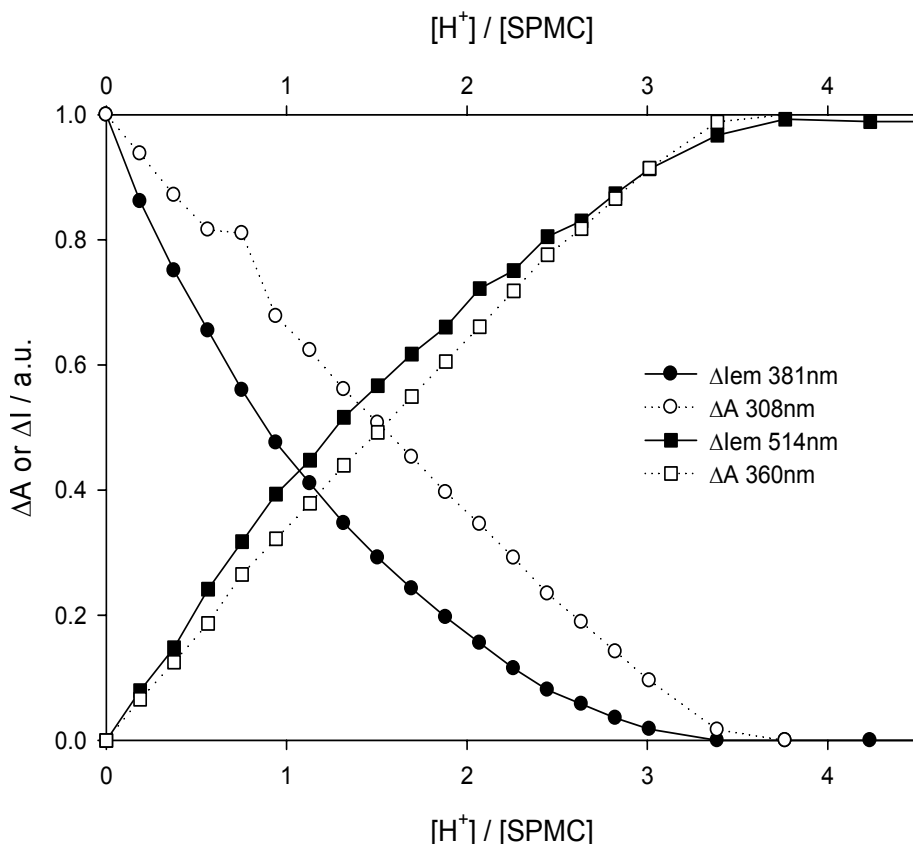


Figure 7.4. Spectral changes of a CH<sub>2</sub>Cl<sub>2</sub> air-equilibrated solution of SPMC ( $c = 3.4 \times 10^{-6}$  M) at 298 K upon addition of CF<sub>3</sub>SO<sub>3</sub>H (triflic acid): legend assigns symbols to observed changes in absorption and emission spectra of Figures 7.2. and 7.3., respectively.

The new absorption (with a maximum at 360 nm) band appearing upon protonation can be attributed to the mono- and diprotonated species. The absorption spectra of these two species seem to be very similar in shape, but quantitatively different: the diprotonated species should have molar absorption coefficients two times higher than that of the monoprotonated

one. In fact, trends of spectral changes upon protonation at 308 and 360 nm are linear and mirror image of each other.

The comparison of the changes in emission (at 381 and 514 nm) during the titration such a mirror image trend does not occur indicating that (i) emission spectra of mono- and diprotonated species are qualitatively the same but, the relative intensity of **SPMC·2H<sup>+</sup>** species has to be two times higher than that of **SPMC·H<sup>+</sup>** species as shown by filled square growing linearly in Figure 7.4.; (ii) there is no energy transfer from the excited state of the unprotonated macrocycle to the protonated forms (using light of 278 nm enable direct excitation of both the unprotonated and protonated forms of the macrocycle with the same probability); (iii) in the monoprotinated species the emission of the unprotonated unit of the same macrocycle is quenched by the protonated one.

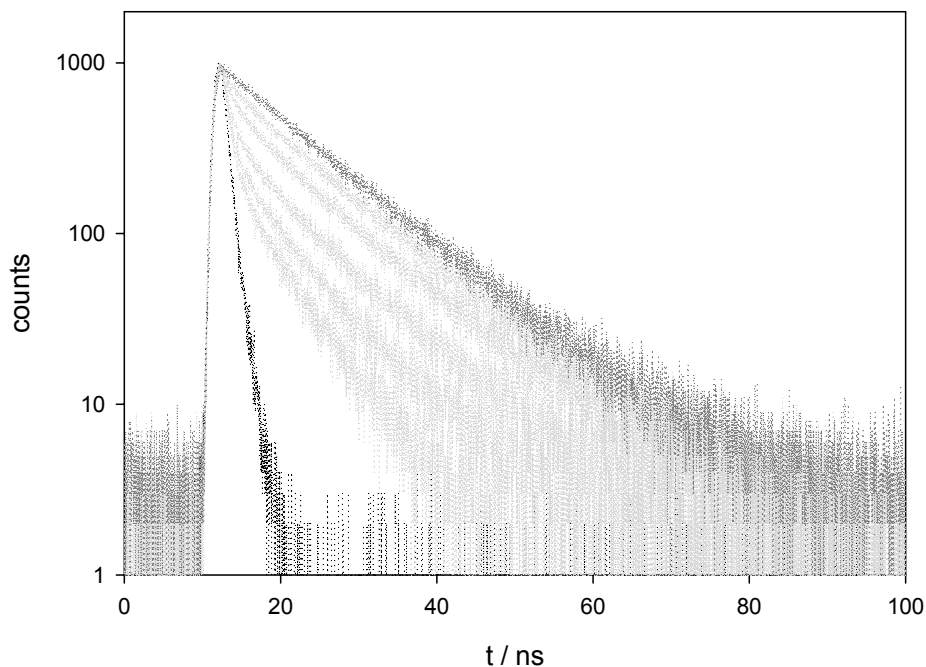


Figure 7.5. Fluorescence lifetime decay changes upon excitation at 278 nm of a  $\text{CH}_2\text{Cl}_2$  air-equilibrated solution of SPMC ( $c = 3.4 \times 10^{-6}$  M) at 298 K upon addition of  $\text{CF}_3\text{SO}_3\text{H}$  (triflic acid). Black decay is SPMC, dark grey decay is **SPMC·2H<sup>+</sup>**.

Time-resolved fluorescence measurements fully confirm the statistical nature of the protonation process in **SPMC**. It is shown (Figure 7.2.) that the choice of 278 nm as excitation wavelength guarantees the same probability of exciting an unprotonated or a protonated residue of a macrocycle, since they behave independently.

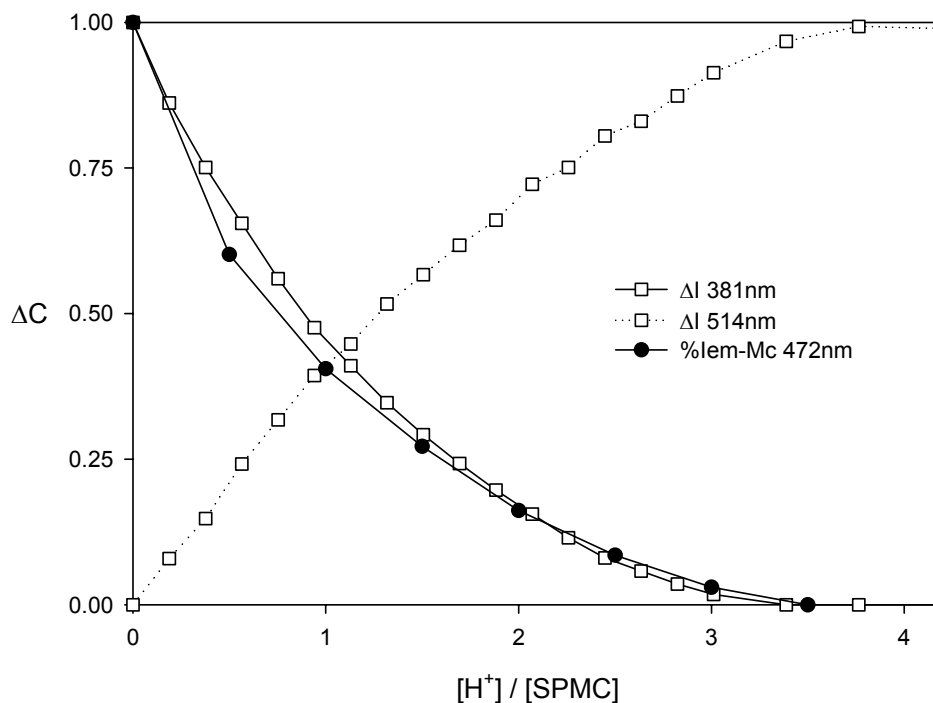


Figure 7.6. Emission intensity changes of a CH<sub>2</sub>Cl<sub>2</sub> air-equilibrated solution of SPMC ( $c = 3.4 \times 10^{-6}$  M) at 298 K upon addition of CF<sub>3</sub>SO<sub>3</sub>H (triflic acid) are related to SPMC concentration: empty and filled symbols have been derived from steady-state (Figure 7.3.) and time-resolved (Figure 7.5.) fluorescence measurements, respectively.

The pre-exponential factor  $B$  of the function (obviously an exponential function) is proportional to the concentration  $C$  of the excited species following eq. 41:

$$B \propto C \times k_r \tag{41}$$

$$\text{where, } k_r = \tau / \phi \quad (42)$$

so knowing the total macrocycle concentration and by experimental measure of quantum yields, lifetimes, and pre-exponential factors of **SPMC** and **SPMC•2H<sup>+</sup>**, the concentration of the unprotonated macrocycle during titration can be calculated. It decreases following the same trend observed in steady state fluorescence measurements (Figure 7.6.).

It has now to be understood the mechanism leading to the deactivation of the excited localized on the unprotonated residue in monoprotinated macrocycles. The possibility of an oxidative quenching process (see eq. 11), where the unprotonated residue (indicated as A in eqs. 43 and 44) at the excited state reduces the protonated residue (indicated as AH<sup>+</sup> in eqs. 43 and 44), has been investigated.

The thermodynamic availability for an oxidative quenching process of the type:



can be calculated from the following equation:

$$\Delta G \approx F[E^{\circ}(A^+/A) - E^{\circ}(AH^+/AH)] - E_{00}({}^*A) - w \quad (44)$$

where  $F$  is the Faraday constant,  $E^{\circ}(A^+/A)$  and  $E^{\circ}(AH^+/AH)$  are the standard potentials of the ground state couples,  $E_{00}$  is the zero-zero spectroscopic energy of  ${}^*A$  and  $w$  is the coulombic work term, which can be neglected in polar solvents.

Unfortunately, the oxidation peak of a distilled THF solution of **SPMC** 1 mM (TBAPF<sub>6</sub> 0.1 M as supporting electrolyte) does not fall within the potential window allowed by the solvent, though its good width (−2 to 2 V). The reduction peak of **SPMC•2H<sup>+</sup>** is, instead, irreversible preventing determination of  $E^{\circ}(AH^+/AH)$ . The only measurable standard potential

value is the useless  $E^q(A/A)$  from the cyclic voltammetric curve shown in Figure 7.7.. This value only gives an idea of the lower limit of the first right term in eq. 44. This value of 3.8 eV is really close to the zero-zero spectroscopic energy of  $^*\text{SPMC}$ , that is 3.5 eV. The high uncertainty on these values does not permit to assume an intra-macrocycle electron-transfer mechanism to explain the deactivation pathway of the excited state localized on the unprotonated residue in monoprotonated macrocycles.

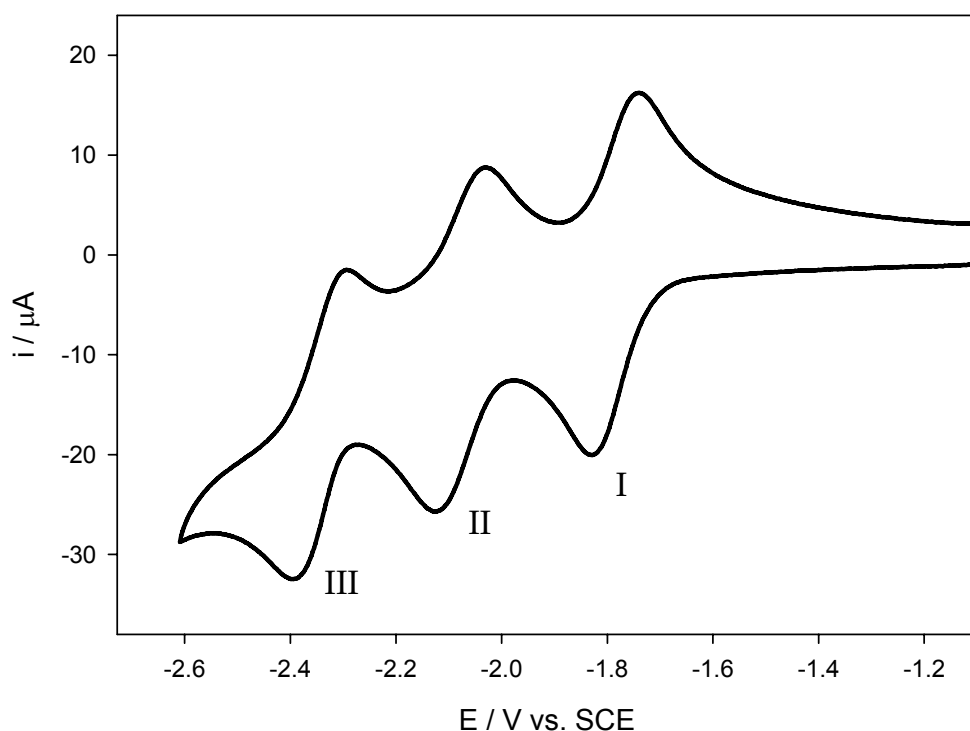


Figure 7.7. Cyclic voltammetric behavior of a distilled THF solution of SPMC ( $c = 1 \times 10^{-3}$  M) at 298 K (TBAPF<sub>6</sub> 0.1 M as supporting electrolyte):  $E_{1/2}^{\text{I}} = -1.77$  V;  $E_{1/2}^{\text{II}} = -2.07$  V;  $E_{1/2}^{\text{III}} = -2.33$  V.

An alternative explanation could be found in a photoinduced proton-transfer reasonably assuming  $^*\text{SPMC}$  a stronger base than **SPMC**. In order to investigate this hypothesis, pump probe experiment have been conducted on **SPMC** and **SPMC•2H<sup>+</sup>** as models to

understand the behaviour of the macrocycle when half of the protons needed to diprotonate it are added. It has been predicted that transient absorption spectrum of monoprotonated macrocycle will present features (i) having references to the spectra of **SPMC** and **SPMC•2H<sup>+</sup>** in case of proton-transfer because the chemical species involved are qualitatively the same, while (ii) in case of electron-transfer, a chemical species not related with **SPMC** and **SPMC•2H<sup>+</sup>** will form upon photoexcitation. Also this explicative attempt is prevented due to the failure of aforementioned predictions: **SPMC** transient absorption spectrum does not kinetically evolve as find out by its fluorescence lifetime, making the situation too complicated to be solved.

Further investigation on the mechanism for the deactivation pathway of the excited state localized on the unprotonated residue in monoprotonated macrocycles is necessary.

Reversibility of protonation is achieved adding equimolar quantity of Bu<sub>3</sub>N; when macrocycle emission is quenched, protonated macrocycle emission raises up and viceversa. (Figure 7.8.).

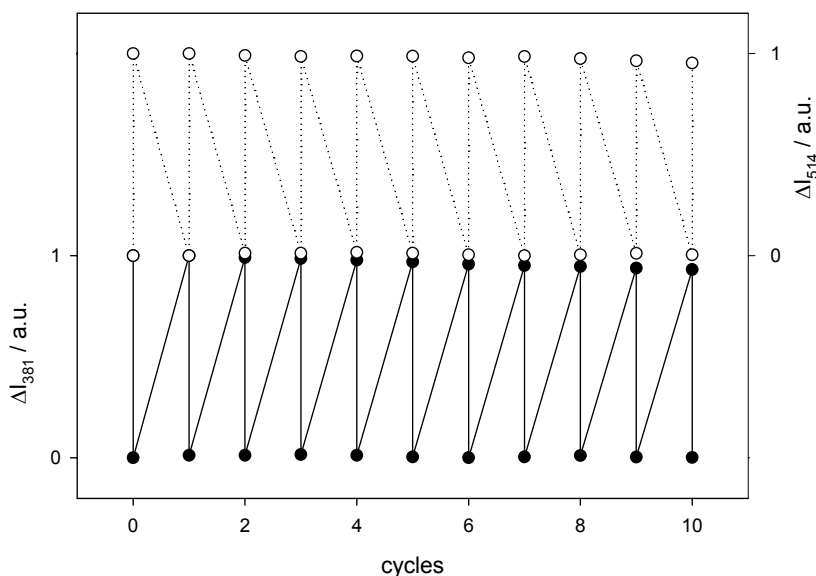


Figure 7.8. Normalized emission intensities ( $\lambda_{\text{em}} = 381 \text{ nm}$ , filled circles;  $\lambda_{\text{em}} = 514 \text{ nm}$ , empty circles) of a  $\text{CH}_2\text{Cl}_2$  solution of SPMC at 298 K during reversible protonation cycles with  $\text{CF}_3\text{SO}_3\text{H}$  and  $\text{BU}_3\text{N}$ .

Laser dye coumarins (**C2** and **C343** in Figure 7.1.) have been covalently linked to **SPMC** in order to construct three component photoactive systems undergoing intercomponent energy and/ or electron transfer processes. N-benzyl **C2** results a more suitable model compound than **C2** for the coumarin 2 appended to the macrocyclic scaffold (see Figure 7.10. and compare it with following spectra of coumarin functionalized macrocycle:  $\lambda_{\text{abs}} = 346$  nm instead of 354 nm,  $\epsilon_{346} = 15300 \text{ M}^{-1}\text{cm}^{-1}$  instead of  $19700 \text{ M}^{-1}\text{cm}^{-1}$ ;  $\lambda_{\text{em}} = 436$  nm instead of 413 nm,  $\phi_{\text{em}} = 0.81$  vs.  $\phi_{\text{C2}} = 0.78$  in air-equilibrated dichloromethane solution at room temperature).

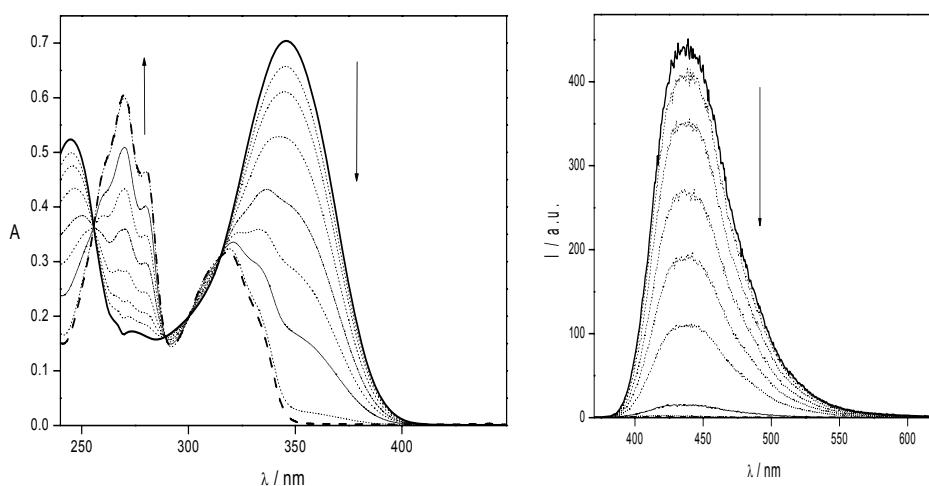


Figure 7.10. Absorption (left side) and emission ( $\lambda_{\text{ex}} = 320$  nm, right side) changes of N-benzyl C2 (solid lines) upon protonation with  $\text{CF}_3\text{SO}_3\text{H}$ .

It follows that there is a better model for the appended coumarin 343 than **C343** shown in Figure 7.1. that is the benzyl ester of **C343** result more suitable model compounds for the appended coumarins (see Figure 7.11. and compare it with following spectra of coumarin functionalized macrocycle:  $\lambda_{\text{abs}} = 436$  nm instead of 450 nm,  $\epsilon_{436} = 46000 \text{ M}^{-1}\text{cm}^{-1}$  instead of  $45200 \text{ M}^{-1}\text{cm}^{-1}$ ;  $\lambda_{\text{em}} = 471$  nm instead of 484 nm,  $\phi_{\text{em}} = 0.92$  vs.  $\phi_{\text{C343}} = 0.94$  in air-equilibrated dichloromethane solution at room temperature).

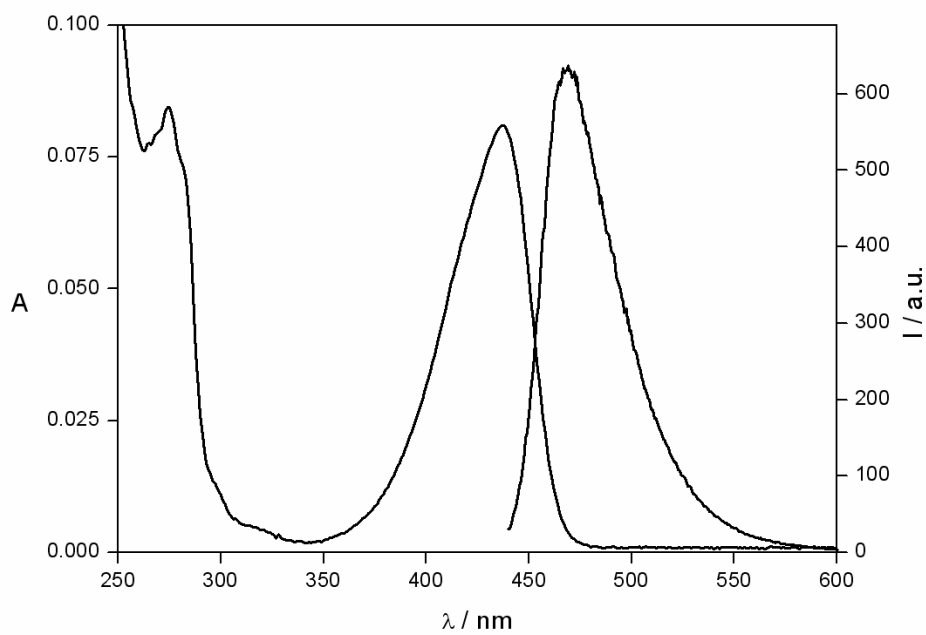


Figure 7.11. Absorption (left spectrum) and emission ( $\lambda_{\text{ex}} = 430$  nm, right spectrum) changes of-benzyl ester of C343 upon protonation with  $\text{CF}_3\text{SO}_3\text{H}$ .

Symmetrically substituted macrocycle with C2

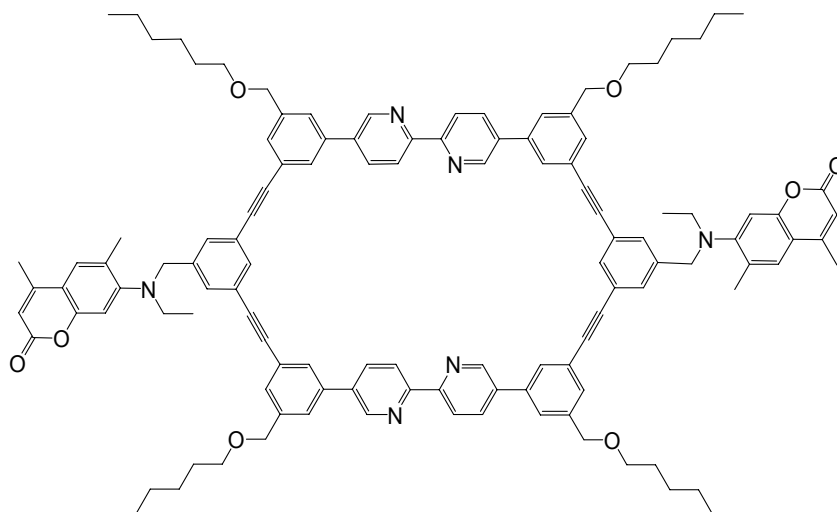


Figure 7.12. Formula of C2-SPMC-C2.

The absorption spectrum of **C2-SPMC-C2** is consistent with the sum of the absorption spectra of the component units, indicating that such units do not interact at the ground state (solid spectrum in Figure 7.13.). The situation is, however, completely different as far as the emission properties are concerned. By exciting at 278 nm (absorbed by the macrocyclic unit), only the emission of **C2** at 427 nm is observed (solid spectrum in Figure 7.14.). This result can be accounted for by an almost unitary efficient energy transfer from the excited state of the **SPMC** to **C2**.

On addition of acid, quenching of the coumarin-emission and absorption changes (Figures 7.13. and 7.14., respectively) has been observed, consistent with the protonation of the macrocycle, again in a statistical way.

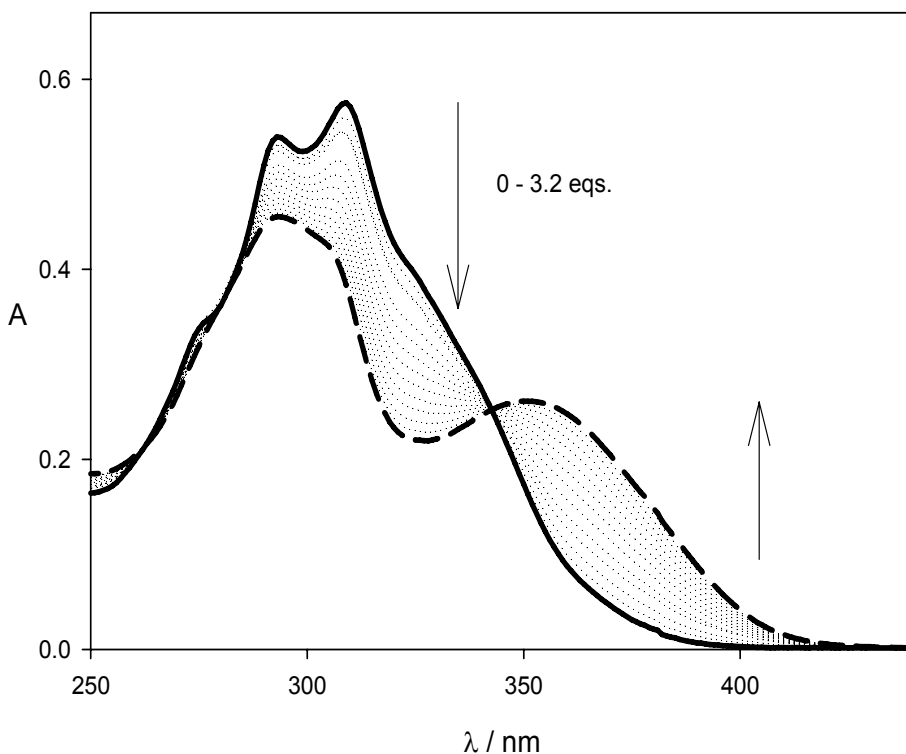


Figure 7.13. Absorption spectra of a  $\text{CH}_2\text{Cl}_2$  air-equilibrated solution of C2-SPMC-C2 ( $c = 3.2 \times 10^{-6}$  M) at 298 K upon addition of 3.2 eqs. of  $\text{CF}_3\text{SO}_3\text{H}$  (triflic acid). Solid spectrum is C2-SPMC-C2, dashed spectrum is C2-SPMC· $2\text{H}^+$ -C2.

When 3.2 equivalents of acid are added (the amount of protons necessary to diprotonate the macrocycle), the coumarin-emission is only 5% of the initial value. It is interesting to notice that the quenching of the coumarin-emission is not accompanied by the appearance of the emission in the 520 nm region characteristic of the diprotonated macrocycle. Further addition of acid (3.2-10 equivalents), however, causes the appearance of such an emission (Figure 7.16.) together with absorption changes (Figure 7.15.), which can be ascribed to the protonation of the coumarin.

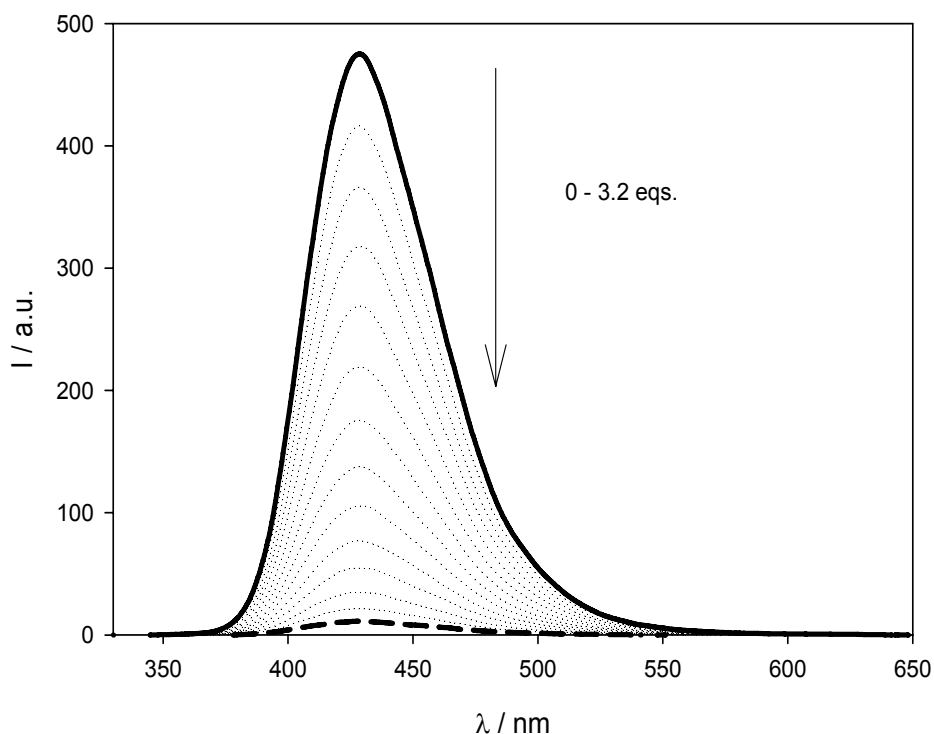


Figure 7.14. Emission spectra of a  $\text{CH}_2\text{Cl}_2$  air-equilibrated solution of C2-SPMC-C2 ( $c = 3.2 \times 10^{-6}$  M) at 298 K upon addition of 3.2 eqs. of  $\text{CF}_3\text{SO}_3\text{H}$  (triflic acid). Solid spectrum is C2-SPMC-C2, dashed spectrum is C2-SPMC $\cdot$ 2H $^+$ -C2.

Although further investigations are needed (electrochemical measurements and absorption time-resolved experiments) to establish the energy-level diagram of the states involved and the rate constants of the processes, these results can be accounted for by assuming that, for an amount of acid added less than or equal to 3 equivalents, an electron transfer from the lone pair on the coumarin nitrogen atom to the excited state of the protonated macrocycle occurs that quenches the former characteristic blue emission. This explanation is supported by the fact that, when **C2** is protonated (i.e. for  $> 3.2$  equivalents of protons added), the emission of the protonated macrocycle is observed. It is known, indeed, that amines can quench excited states and that such quenching does not occur any longer by protonation of the amines.

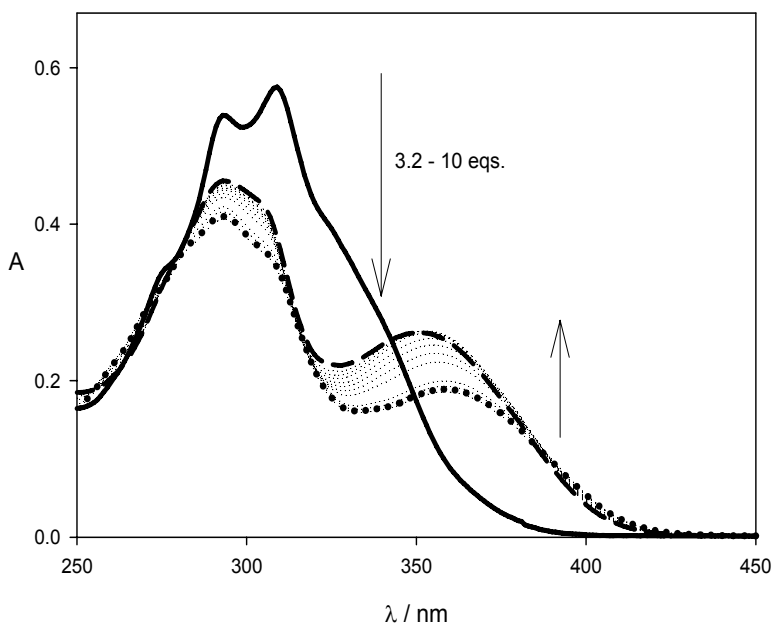


Figure 7.15. Absorption spectra of a  $\text{CH}_2\text{Cl}_2$  air-equilibrated solution of C2-SPMC-C2 ( $c = 3.2 \times 10^{-6} \text{ M}$ ) at 298 K upon addition of 10 eqs. of  $\text{CF}_3\text{SO}_3\text{H}$  (triflic acid). Solid spectrum is C2-SPMC-C2, dashed spectrum is C2-SPMC·2H<sup>+</sup>·C2, dotted spectrum is C2·H<sup>+</sup>·SPMC·2H<sup>+</sup>·C2·H<sup>+</sup>.

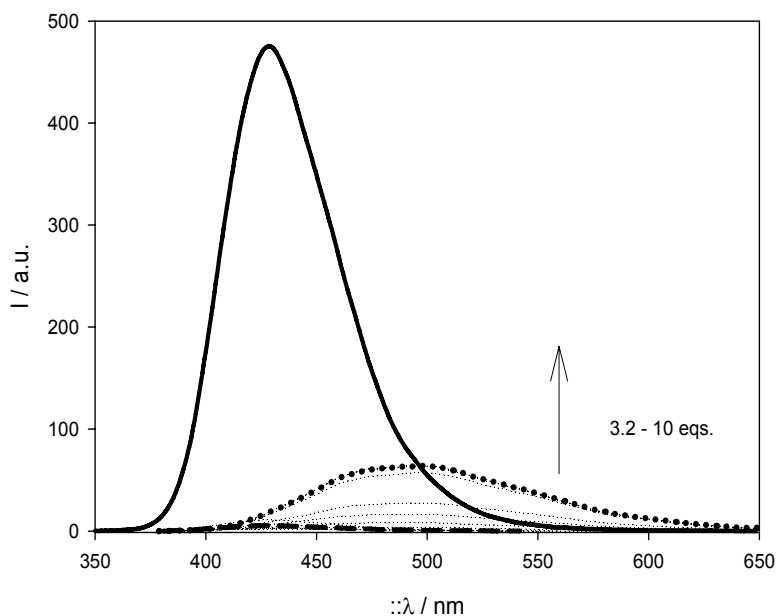


Figure 7.16. Emission spectra of a  $\text{CH}_2\text{Cl}_2$  air-equilibrated solution of C2-SPMC-C2 ( $c = 3.2 \times 10^{-6} \text{ M}$ ) at 298 K upon addition of 10 eqs. of  $\text{CF}_3\text{SO}_3\text{H}$  (triflic acid). Solid spectrum is C2-SPMC-C2, dashed spectrum is C2-SPMC·2H<sup>+</sup>·C2, dotted spectrum is C2·H<sup>+</sup>·SPMC·2H<sup>+</sup>·C2·H<sup>+</sup>.

Fluorescence lifetime measurements show that, when less than 3 equivalents of protons are added, practically only one decay component, attributed to **C2** ( $\tau = 3.6$  ns) is observed and that for further addition of protons a longer lifetime ( $\tau = 11$  ns), similar to that of the protonated macrocycle, appears (Figure 7.17.). These findings are fully consistent with a photoinduced electron-transfer process occurring between **C2** and protonated macrocycle components and responsible of the quenching of coumarin emission.

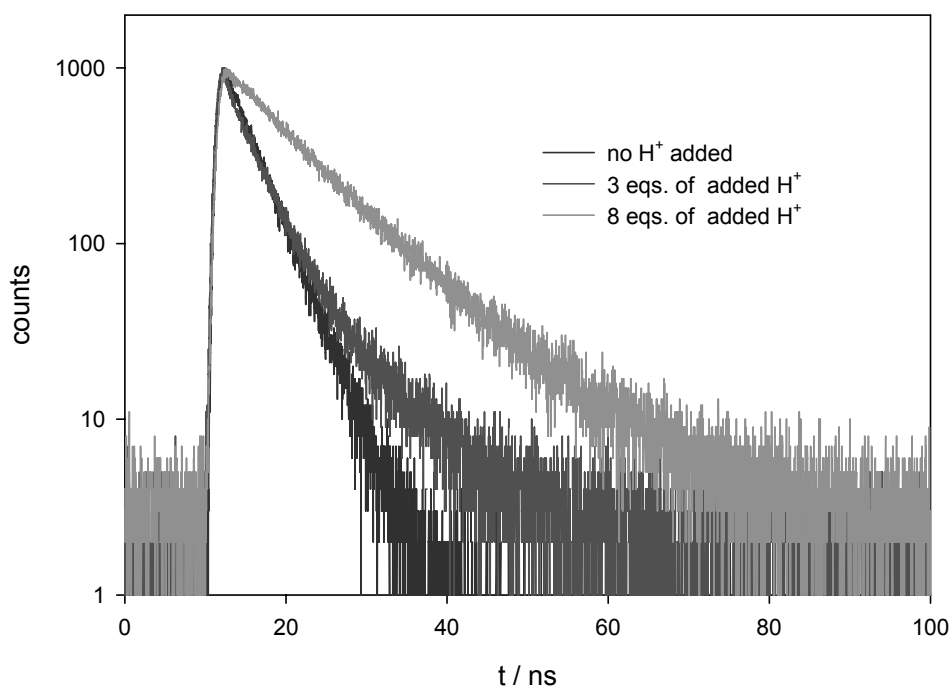


Figure 7.17. Fluorescence lifetime decay changes upon excitation at 278 nm of a  $\text{CH}_2\text{Cl}_2$  air-equilibrated solution of C2-SPMC-C2 ( $c = 3.0 \times 10^{-6}$  M) at 298 K upon addition of  $\text{CF}_3\text{SO}_3\text{H}$  (triflic acid): legend assigns number of proton equivalents added to the colour of the decay curve. Black decay is C2-SPMC-C2, dark grey decay is C2-SPMC $\cdot$ 2H $^+$ -C2, light grey decay is C2H $^+$ -SPMC $\cdot$ 2H $^+$ -C2H $^+$ .

It is noteworthy that protonation of the **C2** units proceeds statistically as shown by the growth of the emission band of the protonated macrocycle (filled squares in Figure 7.18.); only when both coumarins are protonated electron transfer is prevented. If protonation of C2 were

not be statistic, emission of the protonated macrocycle should appear upon addition of 8 eqs. of protons instead of 3.2, that means only after complete protonation of the four protonation sites present in **C2-SPMC-C2**.

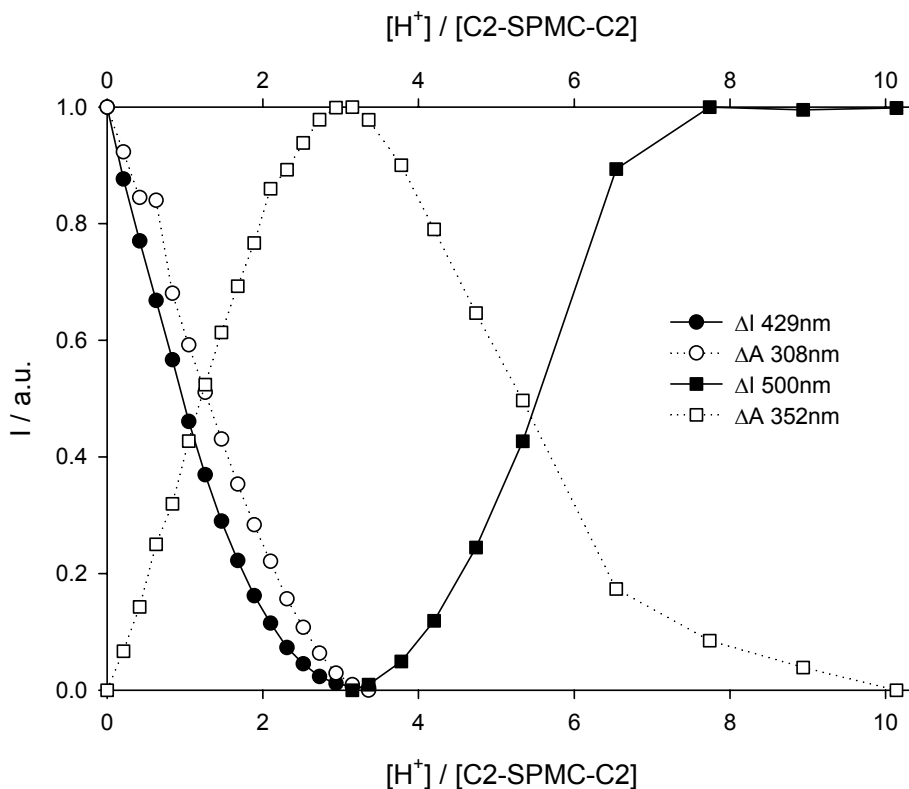


Figure 7.18. Absorption and emission normalized changes of a  $\text{CH}_2\text{Cl}_2$  air-equilibrated solution of C2-SPMC-C2 ( $c = 3.2 \times 10^{-6}$  M) at 298 K upon addition of  $\text{CF}_3\text{SO}_3\text{H}$  (triflic acid): legend assigns empty symbols to observed changes in absorption (Figures 7.13. and 7.15.) and filled symbols to changes in emission (Figures 7.14. and 7.16.) spectra.

Symmetrically substituted macrocycle with C343

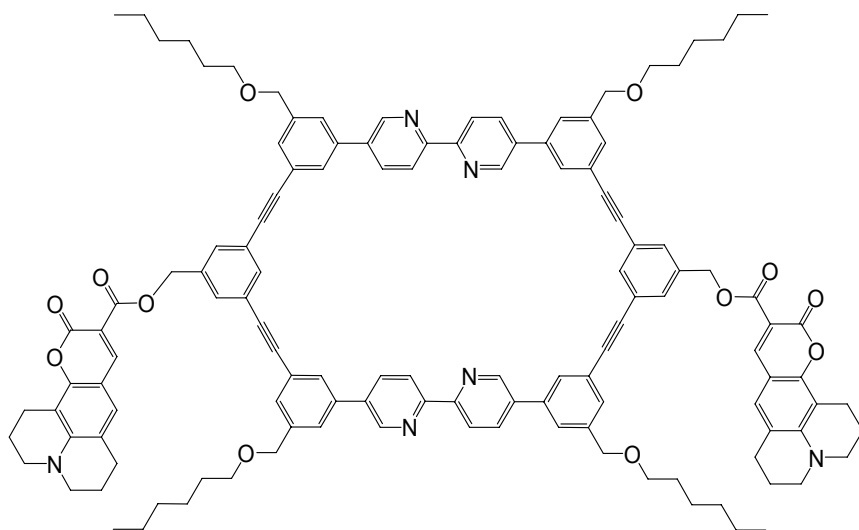


Figure 7.19. Formula of C343-SPMC-C343.

The absorption and emission properties of the macrocycle symmetrically substituted with **C343** can be interpreted by following the same considerations reported for the previously described macrocycle substituted with **C2**. The absorption spectrum of **C343-SPMC-C343** (blue spectrum in Figure 7.20.) is coincident with the sum of the spectra of the components.

Selective excitation of macrocyclic moiety ( $\lambda_{\text{ex}} = 278$  nm) leads to the emission of **C343** with a maximum at 471 nm (solid spectrum in Figure 7.21.), so evidencing that also in this case there is an almost unitary efficient energy transfer process from the macrocycle to the coumarin occurs; further confirmation arises from excitation spectrum of **C343-SPMC-C343** ( $\lambda_{\text{em}} = 471$  nm) resembling the absorption spectrum of C343 shown in Figure 7.11.

It is important to notice that this system is particular sensitive: it must be kept in the dark and the obtained results depend on its concentration and on the environment (for example, it has been found different results for titrations carried out by using a 1:1 dichloromethane/acetonitrile solution of triflic acid and a pure acetonitrile solution of triflic acid).

The better titrations, as far as repeatability is concerned, are those obtained by adding a pure acetonitrile solution of acid. When the titration is performed under such conditions, a behaviour qualitatively similar to that of the macrocycle functionalized with **C2** is observed. The two bpy moieties of the shape-persistent macrocycle undergo protonation before the two **C343** units. The latter undergo electrostatic effects during macrocycle protonation as evidenced by its absorption maximum moving towards longer wavelength (Figure 7.20., dashed spectrum compared to the solid one). During of the macrocycle protonation, concomitant quenching of the coumarin-emission to 5% of its initial value occurs (Figure 7.21., dashed spectrum compared to the solid one). Once again, low-lying fluorescent excited state, localized on the **C343** moieties, is quenched by electron transfer between the lone pair of the coumarin nitrogen atom and the protonated macrocycle.

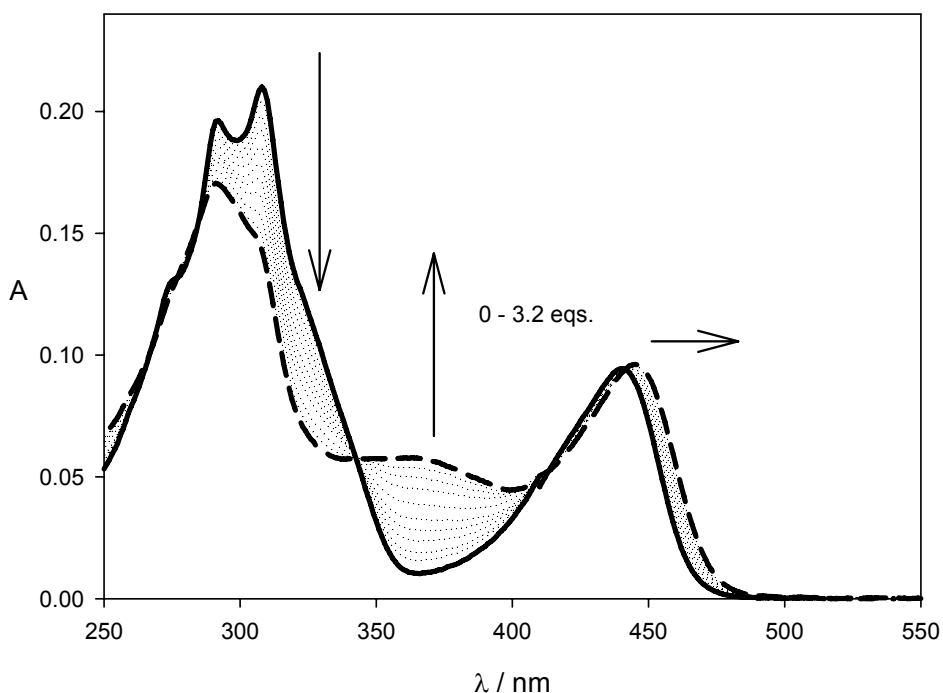


Figure 7.20. Absorption spectra of a  $\text{CH}_2\text{Cl}_2$  air-equilibrated solution of C343-SPMC-C343 ( $c = 1.1 \times 10^{-6} \text{ M}$ ) at 298 K upon addition of 3.2 eqs. of  $\text{CF}_3\text{SO}_3\text{H}$  (triflic acid). Solid spectrum is C343-SPMC-C343, dashed spectrum is C343-SPMC $\cdot$ 2H $^+$ -C343.

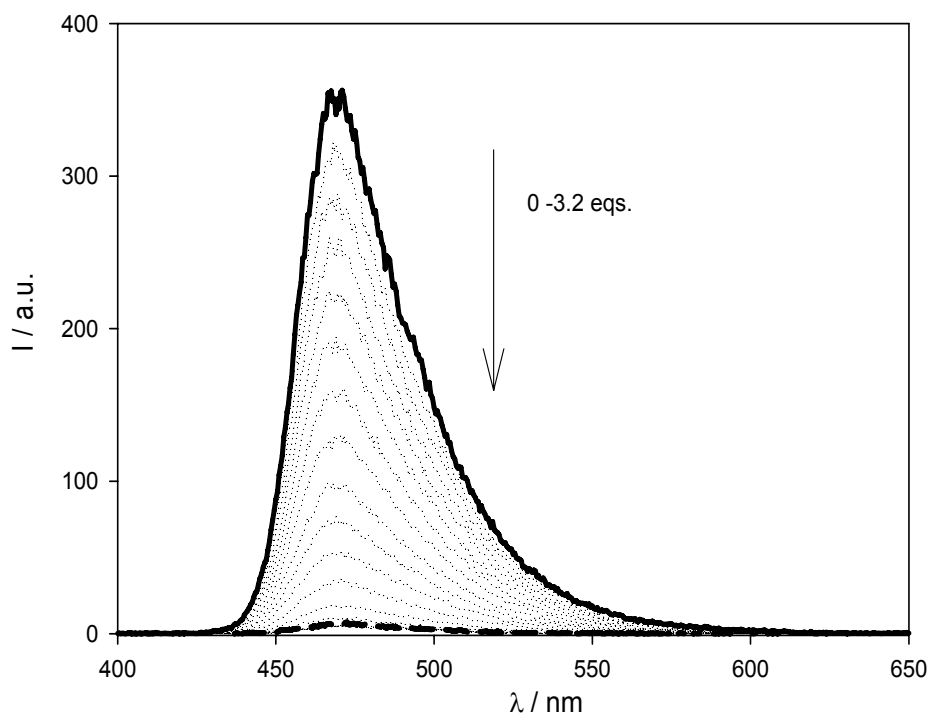


Figure 7.21. Emission spectra of a  $\text{CH}_2\text{Cl}_2$  air-equilibrated solution of C343-SPMC-C343 ( $c = 1.1 \times 10^{-6}$  M) at 298 K upon addition of 3.2 eqs. of  $\text{CF}_3\text{SO}_3\text{H}$  (triflic acid). Solid spectrum is C343-SPMC-C343, dashed spectrum is C343-SPMC $\cdot$ 2H $^+$ -C343.

For a further increase of acid protonation of the coumarin takes place. As a result of **C343** low Lewis base character 50 eqs. of protons are not enough to fully protonate them (Figure 7.22.). Furthermore, other basic sites might be available in the **C343**.

In comparison with the symmetrically substituted macrocycle with **C2** previously described there are, however, some differences: (i) it is impossible to obtain the complete protonation of **C343** (the reaction seems to be incomplete also when 90 equivalents of acid are added, probably because such a coumarin has more than one site of protonation); (ii) the protonated C343 shows a slight emission (Figure 7.23.); and (iii) the emission of the protonated macrocycle does not appear.

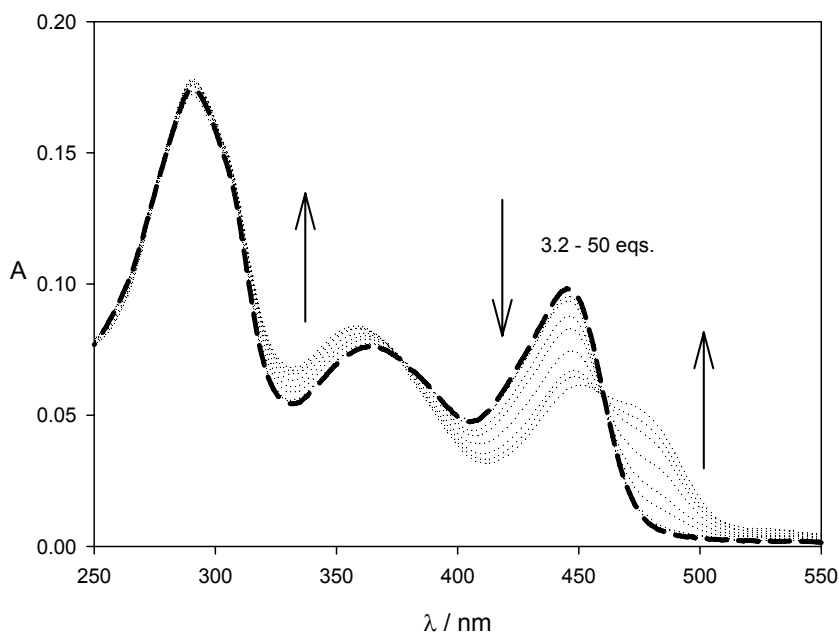


Figure 7.22. Absorption spectra of a  $\text{CH}_2\text{Cl}_2$  air-equilibrated solution of C343-SPMC-C343 ( $c = 1.1 \times 10^{-6} \text{ M}$ ) at 298 K upon addition of a bunch of eqs. of  $\text{CF}_3\text{SO}_3\text{H}$  (triflic acid). Dashed spectrum is C343-SPMC·2H<sup>+</sup>·C343.

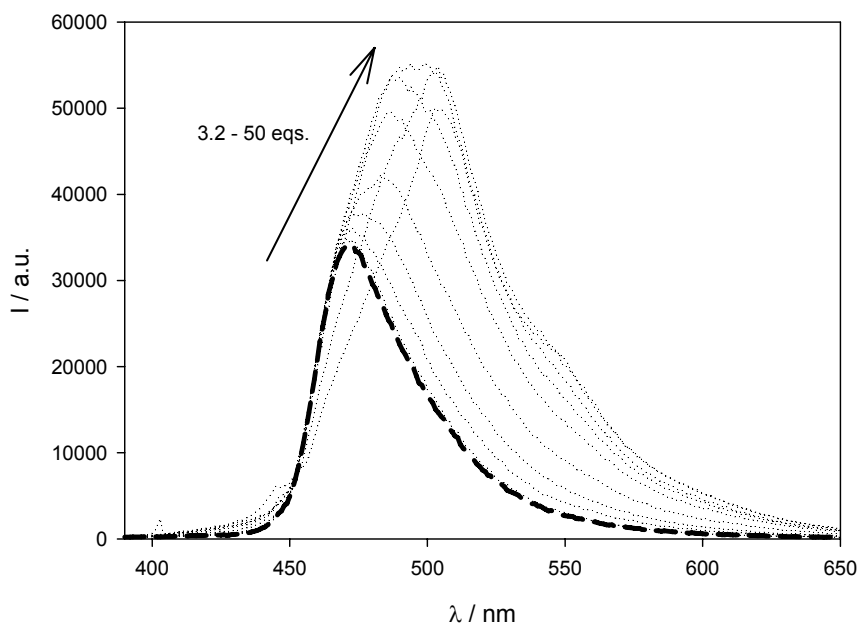


Figure 7.23. Emission spectra of a  $\text{CH}_2\text{Cl}_2$  air-equilibrated solution of C343-SPMC-C343 ( $c = 1.1 \times 10^{-6} \text{ M}$ ) at 298 K upon addition of a bunch of eqs. of  $\text{CF}_3\text{SO}_3\text{H}$  (triflic acid). Dashed spectrum is C343-SPMC·2H<sup>+</sup>·C343.

Protonation of the **C343** units does not result in recovering the protonated macrocycle emission so preventing its quenching by electron transfer. This is explained by the fact that fluorescent excited state localized on protonated **C343** lies below the excited state localized on protonated macrocycle.

Lifetime measurements provides weird results. At least till protonation of the macrocycle is involved, lifetime of the **C343** unit ( $\tau = 3.0$  ns, black decay in Figure 7.24.) is not expected to decrease consistently with an electron-transfer quenching mechanism. Energy transfer, corresponding to a situation where donor lifetime decreases, should result in sensitization of protonated macrocycle emission, but it has never been observed. It has been stated that  $^*\text{SPMC}\cdot 2\text{H}^+$  lies at higher energy compared to  $^*\text{C343}$ .

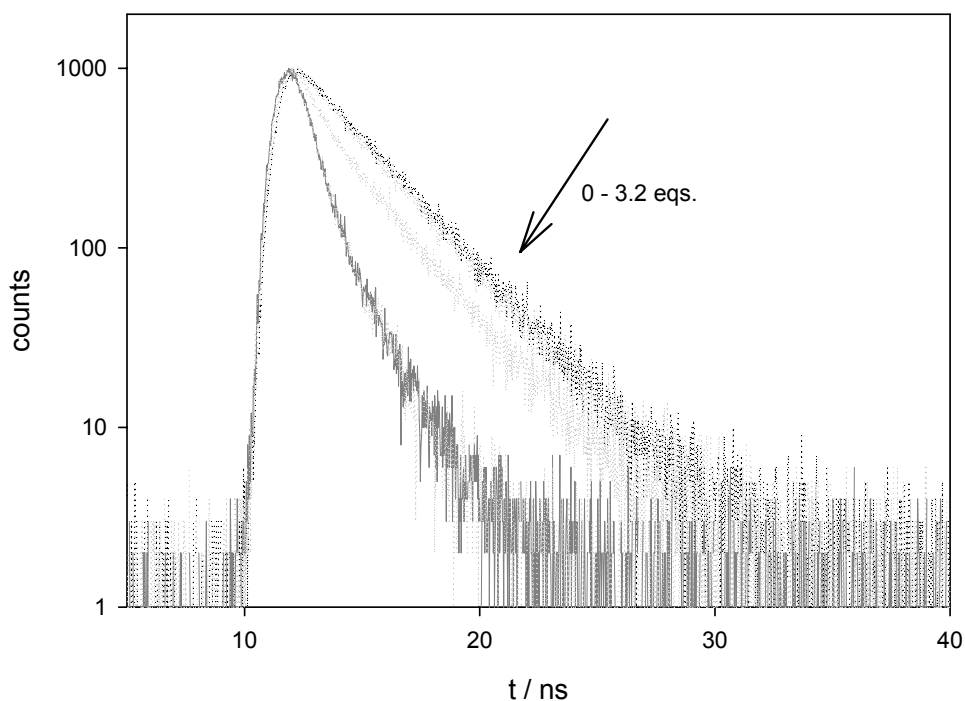


Figure 7.24. Fluorescence lifetime decay changes upon excitation at 278 nm of a  $\text{CH}_2\text{Cl}_2$  air-equilibrated solution of C343-SPMC-C343 ( $c = 3.0 \times 10^{-6}$  M) at 298 K upon addition of  $\text{CF}_3\text{SO}_3\text{H}$  (triflic acid). Black decay is C343-SPMC-C343, dark grey decay is C343-SPMC $\cdot 2\text{H}^+$ -C343.

Plot of the changes in absorbance and emission spectra of **C343-SPMC-C343** (Figure 7.25.) during macrocycle protonation is not fully consistent with the statistical behaviour observed for **SPMC** (Figure 7.4.) and **C2-SPMC-C2** (Figure 7.18.).

Further investigations (electrochemical measurements and absorption time-resolved experiments) are also necessary to establish the energy-level diagram of the states involved in the quenching processes, to estimate their rate constants, and to better verify the reversibility of the protonation reaction (once again it seems that the reaction is reversible at least as far as the protonation of the macrocycle is concerned).

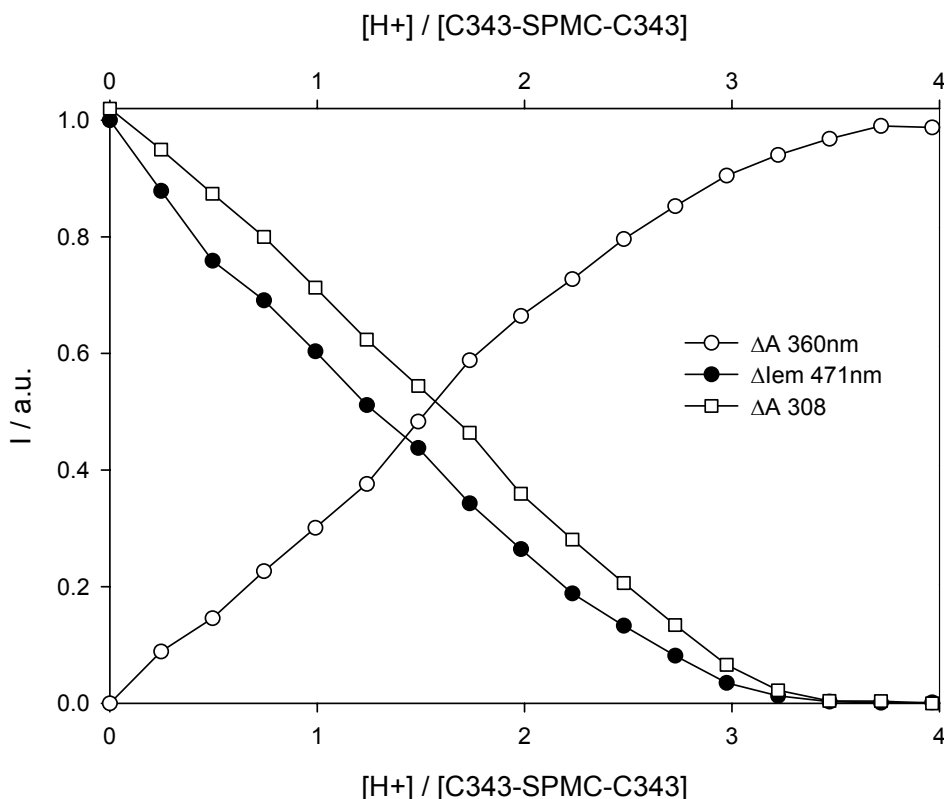


Figure 7.25. Absorption and emission normalized changes of a  $\text{CH}_2\text{Cl}_2$  air-equilibrated solution of C343-SPMC-C343 ( $c = 1.1 \times 10^{-6}$  M) at 298 K upon addition of  $\text{CF}_3\text{SO}_3\text{H}$  (triflic acid): legend assigns empty symbols to observed changes in absorption (Figure 7.20.) and filled symbols to changes in emission (Figure 7.21.) spectra.

*Asymmetrically substituted macrocycle with C2 and C343*

Molecular components presented in Figure 7.1. have been chosen and characterized with the aim of constructing the result three component system (Figure 7.26.) capable of undergoing different photoinduced intercomponent interactions.

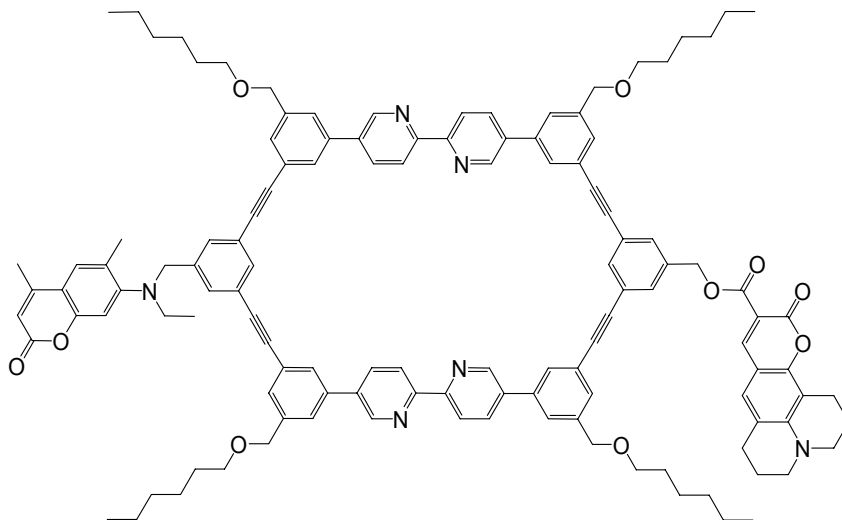


Figure 7.26. Formula of C2-SPMC-C343.

The absorption spectrum of the asymmetric macrocycle (**C2-SPMC-C343**), as already observed in substituted macrocycles (**C2-SPMC-C2** and **C343-SPMC-C343**), coincides with the sum of its components (solid spectrum in Figure 7.27.).

The behaviour upon protonation follows previous findings: the two bpy moieties of the shape-persistent macrocycle undergo protonation before coumarins (dashed spectrum in Figure 7.27.). Further acid addition involves both coumarins simultaneously (compare spectral changes in Figure 7.28 with those observed for substituted macrocycles in Figures 7.15. for **C2-SPMC-C2** and 7.22. for **C343-SPMC-C343**, and for the molecular components).

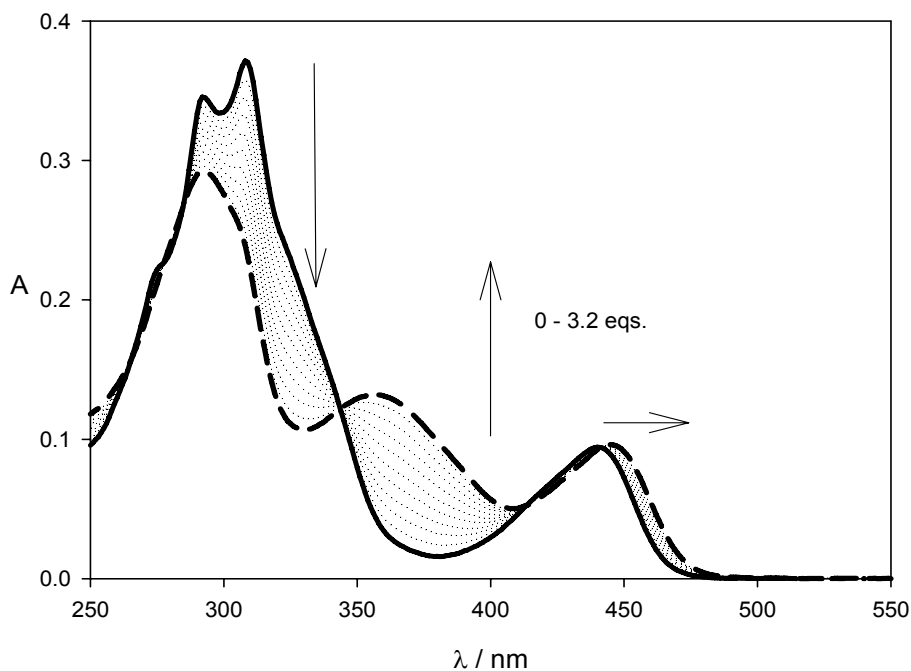


Figure 7.27. Absorption spectra of a  $\text{CH}_2\text{Cl}_2$  air-equilibrated solution of C2-SPMC-C343 ( $c = 2.0 \times 10^{-6} \text{ M}$ ) at 298 K upon addition of 3.2 eqs. of  $\text{CF}_3\text{SO}_3\text{H}$  (triflic acid). Solid spectrum is C2-SPMC-C343, dashed spectrum is C2-SPMC $\cdot$ 2H $^+$ -C343.

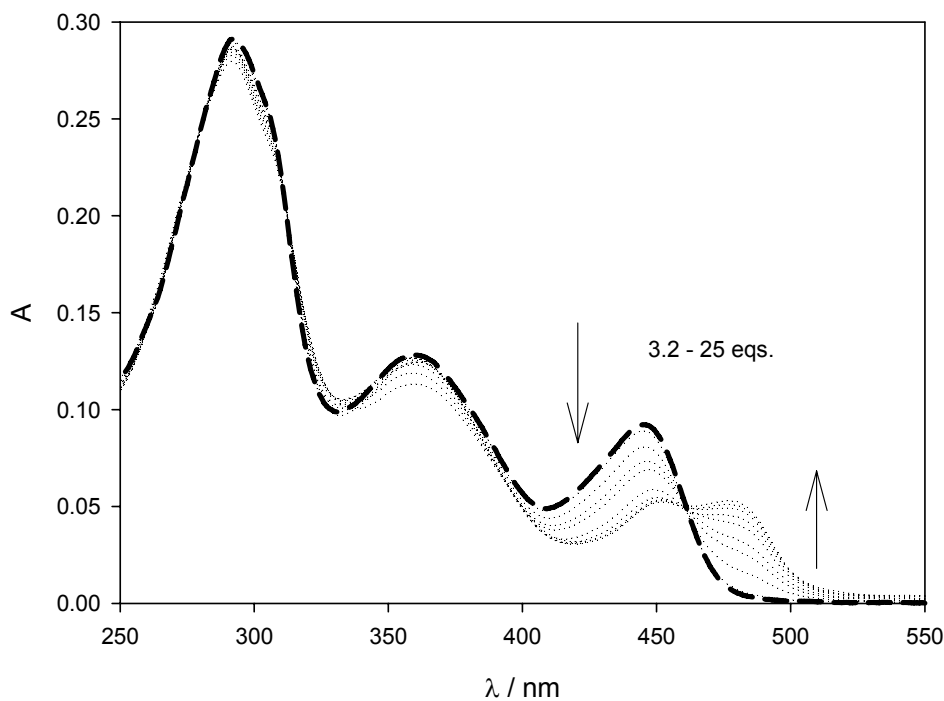


Figure 7.28. Absorption spectra of C2-SPMC $\cdot$ 2H $^+$ -C343 upon further addition of triflic acid

Upon almost selective excitation of the macrocyclic unit ( $\lambda_{\text{ex}} = 278 \text{ nm}$ ), the excitation energy is funnelled to lower lying excited state localized on the **C343** moiety, as far as the emission band characteristic of the latter molecular component is observed (solid spectrum in Figure 7.29.).

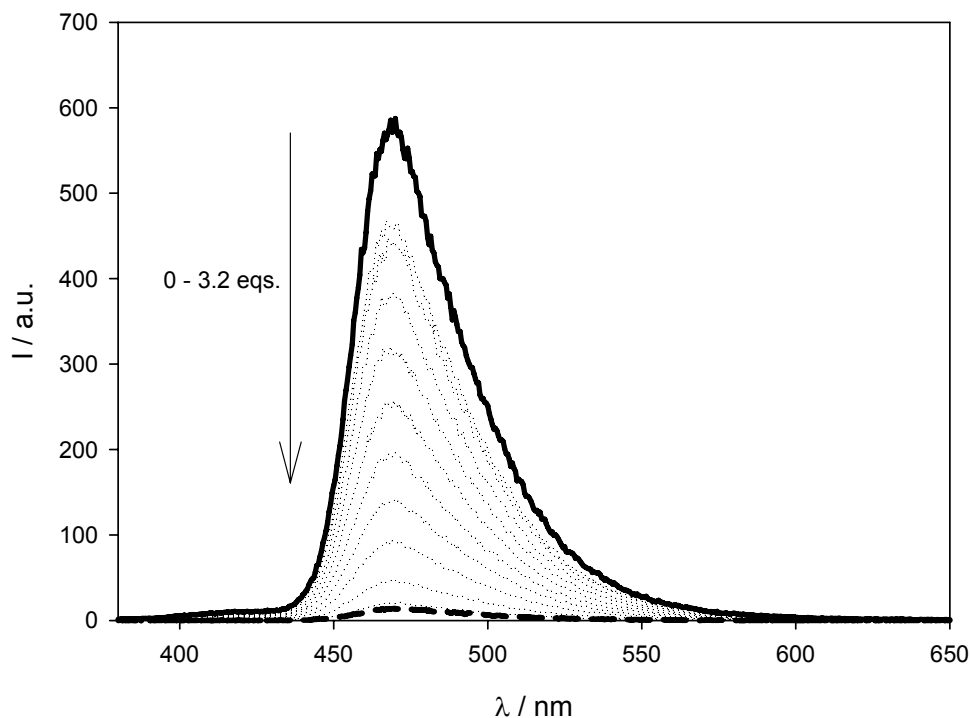


Figure 7.29. Emission spectra of a  $\text{CH}_2\text{Cl}_2$  air-equilibrated solution of C2-SPMC-C343 ( $c = 2.0 \times 10^{-6} \text{ M}$ ) at 298 K upon addition of 3.2 eqs. of  $\text{CF}_3\text{SO}_3\text{H}$  (triflic acid). Solid spectrum is C2-SPMC-C343, dashed spectrum is C2-SPMC· $2\text{H}^+$ ·C343.

It is worth noting the presence of a shoulder at higher energy on the **C343** emission band (solid spectrum in Figure 7.29.); its assignation is not straightforward because its low intensity that does not allow recording of its excitation spectrum and lifetime. Anyway, its position in the visible spectrum and the fact that it disappears upon protonation of the macrocyclic unit accounts for the presence of residual emission of **C2** unit. Such a behaviour may be tentatively explained by taking into account structural organization of **C2-SPMC-**

**C343**: when the macrocycle is excited, the excitation energy can be transfer on excited states localized on both coumarins. The two coumarins are spatially confined by the macrocyclic scaffold and this may result in reduced rate constant of FRET from **C2** to **C343** (because of relevant  $k_{AB}$  in eq. 18); the radiative pathway of  $^*\mathbf{C2}$  competes with the energy-transfer to **C343** pathway.

In analogy with previous results, selective quasi-stoichiometric protonation of the macrocyclic unit occurs in **C2-SPMC-C343** leading to 95% quenching of the **C343** emission by an electron-transfer process between lone pairs on the coumarins and protonated macrocycle. Further protonation does not lead to recover protonated macrocycle emission (Figure 7.30.) because  $^*\mathbf{C343}\cdot\mathbf{2H}^+$  lies at lower energy than  $^*\mathbf{SPMC}$ , as can be deduced by the onset of the corresponding absorption spectrum.

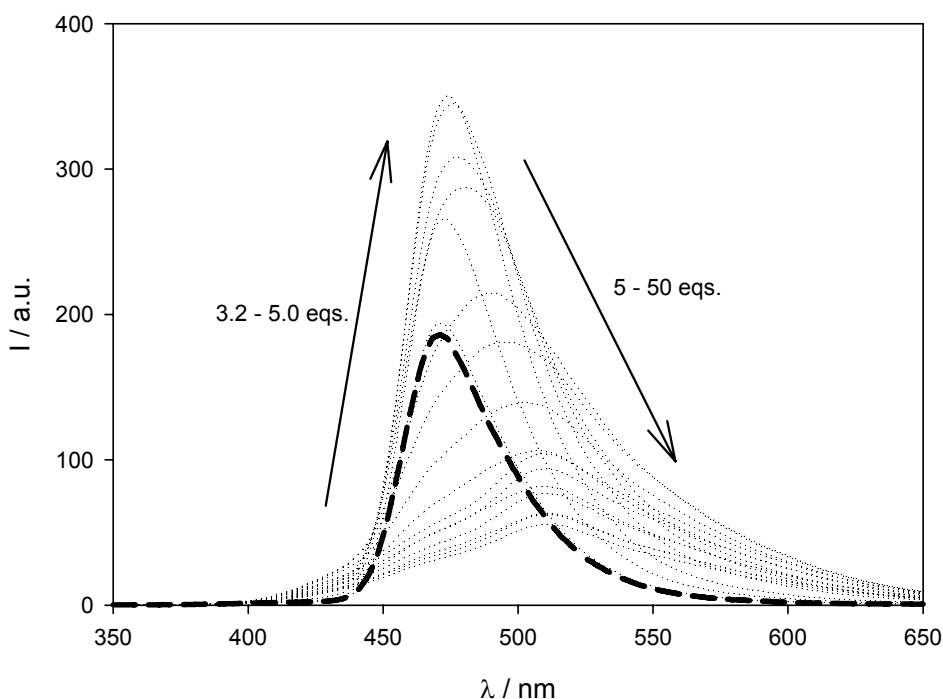


Figure 7.30. Emission spectra of a  $\text{CH}_2\text{Cl}_2$  air-equilibrated solution of **C2-SPMC-C343** ( $c = 2.0 \times 10^{-6}$  M) at 298 K upon addition of a bunch of eqs. of  $\text{CF}_3\text{SO}_3\text{H}$  (triflic acid). Dashed spectrum is **C2-SPMC·2H<sup>+</sup>-C343**.

Informations provided by lifetime measurements are consistent with those obtained in the case of **C343-SPMC-C343**. The evaluation of the **C343** emission quenching mechanism upon macrocycle protonation is not straightforward at all.

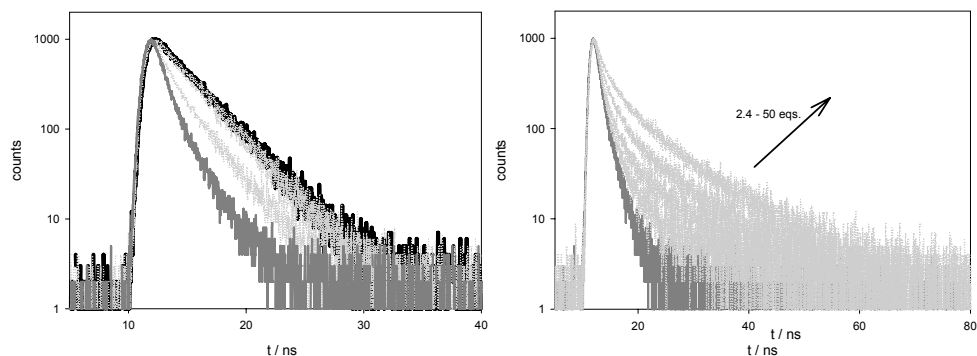


Figure 7.31. Fluorescence lifetime decay changes upon excitation at 278 nm of a  $\text{CH}_2\text{Cl}_2$  air-equilibrated solution of C2-SPMC-C343 ( $c = 3.0 \times 10^{-6}$  M) at 298 K upon addition of  $\text{CF}_3\text{SO}_3\text{H}$  (triflic acid). Black decay is C2-SPMC-C343, dark grey decay is C2-SPMC $\cdot$ 2H $^+$ -C343.

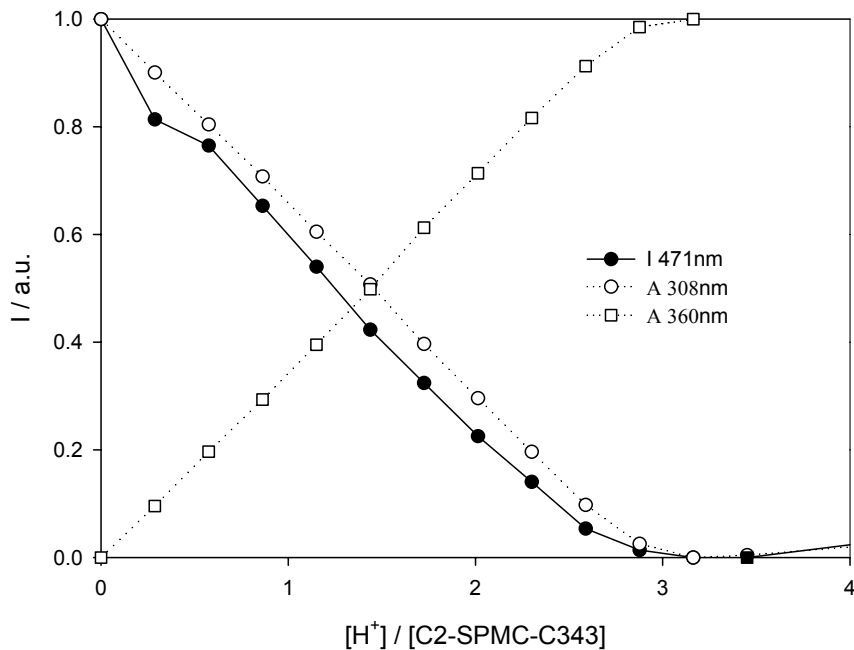


Figure 7.32. Absorption and emission normalized changes of a  $\text{CH}_2\text{Cl}_2$  air-equilibrated solution of C2-SPMC-C343 ( $c = 2.0 \times 10^{-6}$  M) at 298 K upon addition of  $\text{CF}_3\text{SO}_3\text{H}$  (triflic acid): legend assigns empty symbols to observed changes in absorption (Figure 7.27.) and filled symbols to changes in emission (Figure 7.29.) spectra.

Once again, since **C343** units are involved, the plot of its quenching upon macrocycle protonation markedly diverges from statistical trend (Figure 6.32).

If only the amount of acid necessary to protonate the macrocycle is added, the emission of the **C343** is totally restored by deprotonation of the macrocycle, with appreciable reversibility.

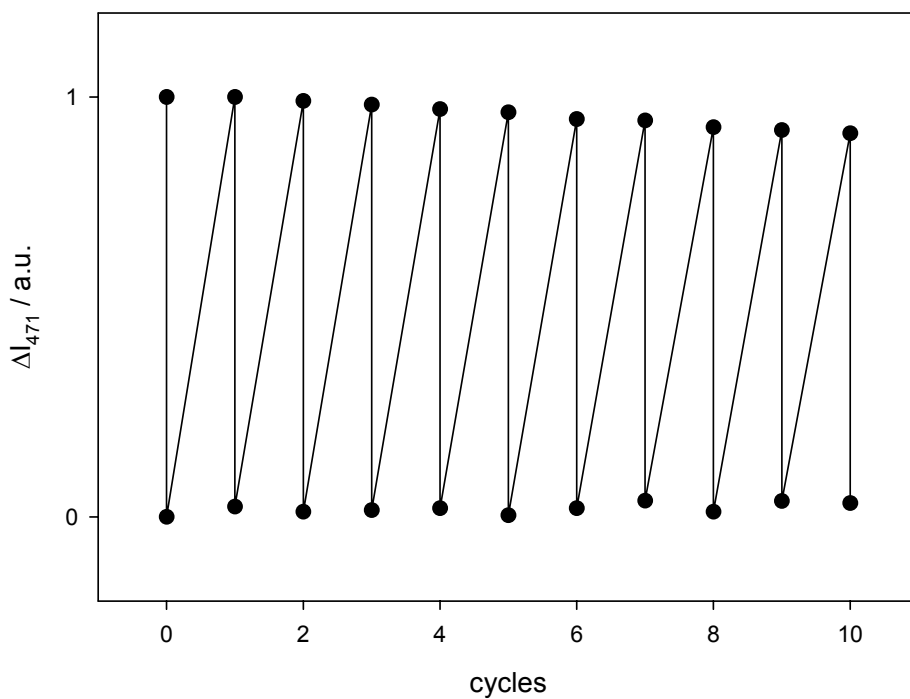


Figure 7.33. Normalized emission intensities ( $\lambda_{\text{em}} = 471 \text{ nm}$ ) of a  $\text{CH}_2\text{Cl}_2$  solution of C2-SPMC-C343 at 298 K during reversible protonation cycles with 3.2 eqs. of  $\text{CF}_3\text{SO}_3\text{H}$  and  $\text{BU}_3\text{N}$ .

Table 7.1. Photophysical parameters of the investigated compounds.

	$\lambda_{em} / \text{nm}$	$\phi^a$	$\tau / \text{ns}$	$\eta_{et}$
<b>SPMC</b>	381	.90	0.75	-
<b>SPMC•2H<sup>+</sup></b>	514	.12	11.5	0 <sup>b</sup>
<b>C2-SPMC-C2</b>	427	.73	3.6	$\approx 1^c$
<b>NB-C2</b>	436	.79	3.2	-
<b>C343-SPMC-C343</b>	471	.92	3.0	$\approx 1^d$
<b>BE-C343</b>	470	.93	3.0	-
<b>C2-SPMC-C343</b>	471	.92	3.0	.85 <sup>e</sup>

<sup>a</sup> calculated vs. 9-10 diphenylanthracene;

<sup>b</sup> energy transfer does not occur between protonated and unprotonated residues within the same macrocycle;

<sup>c</sup> from macrocycle to **C2**;

<sup>d</sup> from macrocycle to **C343**;

<sup>e</sup> from macrocycle to **C343** through **C2**.

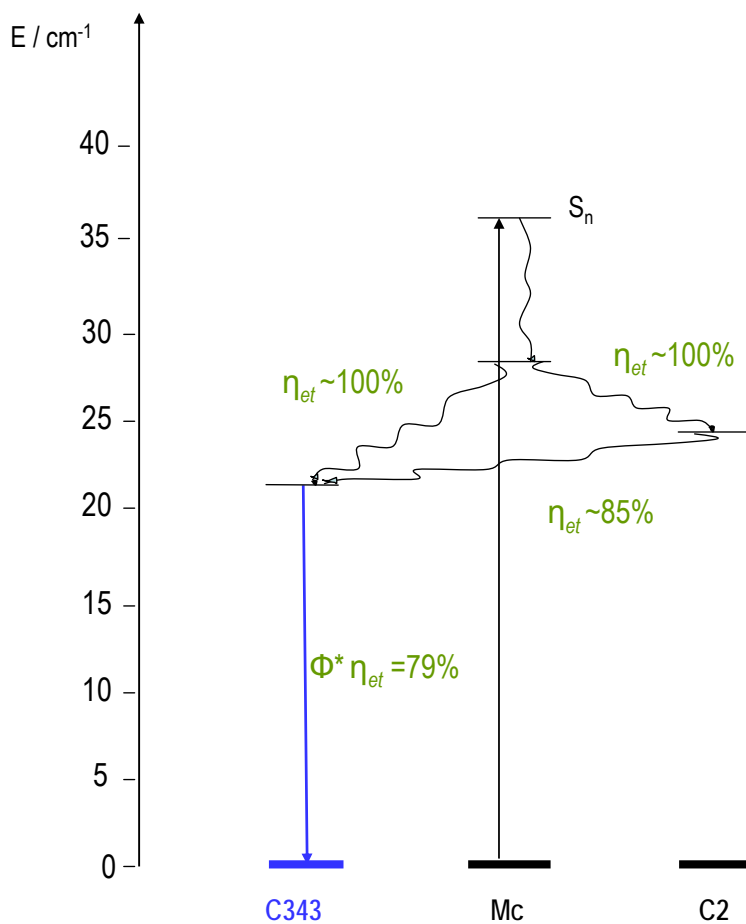


Figure 7.34. Energy level diagram of intercomponent energy transfer processes and relative efficiencies in C2-SPMC-C343.

## 7.2. Furan-containing [n.2] Cyclophanes

Studies on the relationship between the structures of organic conjugated systems and their molecular hyperpolarizabilities have been extensive because they may provide useful information for the application of nonlinear optical (NLO) properties in electrooptical devices. The criterion for an organic molecule to exhibit second-order optical nonlinearity is the lack of a center of symmetry. The presence of donor and acceptor moieties conjugated with the linking  $\pi$  system is known to facilitate the formation of intramolecular charge transfer, which will induce second-order NLO properties.<sup>231</sup> Recently, a series of [2.2]paracyclophane derivatives has been shown to demonstrate three-dimensional dipolar and octupolar NLO properties as a result of through-space delocalization of the chromophores.<sup>232</sup> It is envisioned that interactions between the heteroarene rings and the bridging double bond(s) in [2.2]heterophenes may lead to a dipolar resonance structure.

Recently, it has been reported that furan-containing [2.2]cyclophane (Figure 7.35.) exhibits extraordinary photophysical properties relative to those of its saturated analogue.<sup>233</sup>

The emission band of the saturated cyclophane appears at a similar wavelength to that of the unbridged teraryl constituents (ca. 380 nm). The observation of similar vibronic structures suggests that there is no delocalization between the two teraryl moieties in the saturated cyclophane. In the absorption spectrum of [2.2]cyclophane there is a low-energy band at about

---

[231] a) *Nonlinear Optics of Organic Molecules and Polymers* (Eds.: H.S. Nalwa, S. Miyata), CRC, Boca Raton, FL, 1997; b) G.D.L. Torre, P. Vázquez, F. Agulló-López, T. Torres, *Chem. Rev.* 2004, 104, 3723; c) J.A. Delaire, K. Nakatani, *Chem. Rev.* 2000, 100, 1817; d) D.R. Kanis, M.A. Ratner, T.J. Marks, *Chem. Rev.* 1994, 94, 195; e) S. Marder, *Chem. Commun.* 2006, 131, 131; f) M. Ahlheim, M. Barzoukas, P.V. Bedworth, M. Blanchard-Desce, A. Fort, Z.-Y. Hu, S.R. Marder, J.W. Perry, C. Runser, M. Staehelin, B. Zyssset, *Science* 1996, 271, 335.

[232] a) G.P. Bartholomew, I. Ledoux, S. Mukamel, G. C. Bazan, J. Zyss, *J. Am. Chem. Soc.* 2002, 124, 13480; b) J. Zyss, I. Ledoux, S. Volkov, V. Chernyak, S. Mukamel, G.P. Bartholomew, G.C. Bazan, *J. Am. Chem. Soc.* 2000, 122, 11956.

[233] J.-C. Tseng, S.-L. Huang, C.-L. Lin, H.-C. Lin, B.-Y. Jin, C.-Y. Chen, J.-K. Yu, P.-T. Chou, T.-Y. Luh, *Org. Lett.* 2003, 5, 4381.

380 nm, as well as an absorption band at about 330 nm arising from the teraryl chromophore.

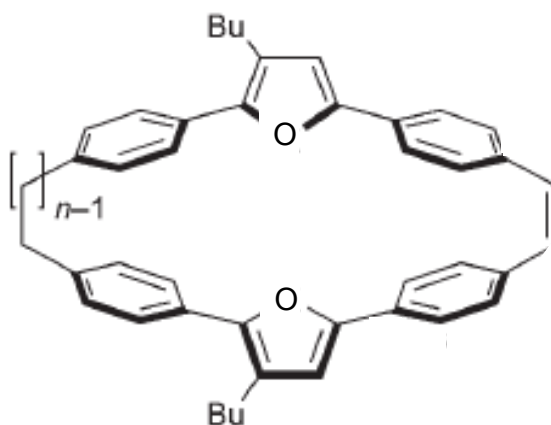


Figure 7.35. Formula of the investigated [n.2] cyclophanes; the saturated homolog [n.2] cyclophane does not show the alkene bridge.

The emission spectrum of [2.2]cyclophane is striking, with a large Stokes shift (178 nm) being observed. It seems likely that interactions between the teraryl sections and the double bond in [2.2]cyclophane may be different in the ground and the excited states. The teraryl moieties and the double bond in [2.2]cyclophane are clearly not in the same plane. Recently, it has been shown that chromophores with twisted  $\pi$ -electron systems in a biaryl system having charged donor and acceptor moieties exhibit ultralarge molecular hyperpolarizability with exceptionally high  $\mu\beta$  values.<sup>234</sup> It is therefore envisaged that [2.2]cyclophane may have second-order NLO activity even in the absence of any apparent electron-withdrawing substituents. A systematic investigation of the NLO properties of a series of furan-containing

[234] a) I. D. L. Albert, T. J. Marks, M. A. Ratner, *J. Am. Chem. Soc.* 1998, 120, 11174; b) H. Kang, A. Facchetti, P. Zhu, H. Jiang, Y. Yang, E. Cariati, S. Righetto, R. Ugo, C. Zuccaccia, A. Macchioni, C.L. Stern, Z. Liu, S.-T. Ho, T. J. Marks, *Angew. Chem.* 2005, 117, 8136; *Angew. Chem. Int. Ed.* 2005, 44, 7922; c) C. M. Isborn, E.R. Davidson, B.H. Robinson, *J. Phys. Chem. A* 2006, 110, 7189.

[n.2]cyclophanes with tethering chains of different lengths has been recently reported.<sup>235</sup> Electric-field-induced second-harmonic generation (EFISH) measurements at 1.91  $\mu\text{m}$  have been employed for the NLO investigations.<sup>236</sup>

A detailed study of linear and nonlinear optical properties of [3.2] cyclophane (Figure 7.35.) has been carried out at the UCSB Optical Characterization Facility managed by Dr. Mikhailovsky following procedures mentioned in section 3.1.

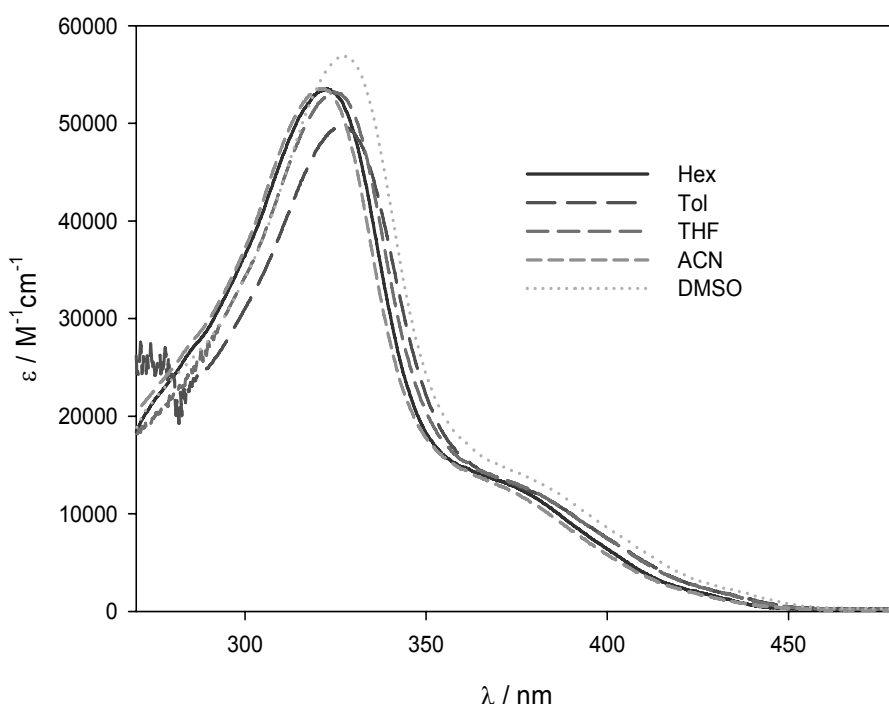


Figure 7.36. Absorption spectra of [3.2] cyclophane at 298 K: legend assigns line styles relative to the solvent where sample have been dissolved.

[235] Hsin-Chieh Lin, Dr., Wei-Yu Lin, Dr., Hao-Tien Bai, Jia-Hong Chen, Bih-Yaw Jin, Prof., Tien-Yau Luh, *Angew. Chem. Int. Ed.*, 2006, 46, 897.

[236] a) K.D. Singer, A. F. Garito, *J. Chem. Phys.* 1981, 75, 3572; b) I. Ledoux, J. Zyss, *Chem. Phys.* 1982, 73, 203; c) L.-T. Cheng, W. Tam, S.H. Stevenson, G.R. Meredith, G. Rikken, S.R. Marder, *J. Phys. Chem.* 1991, 95, 10631; d) D. Roberto, R. Ugo, S. Bruni, E. Cariati, F. Cariati, P. Fantucci, I. Invernizzi, S. Quici, I. Ledoux, J. Zyss, *Organometallics* 2000, 19, 1775

All measurements have been performed in several solvents, namely hexanes (HEX), toluene (TOL), tetrahydrofuran (THF), acetonitrile (ACN), and dimethylsulfoxide (DMSO), to establish the solvent-dependence of [3.2] cyclophene optical properties. UV-Vis absorption spectra do not show relevant solvent dependence (Figure 7.36.). [3.2] cyclophene exhibits two absorption bands peaked around 325 and 375 nm almost insensitive to the dielectric properties of the medium.

One-photon induced fluorescence spectra show, instead, dependence on either solvent and excitation wavelength (Figures 7.37. in HEX, 7.38. in TOL, 7.39. in THF, 7.40. in ACN, and 7.41. in DMSO).

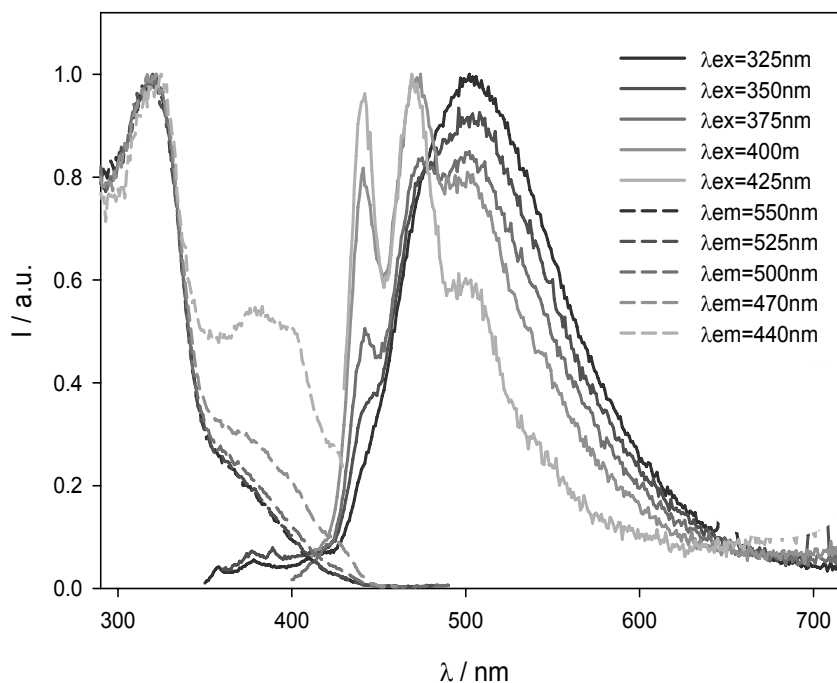


Figure 7.37. Emission (solid line) and excitation (dashed line) spectra of [3.2] cyclophene in HEX ( $c = 1.5 \times 10^{-6}$  M) at 298 K: legend assigns line styles relative to the excitation (in emission spectra) and emission (in excitation spectra) wavelengths.

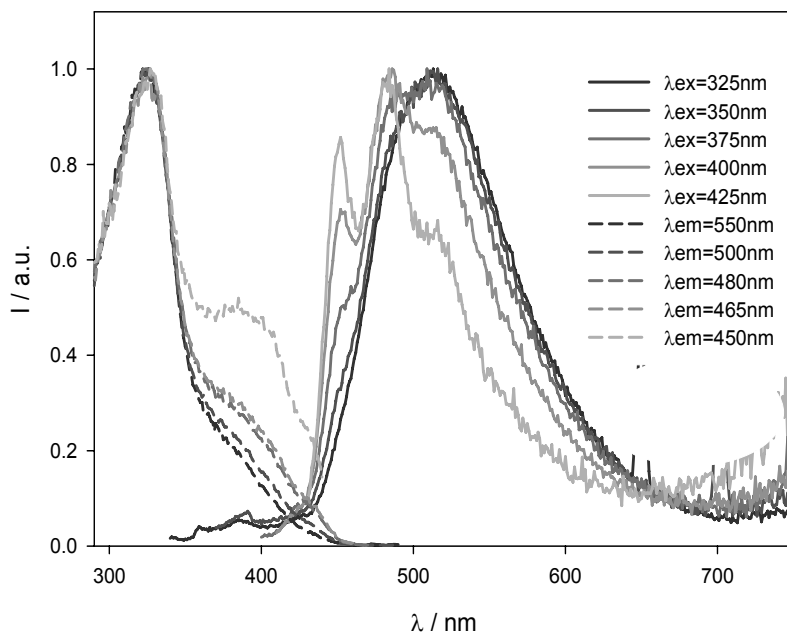


Figure 7.38. Emission (solid line) and excitation (dashed line) spectra of [3.2] cyclophene in TOL ( $c = 1.5 \times 10^{-6}$  M) at 298 K: legend assigns line styles relative to the excitation (in emission spectra) and emission (in excitation spectra) wavelengths.

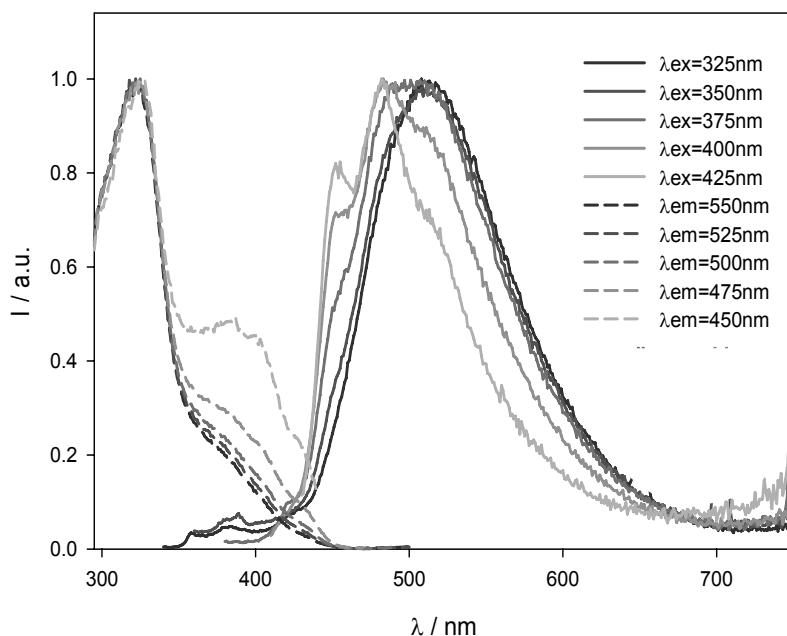


Figure 7.39. Emission (solid line) and excitation (dashed line) spectra of [3.2] cyclophene in THF ( $c = 1.5 \times 10^{-6}$  M) at 298 K: legend assigns line styles relative to the excitation (in emission spectra) and emission (in excitation spectra) wavelengths.

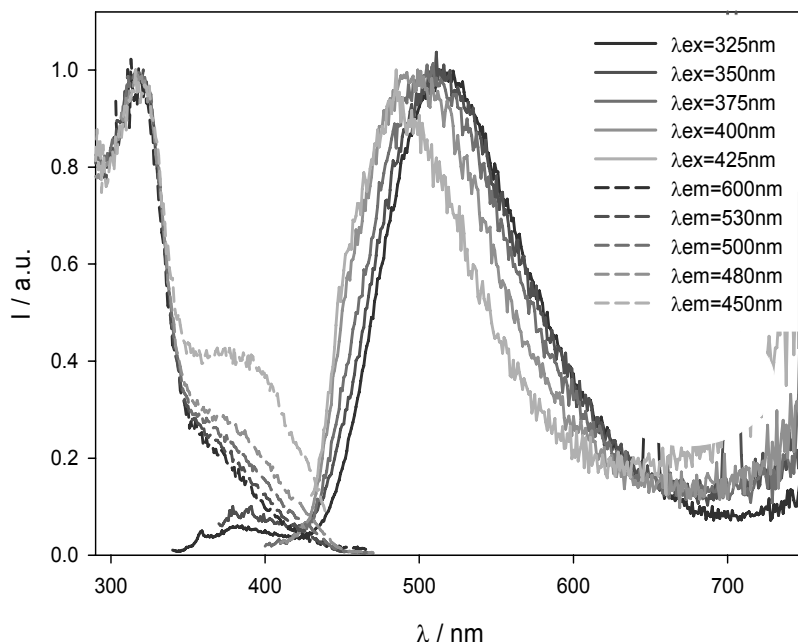


Figure 7.40. Emission (solid line) and excitation (dashed line) spectra of [3.2] cyclophene in ACN ( $c = 1.5 \times 10^{-6}$  M) at 298 K: legend assigns line styles relative to the excitation (in emission spectra) and emission (in excitation spectra) wavelengths.

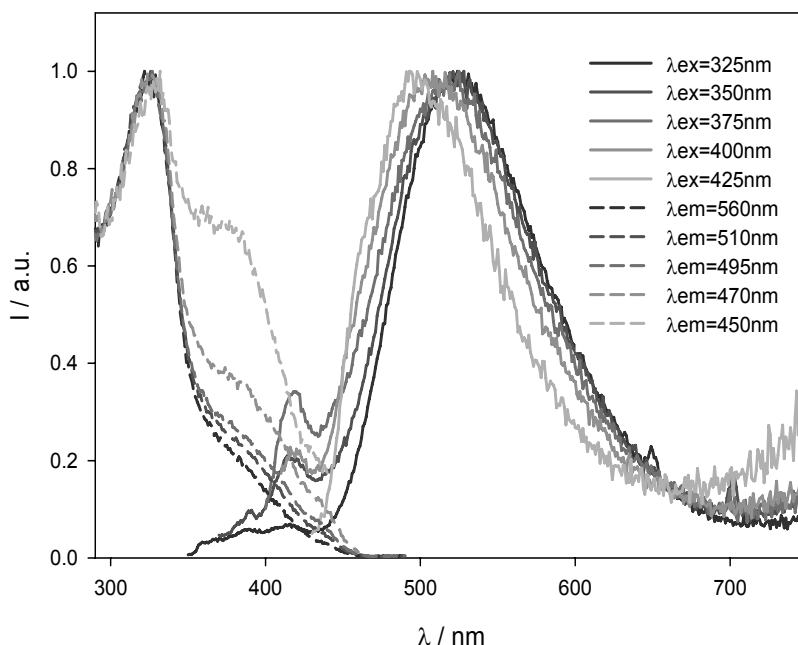


Figure 7.41. Emission (solid line) and excitation (dashed line) spectra of [3.2] cyclophene in DMSO ( $c = 1.5 \times 10^{-6}$  M) at 298 K: legend assigns line styles relative to the excitation (in emission spectra) and emission (in excitation spectra) wavelengths.

Short excitation wavelength (below 350 nm) leads to fluorescence spectra close to that previously reported<sup>235</sup> with a large Stokes-shift, without noticeable vibronic progression, and maximum of the emission band slightly moving toward longer wavelengths increasing solvent polarity (Table 7.2.). These features usually characterize species undergoing electronic transitions with a high charge-transfer character.

Long excitation wavelength (above 400 nm) instead, leads to the observation of a blue-shifted emission band showing vibronic structure that decrease on increasing solvent polarity, while the maximum of the emission band more markedly shifts toward longer wavelengths on increasing solvent polarity (Table 7.2.). These features account for a higher charge-transfer character of the excited state responsible of such a higher energy emission band.

One-photon induced excitation spectra have been measured to understand the origin of the two emission bands. Diluted solutions have been used in order to avoid geometrical and inner filter effects so enabling to correlate linear excitation spectra with linear absorption spectra. The excitation spectrum monitored at long wavelength (above 500 nm, where the emissive state is that obtained exciting below 350 nm) resembles linear absorption spectrum. Recording excitation spectrum below 500 nm leads to a divergence from the linear absorption spectrum: the ratio of the two bands around 325 and 375 nm is markedly decreased. Monitoring excitation spectrum on the onset of the emission band obtain exciting above 400 nm, the excitation band around 375 nm reaches its maximum.

Emission quantum yields, measured versus Fluorescein standard at pH = 11, again show such an excitation wavelength dependence. Concentration of the solutions are low enough to avoid self-quenching and internal filter effects. Generally, quantum yield values are higher when the emission spectrum is dominated by the longer wavelength band (Table 7.2.).

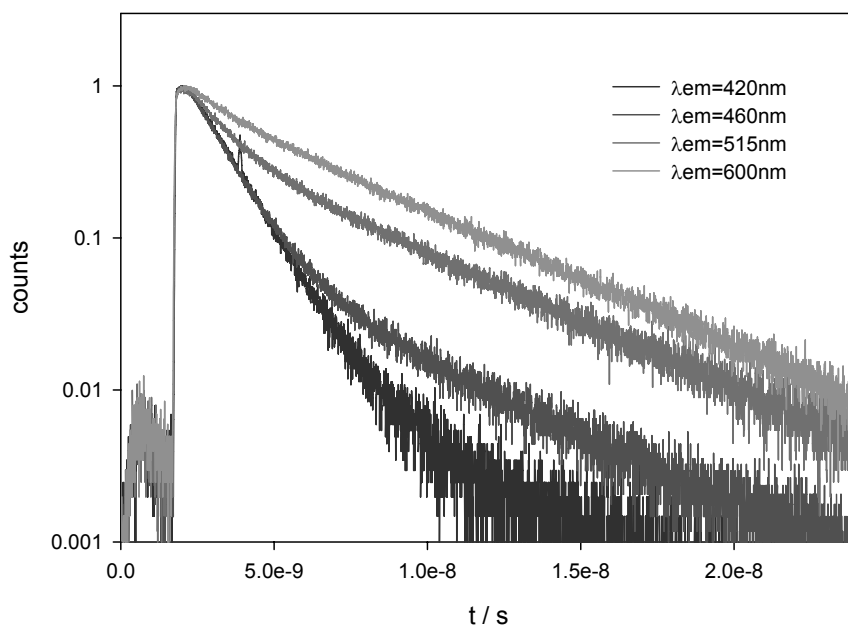


Figure 7.42. Fluorescence lifetime decay of [3.2] cyclophene in TOL ( $c = 1.5 \times 10^{-6}$  M) at 298 K: legend assigns line styles relative to the excitation wavelengths.

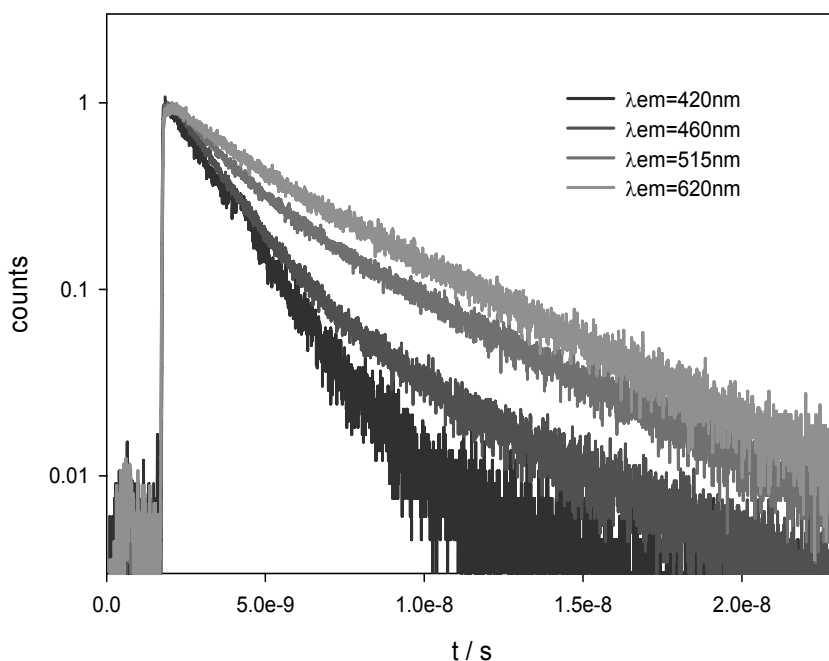


Figure 7.43. Fluorescence lifetime decay of [3.2] cyclophene in DMSO ( $c = 1.5 \times 10^{-6}$  M) at 298 K: legend assigns line styles relative to the excitation wavelengths.

Time-resolved fluorescence measurements have been also performed using TCSPC technique and listed in Table 7.2. Monoexponential decays have been observed using excitation wavelengths on the sides of absorption spectrum. In analogy, monoexponential decays have been observed monitoring the emission decay on the sides of the emission spectrum (shorter black decays in Figures 7.42. and 7.43. monitoring emission below 420 nm, while longer light grey decays in Figures 7.42. and 7.43. monitoring emission above 600 nm).

The results obtained by analysis of the linear optical properties of [3.2] cyclophene clearly suggest that the fluorescence is generated from two excited states, however their origin is not clear. Two emissive states in the same chemical species or two different conformers? This question is still to be answered.

In this regard, the discussion may appear pointless and further characterization useless. Anyway, two-photon induced fluorescence spectra of [3.2] cyclophene provide interesting informations.

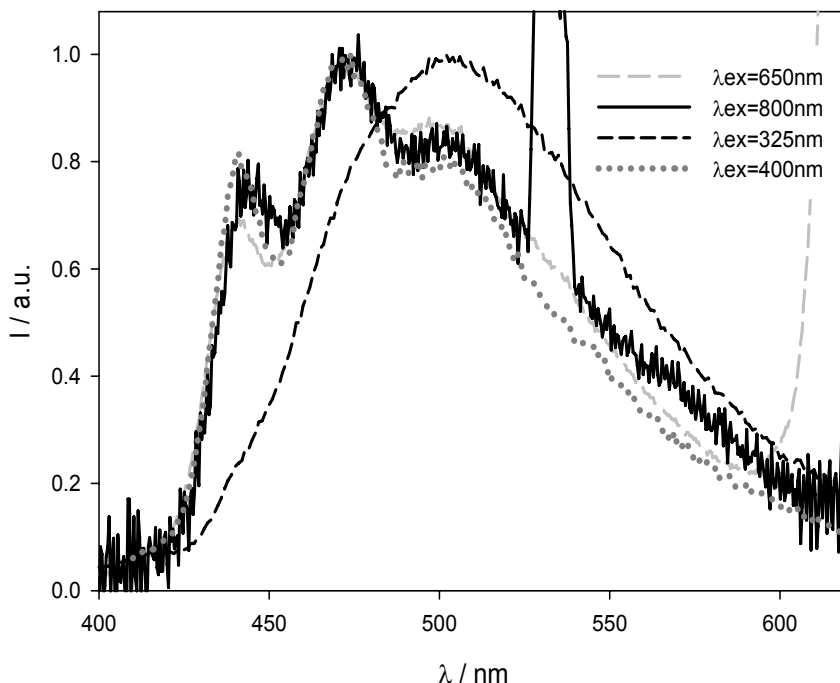


Figure 7.44. One- and two-photon induced fluorescence spectra of [3.2] cyclophene in HEX ( $c = 1.0 \times 10^{-5}$  M) at 298 K: legend assigns line styles relative to the excitation wavelengths.

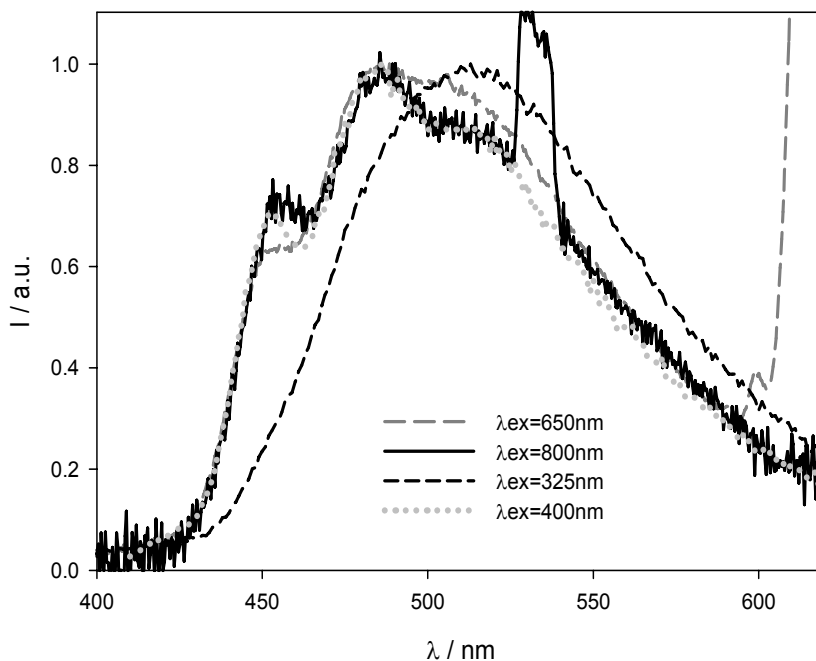


Figure 7.45. One- and two-photon induced fluorescence spectra of [3.2] cyclophane in TOL ( $c = 1.0 \times 10^{-5}$  M) at 298 K: legend assigns line styles relative to the excitation wavelengths.

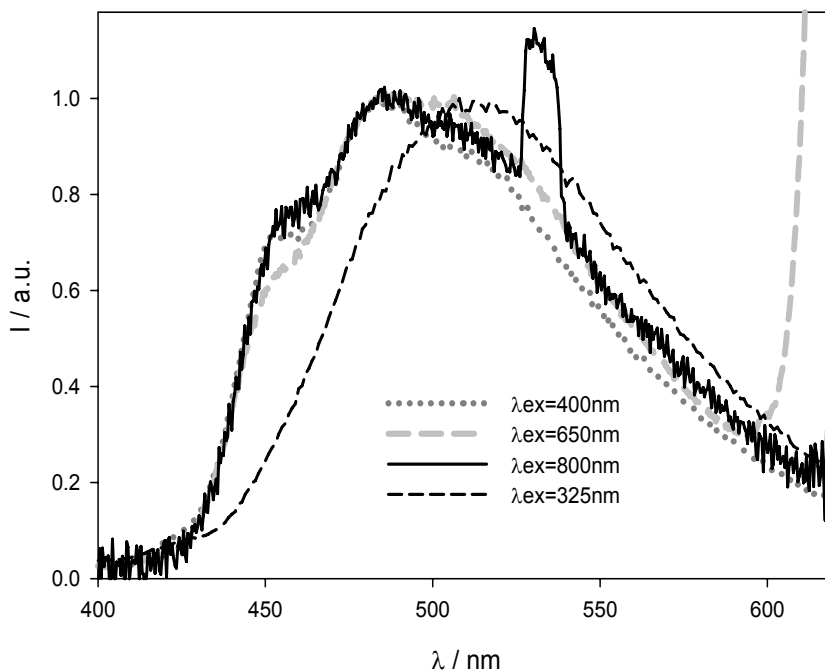


Figure 7.46. One- and two-photon induced fluorescence spectra of [3.2] cyclophane in THF ( $c = 1.0 \times 10^{-5}$  M) at 298 K: legend assigns line styles relative to the excitation wavelengths.

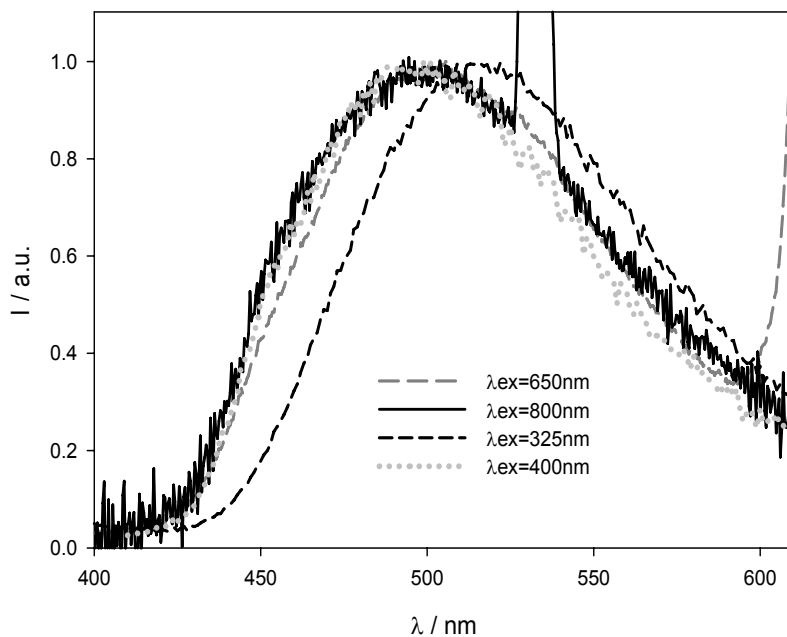


Figure 7.47. One- and two-photon induced fluorescence spectra of [3.2] cyclophane in ACN ( $c = 1.0 \times 10^{-5}$  M) at 298 K: legend assigns line styles relative to the excitation wavelengths.

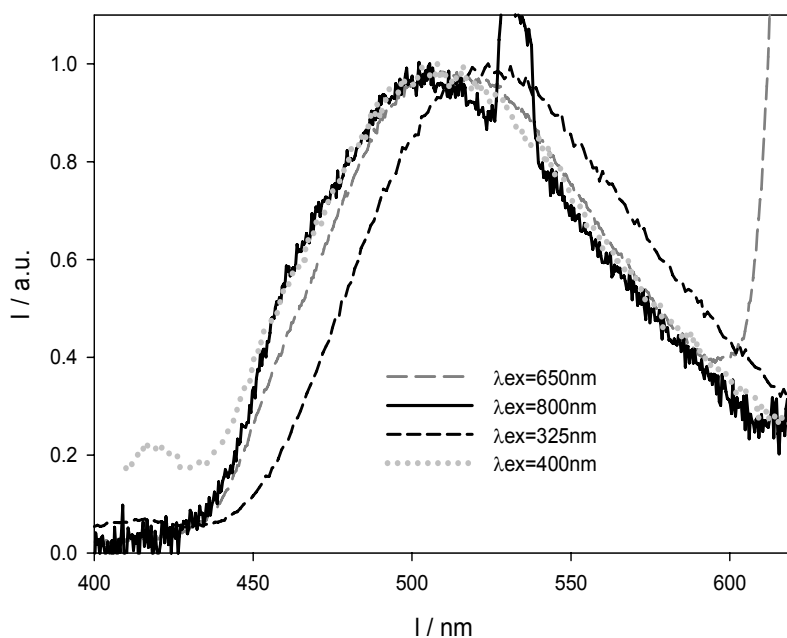


Figure 7.48. One- and two-photon induced fluorescence spectra of [3.2] cyclophane in DMSO ( $c = 1.0 \times 10^{-5}$  M) at 298 K: legend assigns line styles relative to the excitation wavelengths.

It is worth noting that, in contrast to one-photon induced fluorescence, two-photon induced fluorescence spectra do not exhibit dependence on the excitation wavelength. It clearly appears in the previous Figures 7.44., 7.45., 7.46., 7.47., and 7.48. Two-photon induced fluorescence spectra, in spite of the excitation wavelength, match the linear emission spectra obtained exciting at longer wavelengths (above 400 nm). This means that two-photon absorption process leads to selective generation of only one of the two emissive excited states evidenced by linear optical characterization. These findings do not enable a straightforward assignments of such excited states.

Prof Luh et al. have detailed a new series of furan-containing teraryl cyclophene derivatives which exhibit unusually large Stokes shifts and NLO properties. These [n.2] cyclophenes have neither particularly strong electron-donating moieties nor electron-withdrawing groups and have relatively low polarity. Yet they exhibit exceptionally high  $\mu\beta$  values. Structurally, the strained cyclophenes furnish a unique feature that dictates these unusual photophysical properties: strain results in the  $\pi$  systems of the teraryl system and the bridging double bond being twisted. Such a twisted system may thus induce significant enhancement in hyperpolarizability.<sup>234</sup> They have speculated that the five-membered heteroaromatic rings in [n.2] cyclophenes may not only serve as electron donors, but may also accommodate the appropriate geometry to enable the interactions to occur between the oligoaryl systems and the double bond that lead to unusual photophysical and NLO properties.

Presented characterization does not provide confirmation of Prof. Luh et al. results, since the [3.2] cyclophene they have been provided is the same sample they used in their investigations. The excited state populated by the two-photon absorption process has not been evidenced in their work. The two-photon absorption cross section values (Figure 7.49. and Table 7.2.) calculated using methods discussed in Section 3.1.7. and eq. 30 are not that high, too. Square dependence of emission intensity to pump fluence has been verified at all investigated wavelength.

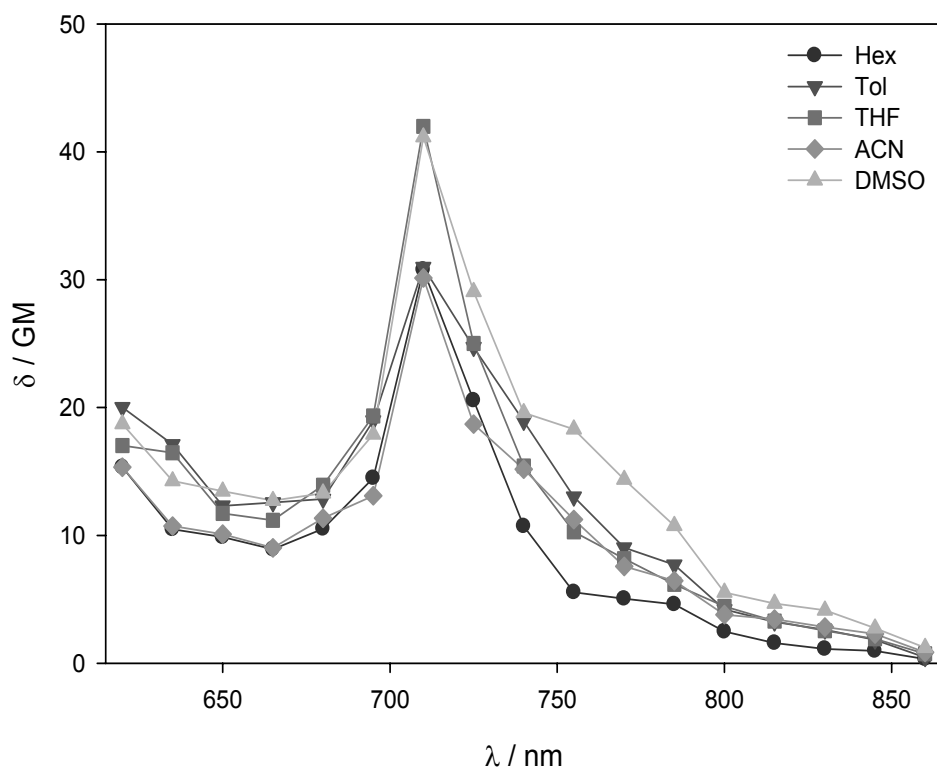


Figure 7.49. Two-photon excitation spectra of [3.2] cyclophene at 298 K: legend assigns symbols relative to the solvent where sample have been dissolved.

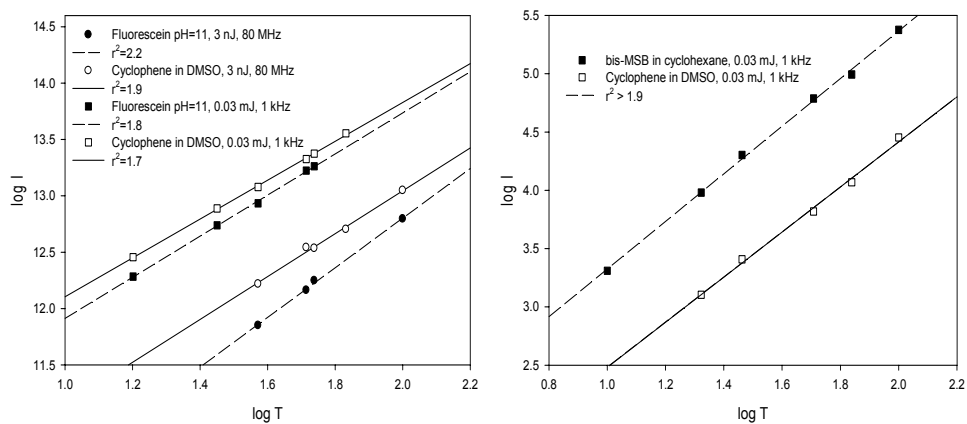


Figure 7.50. Square dependence of the fluorescence intensity of [3.2] cyclophene to pump fluence: legend assigns line styles and symbols relative to sample in TOL and DMSO and references excited at 710 nm.

Figure 7.50. show the case of  $\lambda_{\text{ex}} = 710$  nm. At this wavelength, in fact, the high repetition rate and low energy pulse excitation source (used for longer wavelengths generation, named Tsunami in Section 3.1.7.) overlaps the spectral range covered by the low repetition rate and high peak power pulse excitation source (used to generate shorter wavelengths by using SHG crystals, named OPA in Section 3.1.7.). The four two-photon absorption cross section values found with two different excitation sources and two different references match within experimental errors, providing reliability to here discussed results.

As previously demonstrated, one-photon absorption spectra show almost no solvent dependence. The same can be stated for two-photon absorption spectra (Figure 7.51.). The onset of the one- and two-photon absorption spectra lies at the same energy, but their maximum do not coincide, as it is supposed for molecules with lack of a center of symmetry.

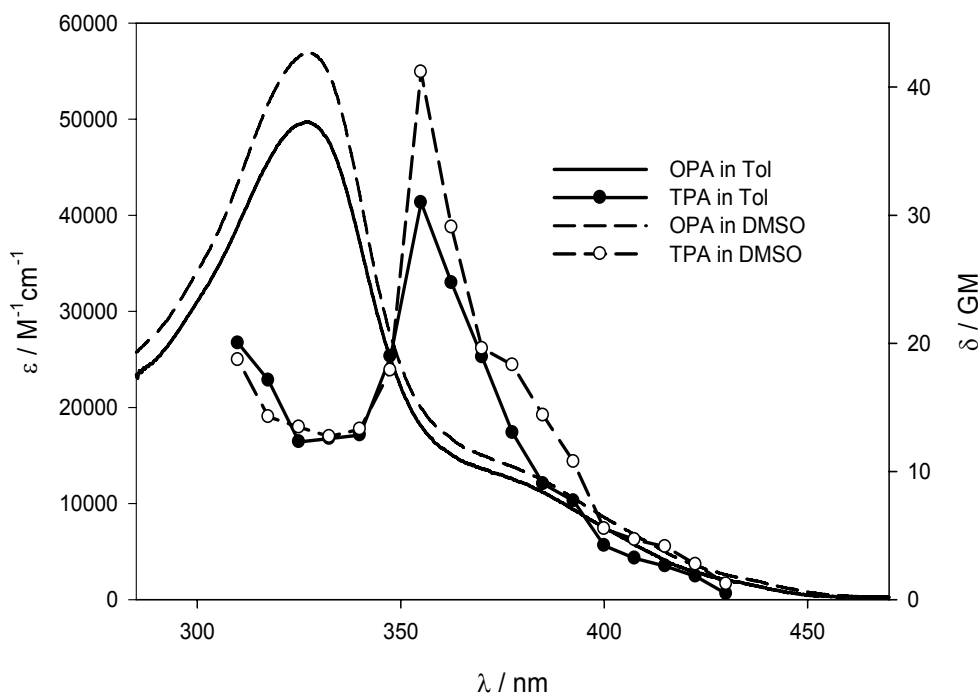


Figure 7.51. One-photon (lines) and two-photon (circles) absorption spectra of [3.2] cyclophene ( $c = 1.0 \times 10^{-5}$  M) in TOL (solid lines) and DMSO (dashed lines) at 298 K.

Furthermore, the two-photon absorption spectra show their maximum where the linear absorption spectra present the band around 375 nm. Such a band has been proven to originate the luminescence signal reminiscent of that obtained upon two-photon excitation.

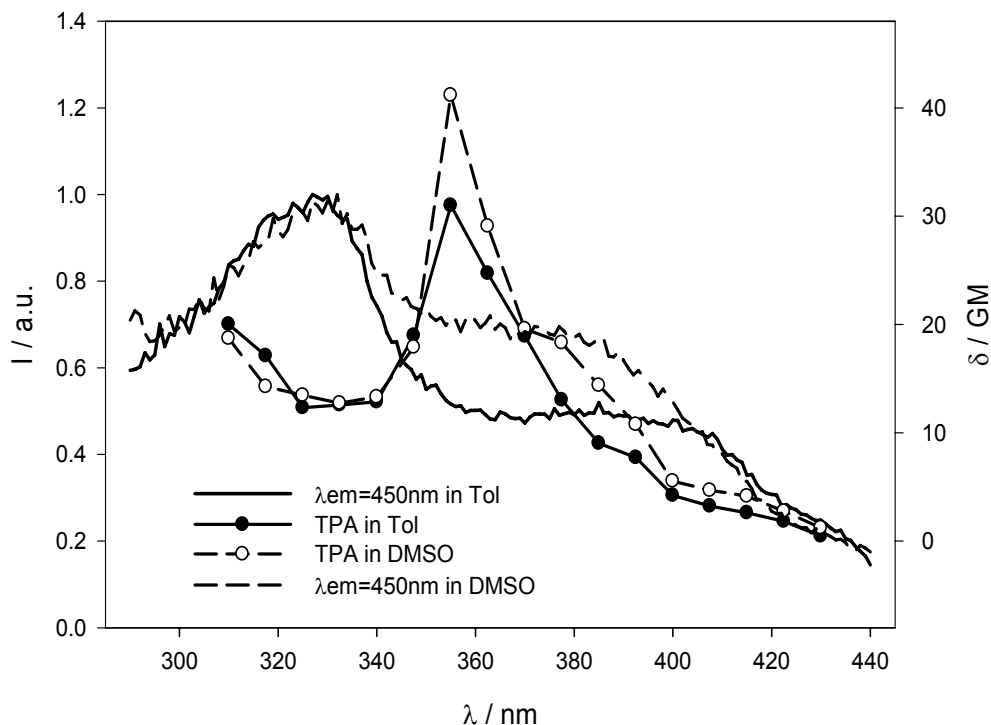


Figure 7.52. One-photon ( $\lambda_{em} = 450 \text{ nm}$ , solid lines) and two-photon (circles) excitation spectra of [3.2] cyclophane ( $c = 1.0 \times 10^{-5} \text{ M}$ ) in TOL (solid lines) and DMSO (dashed lines) at 298 K.

Table 7.2. Photophysical parameters of investigated [3.2] cyclophene in different solvents at 298 K.

	$\lambda_{\text{OPA}}^a, \epsilon^b$	$\lambda_{\text{em}}^a, \Phi$	$\tau_{\text{int}}^c$	$\lambda_{\text{TPA}}^a, \delta^d$	$\delta\Phi$
<b>Hex</b>	323, 53500	442, 0.51	1.8	710, 31	23
		502, 0.73	4.3		
<b>Tol</b>	327, 49700	452, 0.52	1.8	710, 31	28
		509, 0.90	3.6		
<b>THF</b>	325, 53200	455, 0.52	2.0	710, 42	28
		511, 0.66	6.0		
<b>ACN</b>	321, 53500	485, 0.45	2.5	710, 30	15
		515, 0.49	6.8		
<b>DMSO</b>	327, 56900	493, 0.56	2.4	710, 41	28
		524, 0.69	5.8		

<sup>a</sup> nm;<sup>b</sup> M<sup>-1</sup>cm<sup>-1</sup>;<sup>c</sup> ns;<sup>d</sup> GM.

## 8. Conjugated Polymers

### 8.1. Polyfluorene

As already stated in section 4.1., conjugated polymers are large molecules. Figure 8.1. clearly shows how  $\pi$ -electrons are delocalized along the fluorene derivative depending on its conjugation length. Therefore, fluorene dimer cannot be described in terms of two fluorene molecules and so is for any conjugated oligomer or polymer.

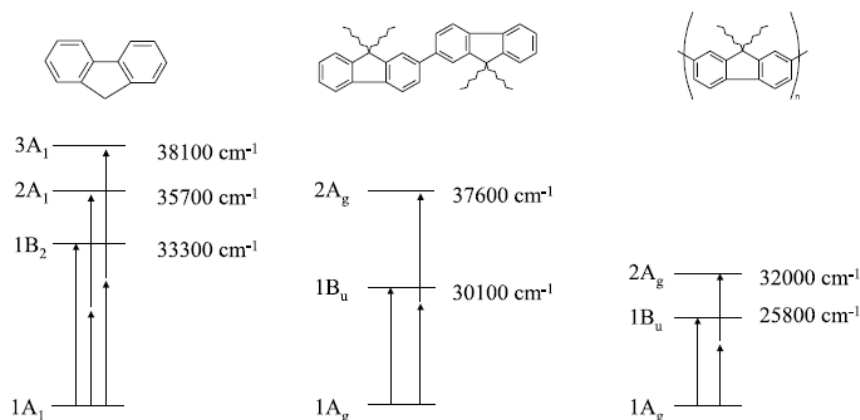


Figure 8.1. Energy level diagrams for fluorene, bifluorene, and polyfluorene.<sup>237</sup>

Polyfluorene represent an interesting class of CPs due to its high luminescence quantum yield, thermal stability, good charge-transport properties, and the possibility of fine tuning physical parameters through chemical functionalization and copolymerization (in this regard see Section 8.2.). In addition, polyfluorene undergoes easy substitution in the ninth position enabling the grafting of different side chain. Solubility in high dielectric media is achieved

[237] P.I Najechalski, Y. Morel, O. Stéphan and P. L. Baldeck, 2001, 343, 44.

functionalizing the  $\pi$ -conjugated backbone with ionic side chains. The introduction of ionic groups opened the way in using conjugated polymers (polyelectrolytes when water soluble, termed CPEs) for the development of biological detection protocols that take advantage of the optical amplification due to the collective response afforded by CPEs. Fluorescence is a highly sensitive method for optical transduction. Sensing strategy relies on the large optical cross section of CPEs (due to large number of repeated chromophoric units) in combination with a recognition event that triggers (quenching, enhancing or changing the wavelength of emission) the fluorescence of the polymeric chemosensor.

Poly[(9,9-bis-(6'-N,N,N-trimethylammoniumbromide)hexyl)fluorene] (**PFHTMABr**) and its neutral precursor Poly[9,9-bis-(6'-bromohexyl)fluorene] (**PFHBr**) are shown in Figure 8.2. Their linear and nonlinear optical properties have been investigated in order to develop new strategies for biological assays.

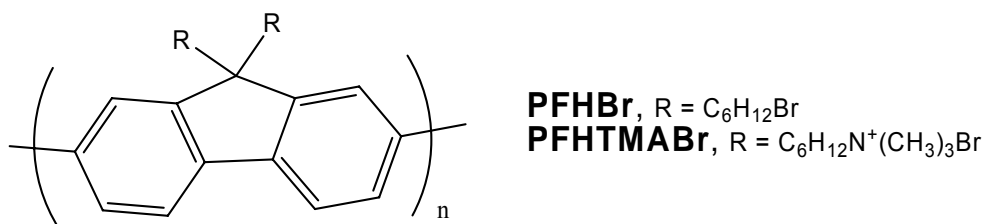


Figure 8.2. Formula of the investigated polyfluorenes.

Measurements have been carried out at the UCSB Optical Characterization Facility managed by Dr. Mikhailovsky following procedures mentioned in section 3.1. All measurements have been performed in several solvents, namely hexanes (HEX), toluene (TOL), tetrahydrofuran (THF), acetone (AC), acetonitrile (ACN), dimethylsulfoxide (DMSO), and water, to establish the solvent-dependence of polyfluorenes optical properties.

Table 8.1. Linear optical parameters of PFHBr.

<b>PFHBr</b>	$\lambda_{\max}^a, \epsilon^a$	$\lambda_{\text{em}}^a, \phi$	Stokes shift <sup>a</sup>	$\tau_{\text{exp}}^c$
Hex	385, 38500	410, 0.80	25	440
Tol	384, 35800	415, 0.83	31	450
THF	392, 38800	416, 0.79	24	460
Ac	404, 34800	438, 0.62	6	320
ACN	403, 25800	438, 0.58	5	360
DMSO	433, 22800	438, 0.54	5	350
<b>PFHTMABr</b>				
DMSO	405, 26800	423, 0.16	18	.44
H2O	396, 30900	421, 0.76	22	.43

<sup>a</sup> nm;

<sup>b</sup>  $\text{M}^{-1}\text{cm}^{-1}$  per repeated unit;

<sup>c</sup> ps,  $\lambda_{\text{ex}} = 380$  nm.

Linear absorption spectra of **PFHBr** show a progressive red shift on increasing solvent polarity; absorption spectra in poor solvents exhibit vibronic progression (Table 8.1. and Figure 8.3.). One-photon induced emission spectra show vibronic structure moving toward longer

wavelength in increasing solvent polarity (Table 8.1. and Figure 8.3.). Anyway, the Stokes shift in higher dielectric media gets smaller.

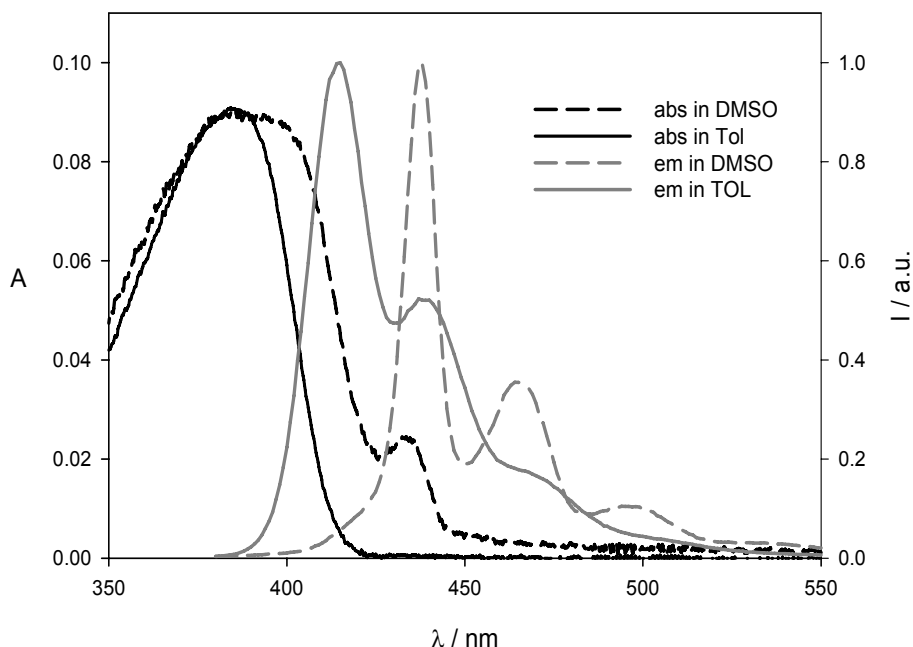


Figure 8.3. Absorption (black lines) and emission ( $\lambda_{\text{ex}} = 380 \text{ nm}$ , gray lines) spectra of PFHBr in TOL (solid lines) and DMSO (dashed lines) solutions at 298 K.

Quantum yield of **PFHBr** solutions have been measured using 9,10-diphenylanthracene as standard. Figure 8.4. shows the drop of the quantum yield of **PFHBr** on increasing solvent polarity, while the intrinsic lifetime does not show a monotonic trend. Figure 8.5. shows a long-lived excited state that emits at lower energy in more polar solvents (in TOL such a longer component is less than 1%), while exciting **PFHBr** above 500nm a long-lived excited state emits independently from excitation energy in poor solvents (in TOL no detectable emission at  $\lambda_{\text{ex}} = 433\text{nm}$ ).

Excitation spectra in all media belong resemble the absorption spectra.

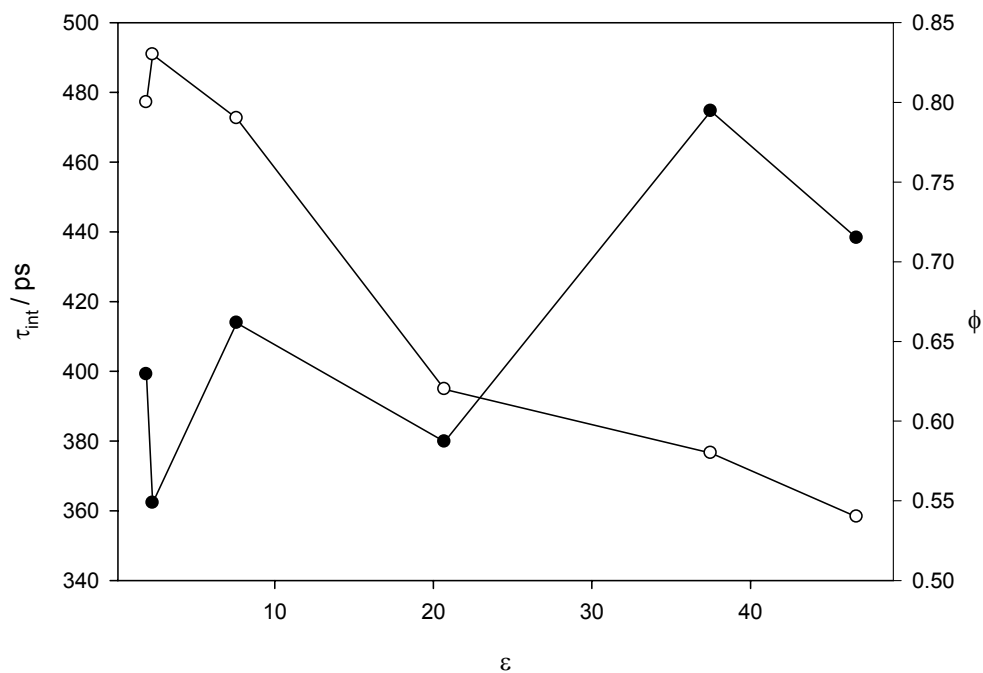


Figure 8.4. Plots of the quantum yields (empty circles) and of intrinsic lifetimes (filled circles) of PFHBr versus dielectric constant of the medium.

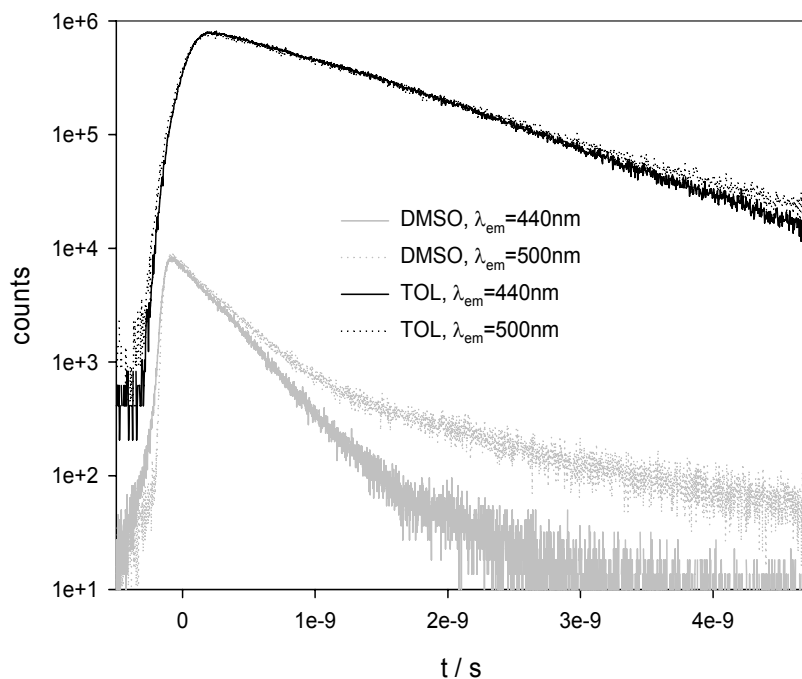


Figure 8.5. Fluorescence lifetime decay ( $\lambda_{ex} = 380\text{nm}$ ) of PFHBr in TOL (black lines) and DMSO (gray lines) solutions at 298 K.

Within the investigated range (710 – 960 nm) only the tail of the two-photon absorption spectra of **PFHBr** is detectable (Figure 8.6.). Emission spectra ( $\lambda_{\text{ex}} = 710 - 960 \text{ nm}$ ) collected to determine the cross section of **PFHBr**, come from two-photon absorption process using an average radiant power in the range 80 to 480 mW, where all samples exhibit square dependence.

**PFHBr** in higher dielectric media shows higher cross section values, but is seems to resemble the trend of linear absorption spectra. These results are indicative of the presence of a centre of symmetry in the polymeric chain: this sounds weird. Anyway for molecules with lack of centre of symmetry. the parity inversion rule for photon absorption allows the population of the same excited states via one- and two-photon absorption.

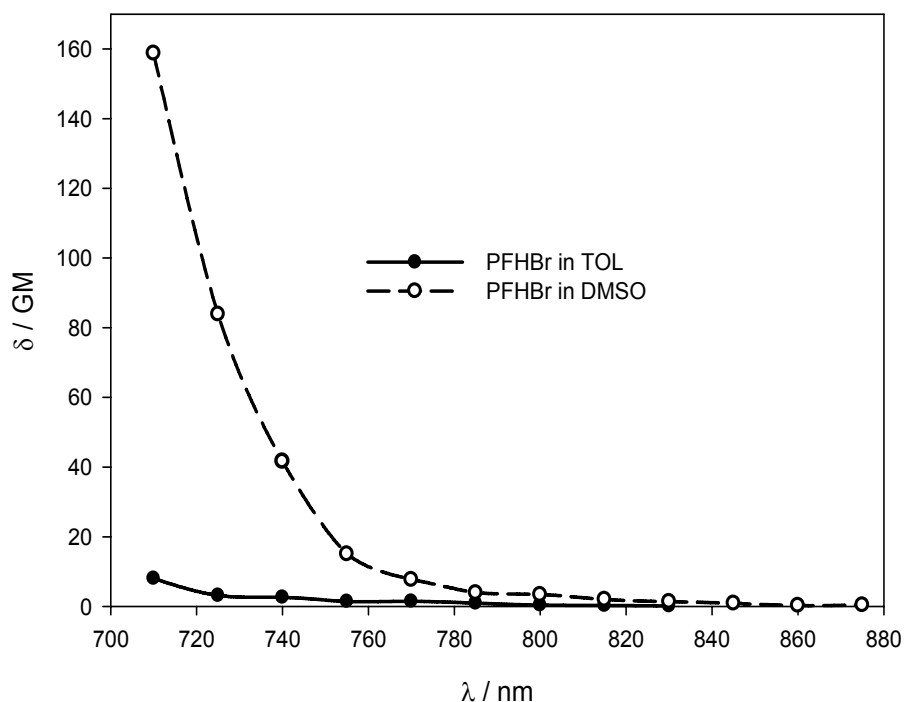


Figure 8.6. Two-photon excitation spectra of PFHBr in TOL (filled circles) and DMSO (empty circles) solutions at 298 K.

**PFHTMABr** (in Figure 8.2.) shows a blue shift in linear absorption and emission spectra in DMSO compared to its neutral homolog **PFHBr** (Table 8.1. and Figure 8.7.).

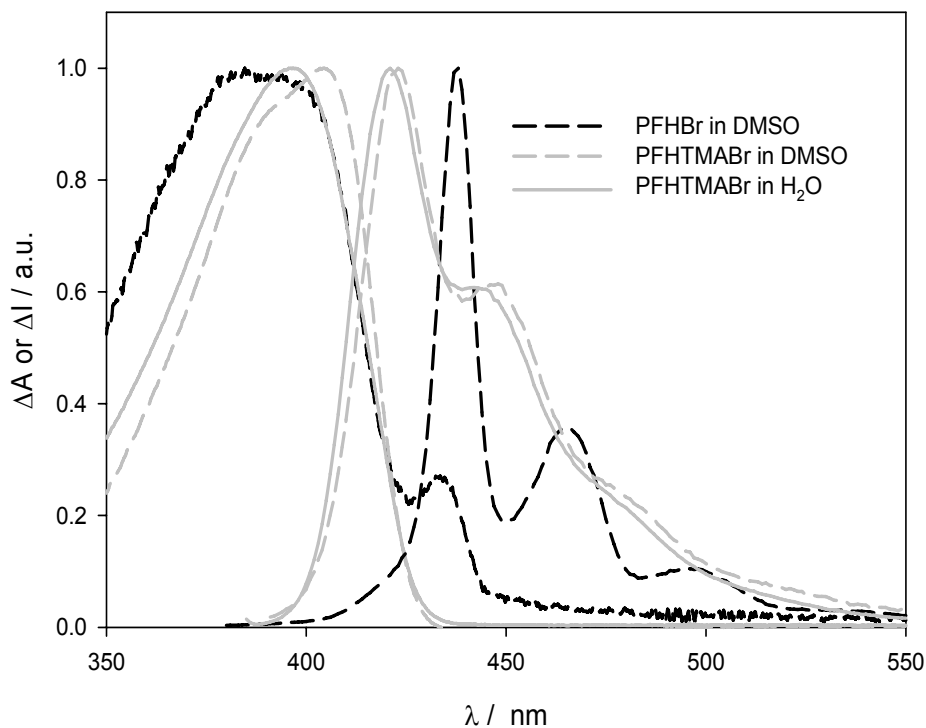


Figure 8.7. Absorption and emission spectra of PFHBr in DMSO (black lines) and of PFHTMABr in DMSO (gray dashed lines) and in water (gray solid lines) solutions at 298 K.

**PFHTMABr** shows less marked solvent dependence in both linear (Table 8.1. and Figure 8.7.) and nonlinear optical properties (Figure 8.8.). Absorption and emission spectra of **PFHTMABr** in water are blue-shifted compared to its DMSO solution; furthermore quantum yield is much higher in water and consequently the intrinsic lifetime is shorter (Table 8.1.). It is difficult to evaluate differences in two-photon excitation spectra of **PFHTMABr** in water and DMSO since only the tail of the two-photon absorption process has been detected (Figure 8.8.). TPA spectra of **PFHTMABr** and **PFHBr** in DMSO seem to resemble the onset of the absorption bands relative to their linear absorption.

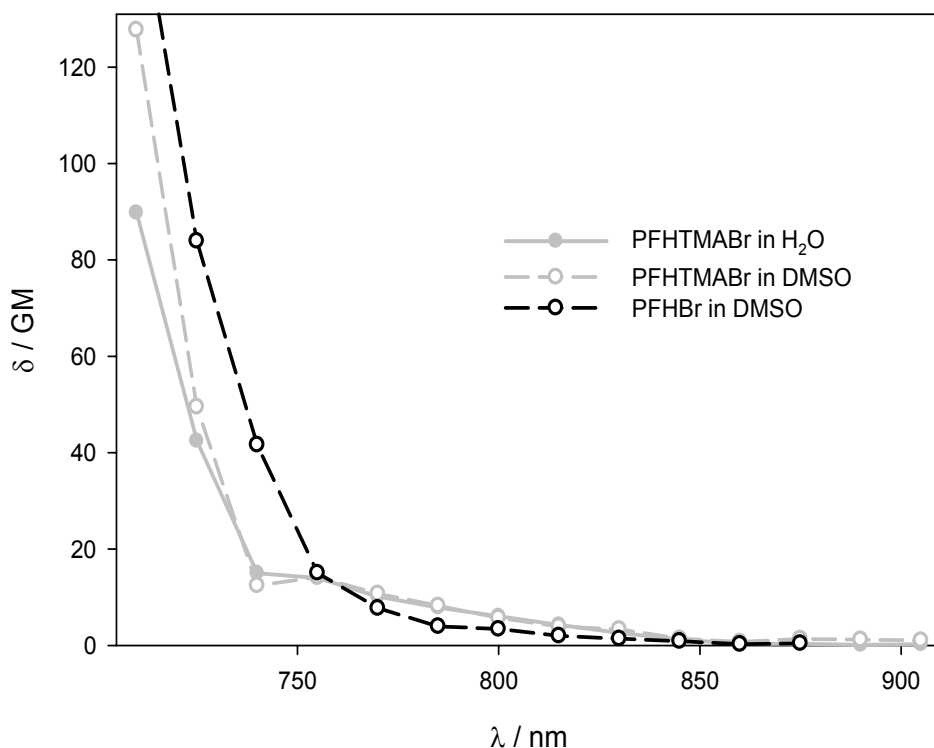


Figure 8.8. Two-photon excitation spectra of PFHTMABr in water (gray filled circles) and in DMSO (gray empty circles) and of PFHBr DMSO (black empty circles) solutions at 298 K.

It is worth noting how the active cross section of **PFHTMABr** in water is close to that obtained for **PFHBr** in low polarity solvents because of their high quantum yield of radiative decay. The reliability of the latter consideration is fully confirmed by the results simultaneously obtained by Tian and Xu <sup>94</sup> mentioned in section 4.5.

A tentative explanation to the observed solvent dependence for the investigated polyfluorenes may reside in interchain interactions. Hydrophobic interactions, in fact, increase raising solvent polarity. Poor solvents force polyfluorene chains to closer proximity leading to higher delocalization of the exciton. Concentration dependence measurements of linear emission and excitation spectra of these polyfluorene have been performed, but failed in providing explanations. Anyway, depletion of fluorescence quantum yield of polyfluorene coming with longer intrinsic radiative lifetime, red shift of the vibronic transitions in both linear absorption

and emission spectra and smaller Stokes shifts in increasing solvent polarity account for aggregates formation in poor solvents. Since the ionic groups introduced on the side chain cannot affect the electronic properties of the conjugated backbone, the differences observed between neutral and charged polyfluorenes may account for different interchain interactions. The more the solvent polar the more it is poor in the case of **PFHBr**, while for **PFTMAHBr** DMSO represents a less good solvent than water. Colloidal suspension in poor solvents solutions is observable by eyes, increasing concentration or minutes to hours after sample preparation.

Interchain interactions are known to play a relevant role in determining optical properties of conjugated polymers both in solution and in solid and the investigated **PFHBr** and **PFTMAHBr** do not make exception: conjugated polymer structures that change emission color as a result of conformational and aggregation changes may serve to allow energy migration to low-lying energy excited state. Conformational changes and aggregation are encouraged taking advantage of conjugated polyelectrolytes binding with oppositely charged biomolecules due to electrostatic interactions. Bringing chains together led to the possibility of realizing multicolour bioassays.<sup>238</sup>

---

[238] a) Bin Liu and Guillermo C. Bazan *J. Am. Chem. Soc.*, 2004, 126, 1942; b) Chi, C.; Mikhailovsky, A.; Bazan, G. C. *J. Am. Chem. Soc.*, 2007; 129, 11134.

## 8.2. Fluorene-based Conjugated Copolymers

Conjugated polyelectrolytes (CPEs) are water soluble organic semiconductors, where semiconducting properties are related to the delocalization of  $\pi$  molecular orbitals along the polymeric backbone and solubility in high dielectric media is achieved functionalizing such a  $\pi$ -conjugated backbone with ionic side chains so providing new features in the fabrication of optoelectronic devices by multilayer deposition<sup>239</sup> and in biological<sup>240</sup> and analytical<sup>86</sup> sensing.

Copolymerization of fluorene enable the spreading of exploitation of one-dimensional delocalized electronic structures that allow for electronic coupling between optoelectronic segments and efficient intra- and inter-chain energy transfer. An investigation of one- (OPA) and two-photon absorption (TPA) and consequent induced emission processes of a fluorene copolymer alternating benzothiadiazole (BT) units is here presented: Poly[(9,9-bis-(6'-N,N,N-trimethylammoniumbromide)hexyl)fluorene-*a*/*t*-4,7-(2,1,3-benzothiadiazole)]<sup>241</sup> (**C**) and its neutral precursor Poly[9,9-bis-(6'-bromohexyl)fluorene-*a*/*t*-4,7-(2,1,3-benzothiadiazole)]<sup>242</sup> (**N**) are shown in the Figure 8.9. TPA is attracting considerable attention since its probability is proportional to the square of the incident light intensity resulting in the confinement to the focal point of the absorption as well as the up-converted luminescence: these features lead to promising applications for optical data storage,<sup>243</sup> microfabrication techniques,<sup>244</sup> photodynamic therapy,<sup>245</sup> two-photon induced fluorescence microscopy.<sup>246</sup>

---

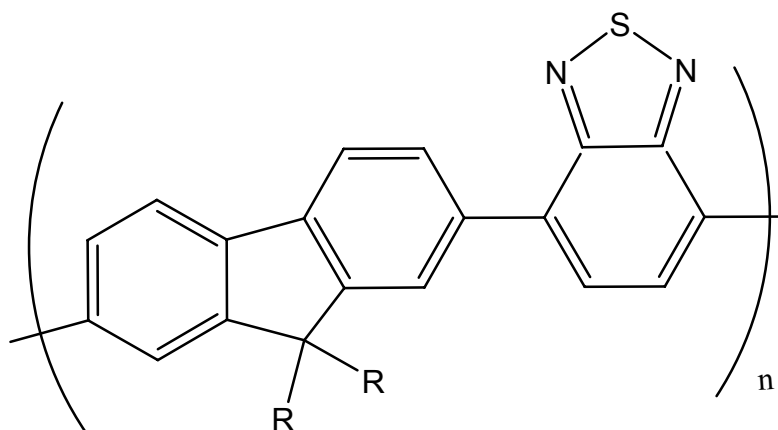
[239] W. Ma, P. K. Iyer, X. Gong, B. Liu, D. Moses, G. C. Bazan, A. J. Heeger *Adv. Mater.* 2005, 17, 274.

[240] Liaohai Chen, Duncan W. McBranch, Hsing-Lin Wang, Roger Helgeson, Fred Wudl, and David G. Whitten *PNAS*, 1999, 22, 12287.

[241] Yang, R.; Garcia, A.; Korystov, D.; Mikhailovsky, A.; Bazan, G. C.; Nguyen, T.-Q. *JACS* 2006, 128, 16532.

[242] L. Bin, and G. C. Bazan *PNAS*, 2005, 102, 589.

[243] Brian H. Cumpston, Sundaravel P. Ananthavel, Stephen Barlow, Daniel L. Dyer, Jeffrey E. Ehrlich, Lael L. Erskine, Ahmed A. Heikal, Stephen M. Kuebler, I.-Y. Sandy Lee, Dianne



**N**,  $R=C_6H_{12}Br$

**C**,  $R=C_6H_{12}N^+(CH_3)_3Br^-$

Figure 8.9. Formula of the investigated conjugated copolyelectrolytes.

Choice of this copolymeric material arises from the presence of the BT whose electron-acceptor (A) character it's due to the presence of two imine electron-withdrawal units so resulting in an  $(-A-\pi)_n$  alternating structure, where fluorene moieties act as  $\pi$ -conjugated spacers, that should lead to high TPA cross section values related to its predictable intramolecular charge transfer (ICT) character upon excitation.<sup>247</sup> TPA is a powerful tool in identifying excited states occurring above the lowest optical exciton and involved in exciton confinement in conjugated polymers that could affect charge transport ability in optoelectronic

---

McCord-Maughon, Jinqi Qin, Harald Röckel, Mariacristina Rumi, Xiang-Li Wu, Seth R. Marder, Joseph W. Perry *Nature* 1999, 398, 51.

[244] Maruo, Shoji; Nakamura, Osamu; Kawata, Satoshi *Opt. Lett.* 1997, 22, 132.

[245] Frederiksen, P. K.; Jorgensen, M.; Ogilby, P. R. *JACS* 2001, 123, 1215.

[246] W. Denk, J. H. Strickler, and W. W. Webb *Science* 1990, 248, 73.

[247] M. Albota, D. Beljonne, J.-L. Brédas, J. E. Ehrlich, J.-Y. Fu, A. A. Heikal, S. I. E. Hess, T. Kogej, M. D. Levin, S. R. Marder, D. McCord-Maughon, J. W. Perry, H. Röckel, M. Rumi, G. Subramaniam, W. W. Webb, X.-Li Wu, and C. Xu *Science* 1998, 281, 1653.

devices.<sup>248</sup> Moreover, focalization of excitation and emitted light combined to less scattering and autofluorescence upon IR excitation of living tissues providing deep sample penetration render two-photon induced fluorescence microscopy exponentially growing;<sup>249</sup> CPEs are known to give non-specific interactions with biological substrates<sup>250</sup> making their use as fluorescent tags for two-photon imaging of biological samples promising.

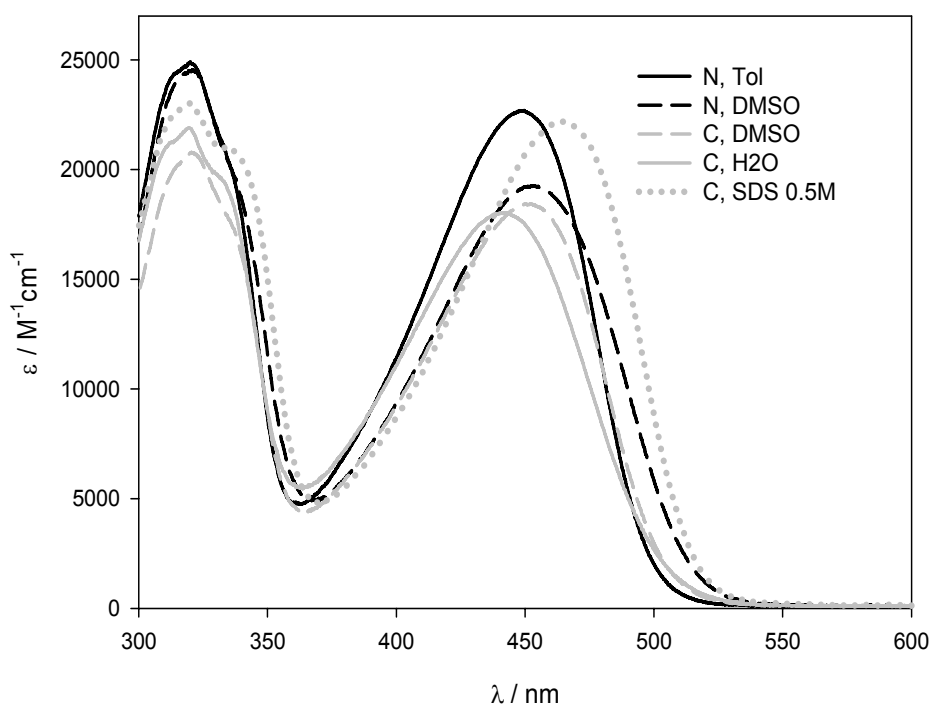


Figure 8.10. Linear absorption spectra of N and C: line styles in legend are associated to the solvent used.

[248] A. Kohler, D. A. dos Santos, D. Beljonne, Z. Shuai, J.-L. Bredas, A. B. Holmes, A. Kraus, K. Mullen, R. H. Friend *Nature*, 1998, 392, 903.

[249] W. R. Zipfel, R. M. Williams, W. W. Webb *Nature Biotechnology*, 2003, 21, 1369.

[250] Bronich, T. K.; Nguyen, H. K.; Eisenberg, A.; Kabanov, A. V. *JACS*, 2000, 122, 8339.

Photophysical processes in solution and in the solid state are greatly affected by polymer chain conformation and interchain interactions so variations in the surrounding medium could give informations on polymer conformational arrangements through differences observed in its optical and electronic properties.

Linear absorption spectra of dilute solutions of the investigated polymer are characterized by two bands (Figure 8.10.) generally attributed to a  $\pi \rightarrow \pi^*$  transition delocalized along the polymer backbone in the UV region and a charge transfer transition in the blue region where the excited state is localized on the benzothiadiazole moiety due to the large energy separation between LUMOs of fluorene and BT monomers, thus giving rise to weak interaction between the two polymer building blocks at the excited state.<sup>251</sup> One-photon induced fluorescence spectra (Figure 8.11.a.) confirm the intramolecular charge transfer character of the first excited state: positive solvatochromism arises from a better solvation of the radiative excited state where electron is localized on BT units upon photoexcitation, accompanied by decrease in quantum yield and consequent increase in intrinsic lifetime ( $\lambda_{em}$ ,  $\Phi$ , and  $\tau_{int}$  are reported in Table 8.2.).

Figure 8.15. shows broadening of the first absorption band toward longer wavelengths in going from good to poor solvent solution; introducing ionic groups on the side chains leads to stretch such an absorption band almost matching spectrum obtained in toluene These findings indicate formation of lower-lying energy states in neutral polymer in poor solvents due to interchain aggregates at the ground state, while ionizing side chains confers better solubility in DMSO to the polyelectrolyte **C**. Interchain interactions are also present at the excited state in **N** in DMSO: a shorter component in its radiative decay can be roughly attributed to excimers formation between fluorene monomers because of the analogies with polyfluorene, while **C** in DMSO decays monoexponentially (Figure 8.12.a.).

---

[251] J. Cornil, I. Gueli, A. Dkhissi, J. C. Sancho-Garcia, E. Hennebicq, J. P. Calbert, V. Lemaur, D. Beljonne, and J. L. Brédas *J. Chem. Phys.*, 2003, 118, 6615.

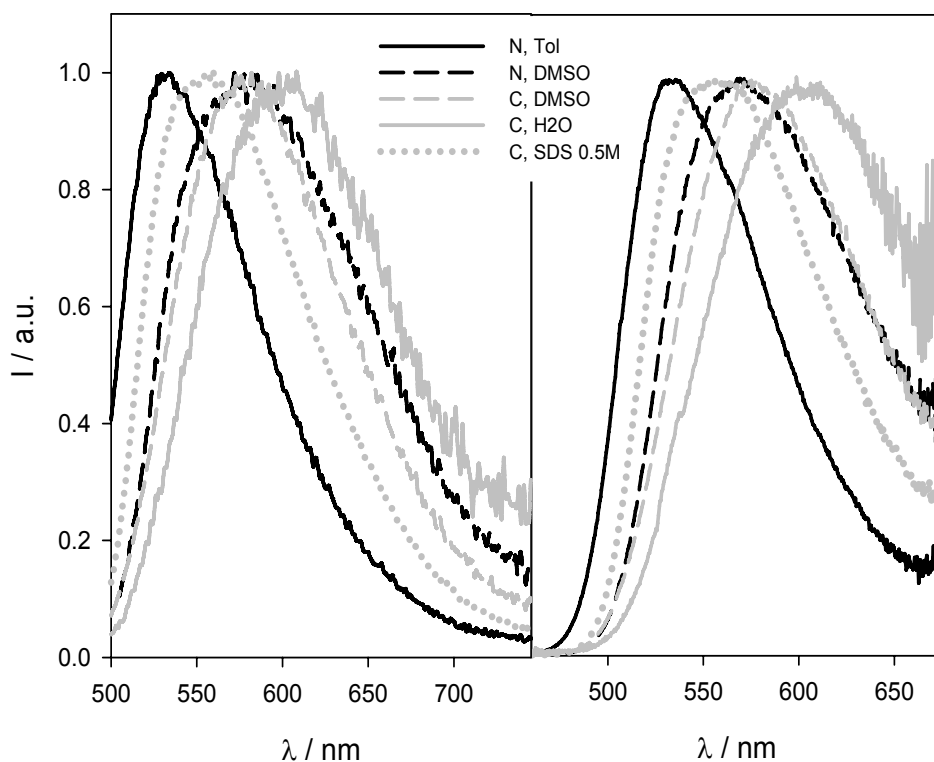


Figure 8.11. Emission spectra of **N** and **C** 10 to 15  $\mu\text{M}$  upon a) one-photon excitation ( $\lambda_{\text{ex}} = 400 \text{ nm}$ ) and b) two-photon excitation ( $\lambda_{\text{ex}} = 800 \text{ nm}$ ). All spectra in a) are corrected for both lamp and detector profile; all spectra in b) are corrected for grating response and BG filter. Legend assigns line styles to solvent used.

In water instead, maximum of the first absorption band is blue shifted (Table 8.2.) while the electronic transition in the UV region is almost unaffected: maybe water induces a partial restriction in the conjugation length due to conformational arrangements in the attempt of screening the hydrophobic backbone. When sodium dodecyl sulfate was added in water solution of **C** since reaching saturation effect (0.5 M) a great decrease in the Stokes shift and an increase in the quantum yield (Table 8.2.) of the radiative, now monoexponential (Figure 8.12.b.), decay process are observed, consistent with inclusion of the polymer chains into micelles and consequently preventing detrimental interactions with water; anyway, spectral features of **C** in micellar solution are different from those characterizing **N** in toluene dilute

solution where polymer chains are assumed to be isolated and so interchain interactions negligible.<sup>252</sup>

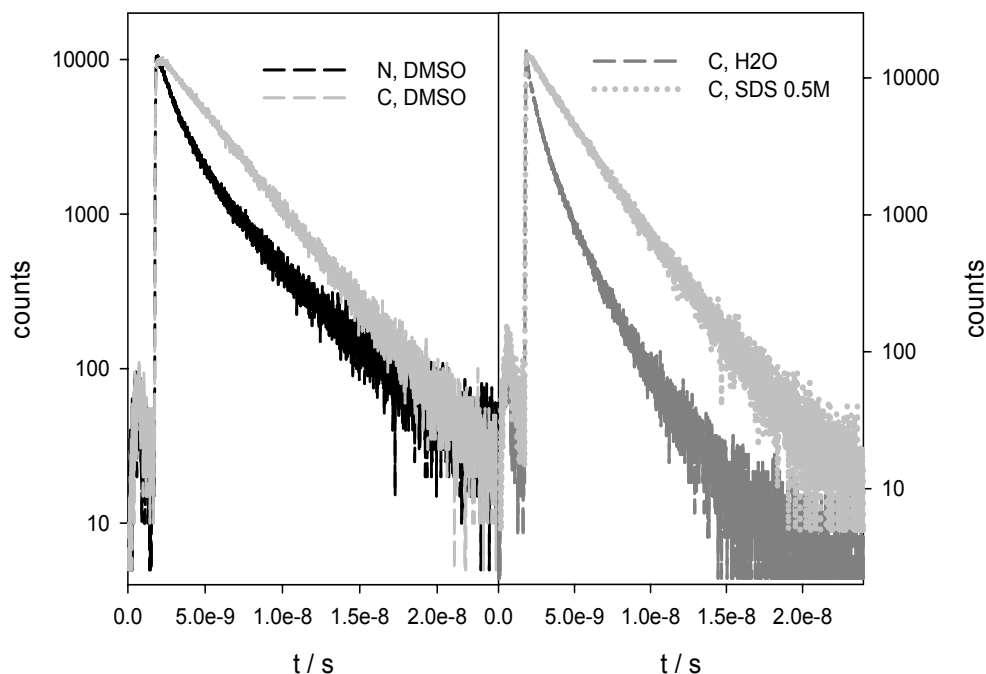


Figure 8.12. Fluorescence decays of a) N and C in DMSO, and b) of C in water and in SDS 0.5 M. Sample concentration ranges between 10 to 15  $\mu\text{M}$ .  $\lambda_{\text{ex}} = 400 \text{ nm}$ . Legend assigns line styles to solvent used.

Mixing the semiconductor band-theory where delocalized electron-hole pairs are produced upon photoexcitation with the molecular picture where electron-hole pairs are confined and strongly bound by Coulomb interactions produces a configuration-interaction description of the intrachain exciton ground state where the electron is confined on the BT moiety and the hole is delocalized on the conjugated backbone of the examined polymer.<sup>253</sup>

[252] Woo, H. Y.; Korystov, D.; Mikhailovsky, A.; Nguyen, T.-Q.; Bazan, G. C. *JACS*, 2005, 127, 13794.

[253] K. G. Jespersen, W. J. D. Beenken, Y. Zaushitsyn, A. Yartsev, M. Andersson, T. Pullerits, and V. Sundström *J. Chem. Phys.*, 2004, 121, 12613

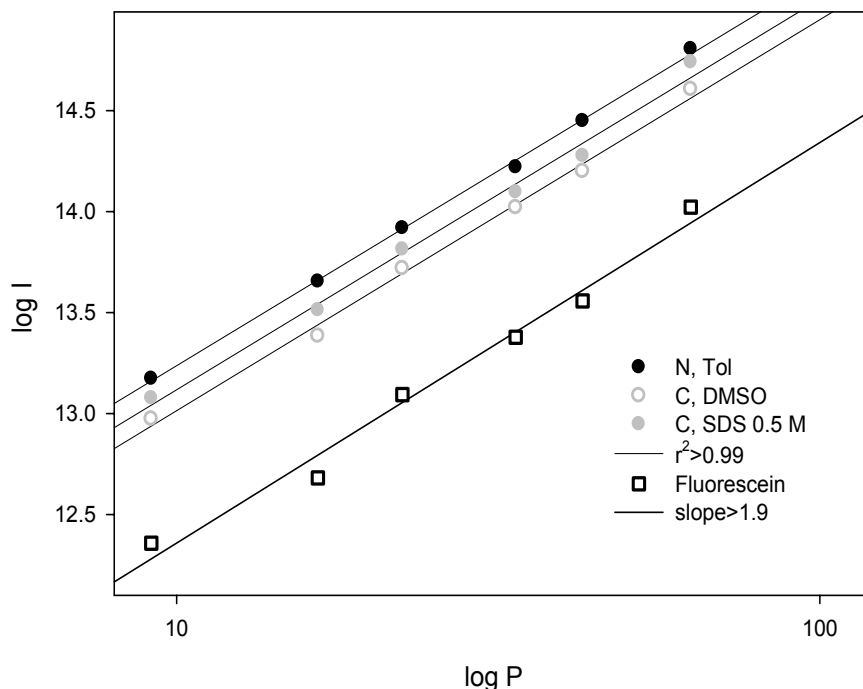


Figure 8.13. Logarithmic plot of the two-photon absorption induced fluorescence intensities of N and C ), and of Fluorescein pH=11 as reference compound (empty squares) vs. excitation light power intensities at 800 nm. Fitting produces slopes close or higher than 1.9 with linear correlation coefficients around 0.99. Legend assigns line styles and symbols relative to the solvent where sample have been dissolved.

The role of higher excited states in charge separation process was pointed out by Kohler and al.<sup>248</sup> for another conjugated polymer (a PPV derivative) involving such a configuration-interaction approach. Upon two-photon excitation (Figure 8.13.), provided by femtosecond laser pulses as previously described in literature,<sup>254</sup> higher-lying transitions are induced in the polymeric material; since a photon carries angular momentum characterized by two possibilities ( $\pm h/2\pi$ ) photoinduced electronic transitions between states which differ by  $\pm 1$  in orbital angular momentum quantum number are allowed, so two-photon absorption will obey to selection rules where symmetry-allowed transitions are characterized by  $\Delta L=0, \pm 2$ .

[254] see Section 3.1.7. and references therein.

Orbital angular momentum quantum number expresses the symmetry of the molecular orbitals so the lack of overlap between OPA and two-photon excitation spectra suggests the presence of a centre of symmetry in the here investigated polymer (Figures 8.15. and 8.16.).

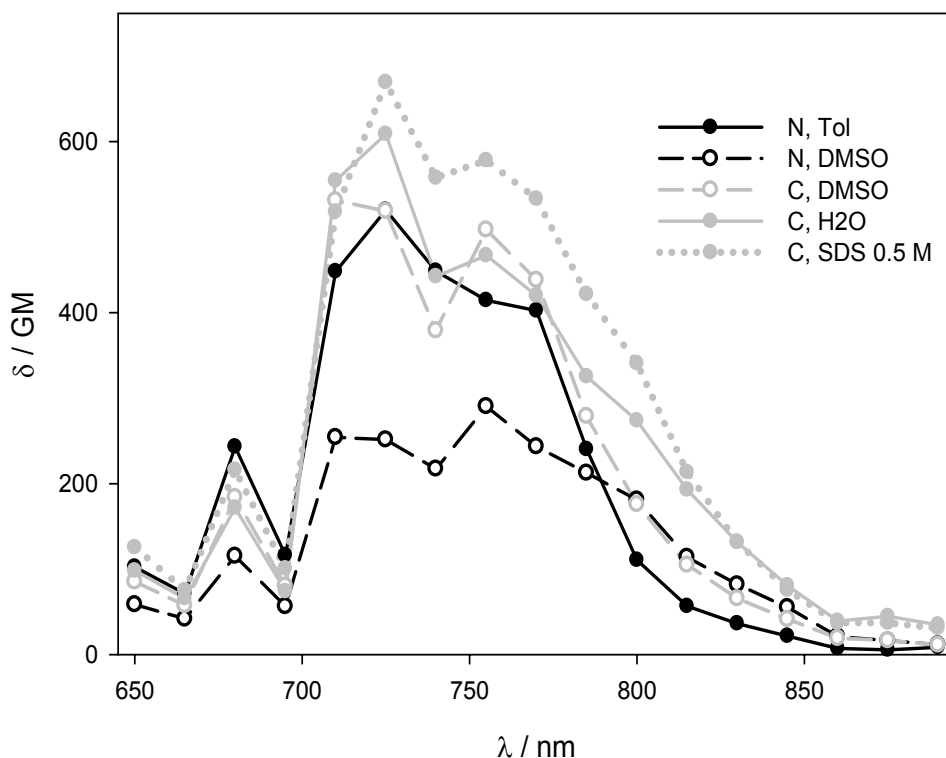


Figure 8.14. Two-photon absorption spectra of N and C. Legend assigns line styles and symbols relative to the solvent where sample have been dissolved.

Conjugated polymer generally belong to the  $C_{2h}$  point group where exciton ground state is labeled as  $1^1B_u$  while even-parity higher excited states ( $m^1A_g$ , where  $m$  is an unknown quantum number) are reached upon two-photon excitation. Two-photon absorption induced fluorescence spectra substantially match fluorescence spectra obtained upon linear excitation (Figure 8.11.) due to rapid thermal relaxation of exciton excited states to the emissive exciton ground state. This internal conversion process has been assumed unitary efficient in order to have the same fluorescence quantum yield upon both one- either two-photon excitation so making possible

assigning dimensionality to the two-photon excitation spectra (GM units on the y-axis in Figure 8.14.): this assumption is based on the exact superimposition of linear absorption and excitation spectra above 340 nm (data not shown) so within the wavelength range where electronic transitions induced by two-photon absorption have been recorded. Figure 8.15. shows normalized linear and two-photon excitation spectra of fluorene-BT copolymer in organic solvents: it is evident how the two-photon absorption processes occur where the linear ones are symmetry-forbidden and vice versa.

The energy difference between  $1^1B_u$  and  $m^1A_g$  excited states of  $\sim 0.5$  eV sets the lower limit for exciton binding energy and represents a non negligible correction to the band-gap. The trend in the onset in two-photon excitation spectra is conserved compared to OPA due to the appearance of a peak centered around 380 nm for **N** in DMSO solution that is less pronounced when the copolymer is in good solvent solution: interchain exciton contribution could account for the formation of this lower-lying excited state. The probability of the two-photon absorption process in the sum-over-state approximation is related to the transition dipole momenta in reaching the final excited state through a virtual one;<sup>255</sup> in Figure 8.15. is shown how the TPA cross section in the case of **N** in DMSO is almost the half compared to **N** in toluene and **C** in DMSO that could be due to a failure in stating the same quantum yield for one- and two-photon induced fluorescence because higher delocalization of the lower-lying interchain exciton may result in an increase in mixing with more charge-separated states thus reducing internal conversion process to the emissive state and so leading to underestimate cross section values. Further confirmation arises by deviation from quadratic dependence of the two-photon induced fluorescence intensity of the sample in poor solvent solution to the pump fluence even though  $\beta_{\text{eff}} \ll 1$  is still valid.

Measurements performed at  $\lambda_{\text{ex}} = 710$  nm at higher pump fluences provided by regenerative amplification show a consistent divergence from quadratic dependence of the two-

---

[255] Shen, Y.R. *The Principles of Nonlinear Optics*, 1984, Wiley, New York.

photon induced luminescence intensity of **N** in DMSO solution, while does not occur in **N** in toluene and **C** in DMSO.

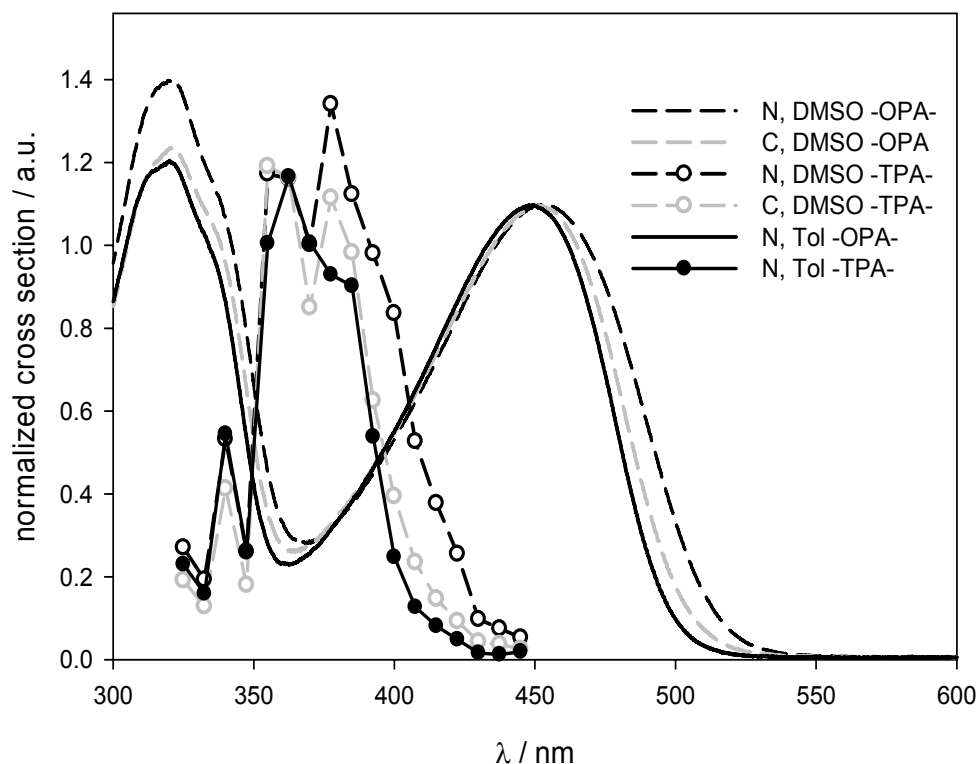


Figure 8.15. Normalized linear absorption spectra of **N** (black lines) and **C** (gray line) and two-photon excitation spectra of **N** (black circles) and **C** (gray circles) in TOL (solid lines) and in DMSO (dashed lines). Sample concentration ranges between 10 to 15  $\mu\text{M}$ .

Friend and coworkers showed efficient exciton dissociation occurring after sequential excitation to higher-lying excited states during ultrafast adiabatic relaxation provided by trailing edge of the pump pulses<sup>256</sup> and through exciton-exciton annihilation via collision-like either energy transfer processes.<sup>257</sup>

[256] C. Silva, A. S. Dhoot, D. M. Russell, M. A. Stevens, A. C. Arias, J. D. MacKenzie, N. C. Greenham, R. H. Friend, S. Setayesh and K. Müllen *Phys. Rev. B*, 2001, 64, 125211.

[257] M. A. Stevens, C. Silva, D. M. Russell, and R. H. Friend *Phys. Rev. B*, 2001, 63, 165213.

The former exciton depopulation mechanism can be ruled out because square dependence of the fluorescence signal to the pump fluence shown by **N** in toluene and **C** in DMSO suggests that no other significant pathway for exciton non-radiative decay is reached at the fluences here used; furthermore, this sort of three-photon absorption process requires saturation of the ground state population that is not supposed to be affected by surrounding medium. Aggregation phenomena in poor solvent solution could overcome diffusion-limiting of bimolecular processes; in agreement with previous results exciton-exciton annihilation could be responsible for the depopulation of the emissive state leading to higher even-parity excited states lying in the continuum band so that electron-hole separation is achieved in the investigated copolymer. Figure 8.16. shows, instead, comparison between OPA and TPA in water.

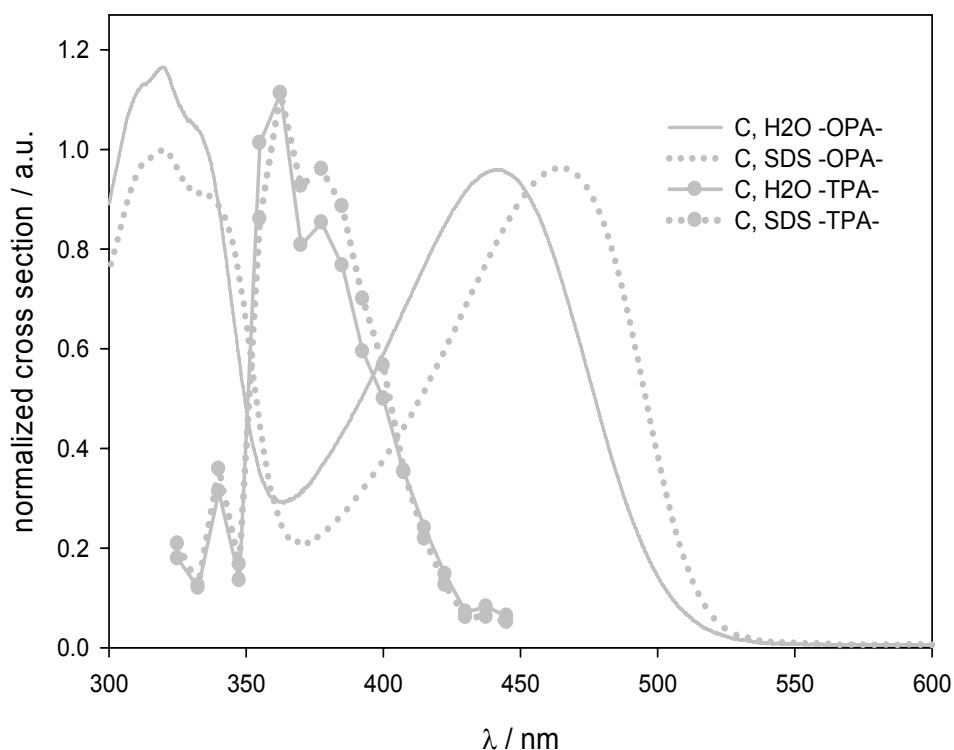


Figure 8.16. Normalized linear and two-photon absorption spectra of C in water (solid lines) and in SDS 0.5 M (dotted lines). Sample concentration ranges between 10 to 15  $\mu$ M.

It's noticeable how red shift in OPA spectrum upon surfactant addition does not occur in two-photon excitation spectrum, and cross sections of both linear and nonlinear processes are slightly higher than in mere water solution. Exciton bimolecular annihilation and subsequent charge generation are supposed to occur also in water solution as indicated by non-square dependence of two-photon induced fluorescence intensity at high pump fluences; it's noteworthy how excited states dynamics is not altered by inclusion in micelle of the polyelectrolyte chain.

Quasi one-dimensional systems are characterized by enhanced Coulomb interactions leading to higher exciton confinement thus exciton binding energy constitutes a relevant fraction of the band gap. Charge transport phenomena require electron-hole spatial separation so photoconductivity in conjugated polyelectrolytes should be very sensitive to the applied electric field. Exciton excited states energy does not result to be affected by surrounding medium polarity suggesting higher electron-hole pairs delocalization compared to the exciton ground state. Anyway, interchain interactions both at the ground and at the excited states can result in potentially efficient carrier generation and enhanced mobility having implications in the fabrication of electrically pumped polymer lasers and photodetection devices.

Table 8.2. Photophysical parameters of investigated conjugated copolyelectrytes in different solvents at 298 K.

	$\lambda_{OPA}^a, \epsilon^b$	$\lambda_{em}^a, \phi$	$\tau_{int}^c$	$\lambda_{TPA}^a, \delta^d$	$\delta\phi^d$
<b>N, Tol</b>	449, 22700	532, 0.93	1.9	725, 520	485
<b>N, DMSO</b>	453, 19400	572, 0.50	1.4, 5.0	725, 250	125
<b>C, DMSO</b>	450, 18500	577, 0.71	3.5	725, 520	370
<b>C, H2O</b>	441, 18000	592, 0.08	2.3, 9.6	725, 610	48
<b>C, SDS 0.5M</b>	465, 22200	560, 0.61	3.2	725, 670	410

<sup>a</sup> nm;

<sup>b</sup> M-lcm-l;

<sup>c</sup> ns;

<sup>d</sup> GM.





## **9. List of Publications**